Alma Mater Studiorum · Università di Bologna
Université de Caen Basse-Normandie

FACOLTÀ DI SCIENZE MATEMATICHE, FISICHE E NATURALI

Dottorato di Ricerca in Fisica
Ciclo XXIV
Settore concorsuale: 02/A1
Settore scientifico disciplinare: FIS/04

Doctorat: Constituants élémentaires et physique théorique
Ecole Doctorale SIMEM

Towards a Reconstruction of Thermal Properties of Light Nuclei from Fusion-Evaporation Reactions

Presentata da
Dott. Giorgio Baiocco

Relatore:
Prof. Mauro Bruno

Directrice de thèse:
Prof. Francesca Gulminelli

Coordinatore del Dottorato:
Prof. Fabio Ortolani

Esame Finale anno 2012

Contents

Abstract

This thesis has been developed in the framework of a new experimental campaign, recently proposed by the NUCL-EX Collaboration (INFN III Group), in order to progress in the understanding of the statistical properties of light nuclei, at excitation energies above particle emission threshold, by measuring exclusive data from fusion-evaporation reactions. These properties notably include the excitation energy dependence of the nucleon effective mass, symmetry energy and pairing correlations. In particular, the determination of the nuclear level density in the $A \sim 20$ region, the understanding of the statistical behavior of light nuclei with excitation energies ~ 3 $A.MeV$, and the measurement of observables linked to the presence of cluster structures of nuclear excited levels are the main physics goals of this work.
On the theory side, the contribution to this project given by this work consists in the development of a dedicated Monte-Carlo Hauser-Feshbach code for the evaporation of the compound nucleus, which explicitly includes all the experimentally measured particle unstable levels from the online archive NUDAT2, and which provides highly constrained predictions to be compared to data, in order to extract quantitative information on the quantities of interest.
Simulations performed with this statistical decay code have been at the basis of an experimental proposal to the PAC - Physical Advisory Committee - of *Laboratori Nazionali di Legnaro* - LNL - INFN, and the reaction $^{12}C + ^{12}C$ at 95 MeV beam energy provided by the LNL Tandem XTU accelerator has been measured, using the GARFIELD+Ring Counter(RCo) apparatuses. The experimental part of this thesis consisted in the participation to the measurement, from the beam-time request to the data taking, data reduction, detector calibrations and data analysis. Several results of the data analysis are presented in this thesis, together with a theoretical study of the system, performed with the new statistical decay code.
As a result of this work, constraints on the nuclear level density at high excitation energy for light systems ranging from $\sim C$ up to Mg are given. Moreover, pre-equilibrium effects, tentatively interpreted as α-clustering effects, are put in ev-

idence, both in the entrance channel of the reaction and in the dissipative dynamics on the path towards thermalisation.

Riassunto

Questo lavoro di tesi si inserisce nell'ambito di una campagna sperimentale, proposta dalla collaborazione NUCL-EX (INFN - Gruppo III), volta ad un avanzamento nella comprensione delle proprietà statistiche dei nuclei leggeri, a energie di eccitazione superiori alla soglia di emissione di particella, mediante misure esclusive di reazioni di fusione - evaporazione. Queste proprietà includono la dipendenza dall'energia di eccitazione della massa effettiva del nucleone, dell'energia di simmetria e dell'interazione di *pairing*. In particolare, gli obiettivi di questa tesi sono la determinazione della densità dei livelli nella regione di massa $A \sim 20$, la comprensione del comportamento statistico di nuclei leggeri ad energie di eccitazione $e^* \sim 3\ A.MeV$, e la misura di osservabili legate alla presenza di strutture a *cluster* di livelli eccitati.
Sul fronte teorico, il contributo di questa tesi consiste nello sviluppo di un codice di decadimento statistico Monte-Carlo Hauser-Feshbach, per simulare l'evaporazione del nucleo composto, che include esplicitamente tutti i livelli sperimentali misurati raccolti nell'archivio *online* NUDAT2. Attraverso il confronto tra le previsioni di questo codice e i dati sperimentali, è possibile ottenere dei *constraint* sulle quantità fisiche di interesse. Le simulazioni effettuate con il codice evaporativo sono state alla base di una proposta di esperimento, presentata al PAC - *Physical Advisory Committee* - dei Laboratori Nazionali di Legnaro - LNL - INFN, e la reazione $^{12}C +^{12} C$, a un'energia di fascio di 95 MeV, è stata misurata con il *set-up* sperimentale GARFIELD+Ring Counter(RCo).
La parte sperimentale di questo lavoro di tesi è consistita nella partecipazione alla misura, in tutte le sue fasi dalla proposta alla presa dati, dalla calibrazione dei rivelatori fino all'analisi. In questa tesi sono presentati i risultati dell'analisi dati, e uno studio teorico del sistema, ottenuto con il nuovo codice evaporativo.
Come risultato dell'analisi, è possibile dare dei *constraint* per la densità dei livelli, nella regione di masse e cariche esplorata dal decadimento (dal $\sim C$ al $\sim Mg$). Inoltre, vengono evidenziate delle deviazioni da un comportamento statistico del

decadimento, sia nel canale di ingresso, legate quindi alla struttura a *cluster* dei *partner* della rezione, che in processi più dissipativi, con l'emissione di *cluster* dal sistema fuso prima del raggiungimento della termalizzazione.

Résumé

Ce travail de thèse se situe dans le cadre d'une campagne expérimentale, proposée par la collaboration NUCL-EX (INFN, 3*ème* Groupe), dont le but est de progresser dans la compréhension des propriétés statistiques des noyaux légers, à des énergies d'excitation au-dessus du seuil d'émission des particules, par le biais de la mesure de données exclusives pour des réactions de fusion-évaporation. Les propriétés d'intérêt incluent notamment la dépendance en énergie d'excitation de la masse effective du nucléon, de l'énergie de symétrie et des corrélations d'appariement. Plus en particulier, les objectives de ce travail sont la détermination de la densité des niveaux dans la région de masse $A \sim 20$, la compréhension du comportement statistique des noyaux légers avec des énergies d'excitation ~ 3 $A.MeV$, et la mise en évidence des effets liés à la presence d'une structure cluster pour certains niveaux nucléaires.
En ce qui concerne la partie théorique de ce travail de thèse, nous avons développé un code Monte - Carlo Hauser - Feshbach, pour l'évaporation du noyau composé, qui inclut d'une façon explicite tous les niveaux mesurés expérimentalement, disponibles dans l'archive en ligne NUDAT2. A l'aide de ce code nous obtenons des prédictions directement comparables aux données expérimentales, afin de contraindre les quantités physiques en jeu.
Les simulations qui ont été effectués avec ce code ont étées à la base d'une proposition d'expérience aux *Laboratori Nazionali di Legnaro* - LNL - INFN, et la réaction $^{12}C +^{12} C$, à une energie de faisceau de 95 MeV, à été mesurée avec le set-up expérimental GARFIELD+Ring Counter(RCo).
La partie expérimentale de ce travail de thèse à consisté dans la participation à cette experience, de la phase de la proposition à la mesure, l'étalonnage des détecteurs, le traitement des données et l'analyse des données.
Dans ce travail de thèse, plusieurs résultats de l'analyse sont présentés, ainsi qu'une étude théorique du système, obtenue avec le nouveau code de décroissance statistique. Suite à l'analyse presentée dans cette thèse, nous pouvons donner des constraintes à la densité des niveaux à haute énergie d'excitation pour les noyaux légers,

du $\sim C$ jusq'au Mg. Par ailleurs, des émissions hors équilibre sont mises en évidence, et interprétées comme des effets liés à la structure en cluster des noyaux dans la voie d'entrée de la réaction, ainsi que du système chaud issu de la fusion, avant que la thermalisation soit achevée.

Chapter 1

Physics Case

Nuclei are finite quantum systems. As such they are characterized by their ground state properties and their excitation spectrum. To access this latter, nuclei must be excited by means of nuclear reactions. The stronger is the nuclear excitation, the larger becomes the number of quantum mechanical states which can be explored by the nucleus, and the more one can access nuclear properties far from the ground state. In a statistical mechanics description of the nucleus, a temperature can be associated to the variation of the number of accessible states with the excitation energy of the system. Dissipative nuclear reactions can therefore be seen as a tool to investigate nuclear properties at finite temperature T, above the zero temperature of the ground state, and, for higher bombarding energies, also at a nuclear density ρ far from the nuclear saturation density $\rho_0 \approx 0.16\ fm^{-3}$.
However, in a nuclear reaction, dynamical aspects always play a role together with structure properties: what is measured in an experiment is always a convolution of different emitting sources and processes taking place in a wide range of excitation energies (and therefore, of temperatures) and at different times. This results in a sort of "hierarchy" in particle emission, and gives rise to a general concern with nuclear reaction experimental studies: the final inclusive yields represent integrated contributions over the whole time evolution of the reaction and, because of that, the information they bear on specific excitation energy regions of the different nuclei explored during the reaction may be model dependent.
Speaking in terms of nuclear "thermal properties" , if the challenge for nuclear theory is to predict correctly the dependence of nuclear properties on excitation energy, the challenge for an experimental measurement will be to perform a highly exclusive and (quasi)complete detection of the different decay products emitted in the nuclear reaction, in order to reconstruct their origin and to backtrace the information they

bear, with the final aim of experimentally constraining nuclear properties at finite temperature. An additional challenge comes into play in the modelization of nuclear reactions: because of the strong interplay of nuclear structure and reactions, statistical (as well as dynamical) codes should be highly constrained by the huge amount of available nuclear data on basic ground state properties and information on low excitation energies, with the aim of gaining a better predictive power on finite temperature observables.
In this chapter we describe the physics framework of this work, consisting in a theoretical and experimental study of the statistical decay of a light nuclear system. Our aim is an attempt to progress in the reconstruction of nuclear thermal properties from fusion-evaporation reactions. Physical issues we aim to shed some light on are the level density of light nuclei, together with possible deviations from a statistical behaviour in their decay, and the temperature dependence of the pairing interaction. We will also justify how this work could be of some help, in a long range plan, in addressing the temperature dependence of the nuclear symmetry energy.

1.1 From Nuclear Ground States to Finite Temperature Properties

Nuclear masses contain a substantial amount of information about nuclear structure at zero temperature. A relatively simple way of extracting this information, is to fit ground state binding energies with various versions of the liquid drop mass formula:

$$E = -a_{vol}A + a_s A^{2/3} + a_C \frac{Z^2}{A^{-1/3}} + a_{sym}\left(1 - 2\frac{Z}{A}\right)^2 + \delta E \tag{1.1}$$

where:

- $-a_{vol}A$ is an attractive volume term;
- $a_s A^{2/3}$ and $a_C \frac{Z^2}{A^{-1/3}}$ are respectively the repulsive surface and Coulomb terms;
- $a_{sym}\left(1 - 2\frac{Z}{A}\right)^2$ is the symmetry term;
- the δE term represents a correction due to pairing and shell effects; the pairing part of it can be parametrized as $\delta E = \chi\ a_P A^{-1/2}$, where $\chi = 1, 0, -1$ respectively for even-even, even-odd and odd-odd nuclei.

The roles of the symmetry and pairing terms in the semi-empirical parameterization of eq.(1.1) are therefore, respectively, to favour the stability of $N = Z$ nuclei and to reproduce the observed mass differences between odd and even neighbouring nuclei. Both these effects can be ascribed to the fermionic nature of the nucleon, and rather simple dependences on the isotopic content of the nucleus are proposed for the two terms [1]. It is clear at this level that no information at all on the variation of these terms with increasing excitation energy is needed if our aim is limited to the description of nuclear ground states. If, on the contrary, we want to investigate finite temperature nuclear properties, we have to introduce the notion of level density, together with the notion of thermal average.

1.1.1 Level Density and Nuclear Thermal Properties

Level densities represent fundamental quantities in nuclear physics. Their knowledge is not only important for the understanding of nuclear structure, but it is also required for different applications of nuclear physics, from nucleosynthesis calculations to reactor science. There exist different experimental methods to provide information on this quantity, but most of them are limited to a relatively low excitation energy domain. Above the thresholds for particle emission, level densities are only accessible in evaporation reactions through the theory of compound nucleus decay, which will be largely discussed in chapter **2**.
Before addressing the issue of isotopic effects in section 1.1.3, we start considering for simplicity a nucleus as characterized by its mass number A only. Then the Level Density (LD) $\rho(A, E^*)$ of the nucleus at the excitation energy E^* (measured starting from the ground-state energy E_0, *i.e.* $E^* = E - E_0$) is defined as the number of energy levels available for the system in the range $(E^*, E^* + dE^*)$, divided by the energy interval dE^*. Low energy nuclear spectra are dominated by correlation effects giving rise to pair correlations and collective modes of rotational and vibrational type, which are superimposed on the single particle motion of the nuclear constituents. The ensemble of these single particle and collective levels constitutes a spectrum which, as for any other quantum system, is discrete at low excitation energy. When the excitation energy becomes high enough, particle degrees of freedom dominate, and independent particle models may provide a useful guidance in the discussion of average properties of energy spectra. Moreover, as the excitation energy increases, because of simple combinatorial reasons the number of available states exponentially increases, making a continuous approximation to the spectrum adequate. Then simple models as the Fermi gas model represent a valid theoretical

framework to calculate level densities in a continuum approximation [1]. Level densities calculations in independent particle models, in the Monte Carlo shell model and also with realistic phenomenological parameterizations will be presented in chapter **2**, together with the discussion of the dependence of this fundamental quantity on other nuclear properties as angular momentum and parity. Here we will concentrate on its dependence on excitation energy and temperature. Nuclear temperature, as anticipated, can be related to the variation of the number of states accessible to the nucleus with an increase in excitation energy. The temperature T can therefore be defined according to the relation:

$$\frac{1}{T} = \frac{\partial \ln \rho(A, E^*)}{\partial E^*} \tag{1.2}$$

In the framework of the Fermi gas model [2], describing the nucleus as an ideal gas of non-interacting fermions in the thermodynamic limit, the temperature is related to the excitation energy via the level density parameter a, according to:

$$E^* = aT^2 \tag{1.3}$$

Then, if a is only a mass-dependent constant $a(A)$ and does not show any energy dependence, the temperature dependence of the LD is completely determined by the functional form of $\rho(E^*)$. This is the case for the Fermi gas model, where the LD parameter can be expressed as a linear function of the mass number A, and is related to the single particle particle level density at the Fermi energy $g(\varepsilon_F)$ according to:

$$\frac{a}{A} = \frac{\pi^2}{6} g(\varepsilon_F) \tag{1.4}$$

where

$$g(\varepsilon_F) = \frac{3}{2}\frac{A}{\varepsilon_F} \tag{1.5}$$

and the Fermi energy reads:

$$\varepsilon_F = \frac{\hbar^2 k_F^2}{2m} \tag{1.6}$$

where k_F is the Fermi momentum. The Fermi gas model can not obviously account for the discrete nature of the spectrum nor for nuclear properties beyond the independent particle picture. More in general, in an independent particle model, correlations among nucleons other than the ones produced by the self-consistent mean field cannot be accounted for, which leads to an underestimation of the LD. To overcome this limitation, a phenomenological approach is currently used in order to get realistic parameterizations for $\rho(A, E^*)$. This approach may consist for

instance in adopting a LD functional form resulting from an independent particle calculation, written in terms of various parameters, and adjust the free parameters in order to provide agreement with known densities and data. Typically, two free parameters are left in the $\rho(A, E^*)$ to be fitted on experimental data: one is the LD parameter a, the other is an energy shift Δ, which is introduced in the excitation energy in order to reproduce the experimentally observed energy gap in the spectrum of even nuclei, coming from the pairing interaction [3]. Then, an energy dependence is commonly attributed to the LD parameter a, in order to take into account the disappearance of shell effects with increasing E^* [4]. One of the results of this approach is therefore an energy dependent $a(A, Z, E^*)$ entering in the LD expression. This reflects the idea that the modification of the LD parameter with respect to the Fermi gas energy independent value can take into account the neglected correlations among nucleons, and therefore provide realistic level densities. The overall temperature dependence of the final $\rho(E^*)$ will therefore result also from the functional form for $a(E^*)$.
We will justify in the following the inclusion of an energy dependent $a(E^*)$ also by means of theoretical considerations on the motion of the nucleons in the strongly interacting nuclear medium, which translates in a temperature dependent effective mass m^* for the nucleons, entering eq.(1.6) and therefore making a a T- dependent quantity. This temperature dependence is thus no simple consequence of a semi-empirical approach but rather a consequence of the strongly interacting nature of the nuclear medium.
Once one has obtained the overall dependence on temperature of the nuclear level density, it is then possible to evaluate the thermal average $\langle \mathcal{E} \rangle_T$ of a nuclear property $\mathcal{E}$ (for instance, the symmetry or pairing energy) by means of the following expression:

$$\langle \mathcal{E} \rangle_T = \frac{1}{\mathcal{Z}} \int_0^\infty dE^* \rho(E^*)\ \mathcal{E}\ \exp -E^*/T \tag{1.7}$$

where we have introduced the nuclear partition function $\mathcal{Z}$:

$$\mathcal{Z} = \int_0^\infty dE^* \rho(E^*) \exp -E^*/T \tag{1.8}$$

A study of nuclear thermal properties therefore requires a precise knowledge of the nuclear level density and of its variation with excitation energy via the level density parameter $a(E^*)$. As anticipated, fusion-evaporation measurements as the one presented in this work are the only way to experimentally access the nuclear level density above particle emission thresholds.

1.1.2 Level Density Parameter and Effective Mass in Nuclei

A mean-field description of the nucleus provides a very powerful framework to describe states close to the nuclear Fermi energy. In this picture, each nucleon moves independently in a static nuclear potential, which is non-local in space coordinates because of the finite range of the nuclear interaction. Within this model, nucleons can only occupy a set of states with definite excitation energies, spins and parities, which constitute the proton and neutron single particle level schemes. Single particle states are generated by the nuclear (plus Coulomb, for the protons) potential. The nuclear ground state is then given by filling the lowest single-particle states according to the Pauli principle up to the Fermi energy ε_F. An illustrative picture of this schematization is shown in fig.(1.1).

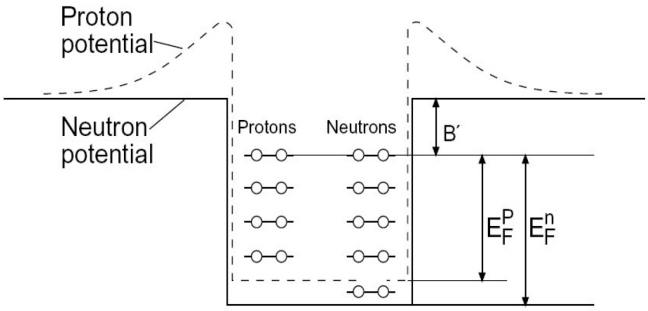

Figure 1.1: Illustrative picture of the neutron and proton square-well nuclear potentials (plus Coulomb potential for protons) in the framework of an independent particle model.

However, in the independent particle picture, collective phenomena as nuclear deformation or vibration can not be taken into account, and such model fails in reproducing the correlated level density of real nuclei. In order to reproduce the rise of collective nuclear modes, fluctuations in the mean field should be included. The coupling of these modes with the single particle motion then gives a dynamical character to the average potential, which becomes also non local in times, *i.e.* it is characterized by an energy dependence.
The effective mass is a powerful concept used to characterize the quasiparticle properties of a particle inside a strongly interacting medium as the nucleus, because it is used to describe space and time non-locality (or, equivalently, momentum and

frequency dependence) of the mean field. Let us give a definition of the nucleon effective mass in nuclear matter. If nucleons are moving in a momentum and energy (or frequency) dependent average potential $\upsilon(k,\omega)$, the energy $\omega(k)$ of a state with momentum k can be written as:

$$\omega(k) = \frac{\hbar^2 k^2}{2m} + \upsilon(k,\omega) \tag{1.9}$$

The effective mass can then be defined in analogy to the free particle case as:

$$d\omega = \frac{\hbar^2 k^2}{m^*} dk \tag{1.10}$$

The mass m^* then coincides with the free nucleon mass only if the potential υ is local and energy independent. In particular, two different effective masses m_k and m_ω can be defined, related respectively to the space and time non localities of the average potential, *i.e.* to its derivatives with respect to momentum and frequency implicit in eq.(1.10).
We can therefore write for the total effective mass m^*:

$$m^* = \frac{m_k m_\omega}{m} \tag{1.11}$$

Different energy scales are associated to the ω and k masses: the energy of low-lying collective vibrations (related to the to ω mass) is of the order of $1-3\ MeV$, while the rigidity of the mean field (related to the k mass) is controlled by the energy difference between major shells, which has a value of about 8 MeV for medium heavy nuclei. A temperature dependence can then be associated to both the m_k and m_ω masses, which are found to decrease with increasing T, and the dominant contribution in the resulting temperature dependence of the total effective mass m^* depends on the energy scale of interest for the different applications [5, 6].
As anticipated, we are interested in this context in the temperature dependence of the level density parameter $a(E^*)$, which is found to be related to the T dependence of the nucleon effective mass m^*. We have already anticipated in the framework of the Fermi gas model that a T dependent m^* modifies the LD parameter because it enters eq.(1.6) for the Fermi energy, and therefore modifies the single particle level density $g(\varepsilon)$ at a given T. To be more general, we describe here a procedure to calculate $a(T)$ at a given T starting from a local mean field modified by the inclusion of a T-dependent m^* [7, 8]. Since we are mainly interested in the implications of this temperature dependence on the final nuclear level density, we do not enter into details on how the single particle level density $g(\varepsilon)$ is obtained from the chosen local mean field, and on how the mean field is parametrized. We simply notice that

the inclusion of $m^*(T)$ modifies the single particle energy ε, which can be written as $\varepsilon = p^2/2m^*(T)+U$, where U is the mean field potential in momentum representation, and we assume that we know how to calculate $g(\varepsilon)$ at any temperature T, given $m^*(T)$. The starting point of the procedure is the main result of the Fermi gas model, *i.e.* the relation between nuclear temperature and excitation energy:

$$a(T) = \langle E^* \rangle_T / T^2 \tag{1.12}$$

The excitation energy is measured starting from the energy of the ground state at zero temperature

$$\langle E^* \rangle_T = \langle E \rangle_T - \langle E \rangle_{T=0} \tag{1.13}$$

The energy at a given temperature T is given by

$$\langle E \rangle_T = \int_0^\infty \varepsilon g(\varepsilon) f(\varepsilon, \mu, T) d\varepsilon \tag{1.14}$$

where the distribution $f(\varepsilon, \mu, T)$ is the finite temperature occupation probability for the single particle states with density $g(\varepsilon)$ generated by the mean field potential:

$$f(\varepsilon, \mu, T) = \frac{1}{1 + \exp\left[(\varepsilon - \mu)/T\right]} \tag{1.15}$$

and the chemical potential μ is determined by the conservation condition:

$$\langle A \rangle_T = \int_0^\infty g(\varepsilon) f(\varepsilon, \mu, T) d\varepsilon \tag{1.16}$$

Following this procedure, starting from a local potential of Wood-Saxon type and calculating the $g(\varepsilon)$ within the Thomas-Fermi approximation, the authors in [7, 8] obtain for the inverse LD parameter:

$$K(T) = A/a(T) \tag{1.17}$$

the results which are here reported in fig.(1.2). The calculations of fig.(1.2) have been confirmed by several measurements of fusion evaporation reactions, among others the ones in ref.[9, 10, 11], respectively for masses $A \sim 160, 120, 40$. However, we have to be aware of the fact that for high excitation energy the results of the theoretical model proposed in [7, 8] can not be trusted, because of the onset of intermediate mass fragment emission, which modifies the temperature-excitation energy correlation of eq.(1.12). This observation is related to the existence of a missing ingredient in [7, 8] and in our discussion, *i.e.* a nuclear limiting temperature,

which will be better discussed in chapter **2**.
To summarize, we can say that the inclusion of a T-dependent LD parameter is indeed necessary to describe the many-body correlated level density of real nuclei, and therefore to make statistical evaporation models reproduce experimental data. This inclusion finds a theoretical justification in the temperature dependence of the nucleon effective mass.

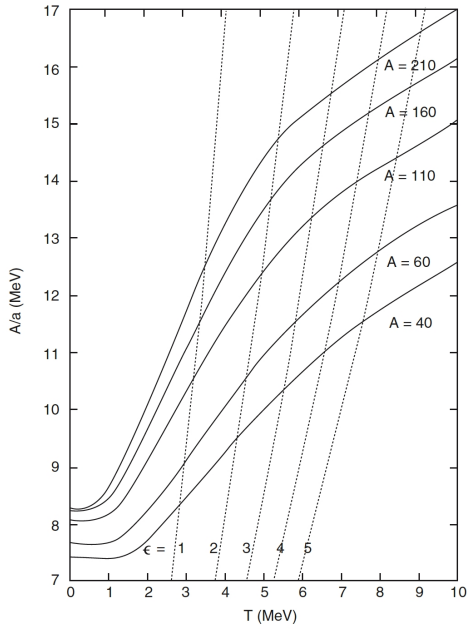

Figure 1.2: Calculated inverse level density parameter $K = A/a$ as a function of temperature for various nuclei with mass A along the line of stability, taken from ref. [8]. Also indicated by the dashed lines are the loci corresponding to constant excitation energies per nucleon of $1 - 5\ MeV$.

1.1.3 Nuclear Symmetry Energy at Finite Temperature

Up to now we have considered the nucleus as made up of a given number of constituents, without making any distinction between protons and neutrons. It is easy to understand that, even in an independent particle picture, the energy of the nucleus (and, consequently, its level density) has to depend on its isotopic content: this is a consequence of the fermionic nature of nucleons, *i.e.* of the Pauli principle. The dependence of the energy on the isospin is given in terms of the so-called symmetry energy. The nuclear symmetry energy is a fundamental quantity

determining the properties of nuclear systems ranging from the atomic nucleus up to the neutron star. Strictly speaking, it is a measure of the energy cost of changing the isotopic content of a nuclear system, going from the symmetric $N = Z$ case (or, rather, from equal proton and neutron densities $\rho_n = \rho_p$ in bulk systems) to the asymmetric case.
As we have anticipated in the liquid drop mass formula of eq.(1.1), for finite nuclei the symmetry energy can be expressed as:

$$E_{sym}(A, Z, T) = a_{sym}(T) \left(1 - 2\frac{Z}{A}\right)^2 \tag{1.18}$$

where the isotopic dependence specified in the factor $\left(1 - 2\frac{Z}{A}\right)^2$ can be easily derived in the framework of the Fermi gas model (already introduced for the calculation of the level density) and the $a_{sym}(T)$ coefficient absorbs the temperature dependence and coincides with the a_{sym} of eq.(1.1) for nuclear ground states.
To investigate the temperature dependence of the symmetry energy, it is useful to define this quantity for bulk systems (as neutron stars), by writing the equation of state of asymmetric nuclear matter, in which the binding energy is expressed as a function of the baryon density ρ (the sum of neutron and proton densities ρ_n, ρ_p) and of the asymmetry $\delta = (\rho_n - \rho_p)/\rho$. The nuclear equation of state at zero temperature reads:

$$e(\rho, \delta) = e(\rho, \delta = 0) + e_{sym}(\rho, \delta) \tag{1.19}$$

where the symmetry energy is written as:

$$e_{sym}(\rho, \delta) = C_{sym}(\rho)\delta^2 + \mathcal{O}(\delta^4) \tag{1.20}$$

The quantity $e(\rho, \delta = 0)$ is the binding energy per nucleon of symmetric nuclear matter (*i.e.* with $\rho_n = \rho_p$), and:

$$C_{sym}(\rho) = \frac{1}{2}\frac{\partial^2 e}{\partial \delta^2}\Big|_{\delta=0} \tag{1.21}$$

is the zero temperature symmetry energy coefficient. The density functional $e(\rho, \delta)$ contains two contributions, a kinetic and a potential one, both having a minimum at $\delta = 0$:

$$e(\rho, \delta) = e^{kin}(\rho, \delta) + e^{pot}(\rho, \delta) \tag{1.22}$$

A Taylor expansion around $\delta = 0$ of the type of eq.(1.19) can therefore be written for both the kinetic and potential energy terms in the equation of state, and two

contributions to the symmetry energy $C_{sym}^{kin}(\rho)\delta^2$ and $C_{sym}^{pot}(\rho)\delta^2$ can be defined. In particular, for the kinetic energy term in eq.(1.22) we can write:

$$e^{kin}(\rho,\delta) = \frac{3}{10}\frac{\hbar^2 k_F^2}{2m^*}\left[(1+\delta)^{5/3} + (1-\delta)^{5/3}\right] \tag{1.23}$$

where m^* is the nucleon effective mass introduced in the previous section, and the coefficient C_{sym}^{kin} of the kinetic contribution to the symmetry energy consequently reads:

$$C_{sym}^{kin} = \frac{\hbar^2 k_F^2}{6m^*} \tag{1.24}$$

For the total symmetry energy we finally have:

$$e_{sym}(\rho,\delta) = \frac{\hbar^2 k_F^2}{6m^*}\delta^2 + \frac{1}{2}\frac{\partial e^{pot}(\rho,\delta)}{\partial\delta^2}\Big|_{\delta=0}\delta^2 \tag{1.25}$$

We are now interested in the dependence of these quantities on the nuclear temperature. First of all, we notice that any local dependence on T of the asymmetry $\delta(T)$ will not modify the global isospin content of the system, and any dependence on T of the nuclear density $\rho(T)$ will be to a first approximation negligible because of the strong incompressibility of nuclear matter. Then, at finite temperature, there will be no variation of the potential contribution to the total $e(\rho(T),\delta(T))$, and consequently, to the symmetry energy, with respect to the zero temperature case. On the contrary, it is clear from eq.(1.23) that the temperature dependence of the nucleon effective mass m^* will make the kinetic contribution to the nuclear symmetry energy a temperature dependent quantity. The reason for this is relatively easy to understand: changing the temperature of the system means changing the occupation probability of single particle energy orbitals. This causes a variation in the kinetic energy contribution to the total energy, because the kinetic energy comes from an expression analogous to the one of eq.(1.14), *i.e.* an average on occupied states at finite temperature, where the occupation probability is different than in the zero temperature case. With the same notation previously introduced in this chapter for average quantities at finite temperature, we can therefore write:

$$\langle e_{sym}(\rho,\delta)\rangle_T - \langle e_{sym}(\rho,\delta)\rangle_{T=0} = \left[\left\langle C_{sym}^{kin}(\rho)\right\rangle_T - \left\langle C_{sym}^{kin}(\rho)\right\rangle_{T=0}\right]\delta^2 \tag{1.26}$$

and the difference of symmetry energy coefficients in the square brackets is in turn equal to:

$$\langle C_{sym}(\rho)\rangle_T - \langle C_{sym}(\rho)\rangle_{T=0} = \frac{\hbar^2 k_F^2}{6}\left[\frac{1}{\langle m^*\rangle_T} - \frac{1}{\langle m^*\rangle_{T=0}}\right] \tag{1.27}$$

where we have neglected any change in the Fermi surface due to finite temperature effects.
The same considerations hold for finite nuclei, and it can be shown that the variation of the $a_{sym}(T)$ parameter with respect to the zero temperature case can also be written in terms of a difference between two kinetic energy contributions, with an expression analogous to eq.(1.27), where the global temperature dependence stems from the temperature dependence of the nucleon effective mass. A coherent description of the symmetry energy in finite and infinite systems can be given under the Thomas-Fermi or local density approximation. The total symmetry energy for a finite nucleus at a given temperature T, defined in eq.(1.18) in terms of the $a_{sym}(T)$ parameter, can be written by means of this approximation as:

$$\langle E_{sym} \rangle_T^{TF} = \int \rho(r) \left\langle C_{sym}^l(\rho(r)) \right\rangle_T \left(\frac{\rho_p(r) - \rho_n(r)}{\rho(r)} \right)^2 d\mathbf{r} \tag{1.28}$$

where $\left\langle C_{sym}^l(\rho(r)) \right\rangle_T$ is the symmetry energy coefficient at temperature T for infinite nuclear matter at the local nuclear density $\rho(r)$. As it is evident in this last expression, under this approximation also the temperature dependence of the local density $\rho(r)$ of the finite nucleus plays a role in determining the T-dependence of the symmetry energy [15, 16].
Finally, it is clear that information on $m^*(T)$, or, equivalently, on the temperature dependence of the LD parameter, from the experimental constraints on nuclear level densities via fusion-evaporation reactions, can be translated into information on the symmetry energy coefficients $C_{sym}(T)$ and $a_{sym}(T)$ respectively for nuclear matter and for finite nuclei.
Before concluding, we may recall that, from an experimental point of view, the temperature dependence of the symmetry energy can also be accessed by means of intermediate (or relatively low-energy reaction), leading the nuclear system into the fragmentation regime (or at its thresholds). Moreover, in such studies, because of the higher bombarding energies, also the density dependence of the symmetry energy can be addressed, since densities lower than the nuclear saturation density can be attained in the expansion phase of the hot nuclear matter formed in the collision. Since this work is mainly devoted to the investigation of nuclear thermal properties by means of fusion-evaporation reactions, we do not enter into details concerning the study of multifragmentation reactions, but we want to stress in any case the important link between these two phenomena, since we believe that this discussion gives an additional value to our choice of particularly investigating light nuclei. First of all, multifragmentation and evaporation indeed deserve a unified description, which is made possible by the statistical nature of the decay of the hot

nuclear source formed in the entrance channel of the reaction: in the framework of a statistical description, the decay is always determined by the number of available states in the final channel. In the case of multifragmentation (*i.e.* at sufficiently high available energy), an instantaneous break-up of this hot source into several excited fragments has a larger statistical weight than a decay by (sequential) emission of light particles, which would be the case of evaporation. Signatures of C_{sym} are then known to be contained in the hot primary fragment isotopic distributions resulting as the first stage output of the nuclear reaction (see for instance ref.[17]), but they can be distorted when the excited primary fragments undergo secondary decays, and recovering them from cold measured distribution may not be straightforward. Previous studies at intermediate incident energies have shown that these primary unstable fragments can be characterized by excitation energies up to 3 $A.MeV$ before they undergo secondary decays [18, 19]. By means of low-energy beams we may be able to observe the decay of compound nuclei at similar excitation energies. The back-tracing of these decays will then provide information on the more complex problem of secondary decays in fragmentation phenomena, helping us in the hard task of extracting quantitative information about the symmetry energy at finite temperature.

1.1.4 Pairing Energy at Finite Temperature

Nuclear binding energies are found to exhibit a systematic variation depending on the evenness or oddness of Z and N. As anticipated, in order to reproduce this empirical observation, a pairing energy is included in the liquid drop mass formula of eq.(1.1), and it can be parametrized as:

$$\delta E = \chi \; a_P A^{-1/2} \; with \begin{cases} \chi = 1 & for \; even \; N, \; even Z \\ \chi = 0 & for \; even/odd \; N, \; odd/even Z \\ \chi = -1 & for \; odd \; N, \; odd \; Z \end{cases} \tag{1.29}$$

This energy shift has the effect to increase the stability of a paired nucleons system, making the nucleus stable against the transfer of an energy lower than the binding energy gain due to the pairing interaction: there exists therefore a minimal amount of energy necessary in order excite such a nucleus. Hence, we easily understand another empirical observation on even nuclei, *i.e.* the presence of an energy gap in their excitation spectra.
Our aim in this section is to give some arguments on the temperature dependence of the pairing interaction [20, 21, 22]. In particular, we will discuss which is the

interplay between these two features, namely the higher binding energy and the gap in the excitation spectrum of even nuclei, at high excitation energy. In order to do this, we make use of the notion of thermal average to compute the average energy $\langle E \rangle_T$ at finite temperature:

$$\langle E \rangle_T = \frac{1}{\mathcal{Z}} \int_0^\infty dE^* \rho(E^*)\ E\ \exp -E^*/T \tag{1.30}$$

We also need to introduce a phenomenological expression for the nuclear level density $\rho(E^*)$, in which pairing correlations are accounted for via the inclusion of a backshift energy Δ. This possibility has been already addressed in section 1.1.1, and it will be better discussed and justified in chapter **2**. For our purposes in this section, we simply adopt the following expression:

$$\rho(E^*) = \mathcal{C}\ \frac{\exp 2\sqrt{a(E^* - \Delta)}}{(E^* - \Delta)^{5/4}} \tag{1.31}$$

Given this expression, we realize that the integrand term in eq.(1.30) is the product of two exponentials of opposite signs, therefore a strongly peaked function, and the integral can be approximated by the value of this function at the peak coordinate $\overline{E^*}$. We can therefore write, for the average excitation energy:

$$\langle E^* \rangle_T = \frac{1}{\mathcal{Z}} \int_0^\infty dE^*\ E^*\ \exp\left(\ln \rho - E^*/T\right) \approx \overline{E^*}\ \exp\left(\ln \rho(\overline{E^*}) - \overline{E^*}/T\right) \tag{1.32}$$

where the peak coordinate $\overline{E^*}$ is obtained by the maximum condition:

$$\frac{d}{dE^*}(\ln E^* + \ln \rho(E^*) - E^*/T)\Big|_{E^* = \overline{E^*}} = 0 \tag{1.33}$$

Working out this condition with the given expression for $\rho(E^*)$ we get:

$$\frac{1}{E^*} + \frac{\sqrt{a}}{\sqrt{\overline{E^*} - \Delta}} - \frac{5}{4}\frac{1}{\overline{E^*} - \Delta} = \frac{1}{T} \tag{1.34}$$

If we are interested in the high temperature average of E, *i.e.* in an excitation energy region where $\overline{E^*} >> \Delta$, we can neglect linear terms in $\overline{E^*}$, thus finally recovering the known result of eq.(1.3) for the uncorrelated Fermi gas model:

$$\overline{E^*} = aT^2 \tag{1.35}$$

This means that the correlations introduced by the pairing backshift are washed out at high temperature. This is easy to understand also intuitively: the average excitation energy at high temperature for an even-even nucleus, with a lower mass but

also a pairing gap in the spectrum, is similar to the one for neighbouring odd nuclei. On the contrary, if we compute the low-temperature average for the excitation energy, the pairing energy persists in affecting the result. We can verify this statement with a very simple model, in which two energy levels are available for the even-even nucleus specified by mass and charge (A, Z), namely the ground-state E_0 and the first excited state at an energy $E_0 + \Delta$. On a relative energy scale, ground-state energies for neighbouring $(A-1, Z)$ and $(A+1, Z)$ nuclei are close to the energy $E_0 + \Delta$ of the first exited state for the (A, Z), due to the increased stability of this latter. Eq.(1.30) for the average energy of (A, Z) yields:

$$\langle E \rangle_T = \frac{E_0 \exp(-\beta E_0) + (E_0 + \Delta) \exp\left[-\beta(E_0 + \Delta)\right]}{\exp\left[-\beta E_0(1 + \exp(-\beta E_0)\right]} \tag{1.36}$$

where a low temperature limit gives:

$$\langle E \rangle_T \sim E_0 \left[1 + \frac{\Delta}{E_0} \exp(-\beta\Delta)\right] \tag{1.37}$$

If we define the pairing energy as a mass difference between neighbouring nuclei:

$$\langle E_{pair} \rangle_T = \langle E(A-1, Z) \rangle_T + \langle E(A+1, Z) \rangle_T - 2 \cdot \langle E(A, Z) \rangle_T \tag{1.38}$$

we find for this simple model:

$$\langle E_{pair} \rangle_T \sim 2\Delta \ (1 - \beta\Delta) \tag{1.39}$$

which means that, as the temperature increase, the pairing energy goes to zero. It is found in the literature that after a critical temperature pairing correlations are completely destroyed, which can also be described in terms of a "phase transition" from a superfluid to a normal fluid behaviour [23]. Our simple arguments have led us to the conclusion that this behaviour is governed by the level density.
In this work we will be mainly concerned with the signature of the pairing interaction in fragment production following a nuclear reaction. The most evident signature of pairing is the manifestation of odd-even effects in isotopic variables, and the next section of this chapter is devoted to this subject. In particular, having discussed the disappearance of pairing correlations at high excitation energy, it is easy to justify the common understanding according to which odd-even effects are related to the low-temperature evaporation phase of a dissipative nuclear reaction. Indeed, in theoretical dynamical or statistical models no odd even effects are associated to finite temperature observables, but they may appear on the asymptotic distributions after secondary decays [24, 25]. Thus, fusion-evaporation reactions are a good tool

to experimentally access the temperature dependence of the pairing interaction.
Two physical ingredients which can be associated to the pairing interaction enter in evaporation models, namely binding energies and level densities. We will discuss in the following how the effects of these two ingredients could be disentangled and how their signatures could be read, respectively, in cold and finite temperature distributions, provided that we are able, experimentally, to reconstruct these latter. Finally, to conclude, we want to state that the understanding of odd-even effects also has a great importance in studies on the symmetry energy. As said before, the symmetry energy can be related to the isotopic distributions resulting from a multifragmentation reaction if these are not too much perturbed by secondary decay. An accurate investigation on the origin of the staggering in measured isotopic observables and on the temperature dependence of the pairing interaction is therefore also required for an experimental evaluation of the finite temperature $C_{sym}(T)$.

1.2 The Odd-Even Effect in Fragment Production

Odd-even effects in fragment production have been experimentally investigated since a long time but never quantitatively understood. They were observed in different reactions with different target-projectile combinations and in a large range of beam energies. It was found that the distributions of light fragmentation residues after violent heavy-ion collisions reveal an even-odd staggering of similar magnitude as in the case of low-energy reactions, suggesting that this "anomaly" is independent on the beam energy and on the acceptance of the experimental devices. In some experiments the magnitude of the odd-even effect is found to be related to the isospin of the projectile and/or the target, becoming slightly suppressed when the emission source is neutron-rich [26]. The effect in final observables was seen to be very large in reactions where at least one of the reaction partner has $N = Z$: globally, an enhancement of the production of even-Z fragments can be observed, even if a detailed look at other selected isotopic chains, as the $N = Z + 1$ chain, usually reveals a reversed effect, which is masked in final inclusive $Y(Z)$ distributions because of the dominant contribution of $N = Z$ nuclei.
A review of experiments with signatures of fine structure in the measured yields is given for instance in Table I of ref. [27], while in fig.(1.3) we report a collection of recent experimental data (more details in the figure caption) showing a clear staggering effect in the production cross section or normalized yields as a function of the fragment charge number Z. In the following we will discuss some of these recent results and their interpretations, which have renewed the interest of the nu-

clear physics community on this topic, especially concerning the production of light fragments. We underline at this point that for lighter fragments, a better isotopic identification can generally be achieved, and as we will see, together with high experimental energy and angular resolution, this is a strong requirement in order to be able to perform more quantitative investigations on odd-even effects.

1.2.1 Phenomenological Interpretation

As anticipated, odd-even effects are clearly linked to the pairing residual interaction and its dependence on temperature. Some attempts to interpret the odd-even effects as a simple consequence of the pairing effect in nuclear masses (*i.e.* at zero temperature) have been done. In particular, the authors in ref. [28] have assumed that the very last step of the evaporation chain, concerning either a proton or a neutron emission, determines the observed staggering, and have found a good resemblance between the trend as a function of Z of the fragments production cross section and of the lowest between their p/n-separation energies, which suggests the validity of the principle that, the larger is the nucleon separation energy of a given nucleus, the more likely will be its production in the ground state. We can verify the reasonable validity of this statement by looking at the top and bottom-left panels of fig.(1.3), where nucleon separation energies are plotted together with the fragment production cross sections $\sigma(Z)$ in mb.
Even if this idea, implemented in an evaporation model, can predict correctly the trend of the experimental staggering, it does not reproduce the amplitude of the staggering quantitatively: the experimental oscillations are less important than the ones predicted in this simple scenario. This suggests that the previous evaporation steps may also play a role. Moreover, if we consider that the last evaporation step may also concern an α-particle, we soon loose the oscillating trend of the lowest separation energy for particle emission, at least for some selected isotopic chain as the $N = Z$ one, since the Q-value for α decay shows a smooth behaviour as a function of Z. This is shown in fig.(1.4).
We also have to take into account the fact that nuclei at the end of the evaporation chain may be populated at excitation energies at which their spectra still show a discrete nature. As we can also see from fig.(1.4), the position of the first particle-unstable excited level of the parent nucleus as a function of Z nicely coincides with the lowest Q-value for particle emission. Additionally, unbound clusters may also be directly evaporated, both in the case of clusters unstable in their ground states (as ^{8}Be or ^{5}Li) or that of clusters excited above particle emission thresholds. Sequen-

tial feeding from particle unstable levels and branching ratios for their decay into different channels can therefore also contribute in determining the abundances in final measured distributions (together with any other inclusive observable as energy spectra) [30, 31].
These observations suggest therefore that the odd-even staggering depend on the whole evaporation chain, and not only on the energy balance of the last evaporation step. It also seems that a control on the discrete level population of hot nuclei may confirm this statement, and to this aim, we introduce in the following section the experimental technique of correlation functions, which can actually give us access to this information.

1.2.2 Experimental Information from Correlation Functions

The information on the discrete level population of hot nuclei is experimentally accessible, at least at the last but one step of the decay, through the technique of correlation functions in relative kinetic energy of coincident pairs of fragments, provided that the measurement is carried out with detectors having high energy resolution and granularity. Experimentally the two particle correlation function [32, 33] $(1 + R(\epsilon_{rel}))$ may be defined as:

$$\sum_{(\vec{p_1}-\vec{p_2})^2/2\mu=\epsilon_{rel}} Y_{12}(\vec{p_1},\vec{p_2}) = C\big[1 + R(\epsilon_{rel})\big] \sum_{(\vec{p_1}-\vec{p_2})^2/2\mu=\epsilon_{rel}} Y_1(\vec{p_1})Y_2(\vec{p_2}) \qquad (1.40)$$

where Y_{12} is the two particle coincidence yield of a given pair of particles with their individual momenta $\vec{p_1}$ and $\vec{p_2}$, respectively, and the $Y_i(\vec{p_i})$ are the single particle yields for the two particles measured under the same impact parameter selection but not in the same event. The summations on both sides of the equation run over pairs of momenta $\vec{p_1}$ and $\vec{p_2}$ corresponding to the same bin in relative kinetic energy ϵ_{rel}. The correlation function describes how the correlation between interacting particles measured in the same event differs from the underlying two particle phase space. This phase space can be modeled by mixing the single particle distributions of particles from different events. The correlation constant C is chosen as the ratio between the total (integrated over momentum) number of generated mixed events and the total number of coincident yields: $C = \sum Y_{12} / \sum (Y_1 Y_2)$. To investigate the decay of particle unbound states it is necessary to consider the modifications of the two particle phase space by the long range Coulomb and short range nuclear interactions and to disentangle these contributions. Having a parameterization of the Coulomb background (as the one proposed in [34]), it is possible to isolate the

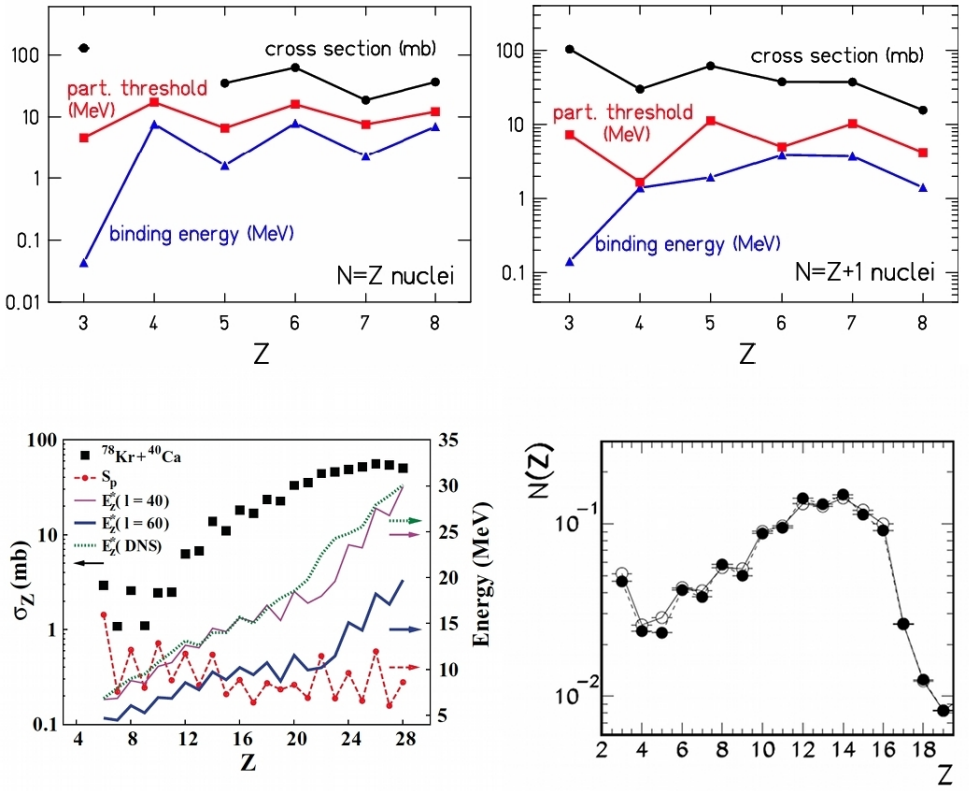

Figure 1.3: Collection of data with signature of fine structure in the measured yields. Top panel: experimental cross section (in mb) of isotopically resolved fragments from the reaction $^{56}Fe + Ti$, 1 $A.GeV$, taken from ref. [28]. The lowest between proton and neutron separation energies (in MeV) is shown to oscillate coherently with the cross section. Bottom panel, left: experimental cross sections for fragments emitted in ^{78}Kr+^{40}Ca (solid squares) reactions at 5.5 $A.MeV$, together with the proton separation energy (red dashed line), taken from ref. [29]. Bottom panel, right: normalized charge distribution for the decay of the QP source in the reactions: ^{32}S+^{58}Ni (full symbols, dashed line) and ^{32}S+^{64}Ni (open symbols, full line) at 14.5 $A.MeV$, ref. [31].

contribution of the nuclear interaction between the two fragments, which in this case is the signature of their common origin from the decay of a resonant state populated in the parent nucleus. Finally, primary yields of warm nuclei populated in discrete states can be directly extracted from the correlation function.

In a recent work by the NUCL-EX collaboration [35], we have applied this tech-

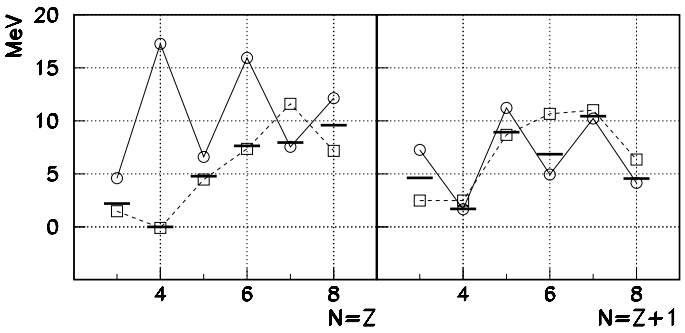

Figure 1.4: For the isotopic chains $N = Z$ and $N = Z+1$, plot as a function of the charge number of the energy of the lowest unstable state (thick lines) decaying in a given daughter isotope, the Q-value for alpha decay (open squares) and the lowest between neutron and proton separation energies (open circles).

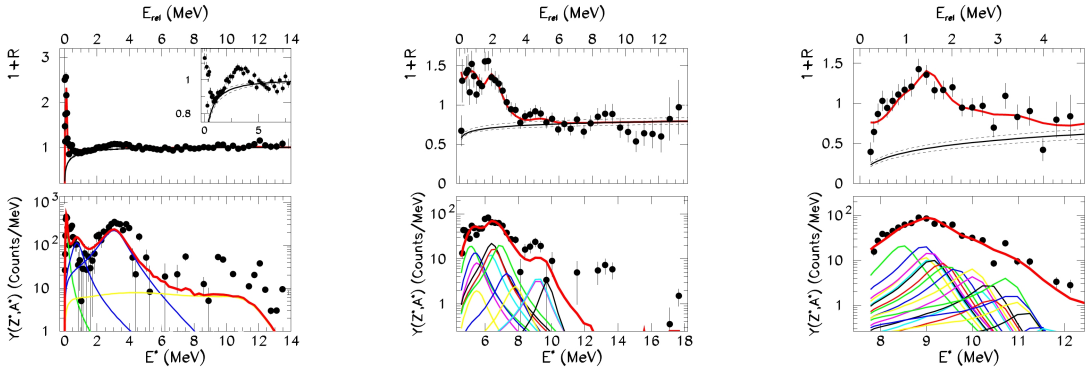

Figure 1.5: Upper part: representative relative kinetic energy correlation functions (symbols) of different isotopes measured in ref.[35] for peripheral ^{32}S+^{58}Ni collisions. The solid line is the Coulomb background, indicated together with its uncertainties (dashed lines). Lower part: experimental population of primary parents (symbols) and single excited state contributions (thin lines) together with their sum (thick line) as a function of the excitation energy: $E^* = \epsilon_{rel} + Q$-value. From left to right: α-α correlations and corresponding excited states of ^8Be (zoomed view around 3 MeV in the insert), α-^6Li correlations and corresponding excited states of ^{10}B, p-^{13}C correlations and excited states of ^{14}N.

nique to data for the reactions $^{32}S+^{58}Ni$ and $^{32}S+^{64}Ni$ at 14.5 $A.MeV$, measured at Laboratori Nazionali di Legnaro - LNL INFN with the Garfield + RCo apparatuses, an experimental set-up which will be largely described in chapter **4**. Representative relative kinetic energy correlation functions of different isotopes measured in ref.[35] for peripheral $^{32}S+^{58}Ni$ collisions are shown in fig.(1.5).
The important result presented in [35] is that the reconstructed distribution of warm fragments corresponding to the last but one decay step of the quasi-projectile source ($\langle Z\rangle = 16$, $A = 2Z$, and $e^* \approx 1$ $A.MeV$) still show a staggering effect, now reversed because of the dominant abundance of odd-Z with respect to even-Z fragments. We report this result in fig.(1.6). This is clearly related to a pairing effect in the level density: even-even nuclei have a lower density of levels at low energy because of the pairing gap, which leads to a reduced population at the last but one evaporation step.

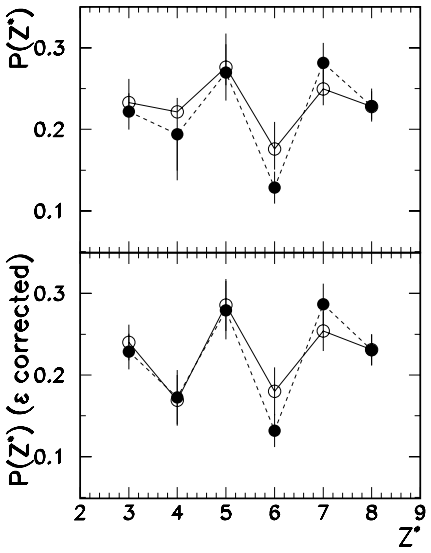

Figure 1.6: Population of the different primary fragments extracted from correlation functions of isotope pairs measured in the decay of the QP source in the reactions $^{32}S+^{58}Ni$ (full symbols, dashed line) and $^{32}S+^{64}Ni$ (open symbols, full line) at 14.5 $A.MeV$, from ref.[35]. Lower part: population of the different primary fragments corrected for the integral efficiency of each correlation function.

The results presented in [35] show indeed that an exclusive measurement of the

decay products for relatively low-energy nuclear reactions can actually help us in disentangling pairing effects on the nuclear masses and on the level densities. As we have discussed in the previous section, the staggering is expected to be especially sensitive to the pairing effects in the level density via the backshift parameter, and thus its quantitative understanding is potentially useful to gather information on the temperature dependence of nuclear pairing.
Finally, it is clear that this understanding requires a global control of the evaporation chain. An upgraded experimental set-up GARFIELD+RCo is now available at LNL-INFN, with an improved detector granularity so that more resonant states can be observed in the correlation functions. Also the study of lighter systems as the one presented in this work will certainly help us in going in this direction, given the higher probability of collecting the total initial charge of the entrance channel of the reaction, due to the lower final multiplicities, and thus achieving a (quasi)complete reconstruction of the decaying source.

1.3 The specificity of $A \sim 20$ nuclei

Our attention in this work is mainly devoted to thermal properties of light nuclei, and our aim is to obtain some information on this topic by means of fusion-evaporation reactions. We want to underline in this section, which are the main reasons which should specifically motivate the study of light nuclear systems.
The discussion of nuclear thermal properties presented in this chapter has started necessarily from the definition of the nuclear level density, which is the fundamental ingredient of any statistical description of the nucleus. Despite the fundamental interest of the issue, only inclusive experiments have been used up to now to constrain this quantity, and very few studies exist altogether concerning the evaporation of light nuclei in the mass region $A \sim 20$ [36, 37]. Among recent works, the analysis of inclusive spectra obtained in the reaction $^7Li + ^6Li$ at $14 - 20\ MeV$ incident energy presented in [37] has produced results which are still in agreement with the statistical model, if the level density parameter is increased to $a = A/4.5$ and deformation is included at high angular momentum [38].
Besides the lack of experimental information on nuclear level density, the mass region $A \sim 20$ is very interesting to explore also for other reasons. First of all, both theoretical and experimental studies [39] point to a nuclear limiting temperature (see chapter **2**) increasing with decreasing compound mass. In this sense, we could say that light nuclei are better suited to high temperature nuclear thermodynamics studies.

From an experimental point of view, in order to access the thermodynamic information, we have of course to be able to carefully select the reaction as well as decay mechanism. In this respect, light nuclei reactions present an additional difficulty: the decay model itself is not well established for nuclei in the mass region $A \sim 20$: besides the Hauser-Feshbach theory of statistical evaporation (also detailed in chapter **2**) a different model, the so-called Fermi break-up [40], foreseeing an instantaneous rather than sequential decay, is known since a long time and has been extensively used, but no unique experimental information exists on the transition, if any, between these two regimes. It is then clear that a highly exclusive measurement is requested, in order to perform a good selection of the reaction mechanism according to criteria on the event-by-event topology.
Finally, another reason to pursue the investigation on light nuclei is the expected stronger interplay between nuclear structure and thermal properties for these "few-body" systems. Besides the interest on nucleon-nucleon correlations giving rise to the odd-even effects previously described, also cluster-cluster correlation are known to be important in nuclei with $A \sim 20$: some excited states of different nuclei in this mass region are known in fact to present pronounced cluster structures. These correlations may also persist in the ground state along some selected isotopic chains [41]. According to the Ikeda diagrams [42], which is shown in fig.(1.7), alpha-clustered excited states are massively expected at high excitation energies close to the multi-alpha decay threshold in all even-even $N = Z$ nuclei. Clustering degrees of freedom should therefore be taken into account in order to reproduce the existence of these states. The presence of such clustered states lead to exotic non-statistical decays which start to be identified in the recent literature. A very interesting case is for instance that of the so-called Hoyle state, *i.e.* the first excited state 0^+ at 7.654 MeV of ^{12}C, which plays a decisive role in stellar nucleosynthesis of ^{12}C. Both calculations and experimental results tends to confirm the fact that this state has a low-density α-clustered structure, which can be compatible with the description of a bosonic condensation phenomenon. In terms of a nuclear state, this translates into a non negligible probability of a simultaneous 3-body decay (alternative to the $^8Be + \alpha$ channel), where the three α particles are characterized by a low kinetic energy and low kinetic energy dispersion [43]. At present an experimental upper limit of 4% exists for the contribution of the direct 3α channel to the decay width of this state. The issues of clustering in nuclear physics and that of the statistical behaviour of the decay are clearly intercorrelated: a trustable modelization of highly correlated alpha-clustered states is very difficult to achieve [44], however such effects might be experimentally seen as an excess of cluster production with respect to the prediction

of the statistical model, provided that the ingredients of the latter are sufficiently constrained via experimental data.
Finally, an additional interest of studies on light nuclei come from the problem of secondary decays in reactions in the fragmentation regime. Light nuclei with excitation energies of the order of $\sim$ 3 MeV per nucleon, are massively produced in multifragmentation reactions and their statistical behaviour is thus essential to access the properties of heavy excited sources at break-up time.

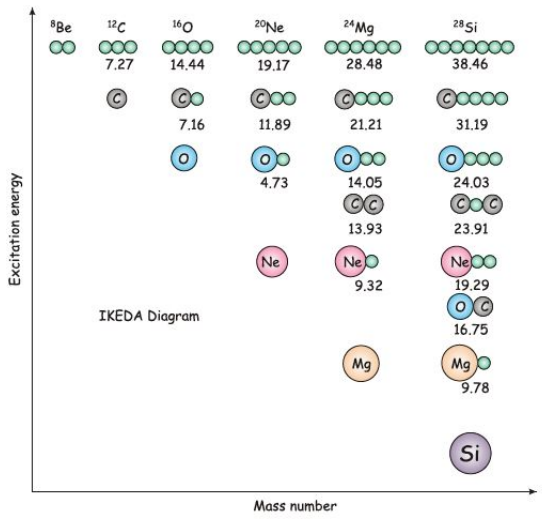

Figure 1.7: Ikeda Diagram: illustrative pictures in the excitation energy - mass number space of possible α-cluster configurations for light self conjugate nuclei, together with the corresponding decay thresholds in MeV.

1.4 Outline of the Thesis

In this chapter we have described the physics framework of this thesis, in which we concentrate on the reconstruction of thermal properties of light nuclei from fusion-evaporation reactions. In order to progress in the understanding of this topic, two main efforts are needed, which are undertaken in this thesis:

- on the experimental side, we have to take care of obtaining an exclusive and (quasi)complete detection of the different decay products emitted in the reaction. This allows to safely select the fusion-evaporation channel and to

perform backtracing techniques based on coincident yields measurements (as the correlation functions), ensuring a global control on the whole decay chain. This requirement translates obviously into an accurate choice of the reaction itself, together with the choice of the experimental apparatus: low thresholds for particle detection and (isotopic) identification, high granularity and high energy resolutions are necessary requirements to pursue this kind of study. The $GARFIELD + RCo$ set-up (see chapter **4**) at the INFN National Laboratory of Legnaro (LNL), now upgraded with respect to the measurements of ref.[35], satisfactorily matches all these conditions. Therefore, a beam-time request was submitted to the PAC Committee of INFN-LNL by the NUCL-EX collaboration [45], and the measurement of the reaction $^{12}C(95\ MeV) +^{12} C$, presented in this thesis, was performed in December 2010. The measurement will be described in chapter **4**, together the data reduction and calibration procedures, and preliminary results will be shown in chapter **5**;

- on the models side, an improvement of existing evaporation codes is important, especially concerning the inclusion of the most realistic available parameterizations for the statistical model ingredients, with a special attention to the nuclear level density. To this aim, we present in this thesis the results of calculations performed with our new Monte Carlo Hauser-Feshbach code, whose development will be the subject of chapter **3**. In the code we have included all the available experimental information on nuclear ground state properties and on low energy particle unstable levels. The first comparisons with experimental data from the reaction $^{12}C(95\ MeV) +^{12} C$ (chapter **5**) will show the trustability of the code and the goodness of the chosen parameterizations. Having highly constrained the code via experimental information, deviations from a statistical behaviour of the system could be identified and eventually ascribed to the presence of nuclear clustering. Our final aim is to test the model predictivity on finite temperature observables, which we will be able to reconstruct from data.

The work presented in this thesis is therefore on both fronts, experiment and theory. We want to underline at this point that, even if existing models as GEMINI [46] have been offering an essential guidance in the modelization, the idea to develop a new code had its rise in our precise will to test in a controlled way which is the influence of different physical ingredients as a discrete level density on the results of the calculations, which could not have been done working on existing codes. The new code also gives us the opportunity to calculate observables which

could not have been calculated otherwise, but which we plan, in the future, to be able to obtain from experimental data, as correlation functions and discrete states population of fragments at some stage of the decay. Hopefully, this will help us, in a long range plan, in experimentally constraining some nuclear properties at finite temperature, and in obtaining a better predictivity on other finite temperature observable which can not be easily accessed, but whose control could be also useful for other interdisciplinary applications. We are thinking in particular of the impact of the temperature dependence of the symmetry energy in nuclear astrophysics: experimental constraints on finite temperature properties from terrestrial experiments are needed for a full understanding of astrophysical processes such as supernova explosions [5].

Chapter 2

Statistical Theory of the Compound Nucleus

Statistical concepts and models have been widely and successfully applied to understand the nucleus and its reactions with other nuclei since the beginning of nuclear physics. The reason for this is simple: the nucleus is a complex many-body system, whose density of quantum mechanical states increases rapidly with excitation energy and soon becomes very large. In particular, a nuclear system issued in a fusion reaction, even if at the lowest bombarding energies at which the reaction can be initiated, can explore many different configurations and then decay in many different ways. Given this complexity, statistical methods come out to be essential for the comprehension and prediction of nuclear phenomena [47].
The Compound Nucleus (CN) is an excited system formed in a fusion reaction which is complex enough to show equilibrium between its degrees of freedom: this means that, a priori, all the states available for the system are characterized by an equal occupation probability. This picture is based on Bohr's independence hypothesis, according to which the formation and decay of the equilibrated CN are independent of each other. It follows that the cross section for the reaction:

$$a + A \rightarrow C \rightarrow b + B \tag{2.1}$$

can be factorized into two independent terms: the fusion cross section in the entrance channel α and the probability for the decay of the CN to the final channel β (also called Branching Ratio, BR):

$$\sigma_{\alpha\rightarrow\beta}^{E,J,\pi(C)} = \sigma_F^C(\alpha) BR^C(\beta) \tag{2.2}$$

In the notation α and β stand for the collection of all good quantum numbers

of the initial and final static problems, *i.e.* respectively, of the systems $a + A$ and $b + B$ if there were no interaction between the two nuclei. The interaction giving rise to the the fused system C has to conserve all the quantities (energy, total angular momentum and parity) which have been specified.
The Statistical Model for the decay of an equilibrated nucleus is based on the assumption that all possibilities for the decay are, intrinsically, equally likely and are thus governed by factors such as the density of final states and barrier penetration factors. The probability for a particular decay to occur is thus inversely proportional to the total number of possible decays, according to:

$$BR^C(i) = \frac{\Gamma^i(E,J)}{\sum_p \Gamma^p(E,J)} \tag{2.3}$$

where the Γ^p are the decay widths (in MeV) associated to the decay in channel p.
In the organization of the first part of this chapter the suggestion of the independence hypothesis is ideally followed: we first discuss the entrance channel of the fusion reaction, obtaining an expression for the fusion cross section, both in the general case and in the case of the population of a resonant state in the CN. We then derive an explicit expression for the decay width of the CN in the framework of the Hauser-Feshbach evaporation model.
In the second part of the chapter we discuss the main physical ingredients of the Statistical Model, with a special attention to the nuclear level density, describing various models to calculate this fundamental quantity and different ways of obtaining information on it from experimental data.

2.1 The Compound Reaction Cross Section

2.1.1 The Fusion Cross Section in the Entrance Channel

Reaction mechanisms can be classified according to the value of the impact parameter b, defined as the distance between the initial asymptote of the projectile trajectory and its parallel through the target nucleus. For large values of b, the interaction is due to the Coulomb force between projectile and target, which is a long range repulsive force, producing essentially elastic scattering or Coulomb excitation. As the impact parameter is reduced, the probability of absorption from the elastic channel due to the short range nuclear forces becomes increasingly important. If we assume a schematic representation, in which only two ways of interaction, namely scattering or absorption, are considered, fusion can be identified with the formation

of a CN system, as the result of a succession of elementary rearrangements reactions among the nucleons of the projectile and the target.
For a first estimate of the fusion cross section we may use a classical picture of a nuclear reaction [48], in which the projectile is moving towards the target in an effective radial potential:

$$V_b(r) = V(r) + \epsilon \frac{b^2}{r^2} \tag{2.4}$$

where $V(r)$ is the Coulomb-plus-nuclear scattering potential, $(\epsilon\, b^2/r^2)$ is a potential term associated with tangential motion and ϵ is the kinetic energy in the center-of-mass reference frame of the system, *i.e.*, the relative kinetic energy between projectile and target. Except when b is very large, the effective potential contains a barrier. There will exists a trajectory for which the barrier height coincides with the energy ϵ of the entrance channel, and we call the corresponding impact parameter the grazing impact parameter b_{gr}. At this energy, one has:

$$V_B + \epsilon \frac{b_{gr}^2}{R_B^2} = \epsilon \tag{2.5}$$

where the barrier radius R_B and the corresponding value of the scattering potential $V_B = V(R_B)$ (assumed independent on b) have been introduced, so that:

$$b_{gr}(\epsilon) = R_B \sqrt{1 - \frac{V_B}{\epsilon}} \tag{2.6}$$

We can then adopt the b_{gr} value as a sharp cut-off value determining the outcome of the nuclear reaction: if the projectile has an impact parameter $b > b_{gr}$ it will be reflected by the barrier, if $b < b_{gr}$ elastic scattering is suppressed, the projectile is absorbed and it fuses with the target. In this simple picture the total absorption cross section is simply given by:

$$\sigma_F = \int_0^{b_{gr}} 2\pi b db = \pi b_{gr}^2 \tag{2.7}$$

Substituting here the value of b_{gr} we find:

$$\sigma_F(\epsilon) = \pi R_B^2 \left(1 - \frac{V_B}{\epsilon}\right) \tag{2.8}$$

where the energy dependence of σ_F is made explicit.
We can now obtain the equivalent expression in terms of the quantized orbital angular momentum, by attributing successive contributions to σ_F to successive values

of $\ell = kb$. We start noticing that the contribution to the barrier coming from the term proportional to b^2 in eq.(2.4) can be expressed as a function of ℓ and assumes the form of a centrifugal barrier:

$$V_\ell(r) = \frac{\ell(\ell+1)\hbar^2}{2\mu r^2} \tag{2.9}$$

where μ is the reduced mass. The cross section for a given ℓ can be defined as the area of the surface between circles with radii $b = \ell/k$ and $b = (\ell+1)/k$, which is:

$$\frac{\pi}{k^2}\left[(\ell+1)^2 - \ell^2\right] = \frac{(2\ell+1)\pi}{k^2} \tag{2.10}$$

Hence σ_F can be written in terms of a sum over angular momenta:

$$\sigma_F = \frac{\pi}{k^2}\sum_0^{\ell_{gr}}(2\ell+1) = \frac{\pi}{k^2}(\ell_{gr}+1)^2 \tag{2.11}$$

which, since $\ell_{gr} = kb_{gr}$, coincides with (2.7) when $\ell_{gr} >> 1$.
We can push the derivation of σ_F a step further, even with this simple model, and consider that, for some values of ℓ, there will be finite probabilities for both scattering and absorption from the elastic channel. If we define the transmission coefficient T_ℓ as the probability that a given partial wave ℓ is absorbed, we can write instead of eq.(2.11):

$$\sigma_F = \frac{\pi}{k^2}\sum_0^{\infty}(2\ell+1)T_\ell \tag{2.12}$$

and the sharp cut-off model we have started our derivation with will be defined by the situation:

$$T_\ell = \begin{cases} 1 & for\ \ell < \ell_{gr} \\ 0 & for\ \ell > \ell_{gr} \end{cases} \tag{2.13}$$

The derivation of eq.(2.12) presented in this section is obviously far too simple. The formation of the CN is also limited by conditions on its mass, on its stability against prompt fission (therefore on angular momentum conditions) and above all by the competition of non-compound processes accompanying fusion in the entrance channel. Nevertheless, eq.(2.12) provides an expression which can be easily generalized, and which is needed in the derivation of the decay widths in the Hauser-Feshbach model, as it will be shown in the following sections.
The general form of eq.(2.12) which will be later needed requires additionally the consideration of the spin degree of freedom in the reaction. This can be easily done by the evaluation of the statistical factors giving us the spin coupling probabilities.

For the entrance channel α of the reaction between a and A, we can define the channel spin S_α as the result of the coupling between the spin of the incident particle i_a and the spin of the target nucleus I_A, for a total amount of $(2i_a+1)(2I_A+1)$ available states, and its inverse multiplied by the degeneracy $(2S_\alpha+1)$ represents the probability of having a channel spin S_α in a reaction with unpolarized beam and target:

$$g(S_\alpha) = \frac{2S_\alpha+1}{(2i_a+1)(2I_A+1)} \tag{2.14}$$

In the very same way, since the presence of a channel spin S_α different than zero implies that the angular momentum of the CN will be the result of the coupling between S_α and the orbital angular momentum ℓ, we have to evaluate the relative probability of having a CN with angular momentum J_C, which is given by:

$$p(J_C) = \frac{2J_C+1}{(2\ell+1)(2S_\alpha+1)} \tag{2.15}$$

In the absence of angular momentum selection rules, which is implicit in the equiprobability hypothesis of CN reactions, the desired expression for the total fusion cross section is obtained by multiplying eq.(2.12) by $g(S_\alpha)p(J_C)$, and substituting the sum over orbital angular momentum values with all the necessary sums coming from angular momentum couplings (which means summing up over all possible entrance channels of the reaction):

$$\sigma_F = \frac{1}{(2i_a+1)(2I_A+1)} \cdot \sum_{J_C} \sum_{S_\alpha=|I_A-i_a|}^{I_A+i_a} \sum_{\ell=|J_C-S_\alpha|}^{J_C+S_\alpha} \frac{\pi}{k_\alpha^2}\,(2J_C+1)\,T^{J_C}_{S_\alpha,\ell} \tag{2.16}$$

At this point, the only missing ingredients to completely specify the fusion cross section are the transmission coefficients T_ℓ and their dependence on the energy ϵ and orbital angular momentum ℓ. These coefficients correspond to the quantum mechanical penetration probability of the effective barrier $V_b(r)$, which is given by the sum of the Coulomb plus nuclear potential $V(r)$ and the centrifugal barrier $V_\ell(r)$, as in eq.(2.4) with the substitution $\ell = kb$. If we adopt for the transmission coefficients the result of the barrier penetration probability for a parabolic barrier [49], we can write:

$$T_\ell(\epsilon) = \frac{1}{1+\exp\left[2\pi(V_b-\epsilon)/\hbar\omega_\ell\right])} \tag{2.17}$$

where ω_ℓ is the curvature of the barrier at its maximum.
In applications, eq.(2.17) is usually compared to the results of optical model fits to elastic scattering data in order to extract realistic values of the parameters V_b and

ω_ℓ. Much more sophisticated approaches exist for the calculation of the transmission coefficients, usually keeping the results of optical model fits (where available) as a reference. Some examples will be given in chapter **3**, when discussing the implementation of transmission coefficients parameterizations in statistical decay codes.

2.1.2 Elements of Resonance Theory

In the previous section we have started the derivation of the total fusion cross-section from simple assumptions, which have led us to eq.(2.8), where $\sigma_F(\epsilon)$ is a monotonic function of the available energy. This classical picture has been modified by the inclusion of the transmission coefficients and of angular momentum couplings, leading us to eq.(2.16). It is evident from eq.(2.16) that the monotonic behaviour of $\sigma_F(E)$ as a function of the incoming energy can not hold anymore: the transmission coefficients are energy and angular momentum dependent quantities, and are therefore related to the probability of creating the CN in a specific state C, characterized by an energy E^*_C and an angular momentum J_C. As a consequence of this, resonances in the fusion cross section may appear. In the following, we will adopt the notation σ_F^C meaning the population of a specific state C of the CN.
We want now to derive which is the energy dependence of the fusion cross section if the CN is excited in a region where only a discrete level with energy E_R (and with a given angular momentum J_R) exists. An excited unstable nuclear state is characterized by a finite lifetime τ. Thus the wavefunction of the resonant state has the form:

$$\begin{aligned} |\psi(t)|^2 &= |\psi_0|^2 \exp(-t/\tau) \\ \psi(t) &= \psi_0 \exp(-i\omega_R t - t/2\tau) \qquad with \qquad E_R = \hbar\omega_R \end{aligned}$$

Using a Fourier transform the wavefunction $\psi(t)$ can be rewritten as:

$$\psi(t) = \frac{1}{\sqrt{2\pi}} \int_0^\infty d\omega \varphi(\omega) \exp(-i\omega t) \tag{2.18}$$

whose inverse is:

$$\begin{aligned}
\varphi(\omega) &= \frac{1}{\sqrt{2\pi}}\int_0^\infty dt\psi(t)\exp(i\omega t) \\
&= \frac{\psi_0}{\sqrt{2\pi}}\int_0^\infty dt\exp[i(\omega-\omega_R)-1/2\tau]t \\
&= \frac{\psi_0}{\sqrt{2\pi}}\frac{\exp[i(\omega-\omega_R)-1/2\tau]t}{i(\omega-\omega_R)-1/2\tau}\Big|_0^\infty \\
&= \frac{i\psi_0}{\sqrt{2\pi}}\frac{1}{(\omega-\omega_R)+\frac{i}{2\tau}} \\
\Rightarrow |\varphi(\omega)|^2 &= \frac{\psi_0^2}{2\pi}\frac{1}{(E^*-E_R)^2+\frac{\Gamma^2}{4}} \quad with \;\; \Gamma=\hbar/\tau
\end{aligned}$$

where we have introduced the energy width Γ of the discrete level, related to its lifetime through the uncertainty principle. The quantity $|\varphi(\omega)|^2$ represents the probability of finding the CN at the energy $E^* = \hbar\omega$ when $E_R = \hbar\omega_R$ is the resonance energy. Here we have to precise that the assumption of a single resonance available for the CN excitation is valid only if the width of this resonance is smaller than the mean spacing between CN levels, which we take as a constant D. This condition is actually satisfied only for rather low excitation energies.
The cross section $\sigma_F^C(E^*)$ for the formation of the CN has to be proportional to this probability:

$$\sigma_F^C(E^*) = \frac{\mathcal{C}(E^*)}{(E^*-E_R)^2+\frac{\Gamma^2}{4}} \tag{2.19}$$

We have to pay attention here to the fact that the variable E^* in this last expression represents an excitation energy value for the CN, and it is related to the available energy by energy conservation:

$$E^* = \epsilon_\alpha + Q \tag{2.20}$$

where α is the reaction entrance channel, ϵ_α is the relative kinetic energy between a and A and Q is the Q-value of the reaction. We will derive in the following the dependence of σ_F^C from the relative kinetic energy variable ϵ_α, instead as from the CN excitation energy E^*, taking advantage of the fact that the difference between these two quantities is given by the constant Q-value. We have therefore $d\epsilon_\alpha = dE^*$, and we can write the Q-value shifted version of eq.(2.19):

$$\sigma_F^C(\epsilon_\alpha) = \frac{\mathcal{C}(\epsilon_\alpha)}{(\epsilon_\alpha-\epsilon_{\alpha R})^2+\frac{\Gamma^2}{4}} \tag{2.21}$$

where in the notation $\epsilon_{\alpha R}$ stands for the value of the relative kinetic energy ϵ_α in the entrance channel producing the resonance in the reaction cross section.
In order to get an explicit expression for the term $\mathcal{C}(\epsilon_\alpha)$ in eq.(2.21), we can make use of the detailed balance principle, which asserts:

$$prob(\alpha \to C) N_\alpha(\epsilon_\alpha) = prob(C \to \alpha) N_C(E_C) \tag{2.22}$$

where the terms indicated by $prob(\cdot)$ are the normalized probabilities (per unit time) of the processes specified between parenthesis, and N_α and N_C are, respectively, the number of available states in the entrance channel and for the CN nucleus. To avoid being repetitive and for the sake of simplicity, we neglect in the counting of available states the angular momentum degeneracy: in fact, we will derive in the following the decay width of the CN, always starting from the detailed balance principle and explicitly including the angular momentum degeneracy from the beginning. Moreover, the angular momentum dependence of the result of this derivation is simply coming from the product of the same spin weighting factors which were discussed in the previous section and are given in eq.(2.14,2.15), further multiplied by the $(2\ell+1)$ factor coming from the decomposition of the fusion cross section into partial waves.
Therefore, for the terms entering the detailed balance principle we have:

- $N_\alpha(\epsilon_\alpha)$ is the number of relative motion states of a and A in the entrance channel:
  $N_\alpha(\epsilon_\alpha) = \frac{d^3 p_\alpha V}{(2\pi\hbar)^3}$, where we have already carried out the integration on d^3r, giving us the geometrical volume V associated to the reaction. The momentum p_α is the one related to ϵ_α by $\epsilon_\alpha = p_\alpha^2/2\mu$;

- the factor $prob(\alpha \to C)$ can be expressed in terms of the CN formation cross section in the entrance channel:
  $prob(\alpha \to C) = \frac{\sigma_\alpha^C v_\alpha}{V}$,
  where we have written for simplicity of notation $\sigma_F^C(\epsilon_\alpha) = \sigma_\alpha^C$, and v_α is the relative velocity;

- $N_C(E_C^*)$ is the number of CN states with energy between $(E_C^*, E_C^* + dE_C^*)$, and since we are assuming that in the energy range for the CN formation only a well-defined resonant state exists, it can be considered equal to 1;

- the factor $prob(C \to \alpha)$ can be defined as the inverse of the lifetime of the CN for the decay into channel α, that is to say:
  $prob(C \to \alpha) = 1/\tau_\alpha^C = \Gamma^\alpha/\hbar$, where Γ^α is the energy width associated to the finite lifetime τ_α.

Substituting these terms in eq.(2.22), we have in the LHS :

$$\begin{aligned} prob(\alpha \to C)N_\alpha(\epsilon_\alpha) &= \int \frac{d^3p_\alpha \cdot V}{(2\pi\hbar)^3} \cdot \frac{\sigma_\alpha^C v_\alpha}{V} \\ &= \frac{1}{2\pi^2\hbar^3} \int dp_\alpha v_\alpha p_\alpha^2 \sigma_\alpha^C(\epsilon_\alpha) \\ &= \frac{1}{2\pi^2\hbar^3} \int d\epsilon_\alpha \; p_\alpha^2 \frac{\mathcal{C}(\epsilon_\alpha)}{(\epsilon_\alpha - \epsilon_{\alpha R})^2 + \frac{\Gamma^2}{4}} \end{aligned} \tag{2.23}$$

where we have also made use of $d\epsilon_\alpha = v_\alpha dp_\alpha$. At this point, if we do the hypothesis that the factor $p_\alpha^2\mathcal{C}(\epsilon_\alpha)$ is a smoother function of ϵ_α than $\frac{1}{(\epsilon_\alpha - \epsilon_{\alpha R})^2 + \frac{\Gamma^2}{4}}$ (which is certainly true for values of ϵ_α near the resonance value $\epsilon_{\alpha R}$) we can further write:

$$\begin{aligned} prob(\alpha \to C)N_\alpha(\epsilon_\alpha) &= \frac{1}{2\pi^2\hbar^3} p_\alpha^2 \mathcal{C}(\epsilon_{\alpha R}) \int d\epsilon_\alpha \frac{1}{(\epsilon_\alpha - \epsilon_{\alpha R})^2 + \frac{\Gamma^2}{4}} \\ &= \frac{k_\alpha^2}{2\pi^2\hbar} \mathcal{C}(\epsilon_{\alpha R}) \frac{2}{\Gamma}\pi \\ &= \frac{k_\alpha^2}{\pi\hbar\Gamma} \mathcal{C}(\epsilon_{\alpha R}) \end{aligned} \tag{2.24}$$

Going back to the detailed balance principle, we have for the constant $\mathcal{C}(\epsilon_{\alpha R})$:

$$\begin{aligned} \frac{k_\alpha^2}{\pi\hbar\Gamma} \mathcal{C}(\epsilon_{\alpha R}) &= \frac{\Gamma_\alpha}{\hbar} \\ \mathcal{C}(\epsilon_{\alpha R}) &= \frac{\pi}{k_\alpha^2} \Gamma\Gamma_\alpha \end{aligned} \tag{2.25}$$

Finally we get the resonant CN formation cross section:

$$\sigma_F^C(\epsilon_\alpha) = \frac{\pi}{k_\alpha^2} \frac{\Gamma\Gamma_\alpha}{(\epsilon_\alpha - \epsilon_{\alpha R})^2 + \frac{\Gamma^2}{4}}$$

As anticipated, in order to take angular momentum into account, we have to introduce a spin dependence, analogous to the one appearing in eq.(2.16). If we assume spinless projectile and target, the resulting spin dependence reduces to a $(\ell + 1)$ factor, and we can write:

$$\sigma_F^C(\epsilon_\alpha) = \frac{\pi}{k_\alpha^2}(2\ell + 1) \frac{\Gamma^\alpha\Gamma}{(\epsilon_\alpha - \epsilon_{\alpha R})^2 + \frac{\Gamma^2}{4}} \tag{2.26}$$

As stated in the introduction of this chapter, in order to find the cross section for a particular (α, β) reaction proceeding through an intermediate given state C it is

sufficient to multiply $\sigma_F^C(\alpha)$ by the Branching Ratio $BR^C(\beta) = \Gamma^\beta/\Gamma$. Doing so for eq.(2.26) we finally get:

$$\sigma_{\alpha\to\beta}^C = \frac{\pi}{k_\alpha^2}(2\ell+1)\frac{\Gamma^\alpha\Gamma^\beta}{(\epsilon_\alpha - \epsilon_{\alpha R})^2 + \frac{\Gamma^2}{4}} \tag{2.27}$$

which is called the Breit-Wigner one-level formula for nuclear reactions. An additional sum over Breit-Wigner resonances will be needed if the CN can be excited in more than one discrete state, and a resulting convoluted fusion cross section has to be evaluated.

Starting from eq.(2.26), we may want to recover the expression of the fusion cross section in terms of transmission coefficients. A single ℓ contribution to the total fusion cross section of eq.(2.12) can be compared to the average of eq.(2.26) in an energy interval large enough to contain several resonances which can be excited by the same entrance channel. The energy range to calculate the average will be a multiple of the constant energy spacing D for CN levels. If we evaluate the energy average of eq.(2.26), we obtain:

$$\begin{aligned} \left\langle \sigma_F^C(\epsilon_\alpha) \right\rangle &\approx \frac{1}{(r_n D)}\frac{\pi}{k_\alpha^2}(2\ell+1)\sum_{r_i}^{r_n}\int d\epsilon_\alpha \frac{\Gamma_{r_i}^\alpha \Gamma_{r_i}}{(\epsilon_\alpha - \epsilon_{\alpha r_i})^2 + \frac{\Gamma_{r_i}^2}{4}} \\ &= \frac{\pi}{k_\alpha^2}(2\ell+1)\frac{2\pi\left\langle\Gamma^\alpha\right\rangle}{D} \end{aligned} \tag{2.28}$$

where the sum runs over all the resonances whose energy falls in the interval of width $(r_n D)$, and we have carried out the energy integration of all the single Breit-Wigner terms (assuming that they dominate the overall energy dependence of the cross section). For a single ℓ contribution in eq.(2.12) we had:

$$\sigma_F^C(\epsilon_\alpha) = \frac{\pi}{k^2}(2\ell+1)T_\ell(\alpha) \tag{2.29}$$

A comparison of the two above equations gives the key result:

$$T_\ell(\alpha) = \frac{2\pi\left\langle\Gamma^\alpha\right\rangle}{D} \tag{2.30}$$

where the transmission coefficient is expressed in terms of average properties of the CN spectrum, namely average decay widths and level spacing. To give a further insight into the meaning of this last expression, we start noticing that the result obtained in eq.(2.26) implies that the fusion cross section in the resonant state is proportional to the probability of the opposite process, *i.e.* the decay of the CN

through the same channel α, which is determined by the width Γ^{α}. This is of course a consequence of the microscopic reversibility of the process, which is assumed in the detailed balance equation. In a very simple picture, we can think of the CN state as created by the particle a entering into the nucleus through channel α. If the excited state is unbound, we may ask after what time τ_{α} the particle would reappear at the nuclear surface, ready lo leave through the same channel it came in. This time could be expressed in terms of the period of the motion of particle a inside the nucleus. Having assumed an average energy spacing D for CN states, we can substitute for the energy E_R in the wavefunction $\psi(t)$ the expression $E_R = E_0 + nD$, where E_0 is the ground state energy of the CN nucleus. Thus $\psi(t)$ comes out to be a periodic function of coordinate t, with period $P = 2\pi\hbar/D$. Since the assumption of the presence of resonant states is valid only if $D >> \Gamma$, the lifetime τ_{α} has to be large compared to P. This can be the case because of the reflection of a at the inner side of the nuclear surface, described by the finite probability $T_{\ell}(\alpha)$ of escaping through channel α. We then get:

$$\tau_{\alpha} \approx \frac{P}{T_{\ell}(\alpha)} \tag{2.31}$$

which gives us back the expression of eq.(2.30).
Summarizing, in this section we have derived the energy dependence of the fusion cross section in presence of discrete states for the CN formation. An illustrative picture of a resonant cross section is given in fig.(2.1), where also the corresponding spectrum of excited levels for the CN is shown. Since in the rest of this work we will be mainly interested in the outgoing channel of the nuclear reaction rather than in the formation of the CN, we want to recall at this point that resonances are of great importance also in the decay of the CN source. Discrete levels can indeed be populated in daughter nuclei, which can further decay delivering cold products which keep memory of their "resonant" origin. Decaying discrete states can then be reconstructed through techniques as the correlation function in relative momentum of coincident measured yields, as discussed in chapter **1**.

2.1.3 The Evaporation Width in the Hauser-Feshbach Model

We want now to derive a general expression for the CN decay width for channel β, which determines the probability for the hot nucleus to decay via this channel, or equally, its decay rate (probability per unit time). We consider CN reactions in which all final channels are made up of light particles (up to $Z = 2$) and a residual nucleus. Obviously this means assuming that the excitation energy of the CN exceeds the nuclear separation energy, *i.e.* the lowest Q-value for particle emission.

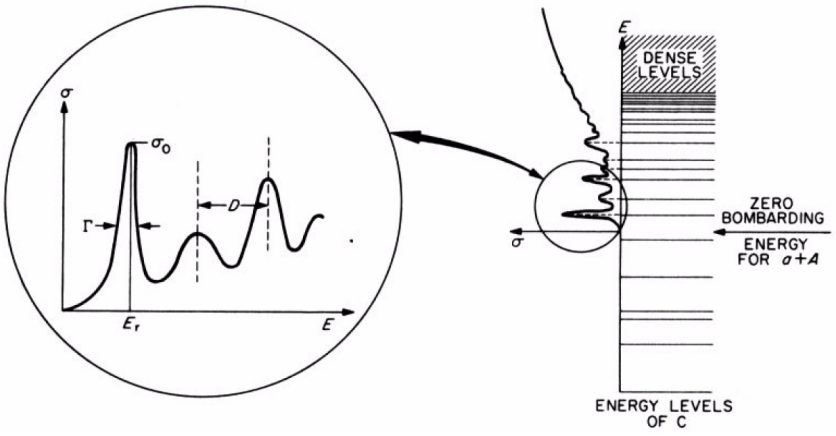

Figure 2.1: Illustrative picture of the population of a discrete state in the fusion reaction $a+A \rightarrow C$, with the consequent appearance of resonances in the fusion cross section and deviation of the energy dependence of the fusion cross section from a monotonic behaviour.

We anticipate at this point that the energy spectrum of the particles emitted in such reactions shows a Maxwellian shape, whose slope is determined by the excitation energy of the emitting source. It is because of the analogy with the spectrum of molecules evaporated from the surface of a hot liquid that the CN is also said to undergo a decay via evaporation.
Let us consider the most general case of the decay of a compound nucleus in a CN state C with energy E^*_C and angular momentum J_C by the evaporation of a light particle b with spin i_b and energy in the range $(\epsilon_\beta; \epsilon_\beta + d\epsilon_\beta)$, leaving a residual nucleus B, excited at an energy $E^*_B = E^*_C - Q - \epsilon_\beta$ and with an angular momentum I_B (here in reality ϵ_β is the relative kinetic energy of the two decay products, associated to the reduced mass μ_β, and it is equal to the energy of the emitted particle only if we can neglect the recoil of the evaporation residue).
The starting point of our derivation is once again the the detailed balance principle:

$$prob(C \rightarrow \beta) N_C(E^*_C, J_C) = prob(\beta \rightarrow C) N_\beta(\epsilon_\beta, i_b\ I_B) \tag{2.32}$$

where we have kept the same notation as for its former application in eq.(2.22). In the detailed balance equation the following terms appear:

- $N_C(E^*_C, J_C)$ is the number of states accessible to the system C in the energy interval $(E^*_C; E^*_C + dE^*_C)$. We know from the previous section that the number of these excited states depends on the excitation energy range for the CN. We assume now that the CN is excited in the continuum region, where the energy overlap of excited levels is such that no isolated resonance can be resolved (*i.e.* $\Gamma >> D$, to make use of the same notation as in the derivation of the fusion cross section). The number of available states can therefore be expressed in terms of the nuclear Level Density (LD) $\rho_C(E^*_C, J^*_C)$, already introduced in chapter **1**, which will be discussed later in details, defined in such a way that: $N_C(E^*_C, J_C) = (2J_C + 1)\rho_C(E^*_C, J^*_C)dE^*_C$.
  We only have to notice at this point that the spin-degeneracy factor $(2J_C + 1)$ is not accounted for in the counting of levels coming from ρ, and therefore has to be explicitly introduced;

- the factor $prob(C \to \beta)$ (probability per unit time) is such that:
  $prob(C \to \beta) = 1/\tau_\beta = \Gamma^\beta/\hbar$.
  and it represents a differential decay rate:
  $dR^J_{\{C\ E^*_C\ J_C\}\to\{b\ \epsilon_\beta\ i_b\ I_B\}}$
  which can be as well expressed in terms of the decay width Γ^β;

- the probability per unit time $prob(\beta \to C)$ can be deduced from the the cross section of the inverse reaction $\sigma^C_F(\beta)$ $(= \sigma^C_\beta$ for simplicity of notation), *i.e.*
  $prob(\beta \to C) = \frac{\sigma^C_\beta(\epsilon_\beta, i_b, I_B)v_\beta}{V}$;

- $N_\beta(\epsilon_\beta, i_b\ I_B)$ is the number of relative-motion states for b and B multiplied by the spin degeneracy of the two final nuclei and by the number of energy states in which the residual nucleus B can be left (we are then assuming that the evaporated particle is emitted in its ground state). Therefore we have:
  $N_\beta(\epsilon_\beta, i_b\ I_B) = \frac{d^3p_\beta V}{(2\pi\hbar)^3} \cdot (2i_b + 1)(2I_B + 1)\rho_B(E^*_B, I_B)dE^*_B$
  where we have already carried out the integration on d^3r.

We can thus rewrite the balance equation and find the following expression for the differential rate:

$$dR^J_{C\to\beta} = \frac{1}{(2J_C + 1)\rho_C(E^*_C, J^*_C)dE^*_C} \cdot \frac{\sigma^C_\beta(\epsilon_\beta, i_b, I_B)v_\beta}{V} \cdot \frac{d^3p_\beta V}{(2\pi\hbar)^3} \cdot (2i_b + 1)(2I_B + 1)\rho_B(E^*_B, I_B)dE^*_B \tag{2.33}$$

where $dE_C^* = dE_B^*$ for a given decay. Integrating in the momentum space the LHS of eq.(2.33) we can further write:

$$\begin{aligned} & \int v_\beta \frac{d^3p_\beta}{(2\pi\hbar)^3} \cdot \sigma_\beta^C(\epsilon_\beta, i_b, I_B)\ \rho_B(E_C^* - Q - \epsilon_\beta, I_B) \\ = \ & 4\pi \int v_\beta \frac{p_\beta^2 dp_\beta}{(2\pi\hbar)^3} \cdot \sigma_\beta^C(\epsilon_\beta, i_b, I_B)\ \rho_B(E_C^* - Q - \epsilon_\beta, I_B) \\ = \ & \frac{4\pi\ 2\mu_\beta}{(2\pi\hbar)^3} \int \epsilon_\beta\ v_\beta dp_\beta \cdot \sigma_\beta^C(\epsilon_\beta, i_b, I_B)\ \rho_B(E_C^* - Q - \epsilon_\beta, I_B) \\ = \ & \frac{\mu_\beta}{\pi^2\hbar^3} \int_0^{E_C^*-Q} d\epsilon_\beta\ \epsilon_\beta \cdot \sigma_\beta^C(\epsilon_\beta, i_b, I_B)\ \rho_B(E_C^* - Q - \epsilon_\beta, I_B) \end{aligned} \tag{2.34}$$

where we have made use of the relations $\epsilon_\beta = p_\beta^2/(2\mu_\beta)$ and $d\epsilon_\beta = v_\beta dp_\beta$ and we have specified the limits of the integration on the relative energy ϵ_β.
Once integrated over the energy, we have to sum over the spins I_B of the residual nucleus to obtain the evaporation rate in the RHS of eq.(2.33). This finally gives:

$$\begin{aligned} R_{C\to\beta}^J \ = \ & \frac{(2i_b+1)}{(2J_C+1)\rho_C(E_C^*, J_C^*)} \cdot \frac{\mu_\beta}{\pi^2\hbar^3} \\ & \cdot \sum_{I_B}(2I_B+1) \cdot \int_0^{E_C^*-Q} d\epsilon_\beta\ \epsilon_\beta \cdot \sigma_\beta^C(\epsilon_\beta, i_b, I_B)\ \rho_B(E_C^* - Q - \epsilon_\beta, I_B) \end{aligned} \tag{2.35}$$

We can then express the fusion cross section for the inverse process in terms of transmission coefficients with the help of the generalized equation (2.16) previously obtained, which we rewrite hereafter for a specific state C of the CN issued from fusion in channel β:

$$\sigma_\beta^C(\epsilon_\beta, i_b, I_B) = \frac{1}{(2i_b+1)(2I_B+1)} \cdot \sum_{S_\beta=|I_B-i_b|}^{I_B+i_b} \sum_{\ell_\beta=|J_C-S_\beta|}^{J_C+S_\beta} \frac{\pi}{k_\beta^2}\ (2J_C+1)\ T_{S_\beta,\ell_\beta}^{J_C} \tag{2.36}$$

This last expression can be substituted into eq.(2.35). If we further write $k_\beta^2 = 2\mu_\beta\epsilon_\beta/\hbar^2$ we finally obtain:

$$\Gamma^\beta = \frac{1}{2\pi\rho_C(E_C^*, J_C^*)} \cdot \int_0^{E_C^*-Q} d\epsilon_\beta \sum_{I_B} \sum_{S_\beta=|I_B-i_b|}^{I_B+i_b} \sum_{\ell_\beta=|J_C-S_\beta|}^{J_C+S_\beta} T_{S_\beta,\ell_\beta}^{J_C} \cdot \rho_B(E_C^* - Q - \epsilon_\beta, I_B) \tag{2.37}$$

where we have written the result in terms of the energy width associated to the CN decay: $\Gamma^\beta = \hbar R_{C\to\beta}^J$. A derivation of eq.(2.37) can be also obtained starting

from Fermi's Golden Rule for the transition $\{C \rightarrow \beta\}$ and making use of the time-reversal invariance, as shown in [48].
In the final channel of the reaction, the residual nucleus B can have an excitation energy again exceeding its separation energy, and therefore it can undergo a successive decay via evaporation. The whole sequence of successive decay steps necessary to reach a final cold daughter nucleus is called an evaporation chain. An illustrative picture of a fusion reaction followed by an evaporation chain is shown in fig.(2.2).

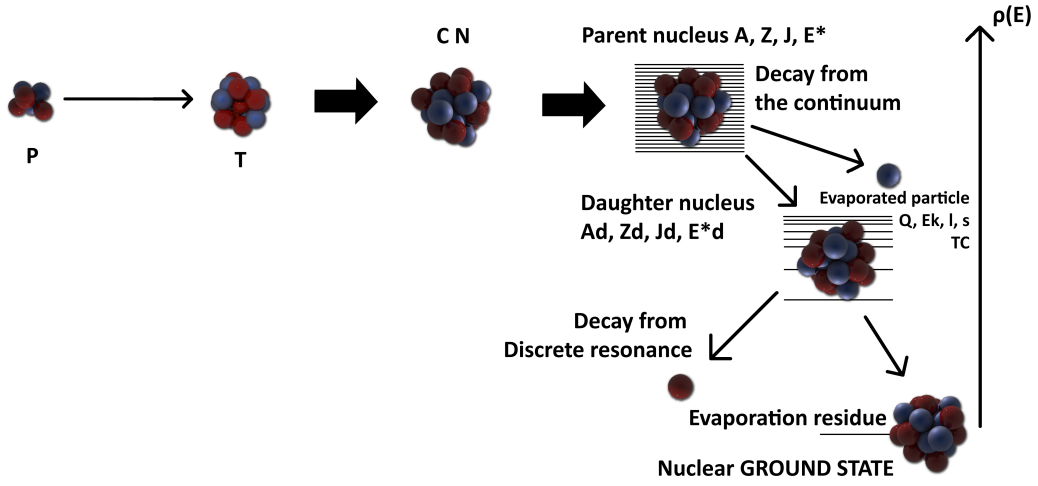

Figure 2.2: Illustrative picture of a fusion-evaporation reaction. In this representation, the decay chain of the CN starts when the nucleus is excited in its continuum, and a discrete state of the daughter nucleus is populated at the last decay step.

Eq.(2.37) is the main result of the Hauser-Feshbach model for the evaporation of the CN [51]. In the framework of this model, as it clearly appears from the derivation, also the spin and angular momentum degrees of freedom are considered in the determination of the decay widths, which represents the main difference with the alternative and simpler approach of Weisskopf and Ewing [52].
In both models however, the decay width is always expressed as an integration over the energy spectrum of the evaporated particle ϵ_β, whose shape is in turn determined by the energy dependence of the transmission coefficients and of the LD $\rho_B(E^*_C - Q - \epsilon_\beta)$. It is out of these quantities that we can extract the maxwellian shape of the energy spectra, which is evident in the examples of fig.(2.3) for experimental fusion-evaporation data taken from ref.[53].
To have a quick understanding of where does this maxwellian shape originate from, we can simply recall the definition of the nuclear temperature T which was given in

chapter **1**:

$$\frac{1}{T} = \frac{\partial \ln \rho}{\partial E^*} \tag{2.38}$$

From this definition we get that the LD has to scale as $\exp(E^*/T)$, where still no assumptions have been made on the relation between excitation energy and temperature. Hence, we can already write:

$$T_\ell(\beta) \cdot \rho_B(E_C^* - Q - \epsilon_\beta) \propto \epsilon_\beta \cdot \exp\left(-\frac{\epsilon_\beta}{T}\right) \tag{2.39}$$

where the expression in the RHS is that of a Maxwell distribution at temperature T. In the following sections of this chapter we will discuss in details the fundamental quantity $\rho(E^*)$, which will allow us for a better understanding of the functional dependence of the LD term in eq.(2.39).
Concluding, we want only to notice that, since we have stated the validity of Bohr independence hypothesis, eq.(2.37), together with the explicit expressions of all the physical ingredients appearing in it, will be all we need to implement the Hauser-Feshbach decay model in a Monte Carlo code, which is the subject of chapter **3**.

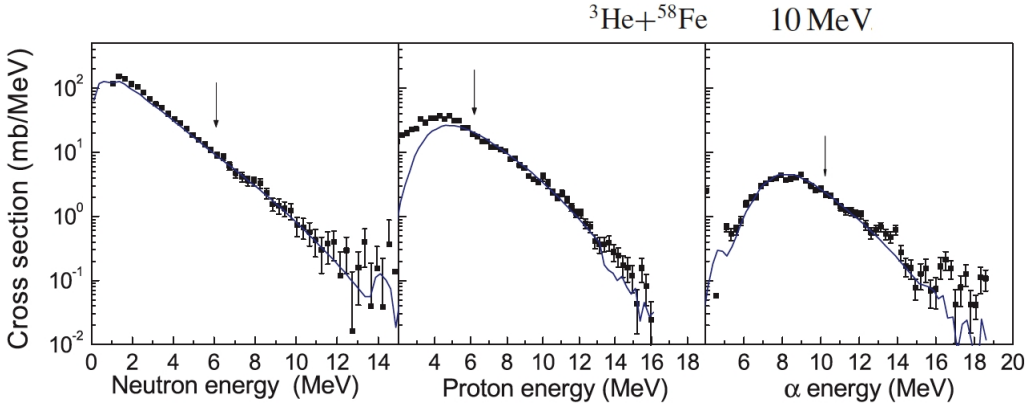

Figure 2.3: Evaporated particle energy spectra for the $^3He + ^{58}Fe$ at 10 MeV beam energy, taken from ref.[53]. The experimental data are shown by points. Solid lines are Hauser-Feshbach calculations. Arrows show energies above which spectra contain only contributions from the first stage of the reaction.

2.2 The Nuclear Level Density

In the framework of the statistical model, the decay of an equilibrated source is governed by the density of final states. For rather low excitation energy the

counting of states in the outgoing channel is dominated by the amount of energy levels corresponding to nuclear intrinsic excitations.
The fundamental quantity bearing this information is called nuclear Level Density (LD), and has already been introduced according to the definition:

$$\rho(A,E) = \frac{dN(A,E)}{dE} \tag{2.40}$$

The density $\rho(A,E)$ corresponds to the number of nuclear levels in the energy interval $(E, E+dE)$, divided by dE. In this chapter, we have made use of $\rho(E^*)$ in order to derive a decay probability for the excited CN, and we want now to investigate the LD and its dependences as a property of the nuclear system.
The most frequently used method to obtain the LD might be called a thermodynamic approach and makes use of the concepts and mathematical techniques of statistical mechanics: a partition function, containing the essential statistical information, is written down in terms of nuclear levels, properties of the system (as the number of nucleons and the energy) are used to calculate the thermodynamic quantities which enter in the calculation of the entropy and of the level density.
Given the discrete nature of the nuclear excitation spectrum, the most general expression for the LD is a sum of δ functions, namely:

$$\rho(A,E) = \sum_{n,i} \delta(A-n)\delta(E-E_i(n)) \tag{2.41}$$

where $E_i(n)$ is the energy of the i^{th} level of the nucleus with n constituents (nucleons). The grancanonical partition function $\mathcal{Z}$ is then obtained by means of a Laplace transform of the LD, *i.e.* :

$$\mathcal{Z}(\alpha,\beta) = \int_0^\infty \int_0^\infty \rho(A,E) e^{-(\beta E - \alpha A)} dA dE \tag{2.42}$$

which, given the discrete nature of $\rho(A,E)$, can be also given as:

$$\mathcal{Z}(\alpha,\beta) = \sum_{n,i} e^{-(\beta E_i(n) - \alpha n)} \tag{2.43}$$

The inverse Laplace transform of the grancanonical partition function reads:

$$\rho(A,E) = \frac{1}{(2\pi i)^2} \int_{-\infty}^{+\infty} \int_{-\infty}^{+\infty} \mathcal{Z}(\alpha,\beta) e^{(-\alpha A + \beta E)} dA dE \tag{2.44}$$

and this last equation shows that, if $\mathcal{Z}$ is known, ρ can be obtained, either numerically or analytically [48, 56].

To further simplify the problem, one generally uses the so-called saddle point approximation, for which still no assumptions on the statistical properties of the nucleus levels are required. This approximation is based on the fact that the integrand in eq.(2.44) has a saddle point around which a Taylor series expansion can be performed in order to calculate ρ. Making use of the expansion, we get:

$$\rho(A,E) = \frac{e^S}{2\pi\sqrt{det}} \tag{2.45}$$

where the entropy S reads:

$$S = \ln \mathcal{Z}(\alpha_0,\beta_0) + \beta_0 E - \alpha_0 A \tag{2.46}$$

and where *det* is the determinant of the matrix whose elements are formed by the second derivative of $\ln(\mathcal{Z})$ with respect to the variables α and β:

$$det = \left| \begin{array}{cc} \frac{\partial^2 \ln \mathcal{Z}}{\partial \beta^2} & \frac{\partial^2 \ln \mathcal{Z}}{\partial \beta \partial \alpha} \\ \frac{\partial^2 \ln \mathcal{Z}}{\partial \beta \partial \alpha} & \frac{\partial^2 \ln \mathcal{Z}}{\partial \alpha^2} \end{array} \right|_{\alpha_0,\beta_0} \tag{2.47}$$

taken at the saddle point (α_0, β_0) defined by:

$$E = -\frac{\partial^2 \ln \mathcal{Z}}{\partial \beta} \tag{2.48}$$

$$A = \frac{\partial^2 \ln \mathcal{Z}}{\partial \alpha} \tag{2.49}$$

2.2.1 Independent Particle Model

Independent particle (or quasi-particle) models are by far the most often applied to calculate level densities. In this framework, the procedure to calculate the nuclear LD is conceptually straightforward: it is sufficient to count the number of different configurations corresponding to a given E^*, J and π. The determination of the LD is thus a combinatorial problem in which the physics is contained in the specification of the single-particle orbitals for non-interacting nucleons.
In practice, this combinatorial problem cannot be solved directly, because of the huge number of possible independent particle configurations entering in the calculation. Nevertheless, the saddle point approximation introduced at the beginning of this section allows a simple calculation of the resulting level density, which we give

hereafter in some details.
In the independent particle model, eq.(2.43) for the partition sum reads:

$$\mathcal{Z}_0(\alpha,\beta) = \prod_k [1+\exp(\alpha-\beta\varepsilon_k(n))] = \prod_k [1+\exp -\beta(\varepsilon_k(n)-\mu)] \tag{2.50}$$

where ε_k are single particle energies (see section 1.1.2) and $\mu = \alpha/\beta$ is the chemical potential. At zero temperature, the chemical potential can be seen as the amount of energy required to add an extra particle to the system. For the sake of simplicity, we start considering only one nucleon species, and the use of the notation $\mathcal{Z}_0$ will be made clear in the following.
For the calculation of the level density, we can make use of the Thomas-Fermi local density approximation, which has already been introduced in chapter **1**. Under this approximation, we can write:

$$\ln \mathcal{Z}_0(\beta,\mu) = \frac{1}{(2\pi\hbar)^3}\int d^3r \int d^3p \ln\left[1+\exp -\beta\left(\frac{p^2}{2m^*}+U(\rho(r))-\mu\right)\right] \tag{2.51}$$

where single-particle energies have been explicitly written as the sum of a kinetic energy term and of the mean-field local potential $U(\rho(r))$. This expression corresponds to the partition sum of an ideal gas of fermions, with shifted local chemical potential given by $\tilde{\mu}(r) = \mu - U(\rho(r))$. Because of the self-consistency of the mean-field $U(\rho)$, it can be shown that this expression has to augmented by an interaction term, representing the interaction part of the pressure [54], as we now show. We evaluate the integral given in eq.(2.51):

$$\begin{aligned}
\ln \mathcal{Z}_0(\beta,\mu) &= \frac{2}{3}\beta\int d^3r \int \frac{d^3p}{(2\pi\hbar)^3}\frac{p^2}{2m^*}\frac{\exp -\beta\left(\frac{p^2}{2m^*}-\tilde{\mu}(r)\right)}{1+\exp -\beta\left(\frac{p^2}{2m^*}-\tilde{\mu}(r)\right)} \\
&= \frac{2}{3}\beta\int d^3r \left\langle e^{kin}\rho(r)\right\rangle_T \\
&= \frac{2}{3}\beta\left\langle E^{kin}\right\rangle_T
\end{aligned} \tag{2.52}$$

where the distribution of states following a finite temperature Fermi gas has appeared in the integration on d^3p, which therefore yields the average density of kinetic energy per units volume, $\left\langle e^{kin}\rho(r)\right\rangle_T$ (e^{kin} is the kinetic energy per nucleon). Integration on d^3r of this quantity yields the total averaged kinetic energy. We notice at this point that the obtained results corresponds indeed to a kinetic pressure

term, which we can explicitly write as $(\beta p_0 V)$ under the assumption of a constant ρ density in the final integration on d^3r. This pressure is only due to the zero point particle motion, even if single particle energies do contain the mean-field. Therefore, an analogous pressure term has to be added, linked to the mean-field $U(\rho)$. By making use of:

$$pV = -V\frac{\partial E}{\partial V} = V\rho^2\frac{\partial e}{\partial \rho} \tag{2.53}$$

in order to write the pressure term as a function of the density and of the energy per nucleon instead of total volume and total energy, we can add to $\ln \mathcal{Z}_0$ the following expression:

$$\begin{aligned} \frac{\ln \mathcal{Z}_{int}}{\beta} &= \int d^3r \rho^2(r) \frac{\partial e(\rho(r))}{\partial \rho} \\ &= \frac{1}{2}\left\langle U^{tot}\right\rangle_T \end{aligned} \tag{2.54}$$

where we have made use of the definition $1/2U(\rho) = \partial(e\rho)/\partial\rho$ and integration on d^3r yields the total averaged energy $\langle U^{tot}\rangle_T$. For a rigorous demonstration of eq.(2.54), see ref.[54].
For the total partition sum, we finally have:

$$\begin{aligned} \ln \mathcal{Z} &= \ln \mathcal{Z}_0 + \ln \mathcal{Z}_{int} \\ &= \frac{2}{3}\beta\left\langle E^{kin}\right\rangle_T + \frac{1}{2}\beta\left\langle U^{tot}\right\rangle_T \end{aligned} \tag{2.55}$$

We can further write:

$$\ln \mathcal{Z} = \frac{2}{5T}\varepsilon_F A + \frac{2}{3T}aT^2 + \frac{1}{2T}\left\langle U^{tot}\right\rangle_T \tag{2.56}$$

where we have written $\beta = 1/T$, and we have made explicit the contribution of the excitation energy $E^* = aT^2$, evaluated starting from the Fermi surface. The fundamental quantity a entering the expression for the excitation energy is the level density parameter, which, in turn, can be written in terms of the single particle level density at the Fermi energy:

$$a = \frac{\pi^2}{6}g(\varepsilon_F) \tag{2.57}$$

In order to calculate average values of observables by making use of the Fermi distribution of states for the independent particle system, also appearing in eq.(2.52), the (numerical) solution of Fermi integrals is necessary. This is usually done in

the low temperature limit, which, in particular, allows us to obtain the following expressions for the chemical potential and the total energy:

$$\begin{aligned} \langle \mu \rangle_T &= \varepsilon_F - \frac{T^2}{3}\frac{a}{A} + \beta \left\langle U^{tot} \right\rangle_T \\ \langle E \rangle_T &= \frac{3}{5} A \varepsilon_F + aT^2 + \beta \left\langle U^{tot} \right\rangle_T \end{aligned} \tag{2.58}$$

At this point, we can make use of the saddle point approximation for the calculation of the entropy, whose expression was given at the beginning of this section in eq.(2.46), and substitute the expressions we got for $\ln \mathcal{Z}$, $\langle E \rangle_T$ and $\langle \mu \rangle_T$ respectively in (2.55,2.58), thus obtaining:

$$\begin{aligned} S &= \ln \mathcal{Z}(\beta_0, \mu_0) + \beta_0 E - \beta_0 \mu_0 A \\ &= 2aT \end{aligned} \tag{2.59}$$

Eq.(2.45) for the LD finally reads:

$$\begin{aligned} \rho(A, E) &= \frac{e^{2aT}}{2\pi\sqrt{det}} \\ &= \frac{e^{2\sqrt{aE^*}}}{2\pi\sqrt{det}} \end{aligned} \tag{2.60}$$

The obtained expression for the LD depends mainly exponentially on the excitation energy E^*, and the pre-factor can only be a slowly varying function of E^* with respect to $\exp\sqrt{E^*}$, depending on the approximations done for the derivation. The dependence on the mass number is mainly contained in the LD parameter $a(A)$. A first important observation is that, in this theoretical framework, it turns out that the LD $\rho(E^*, J^\pi)$ will depend only on the density D_0^{-1} of single-particle states near the Fermi energy (D_0 is therefore the mean spacing of levels around ε_F), all other properties of the single-particle potential being irrelevant. An intuitive explanation for this result is that, for fixed E^* and J^π, the major contribution to the number of configurations comes from the excitation of many nucleons into states right above ε_F, and the number of configurations in which few nucleons take up the whole E^* is relatively small [55].
In the literature, the LD is often given through the Bethe formula [2], obtained for the Fermi gas model, *i.e.* an ideal gas of non-interacting fermions in the thermodynamic limit:

$$\rho(A, E^*) = \frac{1}{4\sqrt{3}E^*} e^{2\sqrt{aE^*}} \tag{2.61}$$

with the same definition of the LD parameter a, and with the pre-factor $\frac{1}{4\sqrt{3}E^*}$ deriving from the low temperature limit.
Explicitly considering the isospin degree of freedom does not change the derivation of the LD, and a usual expression for the result obtained for a two-components independent particle system made up by Z protons and N neutrons, is given by:

$$\rho(A, E^*) = \frac{\sqrt{\pi}}{12} \frac{e^{2\sqrt{aE^*}}}{a^{1/4} E^{*5/4}} \tag{2.62}$$

with

$$a = \frac{\pi^2}{6}(g_\pi(\varepsilon_F) + g_\nu(\varepsilon_F)) \tag{2.63}$$

where g_π and g_ν are the proton and neutron single-particle densities at the average Fermi energy ε_F for the two species.
Let us now specify the values of the independent particle model parameters. The numerical value of the Fermi energy for a nucleon system is $\varepsilon_F \approx 30\ MeV$, and this corresponds to the energy of the highest level occupied by the nucleons in the nucleus at zero temperature, *i.e.* in the ground-state. With this value one can calculate the average single particle level density $g(\varepsilon_F)$, and consequently get for the LD parameter: $a \approx A/12\ MeV^{-1}$. We will later see that this value is too small compared to the empirical value necessary to describe experimental data, and this is of course due to the simplifying assumptions we have done, mainly concerning the independent particle nature of the excitations.
Within the framework of the independent particle model it is also possible to determine the way ρ depends on the quantum numbers M and J, respectively the angular momentum projection and the total angular momentum. We denote by j_k the angular momentum of an individual nucleon, and the resultant of all individual particle momenta will be J. If m_k is the z-component of j_k for particle k, we will have:

$$M = \sum_k m_k \tag{2.64}$$

and provided the number of particle in the nucleus is large, being each m_k a random variable with mean $\langle m \rangle = 0$, the probability law $p(M)$ is of gaussian type, with mean $M = \sum \langle m \rangle = 0$ and dispersion $\sigma^2 = A\langle m^2 \rangle$. The LD as a function of M can then be written as:

$$\rho(A, E^*, M) = \rho(A, E^*) \frac{1}{\sqrt{2\pi}\sigma} \exp\left[-\frac{M^2}{2\sigma^2}\right] \tag{2.65}$$

where σ^2, called the spin cut-off parameter, will shown to be proportional to $\sqrt{E^*}$. The number of states of given total angular momentum J is equal to the number of

states with $M = J$, minus the number of states with $M = J + 1$, *i.e.*:

$$\rho(A, E^*, J) = \rho(A, E^*, M = J) - \rho(A, E^*, M = J + 1) \tag{2.66}$$

which, for large J (*i.e.* high in the continuum) can be approximated by:

$$\rho(A, E^*, J) \approx \left. \frac{\partial \rho(A, E^*, M)}{\partial M} \right|_{M=J+1/2} \tag{2.67}$$

We finally get:

$$\rho(A, E^*, J) = \rho(A, E^*) \frac{2J + 1}{2\sqrt{2\pi}\sigma^3} \exp\left[-\frac{(J + 1/2)^2}{2\sigma^2} \right] \tag{2.68}$$

An estimation of σ^2 can be obtained using again the grandcanonical approximation. Classically, an angular momentum **J** corresponds to an amount of rotational energy given by:

$$E_{rot} = \frac{|\mathbf{J}|^2}{2\mathcal{I}} \tag{2.69}$$

where $\mathcal{I}$ is the moment of inertia. If we go back to the picture of the nucleus as a heat-*reservoir* characterized by a fixed temperature T, the probability to have a given rotational energy would go as $e^{-E_{rot}/T}$. Replacing the square of the angular momentum with the quantum mechanical equivalent, the density would be:

$$\rho(E^* - E_{rot}, J) = \rho(E^*, J = 0) \exp\left[-\frac{J(J + 1)\hbar^2}{2\mathcal{I}T} \right] \tag{2.70}$$

A comparison with eq.(2.68), if we do the approximation $(J + 1/2)^2 \approx J(J + 1)$, leads to the conclusion that:

$$\sigma^2 = \frac{\mathcal{I}T}{\hbar^2} \tag{2.71}$$

This means that σ^2 depends on the square root of the energy E^*, as anticipated. Since the moment of inertia scales with the mass number A, the dependence of σ^2 on A will also be linear: in particular, for spherical nuclei, the moment of inertia $\mathcal{I}$ can be assumed equal to the one of a uniform density sphere of mass number A and radius R, about an axis passing through its centre:

$$\mathcal{I} = \frac{2}{5} m_0 c^2 A R^2 \tag{2.72}$$

We have to notice at this point that eq.(2.70), can be written only as an approximation of $\rho(E^* - E_{rot})$. Indeed the canonical expression given in eq.(2.70 neglects the

energy conservation law, by definition of the canonical ensemble. For an isolated nucleus at a given energy E^*, for some angular momentum J_Y given by:

$$\frac{J_Y(J_Y-1)\hbar^2}{2\mathcal{I}} = E^* \tag{2.73}$$

the rotational energy is equal to the excitation energy and the total density will fall to zero. The plot $J_Y(E^*)$ is usually referred to as the Yrast line, and determines the maximum angular momentum for a given excitation energy E^*.
Finally, the last variable which is usually considered in this framework is the parity distribution. Since the independent particle model does not provide any information on the single particle states parity, it is always assumed that the numbers of states with positive and negative parity are identical, and the expression for the LD, if not integrated on both parities, needs an additional 1/2 factor.
To summarize, the final expression for $\rho(A, E^*, J^\pi)$ provided by the independent particle model reads:

$$\rho(A, E^*, J) = \frac{1}{2} \times \frac{\sqrt{\pi}}{12} \frac{e^{2\sqrt{a(E^*)}}}{a^{1/4}(E^*)^{5/4}} \times \frac{2J+1}{2\sqrt{2\pi}\sigma^3} \exp\left[-\frac{(J+1/2)^2}{2\sigma^2}\right] \tag{2.74}$$

Possible improvements of this expression, consisting mainly in the inclusion of the effects of the neglected correlations among nucleons in a more phenomenological than exact approach, will be discussed in the following sections.

2.2.2 Shell Model and Monte Carlo Shell Model

In a Shell-Model Monte Carlo (SMMC) approach [57, 58] the dominant components of realistic effective interactions, namely shell effects and the residual interaction, can be included at the level of the nuclear Hamiltonian $\mathcal{H}$. The basic idea of this approach is to partially overcome the limitations in the size of the model space, which are characteristic when one needs to apply diagonalization techniques, by the inclusion of fluctuating auxiliary fields, in which non interacting nucleons propagate. The resulting ensemble $\exp(-\beta\mathcal{H})$ of interacting nucleon states can then be seen as a coherent superposition of one-body propagators of non-interacting nucleons moving in these external time-dependent fields, to which a gaussian weight is attributed. The thermal average of an observable is calculated by the Monte Carlo with a sampling of these external fields according to their weights. The expectation value of the Hamiltonian itself corresponds to the thermal energy of the system, which can be given as a function of the inverse temperature β:

$$E(\beta) = \langle \mathcal{H} \rangle_\beta \tag{2.75}$$

The partition function $\mathcal{Z}(\beta)$ is then determined by a numerical integration of $E(\beta)$:

$$\ln\left[\frac{\mathcal{Z}(\beta)}{\mathcal{Z}(0)}\right] = -\int_0^\beta d\beta' E(\beta') \tag{2.76}$$

where $\mathcal{Z}(0)$ is the total number of states within the model space. The LD ρ is the Laplace transform of $\mathcal{Z}$, and it is calculated in the saddle point approximation as given in eq.(2.45) and (2.46). Within this approach, also the dependence of the level density and partition function on good quantum numbers such as parity, spin and isospin can be investigated, by introducing the appropriate projection operators and calculating projected observables.
Our main interest in describing the basic principles of this approach in this context, consists in the fact that the results of the SMMC for the nuclear LD can still be reproduced by the same functional dependences for ρ obtained in independent particle calculations, provided that free fit parameters are left in the level density expression [59, 60]. The free fit parameters are the LD parameter a and a pairing shift Δ in the excitation energy, which is introduced in order to take into account the pairing gap in the spectra of even nuclei. Adapting these parameters to reproduce the SMMC results for ρ provides us with microscopic calculations of the level density parameter a, and of the pairing gap Δ. The typical degree of goodness of the results for SMMC calculations of the LD and for the obtained microscopic parameters a and Δ as a function of the mass number A is evident from the examples of fig.(2.4). We will discuss in the following that the inclusion of free fit parameters in the level density formula is at the basis of very successful semi-empirical approaches, which allow for a determination of the LD through comparison with experimental data on low excitation energy spectra. The success of the same fit procedure in reproducing also the SMMC results provides therefore a theoretical justification of these approaches, and a strong indication of the fact that, if nuclear properties beyond the independent particle model are correctly accounted for, the obtained expression for ρ can be very well be adapted to describe the many-body correlated LD of real nuclei.

2.2.3 Semi-empirical Level Densities

In the independent particle model nucleons are considered as non-interacting particles and any correlation among them, other than the ones produced by the self-consistent mean field, is ignored. In particular, only single-particle excitations can be computed, leading to an underestimation of the LD. Indeed it is well known that, together with single particle excitations, nuclear spectra contain also collective

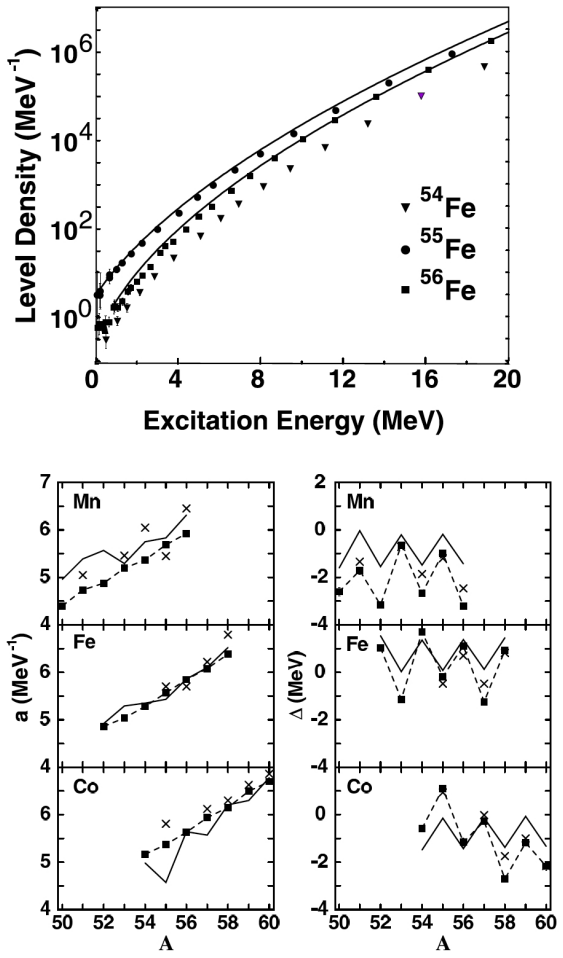

Figure 2.4: Shell Model Monte Carlo calculations of level densities. Upper panel: level densities of three iron isotopes (symbols). Also shown are the experimental level densities of ^{55}Fe and ^{56}Fe (solid lines). Lower panel: single-particle level density parameter a (left) and the backshift parameter Δ (right panels) versus mass number A for different isotopes. The SMMC results (solid squares) are compared with experimental values (crosses) and empirical formulas (solid lines). Fig. taken from ref.[58].

modes of rotational and vibrational type which can be described as coherent superposition of many-particle-many-holes individual excitations. As we have stated before, there are sophisticated approaches in which correlations are introduced at the level of the nuclear hamiltonian, as in the Monte Carlo Shell-Model, in which however the maximal temperature is limited by the the size of the chosen configu-

ration space.
We have also anticipated that a good success in reproducing available experimental data on LD can indeed be achieved using a more phenomenological approach. This approach consists in adopting a LD functional form, which generally comes from a correct derivation under some simplifying approximations. The LD expression is then written in terms of various parameters which can be adjusted to provide agreement with known densities and data.
An example of this approach is given by the inclusion in the independent particle model of pairing correlations, which reflect the tendency of fermions to couple by pairs. The effect of these correlations on the LD is that, for a given excitation energy, the level density of an even-even nucleus is lower than the one of a neighbouring even-odd nucleus, which in turn is lower with respect to the density of an odd-odd system. The reason for this is that, as discussed in chapter **1**, assuming that all nucleons in an even-even nucleus are coupled by pairs, an additional amount of energy have to be spent in order to break a pair and excite the nucleus. As far as LD are concerned, this can be mimicked by the definition of an effective excitation energy, shifted by an amount Δ, so that the LD with pairing correlations included will be equal to the one of a system of independent particles calculated at the energy $(E^* - \Delta)$. This shift will correspond to the pairing gap which can be experimentally observed in the excitation spectra of even nuclei, since the level density $\rho(E^*)$ will be zero for excitation energies lower than Δ (with the exception of the value 1 for the LD at the zero energy of the ground state). The result of the previous independent particle LD calculation can be now re-written with the inclusion of the backshift Δ as:

$$\rho(A, E^*, J) = \frac{1}{2} \times \frac{\sqrt{\pi}}{12} \frac{e^{2\sqrt{a(E^*-\Delta)}}}{a^{1/4}(E^* - \Delta)^{5/4}} \times \frac{2J+1}{2\sqrt{2\pi}\sigma^3} \exp\left[-\frac{(J+1/2)^2}{2\sigma^2}\right] \tag{2.77}$$

where the spin cut-off σ has become:

$$\sigma = \mathcal{I}\sqrt{\frac{E^* - \Delta}{a}} \tag{2.78}$$

The Back-Shifted Fermi Gas Model (BSFG) approach [3] consists in using the analytical expression of eq.(2.77), leaving both the backshift Δ and the LD parameter a as free adjustable parameters for each nucleus of mass A. A good success in reproducing data can be obtained for a LD parameter $a(A) \approx A/8$ for $A \sim 40$ [11], which is bigger than the theoretical result $a(A) \approx A/12\ MeV^{-1}$, and with a parameterization for Δ as a function of mass number A:

$$\Delta = \chi \frac{12}{\sqrt{A}} \tag{2.79}$$

with $\chi = 0, 1$ or 2 for odd-odd, odd-even or even even nuclei. Note that parameterization is the same as the one adopted for the pairing energy correction to the liquid drop mass formula of eq.(1.1).
Another approach of phenomenological type is the one proposed by Gilbert and Cameron [61], in which a different functional form is chosen to describe the density in the low-energy region of nuclear spectra ($E^* \lesssim 5\ MeV$), namely:

$$\rho(E^*) = \frac{1}{T_0} \exp\left(\frac{E^* - E_0}{T_0}\right) \tag{2.80}$$

which is called the Constant Temperature (CT) model, where T_0 and E_0 are also free parameters. Eq.(2.80) obviously derives from the argument that the exponential $\exp\sqrt{aE^*}$ is the main factor governing $\rho(E^*)$, and since $a \propto E^*/T^2$, the LD comes out to be proportional to $\exp(E^*/T)$. The expression of eq.(2.80) is used to better fit the the LD in the energy region where discrete resonances are measured, and it has then to be matched continuously to the continuous region with the expression for $\rho(E^*)$ coming from eq.(2.77) [62].
Both these approaches still do not include an energy dependence for the LD parameter a, which makes them valid only up to low excitation energy. Besides being justified theoretically as discussed in chapter **1**, from an empirical point of view, a parameterization of the type $a(A, E^*)$ has indeed been shown to be necessary in order to account for the shell effects, whose evidence is in the very low LD parameter values needed to reproduce ρ for nuclei close to magicity. One of the simplest prescription to deal with an energy dependent LD parameter a is the one by Ignatyuk [4]. Ignatyuk formula is based on the correlation between the mass evolution of the LD parameter and that of the so-called shell-correction $S(Z, N)$, *i.e* the difference between the experimental mass of the nucleus and the one calculated with a liquid-drop parameterization. The proposed expression reads:

$$a(E^*, Z, N) = \tilde{a}(A)\left[1 + S(Z, N)\frac{1 - \exp(-\gamma E^*)}{E^*}\right] \tag{2.81}$$

with $\gamma > 0$, such that the effect of $S(Z, N)$ in determining how $a(E^*, Z, N)$ reaches the asymptotic mass-dependent values $\tilde{a}(A) = \alpha A + \beta A^{2/3}$ vanishes with increasing excitation energy. Parameters α,β and γ are global best fit parameters, *i.e.* the ones giving the best description of LD over a whole range of nuclides. For instance, evidences for the change in the LD parameter with E^* were found in the mass region $A \sim 120 - 160$, where a transition from a constant value of $A/8$ to $\tilde{a}(A) \approx A/11 - A/13$ is needed in order to reproduce evaporation data [9, 10].
Finally, always in the framework of a phenomenological approach, also the effects

on the LD of collective properties as nuclear vibration or rotation can tentatively be reproduced. It can be shown that these kind of coherent excitations of fermions do enhance the LD, which can be mimicked by the inclusion of enhancement factors damped with increasing excitation energies [63, 64].
Concluding, for any practical application of the statistical model, it is very important to obtain parameters of the LD from reliable experimental data. Huge projects of systematics of these parameters and of their applications to different tasks were - and are being carried out, providing us with complete online libraries with fitted experimental data and theoretical calculations [65, 66]. As an example, a systematics for phenomenological LD parameters determined in ref.[67] for more than 300 nuclei and with three different LD models (namely, BSFG model with constant LD parameter, BSFG model with energy dependent LD parameter and CT model) is reported in fig.(2.5).
It is important to notice however, that the available experimental techniques (which will be listed at the end of this chapter) provide us information on LD in a limited excitation energy range. This is the reason why the parameters systematics is of great importance, since it allows to extrapolate the obtained parameterizations to the higher energy range or even to nuclei for which no experimental data on LD are available, as the ones far from stability.

2.2.4 Nuclear Level Density at High Excitations

In the previous section we have seen that, in the framework of a phenomenological approach, it is possible to extend the validity of the independent particle model result for $\rho(E^*)$ up to relatively high energies, provided that an appropriate energy dependence of the LD parameter $a(E^*)$ is chosen. In any case we have to be aware of the fact that, even for a functional form for $a(E^*)$ of the type of eq.(2.81), the domain of validity for $\rho(E^*)$ has to be upper limited: if the level density is coming from the counting of all the possible configurations of the given CN, it may also configurations with an excitation energy considerably in excess of the nuclear binding energy. The inclusion of such configurations in the LD of an equilibrated system is clearly questionable. An alternative way of seeing the necessity of a cutoff for the LD is to observe that highly excited states, decaying by emission of a successive chains of single-particle emissions, are not strongly coupled to compound nuclear states, or, viewed in the time-reversed sense, the probability of emission of a high energy particle from a compound state is very small.
Shell Model calculations of the LD with a restricted scheme of bound (and qua-

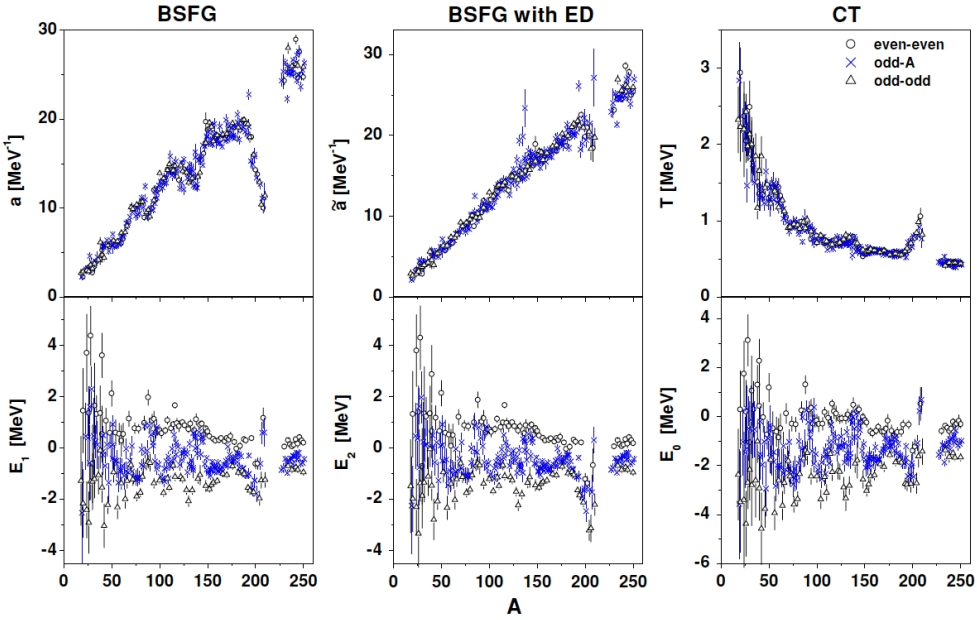

Figure 2.5: Phenomenological LD parameters determined in [67], for 310 nuclei between ^{18}F and ^{251}Cf, by fitting of the complete level schemes at low excitation energies and s-wave neutron resonance spacings at the neutron binding energies. Results are given for three models, from left to right: Back-Shifted Fermi Gas model with constant LD parameter, fit parameters (a, Δ); BSFG model with energy dependent LD parameter, fit parameters $(\tilde{a}, \Delta)$; Constant Temperature model, fit parameters (T, E_0).

sibound) single particle states show indeed a decrease of the $\rho(E^*)$ for increasing excitation energies beyond $8 - 10$ $A.MeV$ [68].
While all these arguments make an upper cutoff necessary, they do not give a definitive prescription for where it should really be. Of course such a cutoff is necessary only for applications at energies in which the evaporation channel is far from being the dominant one. As we have stated in the introduction of this chapter, doing the assumption of a decay governed by statistical laws, the outgoing channel is determined by the density of final available states. At such high energies the disappearance of CN states is indeed compensated by the increasing statistical weight of configurations in which the source, instead of emitting (also sequentially) single

nucleons or fragments, undergoes an instantaneous break-up into more fragments. Thus factors as the number of fragments in the final state, their total kinetic energy or the combinatorics of placing them into a given space volume become determining for the choice of the final configuration. This kind of events are called multifragmentation events, and the onset of this phenomenon determines the limiting excitation energy at which a given nucleus can exist. It comes out, as it will be later discussed, that these limiting energies are lower than the nuclear binding energies, at least for nuclei with a mass bigger than $A = 40$ [39]. A usual way of implementing an independent particle $\rho(E^*)$ in multifragmentation applications [69] is to add an exponential cutoff, obtaining an expression of the type:

$$\rho(E^*) = \rho_{IP}(E^*) \exp -E^*/\tau \tag{2.82}$$

where high energy constraints come from the necessity of reproduction of experimental or theoretical limiting energies.
We have also to notice that, because of the high excitation energy, structure effects in the $\rho_{IP}(E^*)$ are usually neglected, together with the dependence on angular momentum. It is clear at this point that the treatment of the LD is not unique, according to the different applications.

2.2.5 Experimental Methods to determine the Level Density

Since we have stated in the previous sections that a successful approach to the LD calculation is of phenomenological type, we want now to discuss briefly which are the main methods providing us LD data to constrain the parameterizations we want to use.
Experimental information on LD can be obtained:

- from counting of resolved discrete levels, measured with γ- or charged particle - spectroscopy techniques. This method is only effective at low excitation energy, below or at about the particle emission threshold, and requires of course high energy resolution detectors;

- from counting of neutron resonances. This method provides information on LD at about the neutron separation energy, in a narrow spin range (for incident low-energy, neutrons s-waves, *i.e.* with $\ell = 0$, are mainly contributing the resonance-reaction) and a single parity;

- from evaporation spectra in CN reactions. This is actually the only method providing us information on LD at energies higher than the particle emission threshold. LD are indeed an essential ingredient of statistical calculation for the evaporation of the CN, and if the contribution of this reaction mechanism can be safely discriminated from other kinds of reactions (as the direct or inelastic channel), the experimental energy spectra of emitted particles can be compared to model predictions, providing us an indirect experimental determination of LD:

$$\rho_{EXP} = \rho_{TH} \frac{d\sigma/dE_{EXP}}{d\sigma/dE_{TH}} \tag{2.83}$$

Chapter 3

The Statistical Decay Code

This chapter is concerned with the practical application of the Hauser-Feshbach formalism to the problem of sequential evaporation of the compound nucleus. A Monte Carlo Hauser-Feshbach code has been developed in the framework of this thesis, and the implementation of the decay model is discussed in the first part of this chapter. A special attention has been paid to the choice of realistic parameterizations for the nuclear Level Density (LD), which is a fundamental ingredient of any statistical calculation. The level density model implemented in the code is described here in details. A full description of the treatment of angular momentum is also presented, being this aspect specific to the Hauser-Feshbach formalism. At the same time, some features of the GEMINI++[75] binary decay code are discussed, underlining the differences between the parameterizations for the physical quantities of interest implemented in GEMINI and the ones we have adopted for our decay code. Thanks to the choice of level densities highly constrained to experimental data and, as it is later explained, to the inclusion of all available experimental information on low-energy excitation spectra, the newly developed code is intended to be best suited to perform calculations for the decay of equilibrated light nuclei, for which we expect a strong influence of nuclear structure effects even at high excitation energy, whose signature is evident in experimental observables. Our interest in light nuclei also justifies the particular attention paid to the level density model with respect to other ingredients of the statistical code, as transmission coefficients and Coulomb barriers, for which rather simple expressions have been chosen. These latter quantities are indeed the main uncertainty source for medium and heavy nuclei, but are quite under control for light nuclei, and their effects on predicted observables can be easily disentangled.
In the second part of this chapter, we show the results of calculations performed with

our Hauser-Feshbach code and propose different observables related to the thermal behaviour of light nuclei. In this thesis, we discuss the data analysis and present preliminary results for the reaction $^{12}C + ^{12}C$ at 95 MeV beam energy, measured with the GARFIELD+RCo apparatuses at LNL-INFN. The Compound Nucleus (CN) issued in case of complete fusion for this reaction is ^{24}Mg at an excitation energy of $e^* \sim 2.6$ $A.MeV$. With the perspective of comparing the predictions of our statistical code to experimental data, we have performed calculations for the decay of ^{24}Mg at the same energy and angular momentum conditions (specified later on) which we expect to have for the equilibrated fused system in the measurement. To pursue a more general investigation on the statistical properties of light nuclei and contribute to future experimental proposals , we have also made calculations for the decay of the same system at different input energies, always in the excitation region $e^* \sim 3$ $A.MeV$. In order to check the dependence of calculated observables on the physical ingredients entering the decay model, we also present calculations with different values of the code input parameters.

3.1 Monte Carlo Implementation of the Decay Model

The expression for the decay width in channel ξ for a compound nucleus in its state C (specified by the energy E^* and the angular momentum J) in the framework of the Hauser-Feshbach model has been derived in the previous chapter and reads:

$$\Gamma_\xi^C = \frac{1}{2\pi\rho_C(E^*,J)} \cdot \int_0^{E^*-Q} d\epsilon_\xi \sum_{J_d} \sum_{j=|J-J_d|}^{J+J_d} \sum_{\ell=|j-s_p|}^{j+s_p} T_{j,s_p}^J(\epsilon_\xi) \cdot \rho_d(E^*-Q-\epsilon_\xi, J_d) \tag{3.1}$$

where ϵ_ξ is the relative kinetic energy of decay products, i.e. the daughter nucleus (whose properties are labelled by d) and the evaporated particle (labelled by p). For sake of simplicity, with respect to the equation given in chapter **2**, we have dropped the subscript ξ on all the channel dependent quantities, and we have adopted a different notation for the angular momenta which will be made clear in the following. Calculating the widths Γ_i^C for all the possible decay channels, we can define the Branching Ratio (BR) associated to a specific channel ξ as the ratio between Γ_ξ^C and the total decay width for the CN:

$$BR^C(\xi) = \frac{\Gamma^C_\xi}{\sum_i \Gamma^C_i} \tag{3.2}$$

The quantity $BR^C(\xi)$ is therefore the probability for the excited CN to decay via channel ξ, *i.e.* via the emission of particle (A_p, Z_p), leaving a daughter nucleus (A_d, Z_d). This probability depends on all the physical quantities entering eq.(3.1), and it constitutes the main ingredient of the Monte Carlo simulation. It is interesting to notice that the LD of the CN nucleus $\rho_C(E^*, J)$ does not really enter in the calculation of the BR, since the factor $(1/2\pi\rho_C)$ is the same in the width Γ^C_ξ and in all the widths in the denominator of eq.(3.2). Therefore, the relevant LD is only the one of the daughter nucleus $\rho_d(E^*_d, J_d)$ [1].
In this section we describe the main decay algorithm for the implementation of the Hauser-Feshbach decay model given by eq.(3.1). The decay channels implemented in the code are the evaporation of a light particle or of a charged fragment (always in their ground states), among:

$$n,\ p,\ d,\ t,\ ^3He,\ \alpha,\ ^6Li,\ ^7Li$$

In this first version of the code, γ-emission is not explicitly implemented: the underlying hypothesis is that, above particle emission thresholds, γ-emission is not competitive with respect to charged particle decay. Nevertheless, γ unstable levels under the threshold for particle emission are part of the database and can be populated in calculations for complete decay chains. Their further decay does not modify the isotopic yields and does not need to be considered for our purposes. Consequently, in the case of a multi-step decay calculation, the decay chain starting from the initial hot source is stopped whenever an excitation energy lower than the particle emission threshold for the evaporation residue is reached.
These emission thresholds (the decay Q-values) determine the energy interval of integration in eq.(3.1) because of energy conservation. In the code, they are calculated from experimental binding energies taken from Audi and Wapstra compilation [70].
Input for the calculation are the properties of the decaying CN source: its mass and charge numbers (A, Z), its excitation energy E^*, the initial value of the angular momentum quantum number J, the initial orientation of the classical vector **J** in the Center-of-Mass Reference-Frame (**CM** RF) of the system (*i.e.* the system with z-axis parallel to the velocity of the beam).

[1] As already commented in chapter **2**, the $(2J+1)$ spin degeneracy factor is not included in the level density ρ entering equation (3.1). In the following, when needed, we will refer to the effective number of states $(2J+1)\rho(E^*, J)$ as to the nuclear state density.

A complete decay chain calculation is therefore a series of successive binary decays, in which at each step a new decaying source is defined, inheriting the characteristics of the evaporation residue of the previous step. Mass, charge and excitation energy of the new source are coming from conservation laws, also the angular momentum vector is conserved, and how the changes in its module and orientation are taken into account at each decay will be discussed in the following.
In a fusion reaction the angular momentum J of the created CN is the result of the couplings of different momenta in the entrance channel: the spin of the target and the projectile and the orbital angular momentum of the incoming projectile. In the very same way, at each evaporation step, we have a decomposition of the initial J of the decaying source into different angular momenta subject to conservation laws. Angular momentum vectorial couplings in the decay are specified by the following equations:

$$\begin{aligned} \mathbf{J} &= \mathbf{J_d} + \mathbf{j} \\ \mathbf{j} &= \boldsymbol{\ell} + \mathbf{s_p} \end{aligned} \tag{3.3}$$

meaning that the orbital angular momentum of the decay $\boldsymbol{\ell}$ and the spin of the evaporated particle $\mathbf{s_p}$ are coupled to the vector $\mathbf{j}$ (dependent on the decay channel), and the daughter nucleus can be left with every possible value of its angular momentum quantum number J_d coming from the coupling of $\mathbf{J} - \mathbf{j}$. The angular momentum J_d of the daughter nucleus may differ from its ground state spin, since the daughter nucleus can still be excited. The upper limit J_{plus} for the angular momentum of a given evaporation residue with excitation energy E_d^* comes from the Yrast line limitation, *i.e.* $E_d^* \leq E_{yrast}^*$ with:

$$\frac{J_{plus}(J_{plus}-1)\hbar^2}{2\mathcal{I}_d} = E_{yrast}^* \tag{3.4}$$

where $\mathcal{I}_d$ is the moment of inertia of the daughter nucleus, which, assuming a rigid spherical rotator, is given by:

$$\mathcal{I}_d = \frac{2}{5} m_0 c^2 A_d R_d^2 \tag{3.5}$$

with $R_d = R_0 A_d^{1/3}$ and $R_0 = 1.2\ fm$. The lowest value J_{low} the angular momentum can assume has to be either 0 or 1/2, depending on the residue being an even- or odd-mass nucleus.
Once the decay channel is selected by the Monte Carlo according to its weight $BR^C(\xi)$, the relative kinetic energy of the emitted particle and the evaporation

residue has to be drawn up according to the same distribution which is integrated for the calculation of the branching ratio. From the derivation of eq.(3.1) presented in chapter **2**, we know that the integrand term in the calculation of the BR can be seen as the probability distribution $p(\epsilon_\xi)$ for the relative kinetic energy of the decay products in the outgoing channel. In order to extract a value for ϵ_ξ, we calculate the maximum value $max\,[p(\epsilon_\xi)]$ and perform an extraction of ϵ_ξ according to its distribution with the acceptance-rejection method.
At this point of the calculation, we are left with an evaporation residue of given mass, charge and excitation energy, coming from the energy conservation law:

$$E_d^* = E^* - Q - \epsilon_\xi \tag{3.6}$$

We want now to check if, following the decay, the daughter nucleus has a residual excitation energy such that the discrete part of its spectrum is reached.
To this aim, we have to store all the information concerning discrete experimental levels in a database accessed by the code at each decay calculation. The source of this information is the online archive NUDAT2 [71], and for each nucleus a complete list of level energies, energy widths and spins are read and stored in memory, indexed by a progressive counter $[lev]$. We have to be aware of the fact that the experimental determination of nuclear levels is subject to some indetermination, especially concerning the measurement of high lying resonances, and the attribution of their energy, width and spin. This is reflected in the fact that, if we plot the quantity dn/dE^* (shown in fig.(3.1) for two chosen isotopes), defined as the number of measured levels stored in NUDAT2 in bins of excitation energy for a given isotope, we systematically find an energy beyond which this density distribution starts decreasing. Since this cannot be due to the physical behavior of the LD at energies lower than the limiting energy (which, as discussed in the following, can be assumed to be equal to the binding energy for nuclei with $A \lesssim 40$), we attribute the observed decrease to the lack of experimentally resolved high-lying levels, due to the physical emergence of the continuum. We define therefore for each isotope the matching energy between the discrete and the continuum part of the spectrum $E_{match}(A, Z)$, as the excitation energy maximizing the density $dn/dE^*(A, Z)$.

Given this definition, our assumption is that, for energies lower than $E_{match}(A, Z)$, measured discrete levels completely exhaust the physical level density $\rho(E^*)$. This assumption translates in a strong requirement on the LD model to be implemented in the code, which has to provide functional forms for $\rho(E^*)$ good enough to fit the experimental counting dn/dE^* in the low energy region. Our choice for the LD model is discussed in the next section.

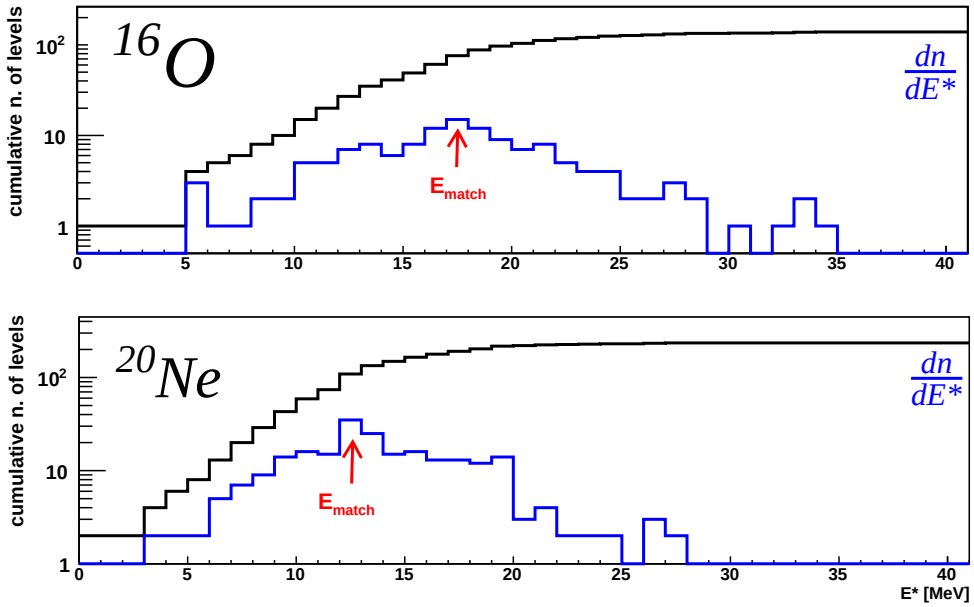

Figure 3.1: Number of measured levels stored in NUDAT2 in bins of excitation energy (dn/dE^* in the text, blue histograms) for ^{16}O and ^{20}Ne; corresponding cumulative distributions are given in black. The red arrow shows the maximum of the dn/dE^* distribution, defined as the matching energy $E_{match}(A, Z)$.

If we additionally define for each isotope the energy $E_{last}(A, Z)$ of the highest energy level listed in NUDAT2, with $E_{last}(A, Z) \geq E_{match}(A, Z)$, we are left with three excitation energy regions:

- the discrete region, defined by $E^* \leq E_{match}$. If the daughter nucleus is populated at an energy E_d^* which falls in this energy region, it means that it has to be populated in one of its discrete levels. We check therefore which is the level nearest to the selected residual energy, denoted by $E_d^{*[lev]}$, and populate it attributing to the daughter nucleus an excitation energy extracted according to the Breit-Wigner distribution of that level:

$$BW(E^{*'}) = \frac{1}{2\pi} \frac{\Gamma^{[lev]}}{\left(E^{*'} - E_d^{*[lev]}\right)^2 + \left(\frac{\Gamma^{[lev]}}{2}\right)^2} \tag{3.7}$$

  In order to keep the total energy conserved, it will be necessary at this point to increment the selected ϵ_ξ by the difference between the first calculated residual energy and the new extracted one. The spin J_d of the daughter nucleus is easily obtained, and it corresponds to the spin of the selected energy level;

- the continuum region, defined by $E^* > E_{last}$. The daughter nucleus is populated in one of its continuum states, at the selected energy E_d^*. The continuum hypothesis lies therefore in the assumption that E^* is a continuous variable, which can assume any selected value. The only missing information at this point is the angular momentum J_d of the evaporation residue. This angular momentum can be drawn up according to a distribution given by $\rho_d(E_d^*, J')$ as a function of J'. This suits the statistical assumption of a decay governed by the number of states available in the final channel, since the most probable value resulting from the extraction will be the one maximizing the LD of the daughter nucleus. In the following section we will show the results of this prescription for the spin distribution of evaporation residues;

- the energy region in-between, *i.e.* with values of excitation energy in the range $E_{match} < E^* \leq E_{last}$, which may be called a "hybrid" region. In this energy region we have some experimental information on measured levels, but the counting of discrete resonances cannot exhaust the level density $\rho(E^*)$, since measured levels are too few and their experimental determination is subject to great indetermination. We may want to treat the "hybrid" region as if there were no discrete levels at all in this energy range, and therefore keep the selected E_d^* for the daughter nucleus and treat it as a nucleus excited in one of its continuum states. But we may also be somewhat interested in having high energy levels populated in a calculation, and compute therefore a population probability for the level $E_d^{*[lev]}$ in proximity of the selected E_d^*, with respect to the probability of populating a continuum energy state at the exact energy E_d^*. Therefore, the population of discrete states in this region is left as an option in the code. If this option is enabled, two different weights are associated to the population of the residual nucleus in the discrete level $E_d^{*[lev]}$ or in its continuum state at E_d^*. In principle, the weight w_{discr} associated to the population of the hybrid region in the discrete should be given by the ratio of the state densities coming from the experimental counting $(2J + 1)dn/dE^*$ and from the continuum expression $(2J+1)\rho(E^*)$, evaluated at the selected residual excitation and angular momentum. The discrete nature of dn/dE^* makes a wiser calculation necessary, and we have therefore adopted the following prescription: we first define the cumulative distributions (integrated

over energy and angular momenta) of the two state densities:

$$\varrho(E') = \int_0^{E'} \sum_{J=Jlow}^{Jplus} (2J+1)\rho(E^*, J)dE^*$$
$$N(E') = \sum_{E*\ [lev]=0}^{E*\ [lev]\leq E'} (2J^{[lev]}+1)\frac{dn}{dE^{*\ [lev]}} \tag{3.8}$$

and evaluate them at the two extremes of an energy interval of 1 MeV centered on the selected E_d^*. The numerical derivatives of these quantities at E_d^* are:

$$\frac{d\varrho(E^*)}{dE^*}(E_d^*) = \frac{\varrho(E_d^*+0.5) - \varrho(E_d^*-0.5)}{1}$$
$$\frac{dN(E^*)}{dE^*}(E_d^*) = \frac{N(E_d^*+0.5) - N(E_d^*-0.5)}{1} \tag{3.9}$$

and the weight $w_{discr}(E_d^*)$ is given by:

$$w_{discr}(E_d^*) = \frac{dN(E^*)/dE^*(E_d^*)}{d\varrho(E^*)/dE^*(E_d^*)} \tag{3.10}$$

since the continuum LD includes experimental levels entering in the dn/dE^* of the hybrid region. It is easy to see that, if no measured resonances fall in the interval of integration of 1 MeV centered on the selected residual energy E_d^*, the weight w_{discr} is zero. In general, because of the large absolute value of the continuum LD and because of the few number of experimental levels in this excitation energy range, the net result of this prescription is that the hybrid region is mostly populated in the continuum. Nevertheless, it has been worthwhile to implement a specific treatment of the hybrid region, because this option may allow us to perform dedicated calculations for the study of the decay of a scarcely populated high lying energy level of a given isotope of interest. In order to do this, it is sufficient to force the population of this level by attributing to it a weight $w_{discr}^{fix} = 1$, and then to weight the results of the decay calculation by the real population weight w_{discr} obtained with the above described prescription. This procedure allows an exact and numerically accessible calculation of extremely rare decay processes.
Concerning the angular momentum selection, J_d is automatically chosen to be the one of the selected level if the discrete is populated, or it is extracted with

the same prescription of the continuum in the alternative case.
Finally, we want to notice that the formalism of this weight calculation nicely extends to a global characterization of the three excitation energy regions in which we have subdivided the full range of E^*, always under the condition of a continuum level density fitting the low energy part of nuclear spectra up to the E_{match}. If this is verified, it is easy to understand that the same prescription of eq.(3.10) will give $w_{discr}(E^*) = 1$ for $E^* \leq E_{match}$, $0 < w_{discr}(E^*) < 1$ for $E_{match} < E^* \leq E_{last}$ (hybrid region), and finally $w_{discr}(E^*) = 0$ for $E^* > E_{last}$, because of the zero derivative of the flat cumulative distribution of experimentally measured levels.

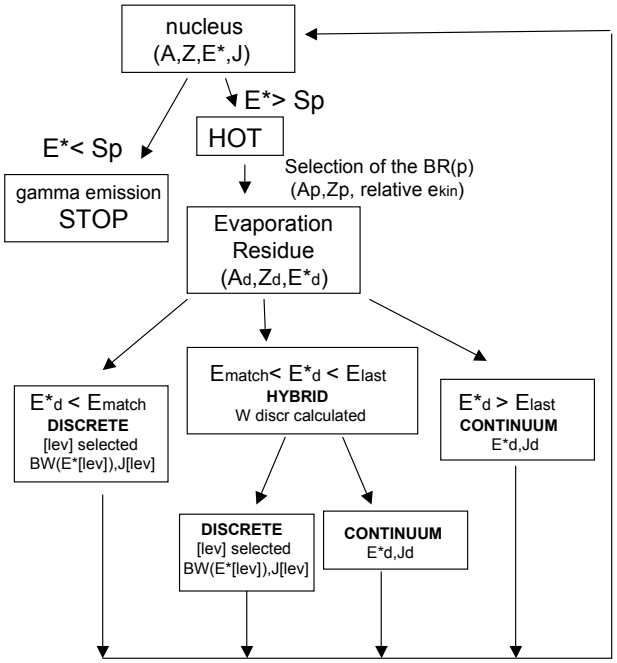

Figure 3.2: Scheme of the main decay algorithm implemented in the code.

A scheme of the above described algorithm is shown in fig.(3.2). We have to spec-

ify that, if no experimental information on discrete levels is available, the decay is always described in the continuum approximation. If the information is only partial but we still want to make use of it, we have to establish some rules to complement it. For instance, in our database, if the width of an energy level is not known, we simply put $\Gamma^{[lev]} = 5\ MeV$, assuming that the uncertainty on the determination comes from the large energy spread of the level.
In the decay calculations, to keep memory of the population of discrete levels in the decay chain, a dedicated $CDL(A, Z, [lev])$ counter exists in the code and it is incremented each time a nucleus is populated in its level indexed by $[lev]$. This allows us to study the population of states of the nuclei produced in the whole evaporation process. The final aim of storing this information is the possibility of comparing the code predictions for the discrete states population at the last but one step of the decay chain with the experimental information coming from reconstructed resonances through the correlation function technique. The population of nuclei in their ground state (and bound excited states) is then checked to be coherent with the abundance of a given nucleus as evaporation residue.
At this point, having discussed the general algorithm for the population of nuclear excitation spectra along the decay chain, we need to define the physical ingredients entering eq.(3.1).
The next section of this chapter is devoted to the description of the LD model.
For the transmission coefficients in eq.(3.1) we adopt the same expression of ref.[72], in which the authors propose a typical parameterization of barrier penetration factors, written in terms of the relative kinetic energy of decay products and of a potential energy barrier, with two free parameters depending on the charge Z_p of the evaporated particle. These parameters can be adapted to provide the best description of experimental evaporation data and are optimized to reproduce the decay of discrete resonances. The expression for the barrier, which is the sum of a Coulomb and a centrifugal term, reads:

$$V_b = \frac{1.44}{r_Z}\frac{Z_p(Z-Z_p)}{(A-A_p)^{1/3}+A_p^{1/3}} + \frac{\hbar^2\ell(\ell+1)}{2r_Z^2}\frac{\frac{A}{A_p(A-A_p)}}{\left[(A-A_p)^{1/3}+A_p^{1/3}\right]^2} \tag{3.11}$$

where (A, Z) are the mass and charge numbers of the parent nucleus and r_Z is one of the free parameters. The parameterization used for the transmission coefficient is:

$$T_\ell(\epsilon_\xi) = \frac{1}{1+\exp\left(\frac{V_b-\epsilon_\xi}{\delta\cdot V_b}\right)} \tag{3.12}$$

where δ is the second free parameter, whose value is different depending on the

emission taking place in the sub- or above-barrier region:

$$\begin{aligned} \delta &= \delta_1 \qquad if\ \epsilon_\xi > V_b \\ \delta &= \delta_2 \qquad else \end{aligned} \tag{3.13}$$

Numerical values of r_Z, δ_1 and δ_2 proposed in ref.[72] are reported in the following table.

Z_p	0	1	2	3	4	5
r_z	1.62	1.62	1.57	1.57	1.55	1.53
δ_1	0.60	0.25	0.07	0.08	0.05	0.04
δ_2	0.10	0.09	0.07	0.06	0.03	0.02

The ℓ value resulting from angular momentum couplings in eq.(3.1) enters as an argument in the routine evaluating the transmission coefficients, hence the dependence of these coefficients on all angular momenta which is made explicit in the notation T^J_{j,s_p}.
More sophisticated approaches are proposed in the literature for the calculation of transmission coefficients, which usually make use of optical model fit to elastic scattering data. As an example, we will later comment on the transmission coefficients implemented in GEMINI++.

3.2 Level Density Model

The choice of the level density model to be implemented in the Hauser-Feshbach code was driven by the will of including, in a coherent way, all the available experimental information on low energy discrete spectra. In some statistical models, a constant temperature formula for the LD is used, in order to take into account the discrete part of the energy spectrum [62]. The expression coming from the constant temperature model has then to be matched continuously to a reliable model for higher excitation energies, as a back-shifted Fermi gas model. As discussed in chapter **2**, within a phenomenological approach, the BSFG model, with the LD parameter and the pairing backshift left as free fit parameters, is very well suited to the description of the many-body correlated nuclear level density: pairing effects are included through the backshift, and all correlations are taken into account in the renormalization of the LD parameter $a(E^*)$. In ref. [67] it is shown that the BSFG model also allows an excellent fit of the complete low-lying level schemes. Then the question arises, if the same functional form can be used to describe the nuclear

LD at any excitation energy, provided that through an appropriate renormalization of $a(E^*, A)$ we are able to match correctly the two energy regimes: the low energy regime in which the LD is strongly affected by structure effects and the higher energy regime in which we have experimental constraints from fusion-evaporation data.

3.2.1 Systematics of nuclear level density parameters

We have chosen to implement in the code the level density model presented in [67], where the parameters of the nuclear level density for the backshifted Fermi gas model (with energy dependent level density parameter a) have been determined for 310 nuclei between ^{18}F and ^{251}Cf, by the fit of complete level schemes at low excitation energies and s-wave neutron resonance spacings at the neutron binding energies.
The variations of these phenomenological parameters for the set of nuclei of interest were then studied and correlated with those of other physical observables. The considered observables are such that they are both well experimentally known quantities, available from mass tables for a large set of nuclei, or quantities accessible with reliable theoretical calculations or extrapolations from existing data. In such a way, from the observed correlations, the authors were able to propose simple formulas for the parameters entering the LD calculation, whose results allow for a description of the main features of empirical low energy spectra. These formulas are also proposed as reliable means for the extrapolation of level density parameters to exotic nuclei, as well as for nuclei which were not part of the studied data set.
The level density model presented in [67] perfectly matches therefore our requests:

- possibility to fit the low energy spectroscopic information with the same functional form known to be adequate to the description of the high energy behavior of the level density;
- explicit inclusion of experimental levels for light nuclei in the fit procedure;
- good reproduction of the low energy information for light nuclei not included in the studied data set (as it is later shown in this section), by means of extrapolation with the proposed formulas for the level density parameters.

Not entering into the details of the experimental data-fitting procedure, we give hereafter the formulas of the phenomenological model used. The LD dependence on the excitation energy E^*, angular momentum J and parity π is assumed to have a separable form:

$$\rho(E^*, J, \pi) = \frac{1}{2}\rho(E^*)f(J) \tag{3.14}$$

where the factor (1/2) accounts for the hypothesis of equipartition of the two parity states, and the angular momentum dependence is given by:

$$f(J) = \frac{2J+1}{2\sigma^2} e^{-J(J+1/2)/2\sigma^2} \tag{3.15}$$

where σ is the spin cut-off factor, for which an energy dependent parametrization will be later reported.
The expression for $\rho(E^*)$, after integration on J and π under the normalization conditions:

$$\sum_{\pi} \frac{1}{2} = 1$$

$$\sum_{J=0}^{\infty} f(J) = 1$$

reads:

$$\rho(E^*) = \frac{\exp[2\sqrt{a(E^* - E_2)}]}{12\sqrt{2}\sigma a^{1/4}(E^* - E_2)^{5/4}} \tag{3.16}$$

where the energy backshift E_2 is left as a free parameter in the data fitting, and the functional form $a(E^*)$ has also to be adapted to data and contains the second free parameter, as we discuss in the following. The level density $\rho(E^*)$ is then chosen to be zero if $0 < E^* \leq E_2$. Moreover, since the function $\exp(2\sqrt{ax})x^{-5/4}$ has a minimum at $x = (25/16)/a$, $\rho(E^*)$ is assumed to be constant below $(E^* - E_2) < (25/16)/a$, which does not influence the final results on the quality of the fit according to the authors. We have indeed verified that the choice of a constant level density value in this energy range, which could be for instance either $\rho(E^*) = 0$ or $\rho(E^*) = \rho(E^* - E_2 = (25/16)/a)$, concerns only few low-lying levels, typically γ-unstable bound excited states. Therefore this choice does not affect the quality of the parameterizations proposed in [67] for our statistical decay calculations, as far as we can drop the information on the population of these few bound states. Finally, $\rho(E^*)$ has to be one at zero energy, where the only available state is the nuclear ground state.
The proposed expression for the spin cut-off parameter as a function of the energy E^* reads:

$$\sigma^2 = 0.0146A^{5/3}\frac{1 + \sqrt{1 + 4a(E^* - E_2)}}{2a} \tag{3.17}$$

and the backshift E_2 and the LD parameter $a(E^*)$ are entering the calculation of σ^2. For the LD parameter $a(E^*, Z, N)$, a phenomenological expression as the one

proposed by Ignatyuk [4] has been chosen, in order to include an energy dependence able to reproduce the damping of shell (and pairing) effects at high excitation energies:

$$a(E^*, Z, N) = \tilde{a}\left[1 + \frac{S(Z,N) - \delta E_p}{E^* - E_2} f(E^* - E_2)\right] \tag{3.18}$$

where $\tilde{a}$ is the asymptotic value of the a parameter at high excitation energies, and:

$$f(E^* - E_2) = 1 - e^{-0.06(E^* - E_2)} \tag{3.19}$$

The term $S(Z,N)$ is the so-called shell correction, defined as:

$$S(Z,N) = M_{exp}(Z,N) - M_{LD}(Z,N) \tag{3.20}$$

where M_{exp} is the experimental mass and M_{LD} is the mass calculated with a macroscopic liquid drop formula for the binding energy not including any pairing or shell correction. The asymptotic value $\tilde{a}$ is thus the second free parameter in the data fitting and the variation of $a(E^*)$ is correlated to shell and pairing effects. More specifically, given the nuclear binding energy as $E_b(N,Z) = [NM_n + ZM_p - M(N,Z)]c^2$, the liquid drop formula used to calculate the shell correction reads:

$$-\frac{E_b}{A} = a_{vol} + a_{sf}A^{-1/3} + \frac{3e^2}{5r_0}Z^2A^{-4/3} + (a_{sym} + a_{ss}A^{-1/3})\left(\frac{N-Z}{A}\right)^2 \tag{3.21}$$

with the following parameter values (fitted to about 2000 mass values): $a_{vol} = -15.65\ MeV$, $a_{sf} = 17.63\ MeV$, $a_{sym} = 27.72\ MeV$, $a_{ss} = -25.60\ MeV$ and $r_0 = 1.233\ fm$. Since the pairing correction term is missing in the chosen liquid drop formula, the shell correction term is further shifted by δE_p in eq.(3.18). The best results for the fit of experimental excitation spectra were obtained considering a pairing term linked to the so-called deuteron pairing P_d, which is on turn written in terms of deuteron separation energies S_d:

$$\delta E_p = \begin{cases} +0.5P_d & for \quad even-even \\ 0 & for \quad odd\text{–A} \\ -0.5P_d & for \quad odd-odd \end{cases} \tag{3.22}$$

where:

$$P_d = \frac{1}{2}(-1)^Z\left[S_d(A+2, Z+1) - S_d(A,Z)\right] \tag{3.23}$$

As a result of the fit procedure, the authors in [67] provide a complete table of values for the empirical parameters $\tilde{a}$ and E_2 for all the nuclei in the studied data set. The global behaviour of these parameters is then investigated.

The parameter $\tilde{a}$ is found to be rather similar to that of other comparable evaluations [73], although its absolute values correspond to the particular approach in [67]. In this approach, the strong dependence on shell effects of the LD parameter is taken into account in the functional form for $a(E^*)$, so that $\tilde{a}$ shows a very gentle behaviour as a function of mass number A, and $\tilde{a}(A)$ can be fitted by a linear dependence with a small quadratic correction.
The parameter E_2 has, generally, a more complicated behaviour, and its variation is found to be correlated to both shell and pairing effects. In particular a strong correlation with the derivative $dS(Z,N)/dA$ of the shell correction with respect to mass number A was put in evidence. This quantity can be calculated from mass tables in different ways, as for instance:

$$\frac{dS(Z,N)}{dA} = \left[S(Z+1,N+1) - S(Z-1,N-1)\right]/4 \tag{3.24}$$

The formula for the fit of $E_2(A,Z)$ is then chosen as simple as possible, namely, a quadratic combination of $dS(Z,N)/dA$ and P_d.
A summary of the proposed formulas for both $\tilde{a}$ and E_2 is reported in the following table.

Formula	Parameters			Type of Nuclei
	p_l	p_s		
$\tilde{a}/A = p_l + p_s A$	0.127(1)	$-9.05(53)\ 10^{-5}$		All
	p_1	p_2	p_3	
$E_2 = p_1 - 0.5P_d + p_4\frac{dS(Z,N)}{dA}$	-0.48(3)	-0.57(2)	-0.24(4)	even-even
$= p_2 - 0.5P_d + p_5\frac{dS(Z,N)}{dA}$	p_4	p_5		even Z-odd N
$= p_2 + 0.5P_d - p_5\frac{dS(Z,N)}{dA}$	0.29(11)	0.70(11)		odd Z-even N
$= p_2 - 0.5P_d + p_5\frac{dS(Z,N)}{dA}$				odd Z-odd N

Table 3.1: Summary of formulas proposed in [67] for the description of the BSFG model with energy dependent LD parameter a. The dimensions of the different p_i constants are such that $\tilde{a}$ is in MeV^{-1} and E_2 is in MeV.

Results of the fit to LD empirical parameters with these formulas are shown in fig.(3.3).
In fig.(3.4) we compare for chosen isotopes the cumulative level densities, obtained by integration of eq.(3.16) with parameters from these formulas, to the cumulative distributions of experimental levels $N(E^*)$. The quality of the proposed LD model in reproducing experimental spectra is evident, and it is also clear that formulas

proposed in [67] can be considered reliable also for nuclei which are not part of the fitted data set, as it is the case for ^{12}C and ^{16}O.
The BSFG model level density with parameters calculated according to [67] is recommended up to the neutron binding energy (or a slightly higher energy), which corresponds to the energy range of experimentally measured levels used for the fit. The authors state in the conclusions of their work that the proposed model may even be reliable up to higher energies ($\approx 15 - 20\ MeV$), because it contains the recommended damping of shell and pairing effects with increasing excitation energy. In the following, we will address the problem of finding an expression for the extrapolation of $a(E^*, Z, N)$ at even higher energies.

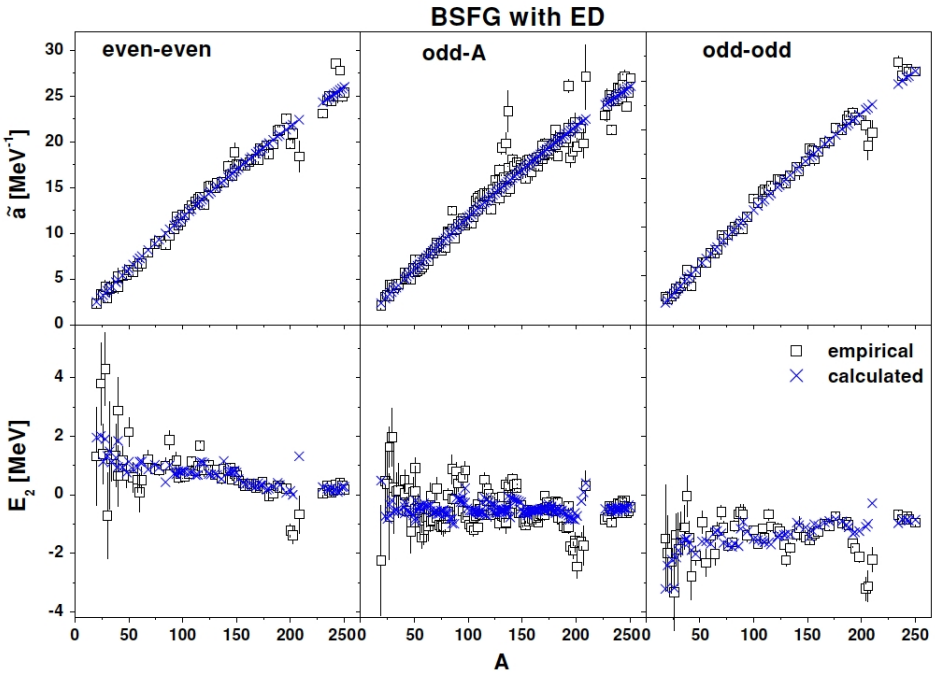

Figure 3.3: Fits to the BSFG model parameters $\tilde{a}$ and E_2 obtained with empirical formulas reported in table 3.1. The same phenomenological best-fit parameters were already shown in chapter **1**, as an example of the application of the BSFG model to level density calculations. Figure taken from ref.[67].

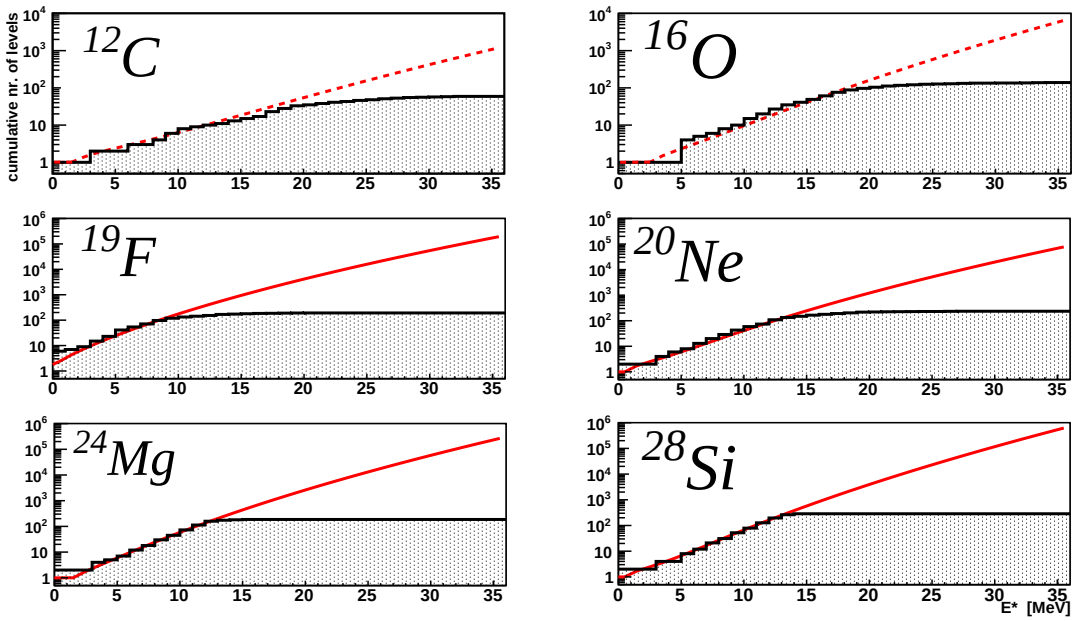

Figure 3.4: Comparison between the cumulative number of levels, calculated with $\rho(E^*)$ from eq.(3.16) (lines), with $\tilde{a}$ and E_2 coming from the formulas given in table 3.1, and the cumulative counting of experimentally measured levels from the NUDAT2 archive (histograms). For ^{12}C and ^{16}O the values of $\tilde{a}$ and E_2 are an extrapolation of the formulas proposed in [67] out of the fitted data set, and the cumulative level density is given by a red dashed line; ^{19}F,^{20}Ne,^{24}Mg and ^{28}Si are part of the fitted data set, and the cumulative level density is given by a continuous line.

3.2.2 Match of the Level Density to Higher Energy

As described in the previous section, the authors of ref.[67] provide us with a reliable semi-empirical model to calculate the level density up to maximum $15 - 20\ MeV$ of excitation energy. We could think of this limitation in the following terms: below this energy limit, the parameters entering the LD calculation in the BSFG model are strongly affected by structure effects, as pairing and shell effects. The results for $\tilde{a}$ and E_2 presented in [67], where these parameters are optimized to describe low energy data, bear therefore a strong signature of these effects. For higher energies, structure effects are supposed to be less relevant. The transition between these two energy regimes can be mainly ascribed to the variation of the LD parameter a with the excitation energy, since the backshift energy, which is needed to reproduce the energy position of the first excited level, becomes negligible as soon as $E^* >> E_2$ in eq.(3.16). As we have stated before, eq.(3.18) for a partially accounts for the vanishing of shell and pairing effects as the excitation energy increases, but

the function $a(E^*)$ keeps memory of structure effects at any energy, because its convexity is uniquely determined by the sign of the term $S(Z,N) - \delta E_p$ and the asymptotic value $\tilde{a}$ itself is obtained with the purpose of fitting low energy data.
We can consider an alternative parametrization for $a(A)$, as the one given in [74]:

$$a = \frac{A}{14.6}\left(1 + \frac{3.114}{A^{1/3}} + \frac{5.626}{A^{2/3}}\right) \tag{3.25}$$

in which we have no energy dependence but instead a more complicated mass dependence which include surface and curvature effects. We can think of eq.(3.25) as to a formula for the asymptotic value a_∞ of the LD parameter at high energy. Indeed, values calculated with this parametrization are generally in agreement with experimental data for fusion-evaporation reactions, in particular even for light systems, when the compound nucleus has an excitation energy of the order of 3 $A.MeV$ [37, 38]. Nevertheless, $a_\infty(A)$ values calculated with eq.(3.25) differ considerably (are generally larger) from the ones predicted by the expression for $\tilde{a}$ given in table 3.2.1. For instance, in the mass region $A \sim 20$, eq.(3.25) approximately gives $a \approx A/5$, while values of $\tilde{a}$ in [67] for nuclei of this kind are generally of a factor of 2 smaller.
In the statistical decay code we have therefore decided to make use of a matched $a_M(E^*, A)$ function, which is written such that the LD parameter is given by eq.(3.18) up to a certain energy, for which we take as an initial guess the same E_{match} introduced in the previous section, and rapidly tends asymptotically to the value predicted by eq.(3.25) for higher energies. Indeed, low-lying levels, whose reproduction is ensured by eq.(3.18) for the LD parameter, are available up to $e^* \sim 1.$ $A.MeV$ for nuclei of mass $A \sim 20$, while constraints from studies on evaporation after fragmentation, reproduced by eq.(3.25), concern nuclei at $e^* \sim 2 \div 3$ $A.MeV$. The transition between calculated values at low and high energy for the chosen $a_M(E^*, A)$ has to take place in an excitation energy range of about ~ 20 MeV. We write therefore:

$$a_M(E^*, A) = \begin{cases} a_D(E^*, A) = \tilde{a}\left[1 + \frac{S(Z,N) - \delta E_p}{E^* - E_2} f(E^* - E_2)\right] \\ \qquad for \quad E^* - E_2 \leq E_{match} \\ a_C(E^*, A) = \alpha \exp\left[-\beta (E^* - E_2)^2\right] + a_\infty \\ \qquad with\ \beta > 0 for \quad E^* - E_2 > E_{match} \end{cases} \tag{3.26}$$

where the gaussian functional form for $a_C(E^*, A)$ is chosen to satisfy the request of rapidity in reaching the asymptotic value a_∞ calculated with eq.(3.25), and the α and β parameters are determined by the following matching conditions:

$$a_D(E_{match} + E_2, A) = a_C(E_{match} + E_2, A) \tag{3.27}$$

$$a_C(E_{cl} + E_2, A) = a_\infty(1 + X) \quad with \ \ |X| \leq 10\% \tag{3.28}$$

The matching conditions imply that the two parameterizations have to give the same LD parameter value in correspondence of the matching energy E_{match}, (to be intended as a given $(E^* - E_2)$ value), and that the asymptotic value a_∞ has to be reached by $a_C(E^*)$ within a certain percentage X at a given energy E_{cl} (which will be on turn a $E^* - E_2 \approx E^*$ value). In the following, we will write for simplicity: $E'_{match} = E_{match} + E_2$ and $E'_{cl} = E_{cl} + E_2$. It is easy to see that the sign of X has to be opposite with respect to that of the difference $(a_\infty - a_D(E'_{match}, A))$.
Resolving the matching equations, we have for the α and β parameters:

$$C = \frac{a_D(E_{match}, A) - a_\infty}{X \cdot a_\infty} \tag{3.29}$$

$$\beta = -\frac{\ln C}{E'^2_{match} - E'^2_{cl}} \tag{3.30}$$

$$\alpha = \frac{X \cdot a_\infty}{-\beta E'^2_{cl}} \tag{3.31}$$

We have now to discuss the choice of the two energy values E_{match} and E_{cl}. E_{match} simply represents the limits of validity of the parameterization $a_D(E^*, A)$ proposed in [67], and we can assume it to be equal to the upper limit of the energy range of discrete levels used for the fit, if the nucleus of interest is part of the fitted data set. As can be inferred from our choice of notation, this upper limit usually corresponds to the energy maximizing the measured dn/dE^* level density distribution for nuclei included in the study done in [67]. We have however to be careful to the fact that this energy value has to be defined also for nuclei which are not part of the fitted data set, or for nuclei for which we have no or too few experimental information on energy spectra: in such cases we can for instance put it equal to $\approx 10\ MeV$, which is typically considered as a critical energy above which a damping of pairing effects is expected (see for instance [62]). This choice corresponds to the assumption that, beyond this critical energy, the LD parameter is no more affected by structure effects. The choice of a uniform value for E_{match} entering the LD parameter calculation ensures to avoid any dependence on the relative range of excitation energy for which the functional form $a_D(E^*, A)$ is used, which we do not want to vary too much from nucleus to nucleus. Therefore, this matching energy is left an input parameter for the calculation, and the default value is set to 10 MeV.
To fix the energy E_{cl} we can refer to ref.[39], in which a study of the limiting nuclear temperature (or excitation energy per nucleon) as a function of nuclear mass is presented. Results for the limiting energy per nucleon e_{lim} are presented in [39] only for the mass region $A \geq 40$. Values for this quantity increase from $e_{lim} \sim 3\ A.MeV$ for heavier nuclei (with $A \sim 100 \div 200$) up to $e_{lim} \approx 8\ A.MeV$ for

the lightest nucleus considered. At such energies, the onset of multifragmentation (or break-up for lighter nuclei) is expected, and compound nucleus states are known to disappear. The corresponding value for the LD parameter has to fall to zero, the more abruptly the more rapid is the threshold process. The decrease of $a(E^*)$ with increasing energy beyond a given limiting value has not been included in our level density model, because no simultaneous break-up channels are implemented in the code in order to compensate the disappearance of CN states. Therefore, the E_{cl} value, left as free parameter of the calculations, does not correspond to the limiting energy of ref.[39], but rather represents an energy limit at which the asymptotic value of the LD parameter has already been reached (within a certain controllable percentage), and after which a decrease of $a(E^*)$ up to the zero value at the limiting energy may start. In order to give constraints on the decrease of the level density parameter, data for reactions in which the fragmentation regime is attained are needed, and this possibility is discussed in some more details in Appendix **B** of this work. On the contrary, the rapidity of the increase of $a(E^*)$ up to the asymptotic value of eq.(3.25) can be constrained with fusion-evaporation data, as it is the case for the reaction under study in this work, and is determined by the parameter E_{cl}. As a first guess, without extrapolating the trend for $e_{lim}(A)$ given in [39] to the unexplored lighter nuclei region, we can assume a constant value $e_{lim} \approx 8\ A.MeV$ for nuclei with mass $A < 40$, and we can vary $E_{cl} \leq (e_{lim} \cdot A)$ between the extremes $(8 \cdot A)$ and $(3 \cdot A)\ MeV$ in our calculations. In the former case, being $8\ A.MeV$ an average estimation of the nuclear binding energy per nucleon, we are asking that, when the nucleus approaches its limit of existence, the asymptotic value of the LD parameter has already been reached; in the latter, the asymptotic limit for $a(E^*)$ is reached at a lower excitation energy. The E_{cl} value, together with the asymptotic value of the LD parameter a_∞, can be varied in the calculations to tune the model in order to reproduce experimental data. The effect of the modification of these parameters will be discussed in the following.

Going back to the LD expression of eq.(3.16), the $a(E^*)$ functional form has to be substituted by the matched $a_M(E^*)$, which assumes the two different forms $a_D(E^*)$ or $a_C(E^*)$, depending on the energy coordinate $(E^* - E_2)$ being $\gtrless E^*_{match}$. Since, as said before, the asymptotic value of $a_C(E^*, A)$ are usually larger than the $\tilde{a}$ values for $a_D(E^*, A)$, we expect that the calculation of $\rho(E^*)$ with the matched $a_M(E^*, A)$ function will give a larger number of availables nuclear levels with respect to the LD calculation with the non matched a of eq.(3.18) in the whole energy range.

In fig.(3.5) we can see the results of the matching procedure for ^{20}Ne. In the figure inset we show both functions $a_D(E^*)$ (in black) and two different evaluations for

$a_C(E^*)$, obtained making two different choices for the limiting energy, *i.e.* $E_{cl} = (8\ ,3\cdot A)\ MeV$ respectively for the blue and red curve. With the same color scheme, we then show the resulting level density $\rho(E^*)$ calculated with eq.(3.16) if we use as LD parameter the $a_D(E^*)$ coming from ref.[67], or the two matched $a_M(E^*)$ with $E_{cl} = (8\ ,3\ \cdot A)\ MeV$. As expected, the LD grows more rapidly if the limiting energy is lower (red curve), and calculations at different limiting energies converge when the LD parameter approaches the same asymptotic value. The nearly constant a_D value causes a very limited growth of the LD absolute value (black curve), and the calculation is stopped at a lower excitation energy, to remind that the use of $a_D(E^*)$ in the whole excitation energy range is by definition not correct.

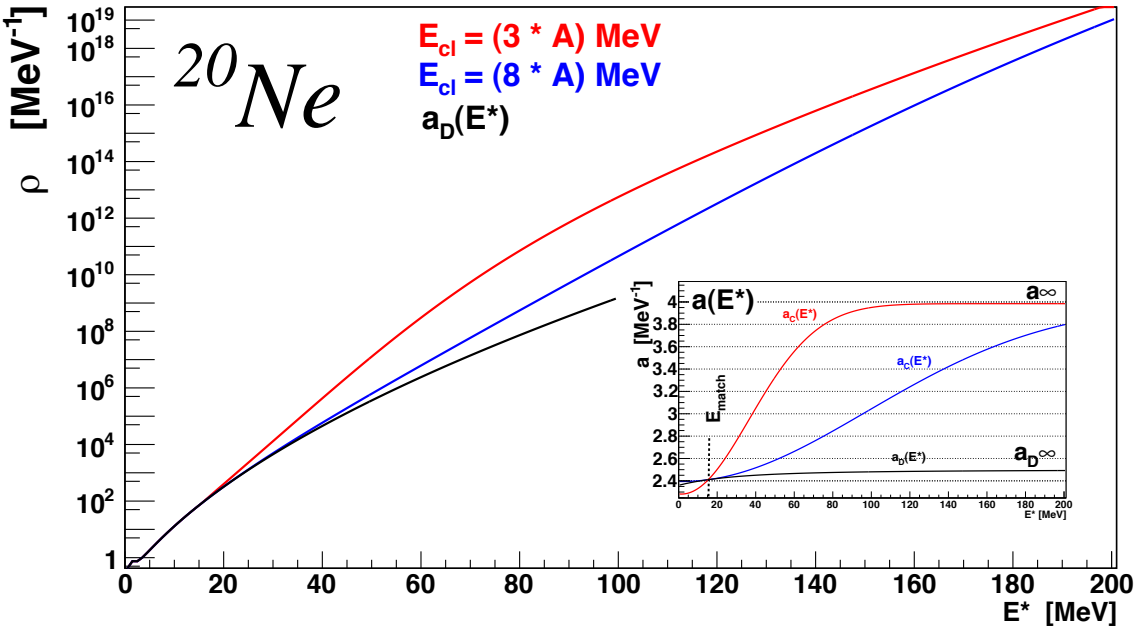

Figure 3.5: Level density calculation for ^{20}Ne. In the figure inset: $a_D(E^*)$ (in black) and two different evaluations for $a_C(E^*)$, obtained with $E_{cl} = (8\ ,3\cdot A)\ MeV$ respectively for the blue and red curve. With the same color scheme: $\rho(E^*)$ calculated with eq.(3.16) with $a_D(E^*)$, and $a_M(E^*)$ with $E_{cl} = (8\ ,3\cdot A)\ MeV$.

3.3 Kinematics of the Decay with Angular Momentum

The treatment of angular momentum is a specific feature of the Hauser-Feshbach formalism, and represents the main advance of this evaporation model with respect to the standard Weisskopf approach. This section is dedicated to the description of how angular momenta couplings are implemented in the Monte Carlo code, with the constraint of total angular momentum conservation, and of how the angular momentum degree of freedom affects the kinematics of the decay.
The approach we have chosen to adopt is of semi-classical type: angular momenta are considered as classical vectors, the angular momentum quantum number J giving the module of vector $\mathbf{J}$. Angular momentum vectors J_1 and J_2 couple under the assumption of equiprobability for the module J_S of their sum vector, ranging from $|J_1 - J_2| \leq J_S \leq |J_1 + J_2|$. A correct quantum mechanical treatment, in which coupling probabilities are given by specifying the angular momenta projections M and making use of Clebsch-Gordan coefficients is therefore missing. The more general procedure which we have decided to adopt, is analogous to the one implemented in the GEMINI++ model and it is detailed in the following.
Input parameters for the initial hot nucleus are the module of its angular momentum vector J_0 and the initial orientation of $\mathbf{J_0}$, the latter being specified by the angles $(\theta_{J_0}; \varphi_{J_0})$ in the **CM** reference-frame of the decaying CN (z-axis parallel to the velocity of the beam).
For each decay we select the emitted particle according to the branching ratio weight calculated within the HF model. As anticipated, the angular momentum J_d of the daughter nucleus is selected maximizing the LD at the given residual excitation energy as a function of J. We want then to consider the disalignment of $\mathbf{J_d}$ with respect to $\mathbf{J_0}$ due to the evaporation. For the couplings of angular momentum vectors in the binary decay we have (fig.3.6):

$$\begin{aligned} \mathbf{J_0} &= \mathbf{J_d} + \mathbf{j} \\ \mathbf{j} &= \boldsymbol{\ell} + \mathbf{s_p} \end{aligned} \tag{3.32}$$

where $\boldsymbol{\ell}$ is the relative orbital angular momentum and $\mathbf{s_p}$ is the spin vector of the emitted particle. We assume at this point that all the values of j in the range $|J_0 - J_d| \leq j \leq |J_0 + J_d|$ are equally probable so that we can randomly select the module of the $\mathbf{j}$ vector in this interval. Given s_p, the same can be said for the module of the orbital angular momentum $\boldsymbol{\ell}$, for which we will choose a random value in the

range $|j - s_p| \leq l \leq |j + s_p|$.
Given the modules of all angular momenta, we can obtain the angles θ_d and θ_ℓ, which are respectively the orientation angle of $\mathbf{J_d}$ with respect to $\mathbf{J_0}$ and of $\boldsymbol{\ell}$ with respect to $\mathbf{j}$, simply thanks to the law of cosines:

$$\theta_d = \arccos\left(\frac{J_0^2 + J_d^2 - (\boldsymbol{\ell} + \mathbf{s_p})^2}{2J_0 \cdot j_d}\right) \qquad (3.33)$$
$$\theta_\ell = \arccos\left(\frac{(\boldsymbol{\ell} + \mathbf{s_p})^2 + \ell^2 - s_p^2}{2\ell \cdot |\boldsymbol{\ell} + \mathbf{s_p}|}\right)$$

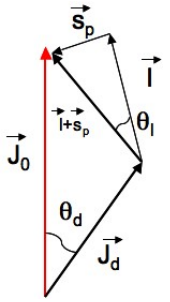

Figure 3.6: Vectorial couplings of angular momenta in the decay.

If we interpret θ_d as a spherical θ coordinate and we attribute to $\mathbf{J_d}$ a φ_d angle randomly chosen in the interval $[0; 2\pi]$, the space orientation of $\mathbf{J_d}$ is then fully determined in the reference frame whose z-axis is parallel to the CN angular momentum $\mathbf{J_0}$, which we call **J0** RF (fig.3.7). The same holds for the orientation of $\mathbf{j}$, which will be given in the same RF by $(\theta_j; \varphi_j = \varphi_d + \pi)$. The space orientation of $\boldsymbol{\ell}$ and $\mathbf{s_p}$ will be instead given in the RF whose z-axis is parallel to $\mathbf{j}$, by the angles $(\theta_\ell; \varphi_\ell)$ and $(\theta_s; \varphi_s = \varphi_\ell + \pi)$.
The angular distribution of the evaporated particle about the classical $\boldsymbol{\ell}$ vector will then be given by $dY/d\Omega = |P_\ell^\ell(\cos\theta)|^2$, where $P_\ell^\ell(\cos\theta)$ is the associated Legendre function for $m = \ell$, and θ is a spherical coordinates angle relative to a z-axis parallel to $\boldsymbol{\ell}$. Finally, the emission angle and all the angles giving the relative orientations of angular momenta have to be transformed back to the **CM** RF performing one (or more successive) rotation of axes (for instance of the type $\mathbf{J0} \xrightarrow{rot} \mathbf{CM}$). Explicit equations for the rotational transformations are derived in Appendix **A**.

To see the effects of including the angular momentum in the kinematics of the decay, we have performed two calculations for the CN ^{24}Mg, at the excitation en-

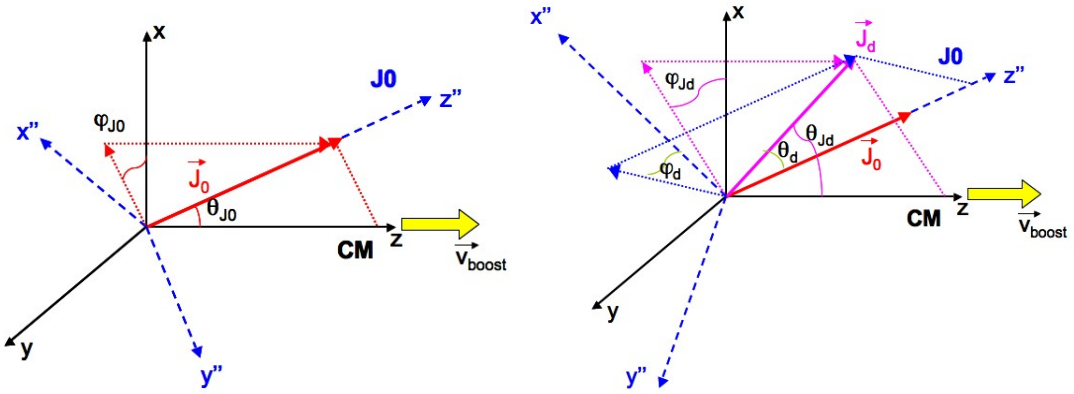

Figure 3.7: Left side: **CM** e **J0** reference frames; right side: components of vector $\mathbf{J_d}$ in the two coordinate systems. The use of the notation $(x^{''}, y^{''}, z^{''})$ for the axes of **J0** is made clear in Appendix A.

ergy $e^* = 2.6\ A.MeV$, with different input values for the initial spin J_0, namely $J_0 = 2;\ 12\ \hbar$, (and with a fixed $E_{cl} = (8 \cdot A)\ MeV$). Given our **CM** RF, the orientation of the CN angular momentum $\mathbf{J_0}$ is chosen to be $(\theta_{J_0}; \varphi_{J_0}) = (\pi/2; 3/2\pi)$ i.e. $\mathbf{J_0}$ is oriented along $-y$, being the beam velocity parallel to the z-axis and the impact parameter of the reaction measured along x in the classical notation.
Moreover, to get rid of the effect of multiple disalignments in the decay chain we have stopped the evaporation after one single emission. We show in fig.(3.8) for the case $J_0 = 12\ \hbar$ the module distribution for the angular momentum of daughter nuclei after one decay step, together with the correlation of the value of J_d to the relative orientation of the residue angular momentum vector with respect to the initial $\mathbf{J_0}$, given by the angle θ_d. As can be understood from the J_d vs. θ_d correlation plot, for each value of the module J_d we have $(2j+1)$ possible orientations of $\mathbf{J_d}$ with respect to $\mathbf{J_0}$, corresponding to the $(2j+1)$ possible values for the module of vector $\mathbf{j} = \mathbf{J_0} - \mathbf{J_d}$. In particular, the orientation angles $\theta_d = 0;\ \pi$, corresponding to the two opposite cases of $\mathbf{J_d}$ parallel or antiparallel to $\mathbf{J_0}$, are always possible, while the number of intermediate orientations increase with increasing J_d value. Being the J_d distribution peaked at around $J_d = 2\ \hbar$, it is not surprising then that the corresponding θ_d distribution will be peaked at $\theta_d = 0;\ \pi$, and only a small fraction of the daughter nuclei has a θ_d in between. As far as the J_0 module distribution is concerned, we can observe that the relative abundance of integer and half-integer values has to reflect the isotopic abundance of the masses of daughter nuclei of a given charge.

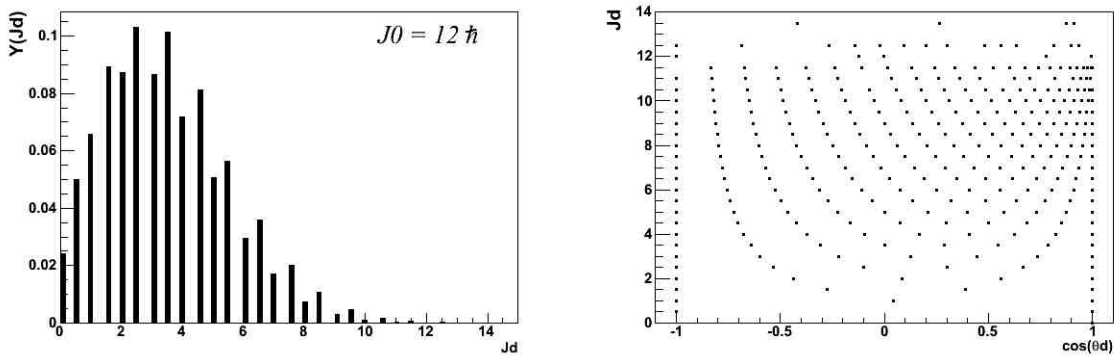

Figure 3.8: Predictions of the Hauser-Feshbach code for the angular momentum of the daughter nuclei in a single-step decay of ^{24}Mg $e^* = 2.6$ $A.MeV$, $J_0 = 12$ $\hbar$. Left panel: J_d module distribution; right panel: correlation between the module J_d and the relative orientation angle of $\mathbf{J_d}$ with respect to $\mathbf{J_0}$. Normalization is to the total number of simulated events.

Once transformed to the **CM** RF, the distribution of θ_{J_d} will be strongly peaked at the initial $\theta_{J_0} = \pi/2$ value, and correspondingly $\mathbf{j}$ will be most probably parallel to $\mathbf{J_0}$. If we consider the coupling $\boldsymbol{\ell} = \mathbf{j} - \mathbf{s_p}$ we can also easily understand that $\boldsymbol{\ell}$ will stay parallel to $\mathbf{j}$ when spin $s_p = 0$or $1/2$ particles are evaporated, which is quite always the case, with the only exception of rare d and Li evaporation.
Moreover, ℓ module distribution will be peaked around the initial J_0 value, as can be seen from fig.(3.9) for both cases $J_0 = 2;\ 12$ $\hbar$.

Finally, what we expect from the $dY/d\cos\theta^{(\ell)}$ angular distributions coming from Legendre associated functions is that, for increasing ℓ value, the emission will take place in the plane perpendicular to vector $\boldsymbol{\ell}$, which correspond to the plane xz for an orbital angular momentum $\boldsymbol{\ell} \parallel \mathbf{J_0}$. This is confirmed by fig.(3.9), where we can see the (θ, φ) emission angles of the evaporated particles in the **CM** RF corresponding to both the initial values of $J_0 = 2;\ 12$ $\hbar$. In the case $J_0 = 12$ $\hbar$, where higher values for the orbital angular momentum ℓ can be attained, in-plane emission ($\theta = 0; \pi$ and $\varphi = 0$) is thus favoured with respect to the lower initial angular momentum case.
In the following sections we will show the results of full decay chain calculations, and we will further comment on how the angular momentum effects acting at each binary decay step are averaged, and on how they affect final inclusive angular distributions.

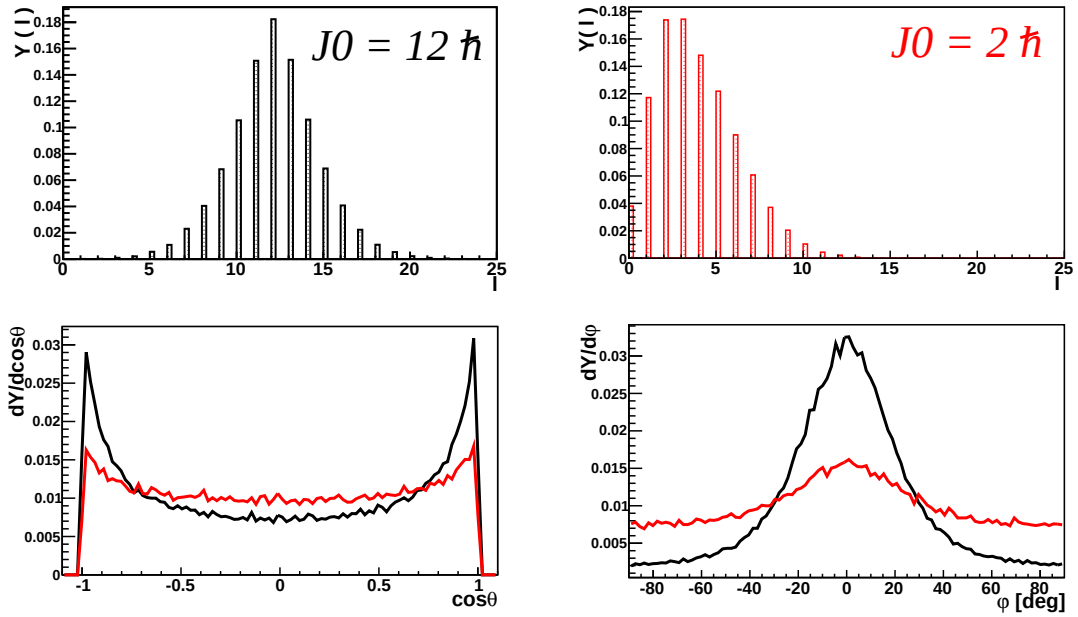

Figure 3.9: Predictions of the Hauser-Feshbach code for the orbital angular momentum for light particle emission in a single-step decay of ^{24}Mg, $e^* = 2.6$ $A.MeV$: ℓ distributions are shown in the upper panel, on the left for an initial $J_0 = 12$ $\hbar$ for the CN (black histogram), on the right for $J_0 = 2$ $\hbar$ (red). In the lower panel, corresponding $dY/d\cos\theta$ and $dY/d\varphi$ distributions for emitted particles, with the same color scheme. Normalization is to the total number of simulated events.

3.4 The GEMINI++ De-Excitation Code

GEMINI is a statistical decay model largely and successfully used by the nuclear physics community. It was first written in FORTRAN in 1988, with the main aim of reproducing data from heavy-ion induced fusion reactions. It has later been further developed and translated in C++, and the original dichotomy between light-particle emission and other binary decays is maintained in the actual version of the code, GEMINI++ [75]: together with the evaporation of light particles within the Hauser-Feshbach model, decay channels as the emission of an Intermediate Mass Fragment (IMF) ($Z \geq 4$) following the formalism of Moretto [76] and nuclear fission, described with the transition-state formalism by Bohr and Wheeler [77], are implemented in the code.

In the literature, we can find many applications of GEMINI to the description of evaporation data, and a systematic study on this topic has been recently published in [46].

The very complete online documentation on GEMINI++ has also provided a necessary guidance in the development of the Hauser-Feshbach code which is presented in the first part of this chapter. This is the reason why, before going to the results of calculations performed for the decay of light nuclear system with our newly developed code, we want to comment in this section on the main differences between our approach and the one followed by the author of GEMINI in the implementation of the decay and level density models in the code. First of all, to our knowledge, few studies exist on the comparison of data for the decay of light nuclear systems, in the mass region $A \sim 20$, to GEMINI++ calculations. As previously described, our efforts in the development of the decay code have been mainly devoted to the choice of parameterizations for the physical quantities of interest which are at most constrained to the available experimental information on nuclear structure and low energy excitations. We could say, on the contrary, that the parameterizations proposed in GEMINI++ are optimized to the description of the decay of generally heavier systems, for which the influence of nuclear structure in the decay is less relevant.
Going into some details, the starting point for the calculation of the nuclear level density in GEMINI++ is a Fermi-gas expression, written in terms of the nuclear thermal energy U:

$$\rho_{FG}^{gem}(E^*, J) = \frac{(2J+1)}{24\sqrt{2}a^{\frac{1}{4}}U^{\frac{5}{4}}\sigma^3} \exp S(U) \tag{3.34}$$

where $S(U)$ is the nuclear entropy, given by $S(U) = 2\sqrt{aU}$, and the energy coordinate U is obtained by subtracting a deformation-plus-rotational $E_{yrast}(J)$ and a pairing energy contribution δP from the excitation energy E^*. The angular momentum J then enters in the definition of the Yrast energy, and as a result, $\rho_{FG}^{gem}(E^*, J)$ has non-separable dependences on J and E^*, contrary to the case of our semi-empirical approach of eq.(3.14). An energy dependence is then attributed to the LD parameter a, in order to reproduce the fluctuations coming from shell effects:

$$a(U) = \tilde{a}\left[1 - h(U/\eta + J\ J_n)\frac{\delta W}{U}\right] \tag{3.35}$$

where δW is the shell correction to the liquid-drop mass and and $\tilde{a}$ is a smoothed level-density parameter. With $h(x) = \tanh(x)$, the best fit to the experimental data is obtained for $\eta = 19\ MeV$ and $\tilde{a} = A/7.3\ MeV^{-1}$. J_n, determining a fading out of shell effects also with spin, is set equal to $50\hbar$. A further modification of $\rho_{FG}^{gem}(E^*, \tilde{a})$ is needed, in order to take into account the enhancement of the LD due to collectivity

induced by long-range correlations. This is done by multiplying $\rho_{FG}^{gem}(E^*, \tilde{a})$ by a an enhancement factor $K_{coll}(E^*)$. In the systematic study done in [46] the prescription:

$$\rho^{gem}(E^*) = \rho_{FG}^{gem}(E^*, \tilde{a}_{eff}) = K_{coll}(E^*)\rho_{FG}^{gem}(E^*, \tilde{a}) \tag{3.36}$$

is adopted, *i.e.* the enhancement due to collectivity and its fade out at higher energies are ascribed to an effective smoothed LD parameter $\tilde{a}_{eff}$, which is parametrized as a function of the thermal energy:

$$\tilde{a}_{eff}(U)\frac{A}{k_\infty - (k_\infty - k_0)\exp\left(-\frac{\mathcal{K}}{k_\infty - k_0}\frac{U}{A}\right)} \tag{3.37}$$

where $k_0 = 7.3\ MeV$ and the asymptotic value at high excitation energy is $\tilde{a}_{eff} = A/k_\infty$. The parameter $\mathcal{K}$ determines how fast the long-range correlations wash-out with excitation energy. k_∞ is typically set to 12, and $\mathcal{K}$ is fitted in the $A > 100$ region as $\mathcal{K}(A) = 0.00517\exp(0.0345A)$.
The excitation energy dependence of $\tilde{a}_{eff}(U)$ is very strong for heavier systems, but it becomes negligible already for $A < 100$. Therefore, according to ref. [46], we can make use of a constant $\tilde{a} = A/7.3$ in this "lighter" mass region. In any case, we have to be aware of the fact that the lightest system which is included in the systematics presented in [46], is a mass ~ 60 nucleus, which means three times heavier than the region we are concerned with in this work.

The transmission coefficients implemented in the GEMINI code are obtained through a sophisticated approach taking into account a distribution of barriers due to thermal fluctuations of the CN. The final transmission coefficient is the average of three different values corresponding to a temperature dependent fluctuation of the radius parameter in the nuclear potential, which enters in the optical model fit to elastic scattering data. In this first version of our model, the adopted prescription for the calculation of transmission coefficients is far more simple. Nevertheless, we expect that being concerned with lighter systems, the absolute values of the barrier is smaller, and the effect of the barrier distribution on the spectra is reduced, as we read in [46]. Moreover, since the transmission coefficients define the shape of evaporated spectra in the Coulomb barrier region, when comparing to data their effect can be easily isolated from the one of the level density parameter, determining the slope of the spectra exponential tail. An improvement of the adopted parameterizations can be therefore planned, if this will result necessary.
Concerning the treatment of angular momentum, a modified expression for the Yrast

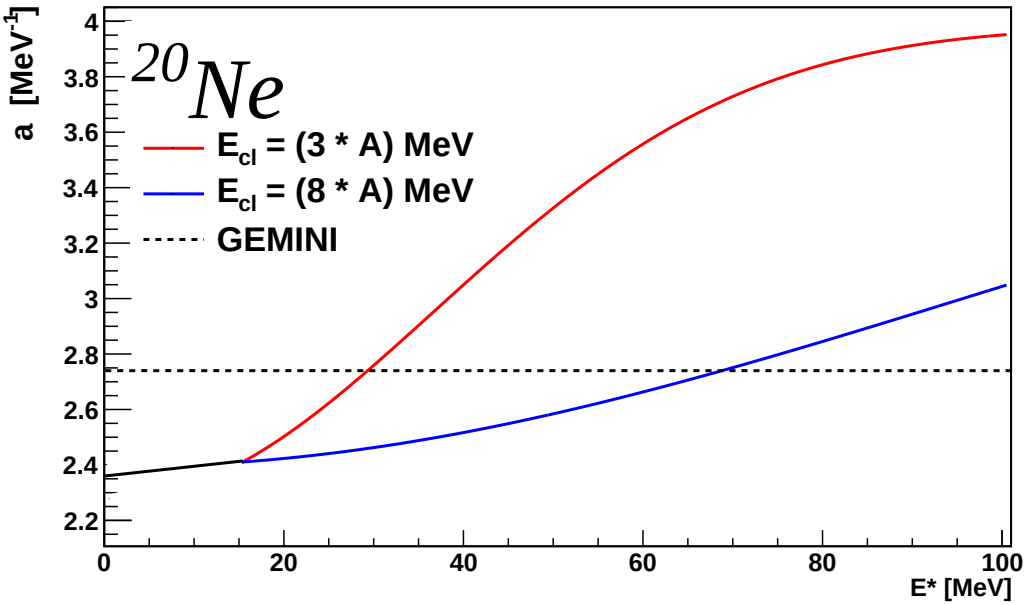

Figure 3.10: For ^{20}Ne, as an example, comparison between the LD parameter $a(E^*)$ implemented in our Hauser-Feshbach calculations, with $E_{cl} = (8 \cdot A)\ MeV$ (blue line) and $E_{cl} = (3 \cdot A)\ MeV$ (red line), where the black line corresponds to the excitation energy region in which the value of this parameter is given by $a_D(E^*)$ of eq.(3.28) [67] for both E_{cl} values, and the almost constant $a(E^*)$ implemented in GEMINI++, calculated with eq.(3.37).

line parameterization is adopted in GEMINI, which differs from our classical expression given in eq.(3.4). The proposed parameterization makes use of Yukawa-plus-exponential finite-range calculations by Sierk [78] and contain free fit parameters to be adapted on the compound nucleus of interest. In particular, this modification allows to take into account the steeper increase of the deformation-plus-rotational energy due to lower values of the moment of inertia for lighter nuclei. Modification of $E_{yrast}(J)$ has a stronger influence on heavier fragments emission, as in the case of α particles, which can remove a larger amount of angular momentum. The E_{yrast} effect, even if affecting both the barrier region and the exponential tail of evaporation spectra, can in principle be disentangled from the effects of the level density parameter and that of the transmission coefficients by comparing data for a lighter particle as a proton to that for a heavier particle as an α. Finally, the problem of the kinematics of the decay in presence of angular momentum is addressed with our same semi-classical approach.

3.5 Observables and Thermal Properties in the Decay of $^{24}Mg^*$

In this section we report the results of the calculations performed with the Monte Carlo Hauser-Feshbach code for the decay of equilibrated light nuclei in the mass region $A \sim 20$ and at an excitation energy of the order of ~ 3 $A.MeV$. Such calculations have been at the basis of a beam-time request, submitted by the NUCL-EX collaboration to the PAC - Physical Advisory Committee - of *Laboratori Nazionali di Legnaro* - LNL - INFN, where we have proposed to measure several reactions involving light nuclei with our GARFIELD+RCo set-up.
In particular, we have performed calculations for the decay of ^{24}Mg at $e^* = 2.6$ $A.MeV$, corresponding to the excitation energy of the CN issued in case of complete fusion for the reaction $^{12}C +^{12} C$ at 95 MeV beam energy. This reaction has been measured, and the description of the measurement is presented in chapter **4**.
The angular momentum input distribution for the fused system in this reaction can be assumed as a triangular distribution with a maximum value $J_{0\ max} = 12\ \hbar$ coming from the systematics. Moreover, in order to respect parity conservation, we have allowed the CN to assume only even values of J_0 extracted from the triangular distribution. The initial space orientation of $\mathbf{J_0}$ is always determined by $(\theta_{J_0}; \varphi_{J_0}) = (\pi/2; 3/2\pi)$. In the following, to avoid being repetitive, we will refer to this set of input parameters for the calculations as "experimental " energy and angular momentum conditions for the CN. All kinematic observables are given in the **CM** reference-frame.
We have performed calculations for two different input values for the free parameter E_{cl} in the LD model, namely $E_{cl} = (8 \cdot A)\ MeV$ and $E_{cl} = (3 \cdot A)\ MeV$. Comparison to data (see chapter **5**) will allow us to constrain the value of this parameter. Together with our calculations, we show for chosen observables the results obtained with GEMINI++, with a twofold purpose: firstly, the good agreement obtained for the computation of global observables ensures the reliability of our code; secondly, in GEMINI++, we have the possibility of enabling/disabling a decay channel competitive to sequential evaporation, namely the emission of IMF, described in terms of the transition state formalism, and this allows us to investigate the effect of the inclusion of this channel on the output of the decay. In fact, any constraint on our evaporation code free parameters, which we aim to obtain from the comparison to data, can be considered reliable only if the presence of additional channels does not strongly affect the observables which we plan to use to extract this information.

Light charged particles

The first observables which we can potentially compare to experimental data are inclusive angular, energy and multiplicity distributions of emitted particles.
Angular distributions for emitted particles in a fusion-evaporation reaction are determined by an average of angular momentum effects on each step of the sequential decay chain, and we have previously detailed the effect of the inclusion of angular momentum in a one-step decay calculation. In fig.(3.11) we compare the obtained angular distributions for protons and α particles for the decay of ^{24}Mg under experimental conditions. As expected from the theory, angular distributions are less sensitive to the input level density model, and calculations for the two chosen values of E_{cl} are indistinguishable. Coherently with the single-step decay calculations, we expect that the overall effect of sequential evaporation is to push the mean module of the orbital angular momentum towards lower values with respect to the first step angular momentum ℓ, which is approximately J_0, thus favouring out-of-plane emission approaching the end of the decay chain. At the same time, $\boldsymbol{\ell}$ space orientation will most probably remain the same of the initial $\mathbf{J_0}$, as far as smaller values of angular momenta are involved in the decay. The net result for complete evaporation calculations is that the angular distributions of emitted particles integrated over all the decay chain still show memory of the reaction plane, as we can see from the figure. This reaction plane has to be randomized before comparing to experimental data, and this has to be done conserving relative φ angles between emitted particles, as it is discussed in chapter **4**.
Finally, as mentioned, the angular momentum treatment implemented in our code is analogous to the one implemented in GEMINI, as it is also evident from fig.(3.11). The inclusion of IMF emission does not further modify protons and α particles angular distributions.

The comparison of evaporated particles energy distributions obtained with different values of E_{cl} allows for a test of the well-known dependence of the slopes of energy spectra on the input level density parameter. As discussed, varying the value of E_{cl} in our level density model corresponds to a modification of the rapidity with which the LD parameter reaches its asymptotic value a_∞. A quicker increase of $a(E^*)$, corresponding to the lower $E_{cl} = (3 \cdot A)\ MeV$ case, implies a lower nuclear temperature for a given excitation energy, according to the relation $E^* = aT^2$, which translates into a steeper kinetic energy spectrum for evaporated particles. In the $E_{cl} = (8 \cdot A)\ MeV$ case, evaporation of particles with a higher average energy will be favoured. This is shown in fig.(3.12). As previously shown in fig.(3.10), at the

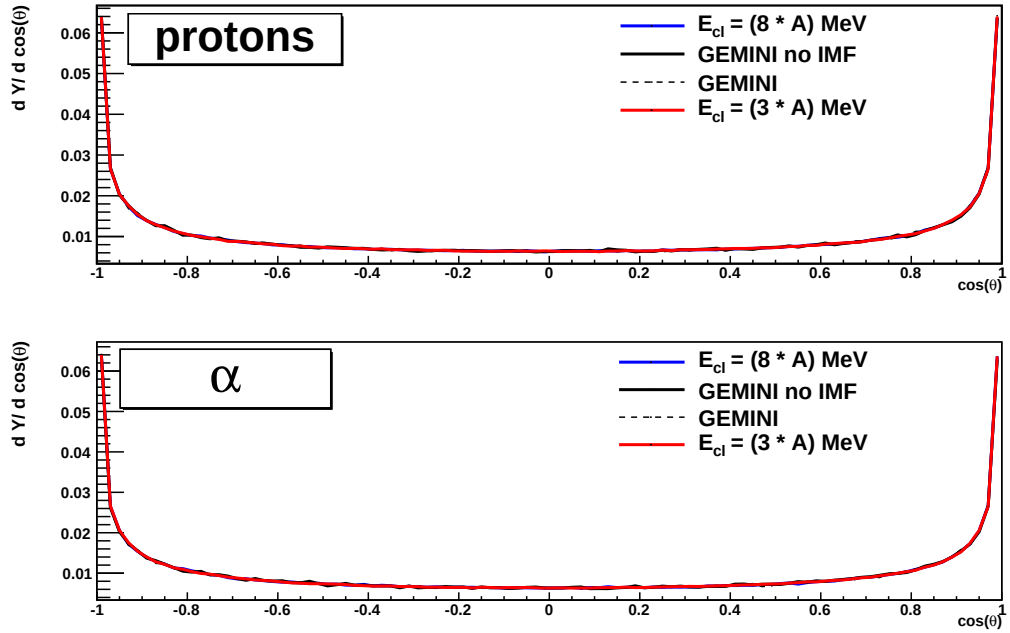

Figure 3.11: Angular distributions for protons (upper panel) and α particles (lower) for the evaporation of ^{24}Mg under experimental conditions. Calculations are shown for the Hauser-Feshbach code, with $E_{cl} = (8 \cdot A)\ MeV$ (blue line) and $E_{cl} = (3 \cdot A)\ MeV$ (red line), and for GEMINI, enabling (black dashed line) or disabling (black continuous line) the IMF emission. All calculations almost give identical results. Normalization is to the total number of produced protons/α particles.

excitation energies of interest for the decay of ^{24}Mg under experimental conditions, the level density parameter implemented in GEMINI++ is intermediate between the values assumed by $a(E^*)$ in correspondence with the two choices $E_{cl} = (8 \cdot A)$ and $(3 \cdot A)\ MeV$. This is also evident in fig.(3.12), where the slope of energy spectra calculated with GEMINI++ are intermediate between our Hauser-Feshbach results for the two cases. A difference between our calculations and GEMINI results can be observed also in the low-energy region, which can be attributed to the different adopted parameterizations for the transmission coefficients. This confirms that, as we have previously commented, the effects of transmission coefficients and of the level density can be easily disentangled. Finally, we notice that the inclusion of IMF emission does not strongly affect the slope of the energy spectra: this ensures the reliability of the constraint to the level density, which can be obtained by tuning our evaporation model parameters in order to reproduce the data.

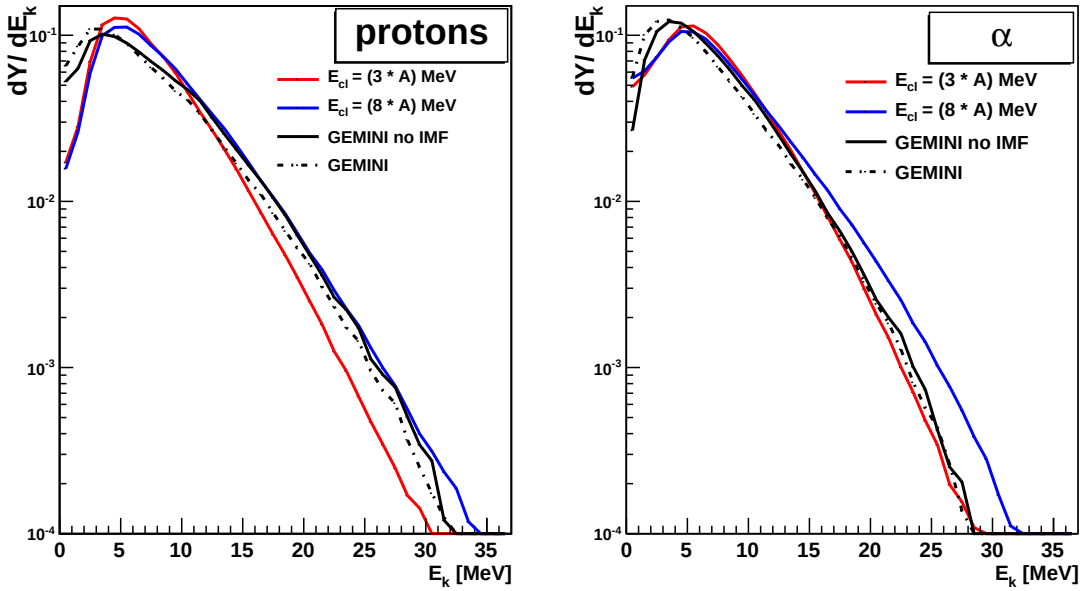

Figure 3.12: Kinetic energy distributions for protons and α particles for the evaporation of ^{24}Mg under experimental conditions, for Hauser-Feshbach calculations with $E_{cl} = (8 \cdot A)\ MeV$ (blue line) and $E_{cl} = (3 \cdot A)\ MeV$ (red line), and for GEMINI++, enabling (black dashed line) or disabling (black continuous line) the IMF emission. Normalization is to the total number of produced protons/α particles.

Finally, concerning light charged particles emission, we show in fig.(5.3) the predicted multiplicity distributions for protons and α particles, for the same experimental source. As it is the case for angular distributions, this observable is less sensitive to the choice of E_{cl} in the level density model. In particular, for protons, almost no differences can be observed between our calculations for $E_{cl} = (3 \cdot A)$, $(8 \cdot A)\ MeV$ and GEMINI++ without IMF emission. As far as α particles are concerned, a difference is observed for the probability of $n_\alpha = 1$ events, and a globally higher α multiplicity is found if IMF emission is taken into account. The particular shape of all α multiplicity distributions, which present a peak at $n_\alpha = 6$, corresponding to the complete disintegration of the ^{24}Mg source, will be better discussed in the following.

Charge distribution and staggering

To have a more global look at the outcome of the calculations, we can check the final charge distribution $Y(Z)$ resulting from the decay of the ^{24}Mg CN under

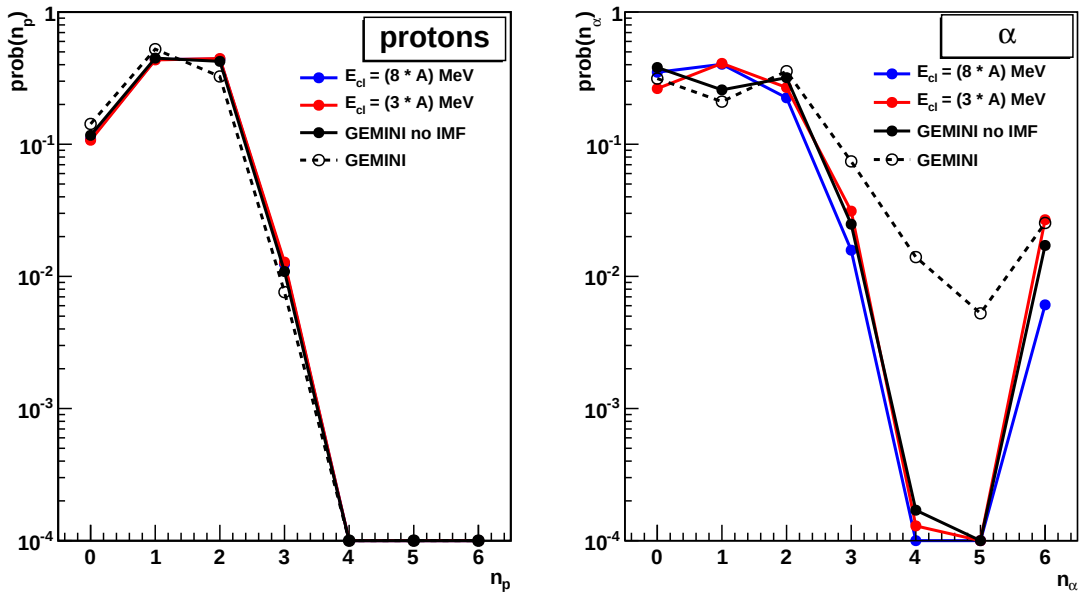

Figure 3.13: Multiplicity distribution of protons (left panel) and α particles (right panel) for the evaporation of ^{24}Mg under experimental conditions. for Hauser-Feshbach calculations with $E_{cl} = (8 \cdot A)\ MeV$ (blue dots and line to guide the eye) and $E_{cl} = (3 \cdot A)\ MeV$ (red dots and line), and for GEMINI++, enabling (empty dots and dashed line) or disabling (full black dots and continuous line) the IMF emission. Normalization is to the total number of simulated events.

experimental conditions, which is shown in the upper panel of fig.(5.9), together with the multiplicity distribution of reaction products, shown in the lower panel. Both observables are evaluated with our Hauser-Feshbach code for the two choices for E_{cl} and for GEMINI++ with/without IMF emission. The variation of the level density parameter is reflected in the average kinetic energy of emitted particles, and therefore, in the average size of evaporation residues and event multiplicity. A higher temperature (as it is the case for $E_{cl} = (8 \cdot A)\ MeV$ with respect to GEMINI++, and for GEMINI++ with respect to $E_{cl} = (3 \cdot A)\ MeV$) corresponds to a reduced event multiplicity and to a heavier evaporation residue, since the available energy is spent in fewer evaporation steps. This can be seen in fig.(5.9). Concerning the shape of the charge distribution, a typical distribution of evaporation products is obtained with our calculations, with a sharp separation between the emitted light particles and the evaporation residue region. If we think of an experimental distribution, this may already seem not realistic. The population of the region between emitted

particles and evaporation residues can indeed be ascribed to decay channels other than sequential evaporation, as the IMF emission. Calculations with GEMINI++ enabling/disabling IMF emission, also shown in fig.(5.9), confirm that the charge region $3 \leq Z \leq 6$ of the calculated $Y(Z)$ could be more populated by including this decay channel. When the IMF emission is disabled, the shapes of the charge distribution calculated by our Hauser-Feshbach code and by GEMINI are found to be in good agreement. A similar enhancement for the IMF yield is also to be expected in case of a Fermi break-up [40] of the fused system. This decay channel is not implemented neither in our decay code, nor in GEMINI++.

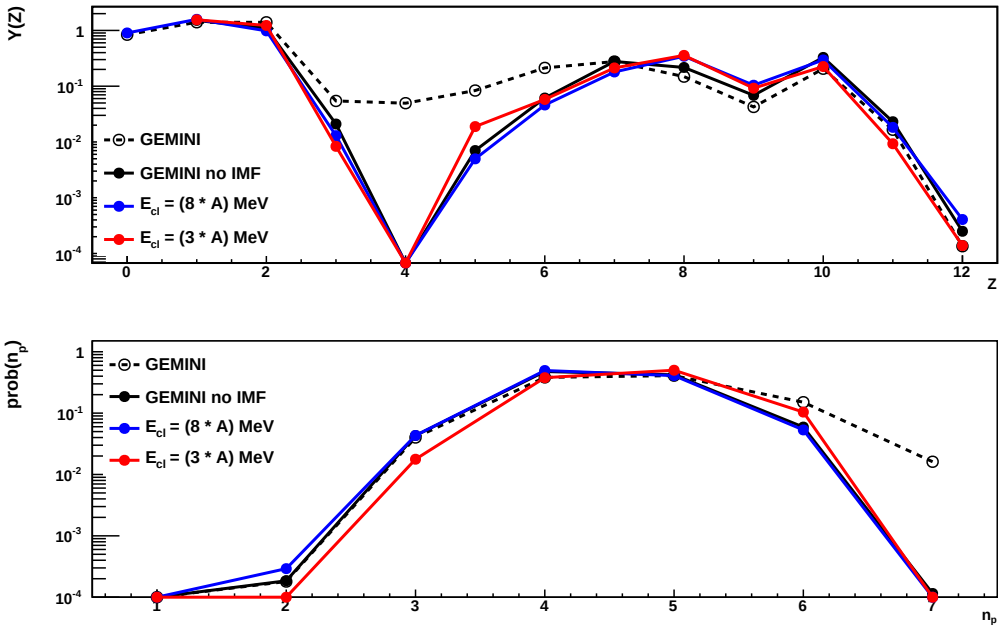

Figure 3.14: Upper panel: charge distribution of reaction products; lower panel: total multiplicity distribution. Hauser-Feshbach model predictions with $E_{cl} = (8 \cdot A)\ MeV$ and $E_{cl} = (3 \cdot A)\ MeV$ are shown respectively with blue and red dots connected by a line to guide the eye. GEMINI calculations enabling /disabling the IMF emission are also shown by empty/full black dots connected by a dashed/continuous line. Normalization is to the total number of simulated events.

As far as the signature of nuclear structure in the reaction is concerned, a clear odd-even effect is visible in the charge distribution in the residue region, and can be made more evident plotting the ratio of $Y(Z)$ to a smoothed $Y_s(Z)$ distribution, obtained by means of a parabolic smoothing on 5 successive points, as proposed

in ref.[31] with the same aim of putting in evidence odd-even effects in experimental data. This is shown in fig.(3.15) for the $Y(Z)$ distribution of fig.(5.9), with $E_{cl} = (8 \cdot A)\ MeV$. The ratio is plotted for a restricted charge region for the residue, where the statistics is such that the smoothed yield can be safely computed with the interpolation method proposed in [31].
We know from the discussion in chapter **1** that odd-even effects in isotopic observables are related to the pairing residual interaction. We have also stated that evaporation models contain two main ingredients which show a signature of the pairing interaction, namely the binding energy and the level density. Odd-even effects in our calculations are therefore a consequence of the use of experimental values for the binding energies, together with the implementation of realistic level densities reproducing the pairing gap. We can ask ourselves which is the relation between the amplitude of the staggering and the initial excitation energy of the CN nucleus. To this aim, we have performed calculations for the ^{24}Mg also at two other energies, namely $e^* = 3.$ and $3.5\ A.MeV$, other input parameters being equal. Results for the $Y(Z)$ distributions and their ratio to the smoothed $Y_s(Z)$ are shown in fig.(3.15).

First of all we notice the shift of the centroid of the residue distributions towards lighter fragments with increasing initial e^*. This is obviously due to the larger excitation energy available for the CN decay, which translates into longer evaporation chains. Moreover, for the same reason, the higher is the initial CN energy, the more populated is the charge region $3 \leq Z \leq 6$, which also means that evaporation residues are found to be lighter. Concerning the staggering, we have to take care of the differences in yields to do some significative remarks. For instance, the amplitude of the oscillation around $Z = 8$, where yields are comparable for the three cases, seems to be reduced when increasing the CN excitation energy. A dependence of the staggering on the initial excitation energy suggests therefore that odd-even effects may affect the whole evaporation chain, and that investigating their strength at finite temperature could give us information on the temperature dependence of the pairing interaction. To understand the interplay between pairing effects in the mass and in the level density, we show in fig.(3.16) the charge distribution at the last but one step of the evaporation chain for the decay of ^{24}Mg under experimental conditions, for the case $E_{cl} = (3 \cdot A)\ MeV$. In the figure (and in the following) we adopt the notation proposed in [35], and we write Z^* when referring to a fragment of charge Z, excited at the last but one step of the decay chain. We also plot in the same figure the ratio of $Y(Z^*)$ to the smoothed $Y_s(Z^*)$, to put in evidence the presence of staggering. By looking at fig.(3.16) it is evident that not only the charge

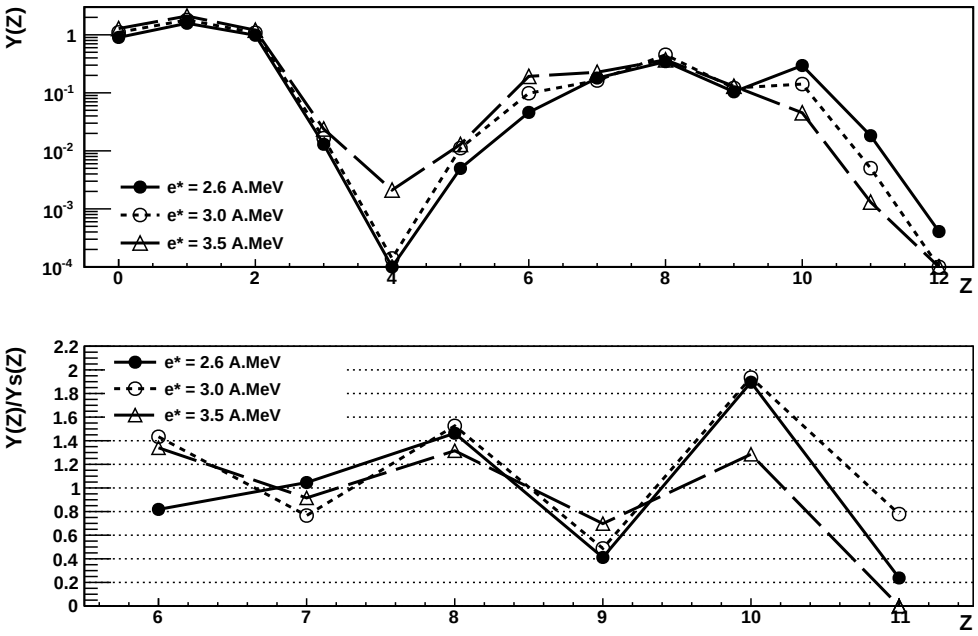

Figure 3.15: Upper panel: charge distribution of decay products corresponding to the evaporation of ^{24}Mg at $e^* = 2.6$ (full dots connected by a continuous line), 3 (empty dots and dashed line) and 3.5 $A.MeV$ (triangles and dashed line), with $E_{cl} = (8 \cdot A)\ MeV$. Normalization is to the total number of simulated events. Lower panel: ratio of $Y(Z)$ to the the smoothed $Y_s(Z)$ distributions obtained by means of a parabolic smoothing, same symbols scheme.

distribution at finite temperature is globally smoother, which can be seen as a reduced strength for pairing correlations at higher excitation energy, but also that, if the ratio to the smoothed distribution is evaluated, an inverse staggering effect is revealed and a peak becomes evident at the odd charge value $Z^* = 7$. This is in agreement with the analysis performed in [35], where the discrete levels population of warm nuclei has been extracted from coincident pairs measurements through the correlation function technique, and the resulting $Y(Z^*)$ distribution has been found to show a reversed staggering behaviour. The analysis done in [35] has been commented in more details in chapter **1**.

The obtained result can be interpreted as a signature of pairing effects in the level density: even nuclei have a lower density of levels at low energy because of the pairing gap. Making use of the principle of microscopic reversibility, we can think of the fusion of two cold decay products as the inverse process of the evaporation of a nucleus excited at the last but one step of a decay chain. It is then easy to

understand that, under the assumption of statistical laws governing the process, a lower probability will be associated to the creation of an excited even nucleus with respect to an odd one in the same energy range, this being due to the smaller number of available states in the final channel for the even system. This reasoning also justifies the behavior of another observable which has been extracted from data in [35], namely the mean excitation energy of populated discrete levels at the last but one step of the decay as a function of the fragment charge, which is found to stagger coherently: even fragments have a larger mean excitation energy, since they have to be populated above the pairing gap. In our calculations, the average energy $\langle E^* \rangle (Z^*)$ at the last but one step is computed by summing, for all simulated events, the relative kinetic energy of the last isotope pair produced at the end of the decay chain to the Q-value for the decay of their parent nucleus, and normalizing this sum to the yield $Y(Z^*)$. In fig.(3.16) we plot the result for this quantity in two cases: if all the events are considered in the average, the behavior of $\langle E^* \rangle (Z^*)$ is globally smoother, with the exception of the peak at $Z^* = 6$, and increases rapidly for bigger charges. This is easy to understand, since a nucleus with a charge close to the one of the CN, populated at the last but one step of the decay chain, implies a low multiplicity event, with high energy emission from the continuum. On the contrary, if we include in the average only events in which the last isotope pair is produced from the decay of a discrete resonance, $\langle E^* \rangle (Z^*)$ is found to oscillate with peaks at even charge values for heavier fragments. This oscillation can be attributed to a level density effect, and it is worthwhile to notice that the calculation of this observable can be compared to data only in this latter case.

In order to verify the hypothesis according to which odd-even effects represent a signature of the pairing interaction in the level density, we have performed two different calculations for the evaporation of ^{24}Mg, always under experimental conditions and with $E_{cl} = (3 \cdot A)\ MeV$, artificially suppressing the energy backshift in the level density in one case, and increasing it by a factor of two in the other. The results of these calculations are shown in fig.(3.17). It is evident that, suppressing the pairing backshift, the staggering is determined uniquely by odd even effects in the binding energy, which tend to favour even Z-nuclei because of their increased stability (*i.e.*, their lower separation energy, as discussed in chapter **1**). On the contrary, if the pairing gap is increased, pairing effects in the level density dominates at finite temperature, and the charge distribution at the last but one step shows a strong reversed odd even effect. Results of our calculations with the values of the pairing backshift adopted in our level density model, as the ones of fig.(3.16), coherently show an intermediate behavior.

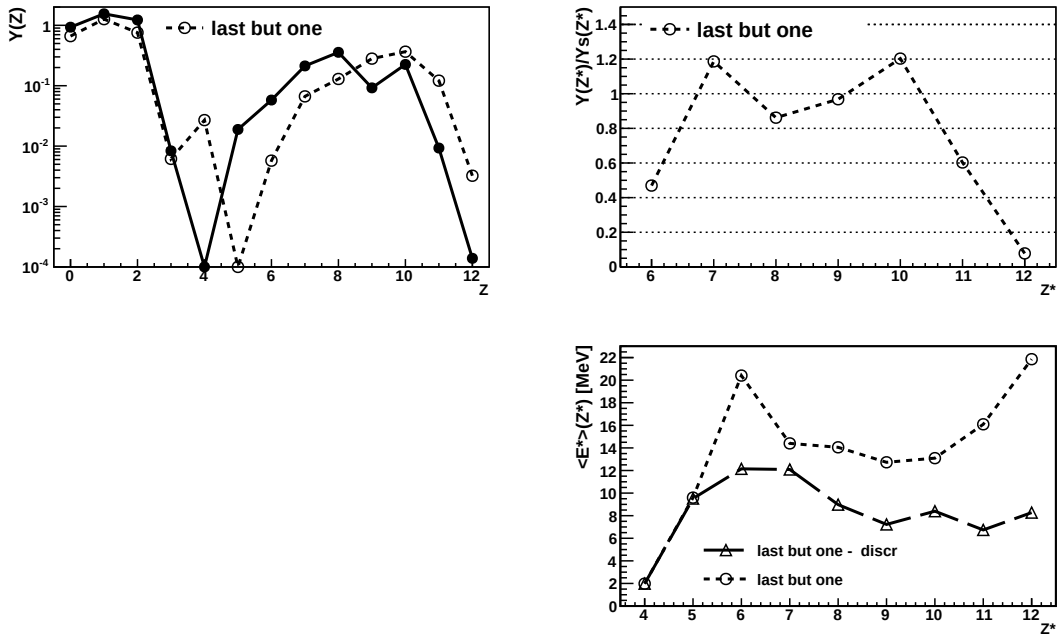

Figure 3.16: Observables showing odd-even effects for the evaporation of ^{24}Mg at $e^* = 2.6$, under experimental conditions and with $E_{cl} = (3 \cdot A)\ MeV$. In the upper panel, on the left: $Y(Z)$ distribution (full dots connected by a continuous line), together with the corresponding charge distribution at the last but one step of the decay chain (empty dots and dashed line), normalization is to the total number of simulated events; upper panel, on the right: ratio between the yield of warm fragments at the last but one step $Y(Z^*)$ and a smoothed $Y_s(Z^*)$ obtained by means of a parabolic smoothing over 5 successive points. Lower panel: average energy $\langle E^* \rangle$ of warm fragments populated at the last but one step of the decay chain, for the complete set of events (empty dots and dashed line), and only for fragments populated in a discrete state (triangles, dashed line).

Correlation functions and α-structure

As explained in the section on the implementation of the decay model in the code, discrete levels can be populated in the decay chain and the information on their population is stored in memory. Binary decays proceeding through discrete states keep a memory of their "resonant " origin, which is reflected in the relative kinetic energy (or, equivalently, relative momentum or velocity) distribution of fragment pairs. Examples of such distributions for the decay products of ^{24}Mg under experimental conditions and with $E_{cl} = (3 \cdot A)\ MeV$ are plotted in fig.(3.18) for the $(\alpha,^{12}C)$,$(p,^{12}C)$ and $(p,^{13}C)$ isotope pairs. Peaks corresponding to the decay from discrete states are clearly visible. Energy conservation allows us to transform the

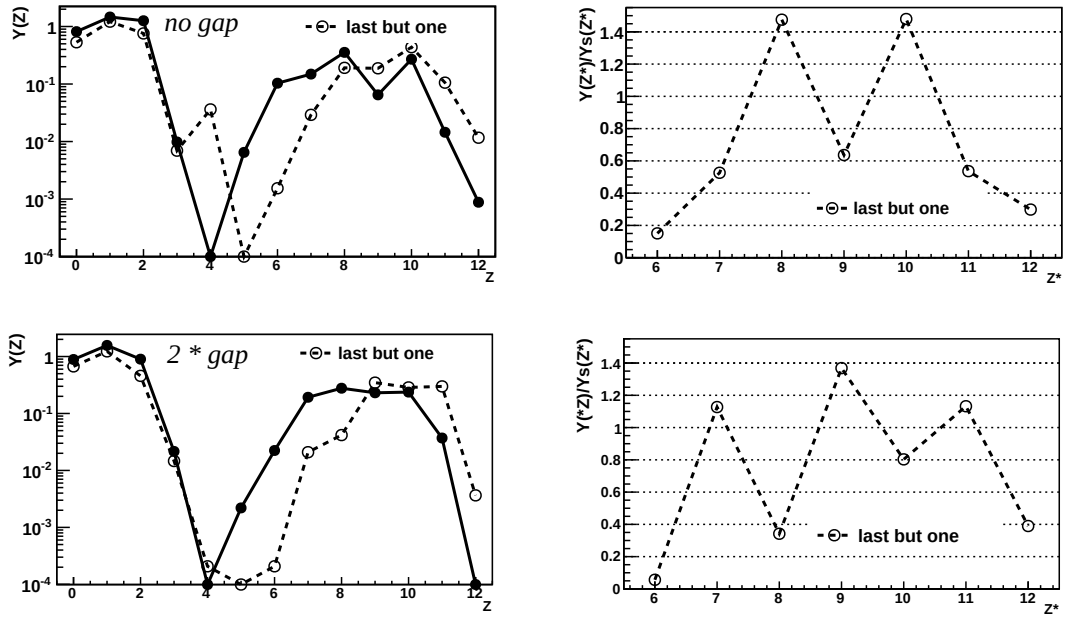

Figure 3.17: Charge distribution of cold products (full dots connected by a continuous line) and at the last but one step of the decay chain (empty dots and dashed line), together with the ratio $Y(Z^*)/Y_s(Z)$, for the evaporation of ^{24}Mg under experimental conditions, with $E_{cl} = (3 \cdot A)\ MeV$ and with a modified pairing backshift. Upper panel: E_2 suppressed; lower panel: E_2 increased by a factor of two. Normalization of charge distributions is to the total number of simulated events.

relative kinetic energy distribution of fragment pairs directly into a scale of excitation energy for the decaying parent nucleus from which they were originated, by adding the Q-value for the decay of the parent nucleus.

The $Y_{corr}(\epsilon_{rel})$ quantity plotted in fig.(3.18) is the numerator of the correlation function in relative kinetic energy, which was already introduced in chapter **1** according to the definition:

$$1 + R(\epsilon_{rel}) = \frac{\sum_{\epsilon_{rel}} Y_{corr}(\epsilon_{rel})}{\sum_{\epsilon_{rel}} Y_{uncorr}(\epsilon_{rel})} \tag{3.38}$$

where $Y_{uncorr}(\epsilon_{rel})$ is the uncorrelated background calculated by the event mixing technique and normalization is set such that the same number of pairs enter both the numerator and the denominator. Correlation functions are also shown in fig.(3.18) for the same isotope pairs, where the horizontal scale corresponds to the excitation energy of the decaying nucleus.
In fig.(3.19), we also show the output of the code concerning the global population

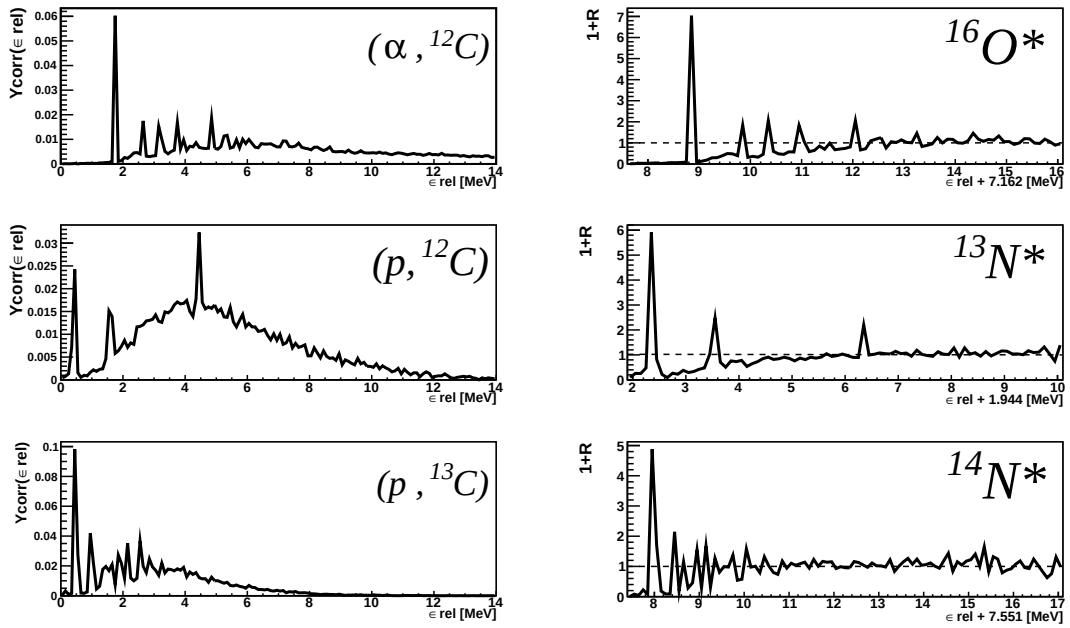

Figure 3.18: For the decay of ^{24}Mg, under experimental conditions and with $E_{cl} = (3 \cdot A)\ MeV$: on the left, relative kinetic energy distribution for $(\alpha,^{12}C)$,$(p,^{12}C)$ and $(p,^{13}C)$ isotope pairs. Normalization is to the total number of coincident pairs . On the right, corresponding correlation functions, given as a function of the Q-value shifted relative kinetic energy, such that the horizontal axis corresponds to the excitation energy of the parent nucleus.

of discrete states of three chosen N isotopes along the whole decay chain for ^{24}Mg under experimental conditions, which is of course not fully experimentally accessible. The population of the ground states and bound excited states of these isotopes give an information on their production as evaporation residues, since γ emission from bound states does not modify the isotopic yield. As already mentioned, the population of discrete states above particle emission thresholds, which is indicated in the figures by a red dashed line, can be reconstructed at the last but one step of the decay chain by measuring correlation functions between decay products. Both these experimental information can finally be compared to the code predictions: if the reproduction of the yield of cold residues and of the population of discrete states at the last but one step of the chain is achieved, then the calculated population probability is strongly constrained along the whole decay chain, and we may use it to extract information as average temperatures.

Other interesting observables which can be calculated concern the α particle production. In the calculations for our ^{24}Mg source we have to deal with an $N = Z$

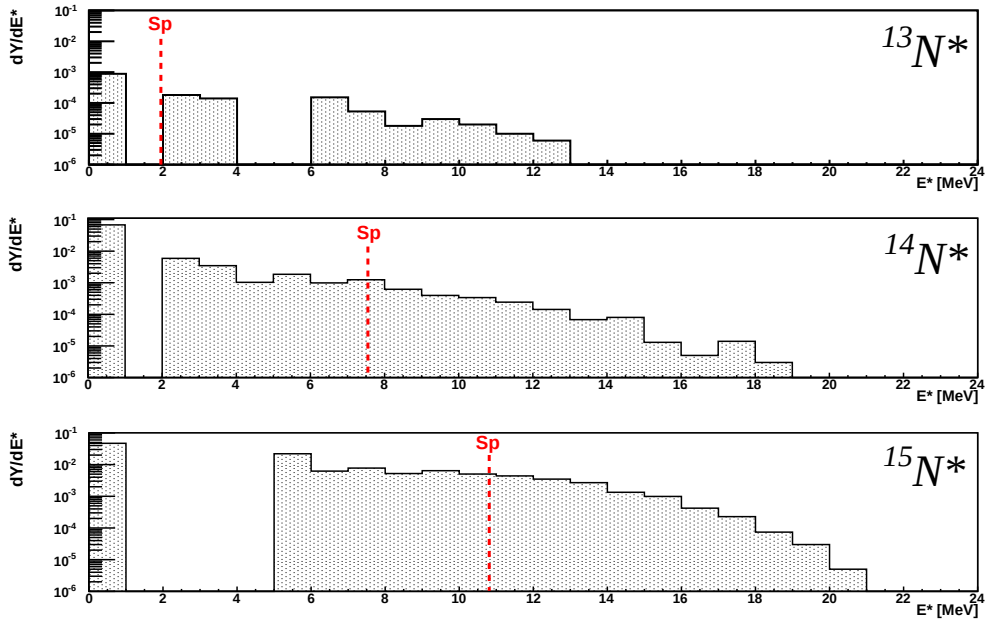

Figure 3.19: Global population dY/dE^* of discrete states for three chosen N isotopes, ^{13}N,$^{14}N$and ^{15}N, as predicted by the code along the whole decay chain for ^{24}Mg under experimental conditions and with $E_{cl} = (8 \cdot A)\ MeV$. The red dashed lines indicate particle thresholds. Normalization is to the total number of simulated events.

even-even system, for which the energy balance of Q-values tends to favour the emission of α particles. It turns out that a non negligible percentage of events in which the CN undergoes a complete (sequential) disintegration into α particles by sequential emission is predicted by the Monte Carlo. The α-particle multiplicity per event for the decay of the CN under experimental conditions is characterized by the probability distribution which was already shown in fig.(5.3), where a peak corresponding to $n_\alpha = 6$ is observed. An event with the maximum n_α multiplicity is an α decay chain, proceeding through a series of $N = Z$ even nuclei. We may be interested in checking which is the dependence of this observable on the input energy for the CN and on parameters of the calculation as the LD parameter. To this aim, in the upper right panel of fig.(3.20) we show again, as a reference, the multiplicity distribution for the decay of the experimental source with the two choices of E_{cl}. In the upper left panel of the figure, we show the same observable calculated for the decay of ^{24}Mg at $e^* = 3.$ and 3.5 $A.MeV$, other parameters being equal to the standard experimental case, with $E_{cl} = (8 \cdot A)\ MeV$. What we can see by varying the CN excitation energy is that the shape of the α-particle multiplicity distribution

changes, and in particular the peak, formerly at $n_\alpha = 6$ for the $e^* = 2.6\ A.MeV$ case, seems to be moved towards lower multiplicities for the highest initial energy calculation. This can be put in correlation to the probability of the 1^{st}-chance α particle emission, which is reduced with increasing the E^* for the CN. If high energy proton or neutron emission in the first steps of the decay is such that an even daughter nucleus with $N = Z$, but with a lowered excitation energy, is produced, then a new α decay chain can start, and this justifies the observed shift of the peak to lower values of n_α for higher initial CN energies.
An α-decay chain starting from ^{24}Mg necessarily proceeds through an excited ^{12}C. We may therefore be interested in the population of carbon discrete levels in such a decay chain, with a particular attention to the population of the so-called Hoyle state, *i.e.* the first excited state 0^+ at 7.654 MeV of ^{12}C, whose peculiarity has been already discussed in chapter **1**. It is known in the literature that this state has a non negligible branching ratio (experimentally upper limited to 4%) for its simultaneous decay into three α-particles. Such a decay-channel can be identified for instance by means of a three-body correlation function, as it is done in [43]. In our Hauser-Feshbach calculations, simultaneous decay channels are not implemented, and the decay of the Hoyle state (when populated) proceeds through the unstable ^8Be ground state, which successively decays in two α particles. The 3α-correlation functions, calculated for the decay of ^{24}Mg under experimental conditions for both choices of E_{cl} in the level density model, are shown in the lower panel of in fig.(3.20). Only a slightly different intensity for the peak corresponding to the Hoyle state is observed for the two cases, implying that this observable is virtually insensitive to the level density. As discussed in chapter **1**, comparing the prediction of the code for observables concerning the production of α particles to experimental data could enlighten the presence of a non-statistical behaviour in the decay, and allow us to distinguish the cases of a high α final multiplicity due to the energetically favoured nature of α-decay chain or, rather, to the presence of α-clustering in nuclear structure at finite temperature.

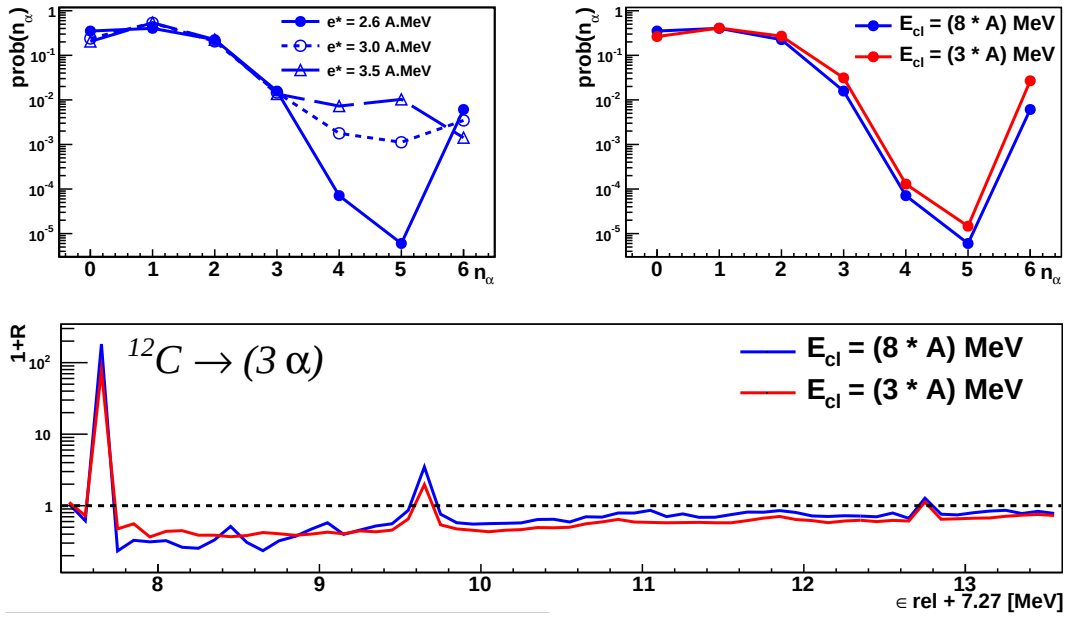

Figure 3.20: Observables related to α particle production for the decay of ^{24}Mg: upper panel, on the left: α multiplicity distributions for three different input energies for the CN, namely $e^* = 2.6$ (full dots connected by a continuous line), 3 (empty dots and dashed line) and 3.5 $A.MeV$ (triangles and dashed line); on the right: dependence of the same observable for the decay of the experimental source on the E_{cl} model parameter value. Normalization is to the total number of simulated events. Lower panel: E_{cl} - dependence of the (3α) correlation function (*i.e.* of discrete states population at the last but one step) in the decay of ^{24}Mg under experimental conditions. The usual color scheme is adopted: calculations for $E_{cl} = (8 \cdot A)\ MeV$ and $E_{cl} = (3 \cdot A)\ MeV$ are respectively given by blue and red lines.

Chapter 4

The Experiment

Calculations performed with the newly developed Hauser-Feshbach decay code presented in chapter **3** have been at the basis of a beam-time request submitted to the PAC - Physical Advisory Committee - of *Laboratori Nazionali di Legnaro* - LNL - INFN, where the NUCL-EX collaboration has currently in charge the experimental set-up made by the coupling of GARFIELD - General ARray for Fragment Identification and for Emitted Light particles in Dissipative collisions - and the Ring-Counter (RCo). Making use of this set-up, we have measured the reaction $^{12}C + ^{12}C$ at 95 MeV beam energy, provided by the LNL Tandem XTU accelerator.
In the first part of this chapter the experimental set-up (section 4.1) and the general features of the experimental measurement (section 4.2) are described. A second part is devoted to the discussion of data reduction (section 4.3), *i.e.* of the necessary steps to go from "raw" experimental data to a series of "physical" events: these steps notably include particle identification and energy calibration. The "physics" events obtained after this preliminary phase finally constitute the data-set used for the analysis. In the data-set used for the analysis presented in this work, all reaction products have been identified, but only particles detected by GARFIELD are calibrated in energy. Energy calibration of particles and fragments detected in the RCo is currently still under progress.
Depending on the physics issues we want to investigate, a sorting of events according to the reaction mechanism is then necessary. In the case of this work, we select the fusion-evaporation channel, in order to compare Hauser-Feshbach calculations to experimental data. How this can be done at present, given the incomplete status of energy calibration, is discussed in section 4.4. Before being able to perform a detailed comparison between data and code predictions, the filtering of code calculations through a softare replica of the experimental set-up is necessary: in section

4.5 we discuss how the information given at the beginning of the chapter on the experimental set-up are implemented in a software filter, in order to check if the detection modifies and eventually distorts the predictions of the statistical decay code.

4.1 The Experimental Set-Up

The RCo coupled to GARFIELD set-up, now fully equipped with digital electronics [79, 80, 81, 82], is installed at LNL - INFN. It is lodged in the III experimental hall of LNL, in a scattering chamber in which vacuum conditions of the order of $1 \div 2\ 10^{-6}\ mbar$ can be reached, when gaseous detectors are used. This set-up allows a nearly-4π coverage of the solid angle. The GARFIELD + RCo apparatuses have the capability to measure the charge, the energy and the emission angles of nearly all the charged reaction products, allowing an excellent discrimination of different reaction mechanisms. They also provide information on the mass of the emitted charged products in a wide range of particle energy and type.

4.1.1 The GARFIELD Apparatus

The GARFIELD apparatus [83] consists in two drift chambers, having cylindrical symmetry, which are placed back to back, covering approximately the angular range $30° \leq \theta \leq 150°$ with respect to the beam direction. Depending on the needs of the measurement, they can also be used separately, leaving place for alternative detectors at forward or backward angles. The forward chamber covers almost completely the azimuthal angle, whereas the second one has a side opening of $\Delta\varphi \simeq 45°$ to allow for the allocation of specialized telescopes or different ancillary detectors. The chambers are filled with CF_4, at a pressure which can be varied in the range $20 \div 80\ mbar$. Standard working conditions are a pressure of $\sim 50\ mbar$ in the forward chamber, and a lower pressure of $\sim 20 \div 30\ mbar$ in the backward one, where reaction products are less energetic. The forward and backward chambers are divided respectively in 24 and 21 azimuthal sectors. A picture of the GARFIELD forward chamber is shown in fig.(4.1).

In each sector four microstrip pads [84] and four $CsI(Tl)$ are present. The GARFIELD apparatus is based mainly on the well-known $\Delta E - E$ technique, which is described in some details in the following. The ΔE signal given by the the *micro*Strip Gas Chamber (μSGC) is the result of the collection and amplification of

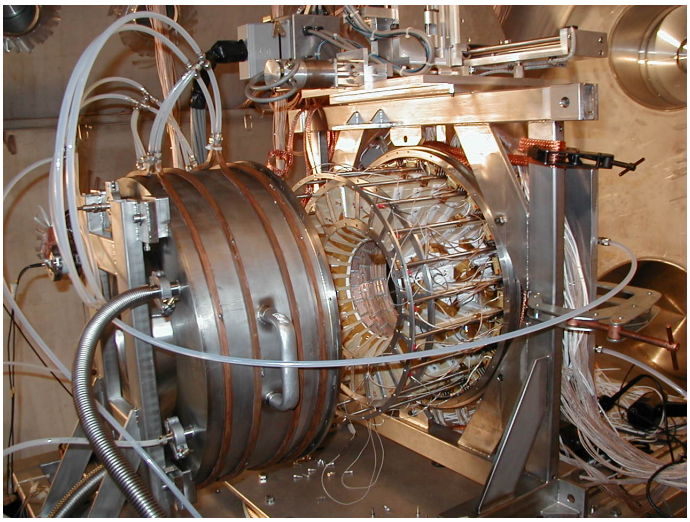

Figure 4.1: Picture of the forward chamber of the GARFIELD detector.

free generated charges along the primary ionization tracks of the impinging particles. Also the information on the polar angle of detection is carried by this signal, and can be deduced through the measurement of the drift time of the electrons. The residual energy E is then obtained from the signals of $CsI(Tl)$ crystals, with photodiode readout, which are located in the same gas volume in a radial configuration with respect to the target. This is shown in the schematic view of fig.(4.2).

Preamplifiers [85] are mounted inside the gas chamber, just behind the CsI crystals. A system has been designed to cool the gas, which allows for the dispersion of the heat generated by the preamplifiers themselves. As a major improvement with respect to the first version of the GARFIELD chambers, the analog electronics has been substituted by a fully digitized treatment of the signal, which has been custom developed by the Florence group [80, 81, 82]. More details on the digital electronics are given in the following.
As general comments on the operating principles of the GARFIELD apparatus, we notice that the use of a gas detectors is fundamental to lower as much as possible the detection thresholds (up to 0.5 $A.MeV$ in this case, depending on the chosen pressure value), while the presence of four microstrip pads and four CsI in each azimuthal sector ensures a sufficiently high number of independent telescopes (a total amount of 360 pseudo-telescopes for the two GARFIELD chambers), in order to minimize the percentage of double hits.

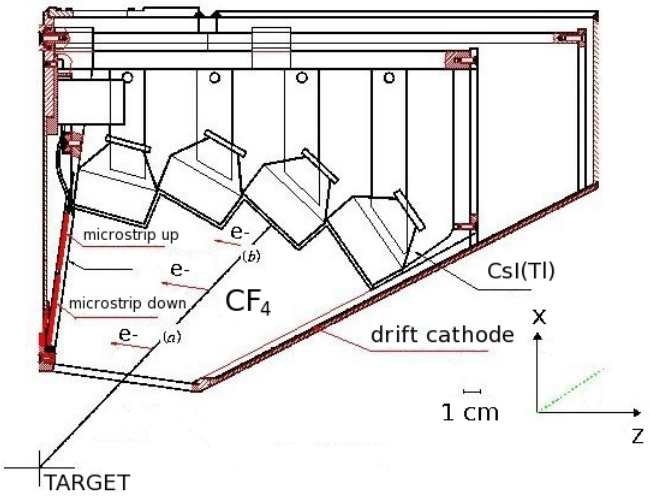

Figure 4.2: Schematic view of one sector of the GARFIELD drift chamber. Reaction products start their flight path from the target. The electrons produced along the path fly towards the two sections of microstrip electrodes allowing the measurement of the energy loss and the drift time.

In particular, in the measurement presented in this work, due to the light nature of the system under study, we have not made use of the information coming from the μSGC up to now, since only light charged particles are produced and detected at the solid angles covered by GARFIELD, with a low average expected multiplicity per event. CsI alone can allow for a good detection and identification of all reaction products in this case. This is possible thanks to the identification of detected particles through the analysis of the so-called $fast$ - $slow$ correlations, which is discussed in the following. Therefore, for the GARFIELD apparatus, in the rest of this chapter we limit ourselves to the description of the CsI detectors and on the analysis of their signals.
As previously mentioned, the residual energy is measured by CsI(Tl) crystals, with resolution (from laboratory tests) close to 3% FWHM for 5.5 MeV α particles from ^{241}Am source. The thickness of the crystals has been chosen in order to stop all the charged products of the reaction, after they have lost part of their energy in the CF_4 gas, in the energy regime of the Tandem-ALPI complex at LNL. The shape of the crystals has been designed in order to optimize the geometrical efficiency, such that the center of the front face of the crystal is always perpendicular to the radial trajectory of the particle emitted from the target. Each of the 180 CsI crystals (96 and 84 in the two chambers, respectively) covers 15° in θ and φ. The doping of the CsI has been chosen in the range of 1200 ppm. The shape of the backward part

of the crystal is like a light guide to optimize the coupling with the photodiode, and a special wrapping of the CsI has been done, aimed at maximizing the light collection [86].

4.1.2 The Ring-Counter

The Ring Counter (RCo) is an annular detector, designed to be centered at 0° with respect to the beam direction. A detailed description of the first version of the RCo is given in ref.[87]. Here we recall the main features of this detector, and we describe the improvements recently done. The detector consists in an array of three-stage telescopes with a truncated cone shape. The first stage is an ionization chamber (IC), filled with CF_4, the second a strip silicon detector (Si) and the last stage a $CsI(Tl)$ scintillator. The apparatus is divided in eight azimuthal sectors. Each sector of the IC has a unique gas volume, perfectly matching one of the eight Si-pads placed behind. Each silicon detector, pie shaped, is segmented into eight independent annular strips. Behind each silicon detector, instead of the two crystals used in the former version, six smaller size $CsI(Tl)$ crystals, 4.0 cm thick, read out by photodiodes, have been placed (for a total number of 48 scintillators), in order to increase the global granularity of the detector. The geometrical shapes of the CsI crystals have been designed to cover the cone subtended by the IC. A picture of the new RCo is given in fig.(4.3).

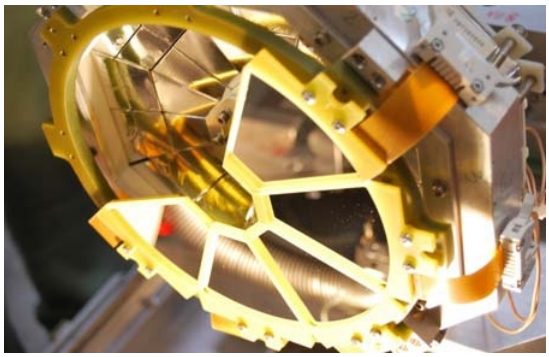

Figure 4.3: Picture of the new RCo detector. The IC and three Si detectors are removed, showing the six $CsI(Tl)$ crystals for each azimuthal sector.

The RCO is designed to operate in high vacuum, with minimal outgassing, and it is mounted on a sliding plate that allows to move it forward and backward by means of a remote control. When the RCo is in the operating position, it is inserted in the conical opening of the forward GARFIELD drift chamber. Also a collimator

system has been designed and built-up, able to interchange different screens in front of the RCo, for protection during beam focalization or collimation, or for calibration purposes. Preamplifiers are mounted inside the scattering chamber, shielded in metallic boxes which are cooled by a water cooling system. As mentioned, the whole detector is now equipped with digital electronics.
Going into more details for each detection stage, the CF_4 gas filling the IC is continuously flowing in the chamber, and typical working conditions are a pressure of 50 $mbar$ and a temperature of 20°C. Under these conditions, the resolution of the IC signal results reasonably good, with a FWHM of the order of 7% for the energy loss of a ^{32}S beam at 550 MeV scattered on Au target, taking into account that a large straggling is present.
With respect to the first version of the RCo the silicon detectors[1] are now of nTD type and are reverse-mounted: taking advantage of the experience of the $R\&D$ phase of the FAZIA project [88], this allows for the application of the pulse shape analysis technique to the Si signals, which is later discussed. As anticipated, each detector covers one sector of the IC, and its front surface (junction side) is segmented into eight strips. The polar angle intervals covered by each strip, when the RCo is in the measuring position at 270 mm from the target (corresponding to the minimal distance allowed by the mechanical structure of the GARFIELD chamber), are reported in Table 4.1. The angular resolution of each strip is $\Delta\theta \sim 1°$. Properly biased guard rings are inserted in the inactive interstrip regions, thus minimizing any field distortion and at the same time reducing the charge split and the cross-talk between contiguous strips. The thickness of the silicon detectors is around 300 μm, as stated by the manufacturer. Therefore the energy thresholds for particles punching through the detectors are of about 6 $A.MeV$ for protons and α-particles and 7-11 $A.MeV$ for light fragments. A resolution of the order of 0.3% for the Si signals has been obtained from laboratory tests, showing the very good quality of silicon detectors. This has been confirmed by measuring elastic scattering on Au targets, both for a ^{32}S beam at 550 MeV, and for the ^{12}C beam at 95 MeV for the reaction under study.

Finally, as mentioned, the actual geometry of the last detection stage of the RCo consists of six CsI crystals for each sector. As in the case of GARFIELD CsI, the resolution obtained with α particles sources for these detectors results of the order of 3%.

[1] Purchased from Canberra. The detectors have been cut along the <111> plane and the are tested to have a very good resistivity uniformity, together with showing a negligible channeling effect.

Strip	R_{int} (mm)	R_{ext} (mm)	θ_{min} $(deg.)$	θ_{max} $(deg.)$
8	26.185	35.050	5.362	7.160
7	35.200	42.175	7.191	8.596
6	42.325	49.300	8.626	10.021
5	49.450	56.425	10.051	11.433
4	56.575	63.550	11.463	12.832
3	63.700	70.675	12.861	14.215
2	70.825	77.800	14.244	15.581
1	77.950	85.035	15.610	16.950

Table 4.1: Internal and external radii and polar angle intervals of RCo silicon strips, when the RCo is in the measuring position at 270 mm from the target.

4.1.3 Digital Electronics

For a complete description of the fully digitized treatment of GARFIELD and RCo signals developed by the Florence group we remand to ref. [80, 81, 82]. Here we want only to recall the main features of this treatment, giving only the details which can be of help for the understanding of the detector operating principles.
As mentioned, signals are coming from the preamplifiers, and they are then directly fed into a specially designed VME module, which can perform different operations. In the analog input stage there is a programmable - gain amplifier followed by the digitizing section (ADC). The data are temporary stored in a First-In-First-Out (FIFO) memory and processed by a Digital Signal Processor (DSP). The digitizing section consists in a 12-*bit* ADC operating at 125 $MSamples/s$ [81]. The ADC output values are continuously written in the FIFO memory which stores up to 8192 samples, corresponding to $\sim 65\mu s$ samples. A good estimate of the signal baseline is mandatory [80, 81] and therefore a suitable portion of the baseline preceding the signal is sampled and collected. The sampled signals are continuously written (circular buffer) while the channel is waiting for a trigger, and when the trigger signal is received, it enables the FIFO memory to be filled up; therefore in the complete sampled events both the baseline and the signal are included. The DSP reads sampled data and stores them in its internal data memory. For each experiment the acquisition system loads once the DSP computing program in DSP internal memory; for each sampled waveform validated by a trigger, the DSP program makes the pulse analysis and outputs the requested data. For instance the program reproduces

the behavior of the standard analog semi - Gaussian shaper, previously employed for the GARFIELD apparatus for all the signals. This requirement was called for in order to simplify and speed up the calibration of the data collected with digitizing electronics, substituting the analog shapers. To get more information various other algorithms have been implemented, such for instance the calculations previously performed by the analog hardware or off-line including constant fraction timing, gated integration, amplitude and rise time estimation [82].

4.2 The Measurement

The reaction $^{12}C+^{12}C$, exploiting the ^{12}C beam at 95 MeV provided by the LNL Tandem XTU accelerator has been measured using the GARFIELD + RCo set-up described in this chapter. Data taking lasted approximately 70 hours with a beam of intensity ≈ 0.05 pnA on a ^{12}C target 200 $\mu g/cm^2$ thick. The beam time structure was pulsed, with a repetition period of 400 ns, and with each ion burst having approximately a gaussian distribution with a FWHM of $\sim$2 ns. The beam arriving on the target is synchronized with the ion accelerating electric field radiofrequency (RF). The RF signal can be therefore used as reference for time measurement.
We also measured the reaction $^{12}C +^{179} Au$, under the same beam conditions, in order to have a reference point for the energy calibration of the detectors given by the elastically scattered ^{12}C ions.
With beam on gold target we were able to check periodically the time structure of the beam, as we will later describe, while an additional target of AlO_2 was present in the target holder, allowing for the initial beam focalization.

4.2.1 The Trigger Configuration

The choice of the logic of the trigger is always based on the selection of the reaction mechanism of interest. In the case of this experiment, the main reaction channel to be selected was fusion-evaporation. Moreover, for the physics motivations discussed in chapter **1**, we were especially interested in achieving a high exclusive measurement and a quasi-complete event reconstruction in case of complete fusion, detecting therefore a high percentage of the total charge available in the entrance channel of the reaction ($Z_{tot} = Z_{proj} + Z_{targ}$). Because of the light nature of the system under study, even a stringent condition on the detection of the total charge (as high as $Z_{det} \approx 80\% Z_{tot}$) can be fulfilled by measuring only a sufficiently heavy

evaporation residue, which, taking the largest part of the boost provided by the beam, flies at forward angles and is detected in the RCo. Therefore, we have decided to adopt as main trigger the OR of trigger signals coming separately from GARFIELD and from the RCO, given that the coincidences can be recovered in the offline analysis. In particular,the trigger signal coming from GARFIELD is the logic OR of all $CsI(Tl)$ signals, while the so called OR-RCO is the logic OR of all signals from Si strips. Additional trigger signals were coming from the pulser, which is used to make routinely control runs to check the stability of the electronics during the measurement, and especially to be able to compare the results obtained from experiments performed in different periods and under different conditions.
The last trigger was coming from a collimated plastic scintillator positioned at $\theta = 2^\circ$, under the grazing angle for the measured reaction ($\theta_{gr} \approx 4^\circ$). The adopted trigger system has been developed by the Florence group, and is described in details in [93].

4.2.2 Settings and Online Checks

The good timing resolution of the plastic scintillator positioned at $\theta = 2^\circ$ is used to control the timing properties of the pulsed beam. The time of flight spectrum is constructed using the difference between the time signal of the scintillator, related to the elastically scattered beam, and the time reference RF signal of the pulsed beam. This is done with beam impinging on a gold target, to maximize the elastic scattering cross section.
Online controls on currently acquired data can be easily done thanks to the graphical interface called GARFIELD Monitor [89]. The monitor program allows to visualize an arbitrary number of pre-defined 1- and 2-dimensional histograms, filled either with raw experimental data or with preprocessed variables (simple combinations of two or more experimental parameters, linear calibrations). In particular, online checks are devoted at the beginning of the measurement to the setting of pedestals and software thresholds. The monitor program can compute all pedestals for ADC/QDC modules on-demand, and the results can be further manually adjusted using the graphical interface. Finally the pedestals are loaded by the acquisition system.
The acquisition dead-time, due to the large number of acquired parameters and to the complexity of the data acquisition system, was kept under control by carefully setting pedestals and thresholds and monitoring the beam intensity and focalization, to keep under control the trigger rate. An average dead time of $\sim 30\%$ was regis-

tered during the measurement. Finally, during all the measurement, the gas pressure stability in the GARFIELD drift chambers and in the RCo ionization chamber was checked, together with the stability of all detectors voltages. Chosen pressure values were $p = 20$ and $p = 48$ $mbar$ respectively for the GARFIELD backward and forward chambers, and $p = 50$ $mbar$ for the RCo IC.

4.3 Data Reconstruction

A "raw"event is a list of acquisition data parameters characterized by the same event number. The event reconstruction consists in the analysis of the acquired parameters in order to reconstruct physical particles, thus attributing to the event a multiplicity of detected particles, each characterized by its charge, mass (when possible), direction of flight (*i.e.*, the geometrical position of the hit detector), and finally its energy loss and/or residual energy, to be further used to recover the information on the incident energy.

4.3.1 Identification Methods

In our GARFIELD+RCo set-up, particles can be identified through various techniques, which we detail in the following.

$\Delta E - E$ correlations

For particles impinging on GARFIELD, the $\Delta E - E$ correlation between the energy loss in the μSGC and the residual energy in $CsI(Tl)$ can be used, which provides charge identification up to $Z \sim 23$, with a threshold of the order of 0.8 $A.MeV$. The principle at the basis of the $\Delta E - E$ identification technique is well known: in the non relativistic limit, the Bethe expression for the energy loss of a charged particle in an absorber of given density is a function of the particle charge, mass and incident energy [90]. Under the assumption that the dependence of the energy loss on the ratio E/A, *i.e.* on the incident energy per nucleon of the impinging particle, is a power law with the exponent left as a free parameter, the Bethe expression can be worked out analytically [91], and a relation between the energy loss in the thickness of the first layer of detection and the energy deposited in the second layer can be obtained. Such a relation is usually called a particle identification function (pif). However, it is experimentally well known that it is quite difficult, by managing one only parameter (the exponent of the power law dependence) to find a unique pif able to linearize the $\Delta E - E$ correlation of each used telescope, in the whole

range of residual energies and for a wide range of charges. Therefore, the addition of other free parameters to take into account possible deviations (due to low residual energies, high charge of the fragments, various instrumental effects, *etc.*) has been described in [91], and the proposed phenomenological correlation for $\Delta E - E$ signals has been adopted and implemented in an event by event identification in ref.[92]. This identification technique allows for a fit of the experimental $\Delta E - E$ correlations for each charge, and, if the ΔE energy resolution is sufficiently good, also for each mass. Results for the fit parameters (seven for each detector in ref.[92]) depend therefore on the considered detector.
As anticipated, in the measurement presented in this work, this kind of correlation does not add substantial information to what can be reconstructed by analyzing the signals coming from GARFIELD $CsI(Tl)$ alone.
On the contrary, the possibility to build such correlations for signals coming from the RCo has been essential in this analysis: for the RCo there are two possible $\Delta E - E$ matrices to be built. For particles stopped in the silicon detectors we can make use of the correlation between the signals coming from the IC (ΔE) and the ones from Si strips, proportional to the residual energy. This allows only for charge identification, up to $Z \sim 24$, with a threshold of the order of 0.7 $A.MeV$ under standard gas pressure conditions. In the specific case of this measurement, as it will be later discussed, this information allows us to select the reaction mechanisms, by gating on detected evaporation residues, which, at this beam energy, are stopped in the $300\mu m$ of Si. For particles punching through the silicon detectors, a $\Delta E - E$ matrix is built with signals from Si strips, as proportional to an energy loss, and signals from $CsI(Tl)$ as a measure of the residual energy. In this latter case, also the isotopic identification of detected particles can be achieved. In this measurement, only light particles up to $Z \sim 2$ were sufficiently energetic to punch through the silicon detectors and to reach the $CsI(Tl)$. $\Delta E - E$ matrices for signals registered by the RCo are shown in fig.(4.4) and (4.5). An offset of 500 channels has been always added to the signals, for a better presentation of all figures.

Fast vs. slow correlations for CsI detectors

For GARFIELD (and for particles punching through the $300\mu m$ of RCo silicon detectors) particles identification can be achieved through a pulse shape analysis technique, namely exploiting the correlation between the so-called *fast* and *slow* components of $CsI(Tl)$ signals. $CsI(Tl)$ scintillators are known to have a light output signal whose shape varies as a function of the type of incident radiation.

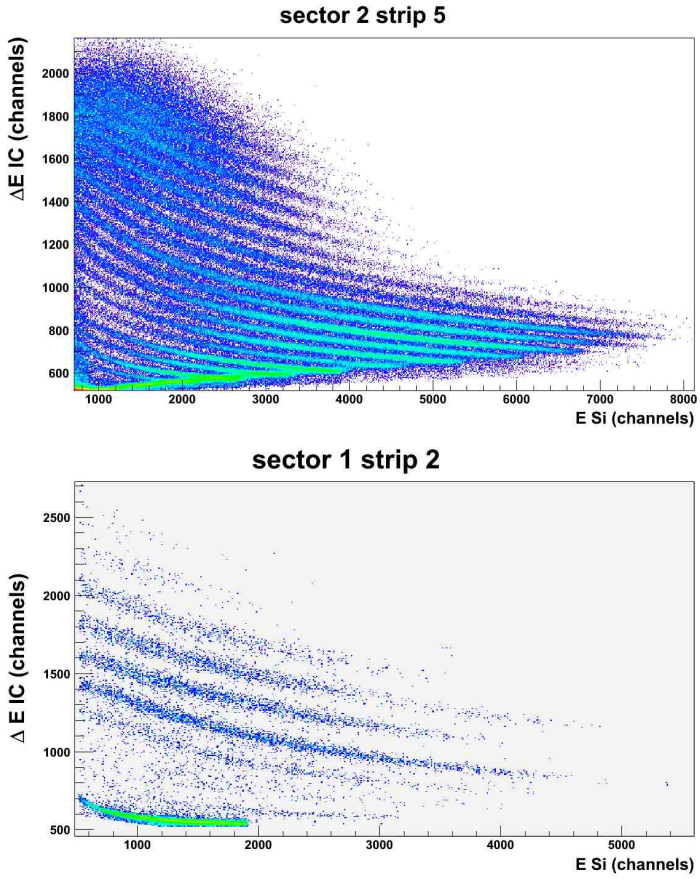

Figure 4.4: Typical $\Delta E - E$ IC vs. *Si* matrices for particles detected in the RCo. Telescope numbers are given in the figure. Data are from: the $^{32}S + ^{48}Ca$ reaction at 17.5 $A.MeV$ in the upper panel; the $^{12}C + ^{12}C$ reaction under study in the lower one.

Indeed, two kinds of physical processes allows the light production in a $CsI(Tl)$ crystal, each with a different time decay constant, and this results in the two different light components [90]. The DSP is able to filter the pre-amplified $CsI(Tl)$ signal with two different time constants, thus trying to disentangle these two components: the short-gate integration of the signal yields the *fast* quantity, which is related to the short component of the light emission, while the overall integration give the so-called *long*. The correlation between *fast* and *long* is used to build an identification scatter plot, while the *long* quantity, being basically proportional to the total light output, is used for energy calibration purposes. In particular, the identification scatter plot shows a better isotopic separation when correlating new quantities obtained from a linear mixing of *fast* and *long*, which partially removes the trivial linear

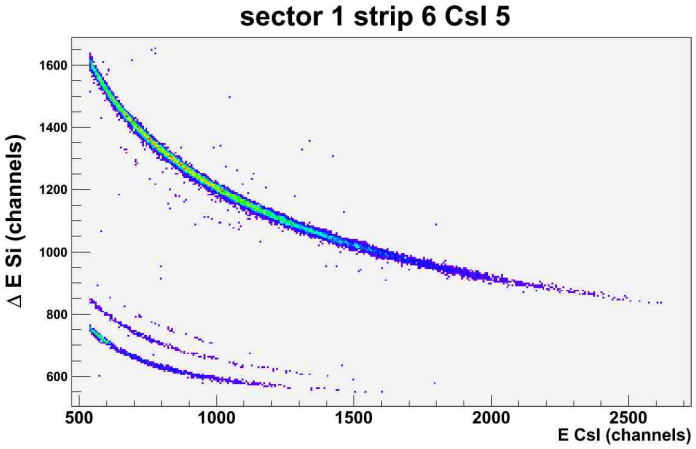

Figure 4.5: $\Delta E - E\ Si$ vs. $CsI(Tl)$ matrix for particles punching through the RCo Si detectors. The telescope number is given in the figure. Data are from the $^{12}C + ^{12}C$ reaction under study.

correlation between these two quantities, coming from the fact that part of the signal produced by the long-time fluorescence of the $CsI(Tl)$ is necessarily integrated within the *short* gate. In our case we choose to correlate *fast* to a re-computed $slow = 3.5(long - 4fast)$ as it is done in ref.[80, 94]. In fig.(4.6) $fast$ vs. $slow$ scatter plots for a chosen GARFIELD CsI are shown. Isotope ridges are clearly visible in the plots, and can be identified up to $Z = 3$. Signals associated to the detection of γ are characterized by a linear correlation of *fast* and *slow*, and can also be easily distinguished.

Energy - rise time correlations for Si detectors

An additional possibility of identifying the reaction products both in charge and mass consists in an application of a pulse shape technique to the signals coming from the Si detectors of the RCo. In this case, the exploited correlation is the one between the energy signal and the so called rise time, defined in our case as the time interval needed by the signal to go from 20% to 80% of its full amplitude. Scatter plots of this kind are shown in fig.(4.8) for chosen Si strips. As it can be seen from the figure, the charge identification is easily achieved for all charged products, with a threshold corresponding approximately to the energy needed by the fragment to pass through the first $\sim 30\ \mu m$ of the detector. This corresponds to a threshold of about 2.5 $A.MeV$. As can be also seen from the figure, we have recently shown the possibility of mass identification via pulse shape on Si signals for fragments with charge up to $Z = 14$. These encouraging results have motivated new efforts,

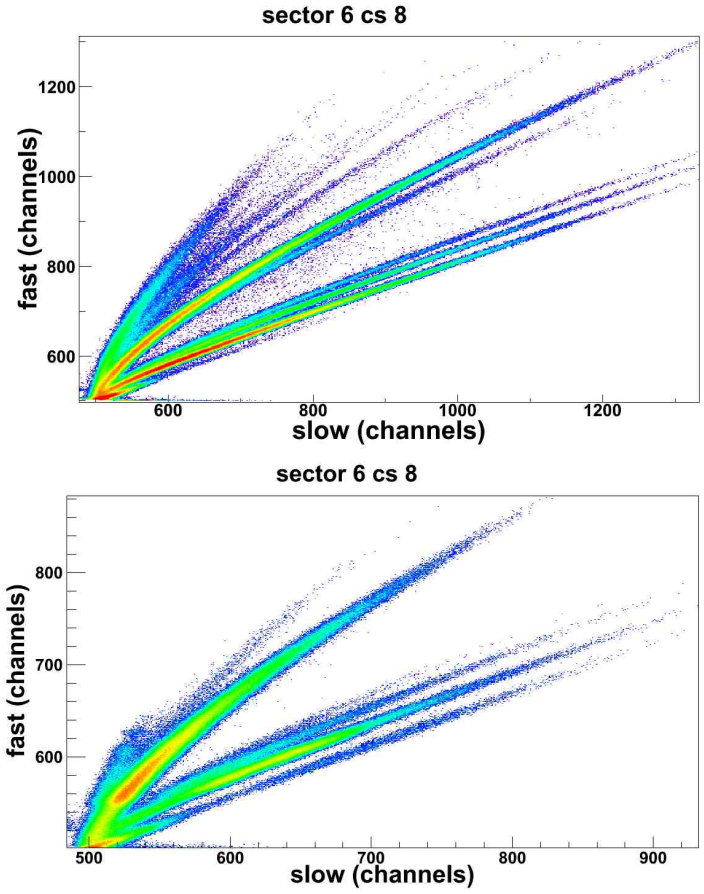

Figure 4.6: Typical *fast* vs. *slow* scatter plots for particles detected by GARFIELD $CsI(Tl)$ crystals in different measurements. For the same detector (CsI 8 sector 6), upper panel: light particles produced in the reaction $^{32}S + ^{48}Ca$ at 17.5 $A.MeV$; lower panel: data for the $^{12}C + ^{12}C$ reaction under study.

which are currently undertaken, in order to optimize the response of Si detectors and to enlarge as much as possible the range in which isotopic identification can be achieved.

4.3.2 Identification Procedures

Having discussed which are the correlations which can be built with signals registered by GARFIELD and by the RCo, we recall hereafter the scheme of the usually employed procedure to identify all reaction products in charge and, when possible, in mass.

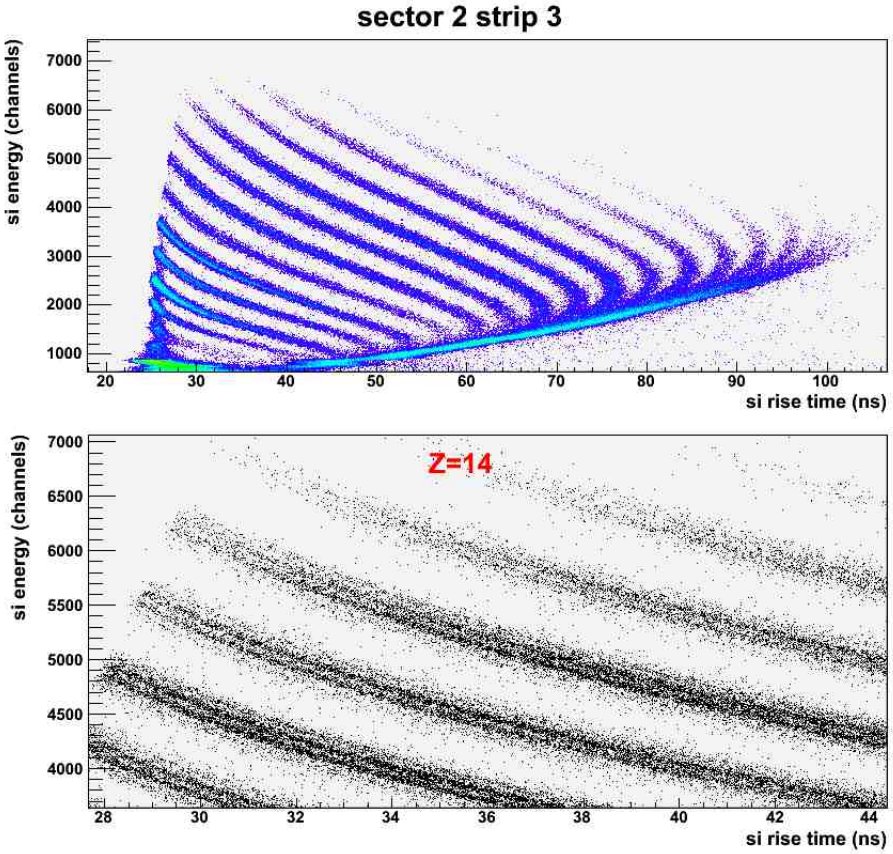

Figure 4.7: Upper panel: typical Si energy vs. rise time correlation for a chosen Si strip, indicated in the figure legend. In the lower panel, zoomed view on a region where mass identification has been achieved (up to $Z = 14$) by measuring the $^{32}S + ^{48}Ca$ reaction at 17.5 $A.MeV$;

General identification procedure

The identification procedure is described in the following in the most general case, valid for any of the signal correlations previously introduced. Different steps are necessary:

- in a bidimensional scatter plot several points are sampled by hand on the ridges of well defined isotopes. Some isotopes are easy to identify, either due to their abundance (^4He) or to their separation from other masses ($^{1,2,3}H$). Charge, mass and coordinates of the sampled points are organized in a table;
- the parameters characterizing the detector response to the charge Z and mass A are determined by fitting the coordinates of the previously sampled points

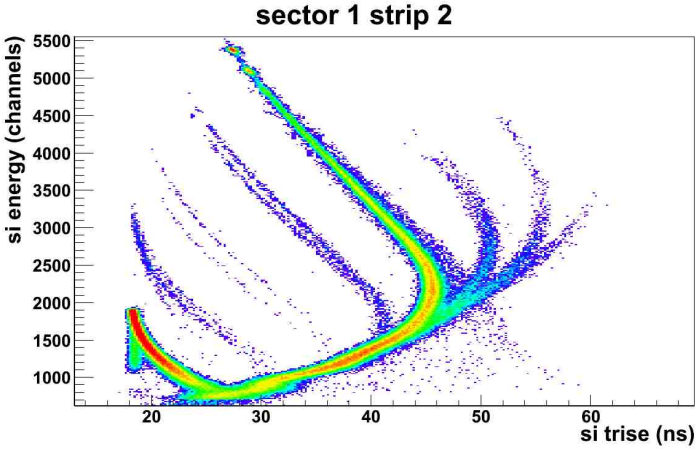

Figure 4.8: Si energy vs. rise time correlation for a chosen Si strip, indicated in the figure legend, with data for the $^{12}C + ^{12}C$ reaction under study. Besides the scattered ^{12}C ions, one can also see the contribution of different direct reactions proceeding through discrete states of the involved nuclei.

with the analytical (or semi-empirical function) describing the correlation between the two variables. Results for the fit parameters are stored in a table;

- an event by event identification is performed, by means a χ^2 minimization. In each event, each detected particle is identified by minimizing the squared distances of its coordinates in the scatter plot under study, with respect to the values provided by the analytic expression for the same correlation with parameters read from the map built in the previous step for each detector. In case of mass and charge identification, the procedure is usually repeated twice: in the first step the charge is attributed, under the assumption of a mass $A = 2Z$, and in the second step the minimization of the distance is done with respect to the mass coordinate.

Obviously, in the case of a large number of detectors/telescopes, the most time consuming step of the identification procedure is the first one, because of the necessity to sample a huge number of points on each isotope branch in order to obtain in the second step a reliable set of parameters. We underline at this point the importance of having analytical expressions for the correlations, which allow for extrapolation of the functional forms to isotopes which cannot be sampled because of the low statistics, as it can be the case for backward detectors.

Results for RCo $\Delta E - E$ matrices

For the data presented in this work, this procedure has been followed for the identification of particles detected in the RCo, for both possible $\Delta E - E$ correlations [92]. As mentioned, analytical particle identification functions are available in this case, which derive from the Bethe expression for the energy loss. Typical results for charge (from IC vs. Si matrices) and charge and mass (from Si vs. CsI matrices) distributions are shown in fig.(4.9) for the same telescopes of fig.(4.4) and (4.5). A similar procedure will be used for GARFIELD $\Delta E - E$ matrices.

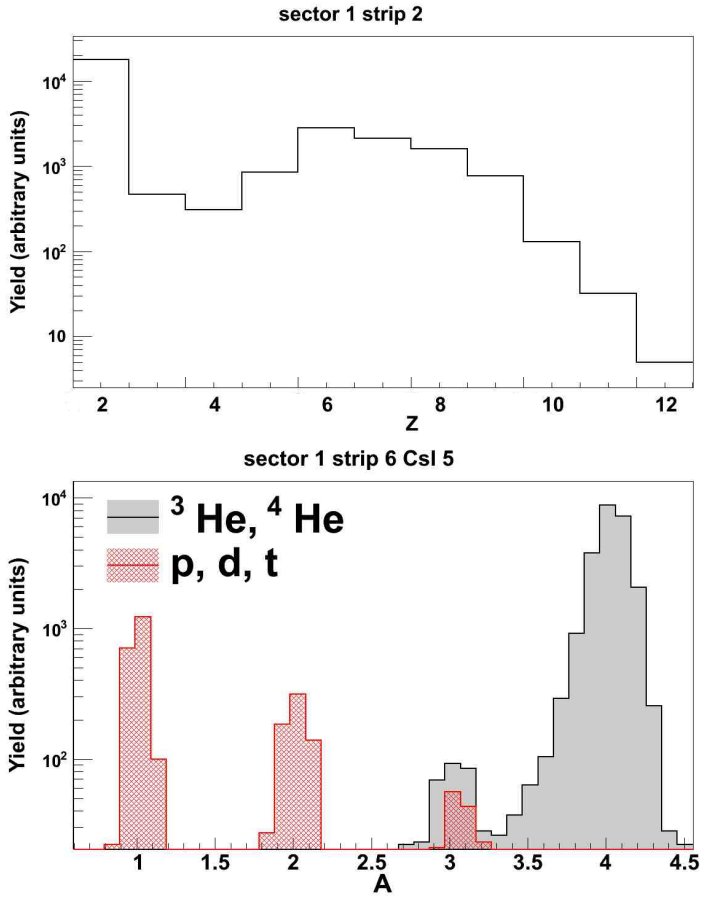

Figure 4.9: Results of the identification procedure on typical $\Delta E - E$ matrices for particles detected in the RCo in the reaction $^{12}C + ^{12}C$. In the top panel, charge distribution obtained from the IC vs. Si matrix shown in fig.(4.4); in the bottom panel, charge and mass distributions from the Si vs. CsI matrix of fig.(4.5).

Semi-automatic procedure and results for GARFIELD fast vs. slow correlations

In the case of $fast$ vs. $slow$ correlations for signals of GARFIELD (and RCo) CsI, we have taken advantage of the semi-automatic procedure described in details in ref. [94], where the analytical function which can be used as a particle identification function is reported.
The first big advantage of this procedure is a great reduction of the time dedicated to the manual sampling of points along the various isotope ridges. Indeed, this can be done in an automatic way within the ROOT environment [95]: ridges are seen as successive monodimensional gaussian distributions, close to each other, and peaks are searched firstly along the x-axis (the $slow$ variable is in abscissa), then along the y-axis ($fast$). Finally, a peak observed on the y-projection is validated only if a peak in the x-projection falls in the same cell of the bidimensional plot. This gives a series of coincident peaks, lying on isotope ridges, to which a label (A, Z) can be assigned. In order to connect with each other the peaks in a given (A, Z) series (called a cluster), we make use of a tracking method, which is essentially a local method of pattern recognition [96]. The propagation of the track starts from a seed (the leftmost point of each cluster), and is based on a local linear equation between each pair of points along the ridge and on a quality criterion, which allows to distinguish good track candidates from ghosts. When several points are possible candidates to propagate a trajectory, the method selects the point giving the minimum change of the angular coefficient of the straight line connecting the previous two points belonging to the ridge. The procedure is continued until the end of the tracking area has been reached, or no further suitable points can be found. The next important result presented in [94] is the analytical function proposed for the fit of the experimental $fast$-$slow$ correlations. The proposed function is based on the consideration that a power law relation can been employed [97] for the total light output of a crystal as a function of the energy. As mentioned, the *long* component of the CsI signal is proportional to the total light output, and the *fast* and *long* components are expected to be almost linearly correlated with each other. This results in a power-law behavior for both $fast$ and $slow$ as a function of the energy, and, consequently, in a power-law relationship between them. We can therefore write:

$$slow(fast, A, Z) = a_1 \; fast^{a_2} \quad with \quad a_1, a_2 \geq 0 \tag{4.1}$$

where an exponential behavior can be attributed to each of the coefficients a_1 and a_2:

$$\begin{aligned} a_1 &= [d_1 + d_2 \exp(-d_3 Z_{eff})] \exp(-d_4 Z_{eff}) \\ a_2 &= [d_5 - d_6 \exp(-d_7 Z_{eff})] \qquad\qquad (d_i \geq 0, i = 1, 7) \end{aligned}$$

In the proposed approach, the use of a dependence on the quantity $Zeff = (AZ^2)^{1/3}$ is the most effective way to take into account the charge and the mass of the analyzed isotope ridge.
The last step of the analysis is the event by event identification procedure, as described for the most general case. By using the table of fit parameters obtained for all CsI, for each detected particle an integer Z and real A value are determined by choosing the minimum distance of the experimental point $(slow, fast)$ from the curve $slow(fast, A, Z)$ of eq.(4.1) for all the possible (A, Z) values. Results for the application of this procedure to the identification of particles detected by GARFIELD in the experiment presented in this work are shown in fig.(4.10), where also the points determined and connected along different isotope ridges by the semi-automatic procedure are shown.

Pulse shape analysis on Si - signals.

As far as the energy - rise time matrices for signals from the RCo Si strips are concerned, we are currently developing an extension of the semi-automatic procedure described for the CsI *fast* vs. *slow* scatter plots. The additional information which can be obtained by performing the identification on these matrices is the mass of particles detected in the RCo and stopped in the Si detectors. At present, this information has not been extracted, as the information on the charge coming from the analysis of IC vs. Si matrices is sufficient to select the reaction channel, in a preliminary but safe way.

4.3.3 Energy Calibration

As anticipated in the introduction of this chapter, for the data-set which is analyzed in this work the energy calibration has not been completed for all the detectors of the experimental set-up.
In particular, at present, only light charged particles detected by GARFIELD CsI have been calibrated in energy. As described in the previous section, such particles are identified by the analysis of *fast* vs. *slow* correlations, where the quantity *slow* is obtained from the *long* component of the signal, proportional to the light output, which in turn depends on the released energy via a power law.
The energy calibration of these particles results therefore from the fit of the detector light output, provided that we have a sufficient number of points of known energy to constrain the free fit parameters [94]. Such points have been gathered over several years of experience of the collaboration working with $CsI(Tl)$ detectors, using

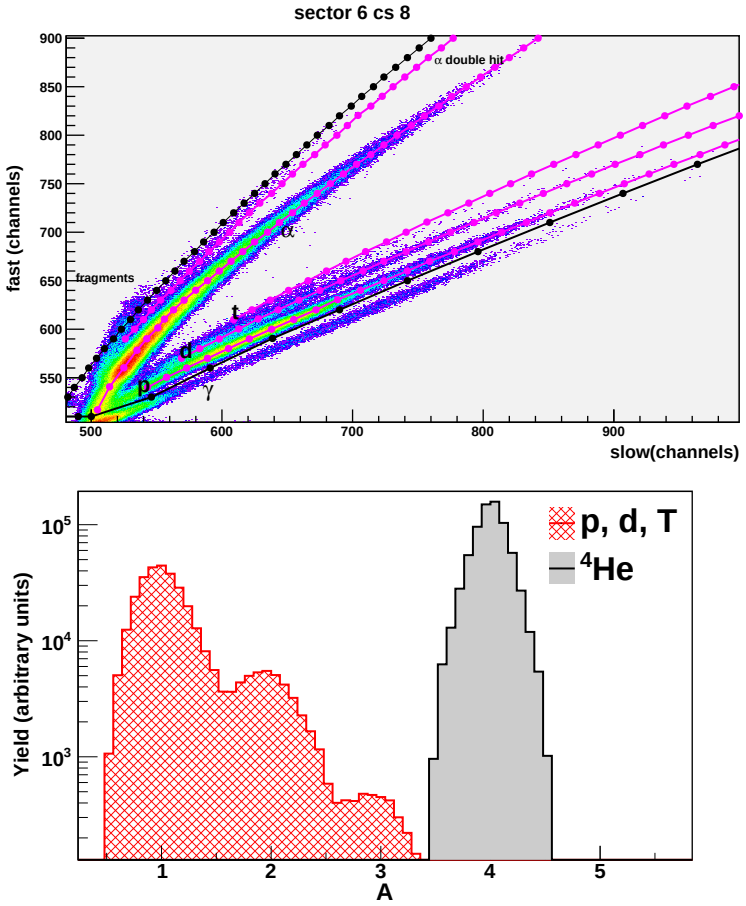

Figure 4.10: Application of the semi-automatic procedure for the identification of particles detected in GARFIELD CsI through *fast* vs. *slow* scatter plots, for the reaction under study. In the top panel: on various isotope ridges points determined and connected by the semi-automatic procedure are shown. The black line labelled *fragments* delimits the upper limit of identification, and signals for $Z > 3$ fragments would fall in a common ridge above this line. Under the lower black line, γ signals are measured. The ridge corresponding to the double hit of α particles is also indicated. In the bottom panel: resulting mass distributions for $Z = 1$ and 2 isotopes.

elastically scattered isotopes ranging from $Z = 1$ to $Z = 28$.

In particular, during dedicated calibration runs for this experiment, we have measured elastic scattering on Au target for ^{12}C at the same 95 MeV beam energy as for the reaction on ^{12}C under study, and at a lower energy of 60 MeV. In this latter case, the measurement of elastically scattered ions on backward GARFIELD detectors is also kinematically allowed. In fig.(4.11) we show the superposition of *fast* vs. *slow* scatter plots for a CsI detector of the current set-up, in which the

spots for elastically scattered ^{12}C ions at the two different energies are evident.

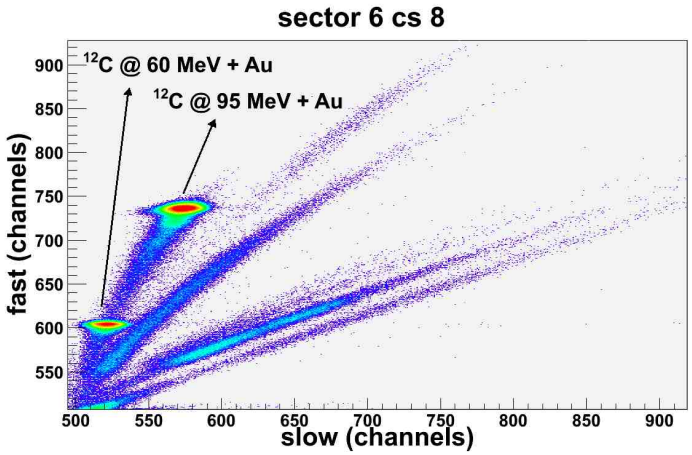

Figure 4.11: Superposition of *fast* vs. *slow* scatter plots for a GARFIELD CsI detector, where elastic scattering for $^{12}C + ^{179}Au$ at 95 and 60 MeV beam energy is measured.

4.4 Data Selection

Given the present status of energy calibration for the data-set analyzed in this work, only static conditions can be employed in order to select the reaction channel. The channel we aim to select is fusion-evaporation, which implies the detection of an evaporation residue. Thus, at a first approximation, the request of the detection of a sufficiently "heavy" fragment at forward angles, *i.e.* in the RCo, could be enough to select the desired channel. With the usual notation, we call Z_{big} the charge of the biggest fragment, detected in our case by the RCo. For the analyzed reaction, an additional difficulty is arising from the very light nature of the system: also according to our simulations (whose results are presented in chapter **3**), evaporation residues for the reaction $^{12}C + ^{12}C$ at 95 MeV beam energy can be as light as the projectile itself, and even lighter. Without having at disposal the information on the fragment momentum, we can not therefore distinguish between an event in which a $Z_{big} \sim 6$ fragment is measured following the decay of a fused source, from an event in which the fragment is the remnant of the projectile after a less dissipative collision, as inelastic scattering, transfer or pick-up. In all these latter cases, fragments detected by the RCo would bear a longitudinal momentum (parallel to the beam direction) close to the one of the incoming ^{12}C projectile. Moreover, the total detected charge

would be close to the charge of the projectile, *i.e.* we will only measure a low percentage of the total charge available in the entrance channel of the reaction.
On the contrary, if such fragments are detected in coincidence with light particles emitted at GARFIELD angles, they may indeed be produced in the fusion-evaporation channel. Having at disposal the information on the momentum we could build the correlation between the total detected charge and the total longitudinal momentum. Because of total momentum conservation, the total longitudinal momentum associated to this kind of event will be close to the one of the projectile, but the total detected charge will be much higher than for peripheral collisions.
As discussed in section 4.2.1, however, the simple request of the RCo - GARFIELD coincidence may be too stringent, since we expect to measure events in which only a fragment with charge close to the charge of the fused system ($Z_{proj} + Z_{targ} = 12$) is detected by the RCo, and we want to attribute such events to the fusion-evaporation channel.
Following this line, we have firstly decided to adopt a criterion on the completeness of the detected event: we have therefore asked for the detection of at least the 80% of the total charge available in the entrance channel of the reaction, which corresponds in our case to the request $Z_{det} \geq 10$.
In particular, the request of completeness can be fulfilled by measuring a sufficiently heavy evaporation residue alone in the RCo, OR by measuring in the RCo an evaporation residue with charge bigger than the charge of the projectile (to avoid any spurious contribution from less dissipative collisions), but in coincidence with other particles in GARFIELD (and/or in the RCo), OR finally by measuring an event with a $Z_{big} \leq 6$ biggest fragment but with a sufficiently high multiplicity of charged particle detected by GARFIELD (and/or by the RCo).
We can therefore write for our final request on data:

$$Z_{det} \geq 10 \quad AND \quad (Z_{big} \geq 6 \;\; OR \;\; m_{GARF} > 0) \tag{4.2}$$

where m_{GARF} is the multiplicity of particles detected by GARFIELD.
In fig.(4.12) we show the experimental charge distribution resulting from data after Z - identification and with the only request of completeness of the detected events, together with the distribution obtained by applying the condition given in (4.2).

As can be seen in the figure, the shape of the distribution obtained with the proposed criteria is compatible with what we expect from the charge distribution following a fusion-evaporation reaction: two different charge regions can be observed, the region of light evaporated particles and the residue region, with average charge bigger than the charge of the projectile. As expected, the additional request

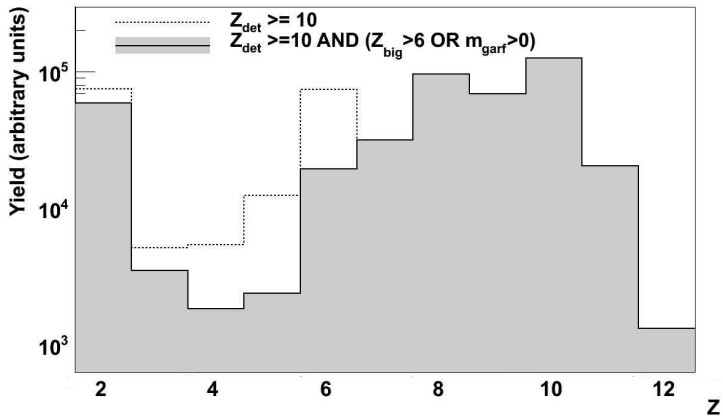

Figure 4.12: Experimental charge distribution of reaction products for $^{12}C + ^{12}C$ at 95 MeV, detected in the RCo. The dashed line histogram corresponds to the inclusive charge distribution as it results from Z - identification from $\Delta E - E$ correlations built with RCo IC and Si signals, with the only request of completeness of the detected events ($Z_{det} \geq 10$); the filled-area histogram gives the charge distribution corresponding to the final selection criterion $Z_{det} \geq 10 \quad AND \quad (Z_{big} \geq 6 \quad OR \quad m_{GARF} > 0)$, which allows us to select the subset of fusion-evaporation events to be used for the analysis.

($Z_{big} \geq 6 \quad OR \quad m_{GARF} > 0$) mainly excludes from the selection events associated to the detection of a $Z_{big} \sim 6$ fragment, which at present we cannot safely identify as evaporation residues. For a detailed comparison of this and other experimental observables with the evaporation code predictions, thus further justifying the proposed criteria, we remand to chapter **5**. Here we want only to notice that this selection may exclude from the data-set some charge partitions also corresponding to the desired channel. We obviously plan to recover the events corresponding to these partitions, by completing the detector calibration, and performing the same analysis proposed in this work with the data-set corresponding to new selection criteria. As it is common to other intermediate and high-energy experiments, this selection can be done by asking conditions on the total detected charge (as already done in this work), the total longitudinal momentum, and directly inferring the "shape" of the measured event from a momentum tensor analysis, and the value of the so-called flow-angle [98].

4.5 The Experimental Filter

Before comparing the experimental data to model predictions, it is necessary to filter simulated events by a software replica of the experimental set-up.
The first operation to be performed is a randomization of the reaction plane for simulated events: this is necessary because in the simulations the initial angular momentum usually has a fixed space orientation, and following the kinematics of the decay in presence of angular momentum, this implies that particle emission takes place preferentially in the plane perpendicular to the initial **J** vector. In order to have the desired effect of reaction plane randomization, but without loosing correlations among particles resulting from the kinematics implemented in the code (which we will be able to compare to data), we can simply add to the φ value of each particle in a given event a random φ_{in} quantity. This will leave constant the difference $\Delta\varphi$ for each considered couple of simulated particles in the same event.
At this point, the filter has still to take into account:

- the geometrical coverage of the experimental set-up;
- the energy thresholds for detection and identification of particles in charge and mass in hit detectors;
- energy losses due to dead layers and to the interaction with the detector material in case of multi-stage telescopes;
- the presence of unsolvable double-hit, *i.e.* the detection of two particles in the same telescope, without any possibility of recovering the information on particle species or energy;
- the smearing out of the predicted energy with which the particle can be detected due to the finite energy resolution of the apparatuses.

Angular ranges covered by GARFIELD and the RCo, typical values for thresholds and detector resolutions have been given in the sections about the experimental set-up and the energy calibration. Taking all this into account, typical values for the set-up efficiency calculated by filtering the code predictions for the reaction under study are:

- an efficiency of the order of 90% for the detection of at least one particle per event, which is a good indication of the nearly 4π coverage of the set-up, together with the low detection thresholds due to the use of gas detectors;

- a final percentage as high as 30% for the reconstruction of quasi-complete events fulfilling the physical request discussed in the previous section for the selection of the fusion-evaporation channel.

In fig.(4.13) we show the effect of the experimental filter on the predictions for a global observable as the residue charge distribution. Evaporation residues are the less energetic reaction products, and therefore the most difficult to detect. As it is evident from the figures, this observables is not substantially modified by the filter, and only a global reduction of the statistics is observed. Together with the high numerical values for the calculated efficiency, this ensures that a representative sample of physical events can be measured by our experimental set-up for the chosen reaction.

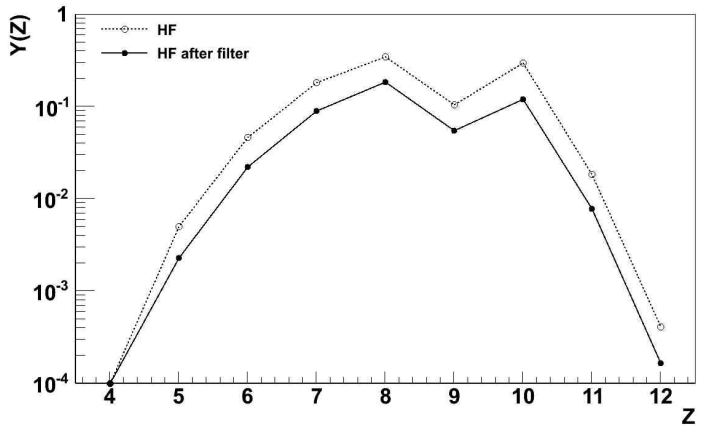

Figure 4.13: Effect of the experimental filter for the GARFIELD+RCo set-up on the predictions of the Hauser-Feshbach code for the evaporation residue charge distribution. Residues are measured at forward angles, by the RCo detector. Code calculations are shown with a dashed line, filtered calculations with a continuous line.

Chapter 5

Comparison to Model Predictions

In this chapter we present the results of the data analysis for the reaction $^{12}C+^{12}C$ at 95.6 MeV beam energy, measured at LNL with the GARFIELD + RCo experimental set-up. The apparatuses and the measurement have been described in the previous chapter, together with the techniques and procedures adopted to go from "raw" data to a set of "physical" events. As previously discussed, we have adopted the following selection criterion:

$$Z_{det} \geq 10 \quad AND \quad (Z_{big} \geq 6 \;\; OR \;\; m_{GARF} > 0) \tag{5.1}$$

where Z_{det} is the total detected charge (corresponding to $\approx 80\%$ of the available charge in the entrance channel of the reaction), Z_{big} is the charge of the biggest fragment detected at forward angles (in the RCo) and m_{GARF} is the multiplicity of particles detected in GARFIELD. This criterion has been applied in order to sort from the collected events an experimental subset of events compatible with the fusion-evaporation channel, and, therefore, which we can compare to the predictions of our Monte Carlo Hauser-Feshbach code for the evaporation of the compound nucleus ^{24}Mg, at $e^* = 2.6$ $A.MeV$, issued in case of complete fusion for the measured reaction. As described in chapter **3**, where a theoretical study of the decay of an equilibrated ^{24}Mg under these conditions is presented, the angular momentum input distribution for the fused system in this reaction can be assumed as a triangular distribution, with a maximum value $J_{0\ max} = 12\ \hbar$ coming from the systematics. Because of parity conservation, only even values of J_0 extracted from the triangular distribution are allowed as an input for the CN angular momentum in the calculations. Finally, code predictions are filtered through a software replica of the experimental set-up, as discussed in chapter **4**.

The comparison of various experimental observables and code calculations is used

to put experimental constraints on the free parameters of the level density model implemented in the code. The results presented in this chapter will also allow us to get an insight into possible deviations from a statistical behavior of the hot fused source formed in the collision, due to the persistence of structure effects as clustering.

5.1 Light Charged Particles and Level Density

In the following, we will present the results for the comparison between experimental data and code predictions for observables which can be built up with light charged particles detected in GARFIELD, by using the information coming from the RCo in the selection criterion given in (5.1).
In particular, these observables include energy, angular and multiplicity distributions for protons and α particles. All kinematic observables are given in the laboratory reference frame.
The adopted normalizations are clarified hereafter:

- for each of GARFIELD CsI detector, the different solid angle coverage is taken into account, and spectra are always integrated on the azimuthal angle φ;

- the global normalization factor for all proton/α energy and angular distributions is the total yield of protons/α detected in GARFIELD. The contribution of $CsI5$ is always excluded from the computation of this normalization factor, because of the reduced efficiency of this detector, as it is shown in chapter **4**. Inclusive spectra (summing the contributions of all CsI) are therefore normalized to a unitary area, while the integral of the spectrum for a single detector bears the information on the percentage of the total yield which comes from that detector;

- multiplicity distributions are normalized to the number of events fulfilling the request given in (5.1), and correspond therefore to probability distributions.

Code predictions for two different values of the level density model free parameter E_{cl} are presented in this section: we recall that this parameter determines how rapidly the level density parameter $a(E^*)$ grows for increasing E^* from the value given in [67], necessary for the reproduction of low-energy spectroscopic information, up to the asymptotic value calculated with the expression given in [74], coming from evaporation after fragmentation studies, which represents therefore a constraint at

higher energy. By tuning the value of this parameter in order to reproduce experimental data we can therefore give an additional constraint to the LD parameter functional form in the "energy" region from ~ 1 up to $\sim 2 \div 3$ $A.MeV$.
The values used in the calculations are $E_{cl} = (3 \cdot A)$ MeV and $E_{cl} = (8 \cdot A)$ MeV. The same color scheme is employed throughout all the figures of this chapter: code predictions for the first case are always presented in red, predictions for the second one in blue. We also recall that a higher value of E_{cl} implies, at a given excitation energy, a lower value of the level density parameter $a(E^*)$, and therefore a higher nuclear temperature. For both choices of E_{cl}, in our level density model, the asymptotic value for $a(E^*)$ for nuclei with mass $A \sim 20$ is $a \approx A/5$.
In fig.(5.1) we show experimental inclusive protons and α particles energy spectra. As it is evident from the figure, the proton energy spectrum is in very good agreement with model calculations for the case $E_{cl} = (3 \cdot A)$ MeV, both concerning the slope (sensitive to the LD parameter value) and the low-energy barrier region (sensitive to adopted values for transmission coefficients and Coulomb barriers). On the contrary, the same choice for the level density model cannot reproduce the energy spectrum of α particles, which differs from the calculations both in the high- and low-energy regions. Even the alternative case of $E_{cl} = (8 \cdot A)$ MeV does not allow for a reproduction of the slope of the α spectrum, and a higher value of E_{cl} would be needed to obtain an agreement. Finally, the reproduction of the slope of the energy spectrum for α particles may be achieved only at the cost of both a wrong reproduction of the proton energy spectrum, and of an unphysical choice for the value of E_{cl}, since, as discussed in chapter **3**, E_{cl} is upper-limited by the nuclear limiting energy as evaluated in ref.[39], which cannot in turn exceed the average binding energy per nucleon.

In fig.(5.2) we present the results for protons and α particles angular distributions. The centers of the bin for these distributions correspond to the average θ angle of each of GARFIELD CsI detector. The reduced efficiency for $CsI5$ is evident in the figure. For this observable, as we expect from the theory, code predictions are less sensitive to the choice of the level density parameter. The experimental angular distribution is well reproduced for protons for both possible values of the E_{cl} parameter. As far as α particles are concerned, the agreement is found to be good for the forward detectors ($\theta \leq 90°$), while a general underestimate of the α yield is evident in the calculations for backward laboratory angles. As for the case of α energy distribution, a higher value of E_{cl} goes in the right direction to reproduce the experimental data, but the maximum possible value $E_{cl} = (8 \cdot A)$ MeV is still

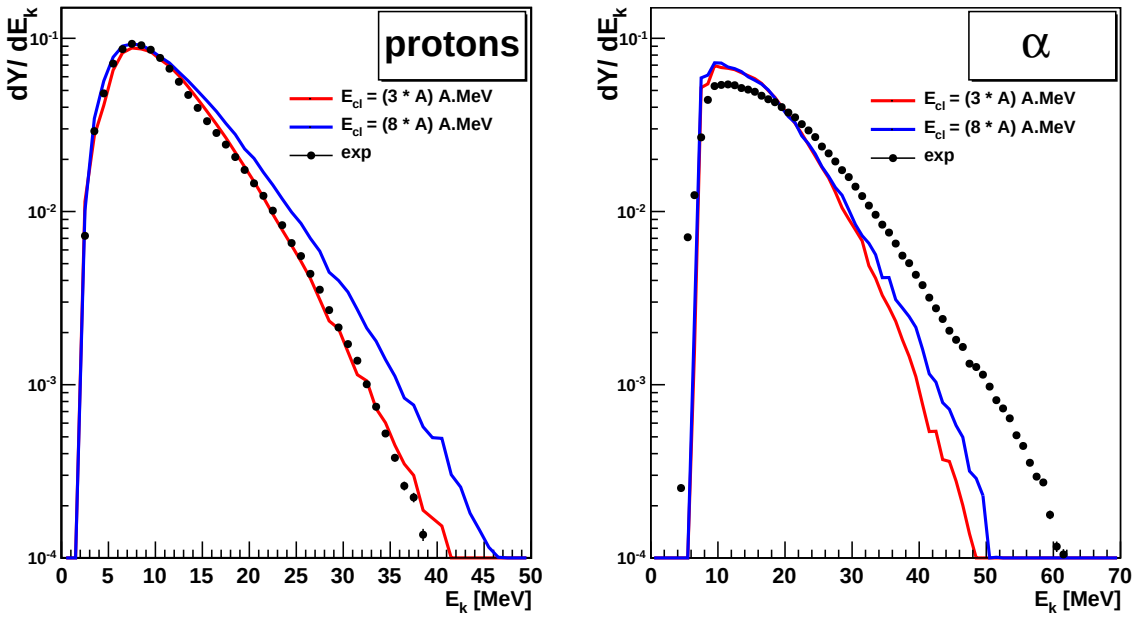

Figure 5.1: Energy spectra for protons and α particles detected in all GARFIELD CsI: in ordinate dY/dE_k, in abscissa the kinetic energy E_k in MeV in the laboratory frame. Experimental data are given by dots, statistical errors are calculated and shown with bars. Model predictions are shown with lines. The red line corresponds to a chosen value of $E_{cl} = (3 \cdot A)\ MeV$, the blue one to $E_{cl} = (8 \cdot A)\ MeV$.

not high enough.

Finally, in fig.(5.3), we plot the multiplicity distributions of detected protons and α particles. As it is evident from the figure, the global behavior of these distributions is reproduced by the code predictions, and also this observable is less sensitive to the level density model. In particular, for the proton multiplicity distribution, almost no differences can be observed between the $E_{cl} = (3 \cdot A)$ and $(8 \cdot A)\ MeV$ cases. Concerning this observable, we have verified that the inversion of the number of protons per event corresponding to the highest probability, which is $n_p = 0$ for the experimental sample and $n_p = 1$ for the calculations, can be at least partially attributed to the reduced efficiency of $CsI5$. Indeed, in the figure we also plot the prediction for the same observable calculated by excluding the contribution of protons detected in $CsI5$, *i.e.* artificially putting to zero the efficiency of this detector in the software replica of the apparatus (red dashed line, for the $E_{cl} = (3 \cdot A)\ MeV$ case). This exclusion allows for a reproduction of the experimentally measured high-

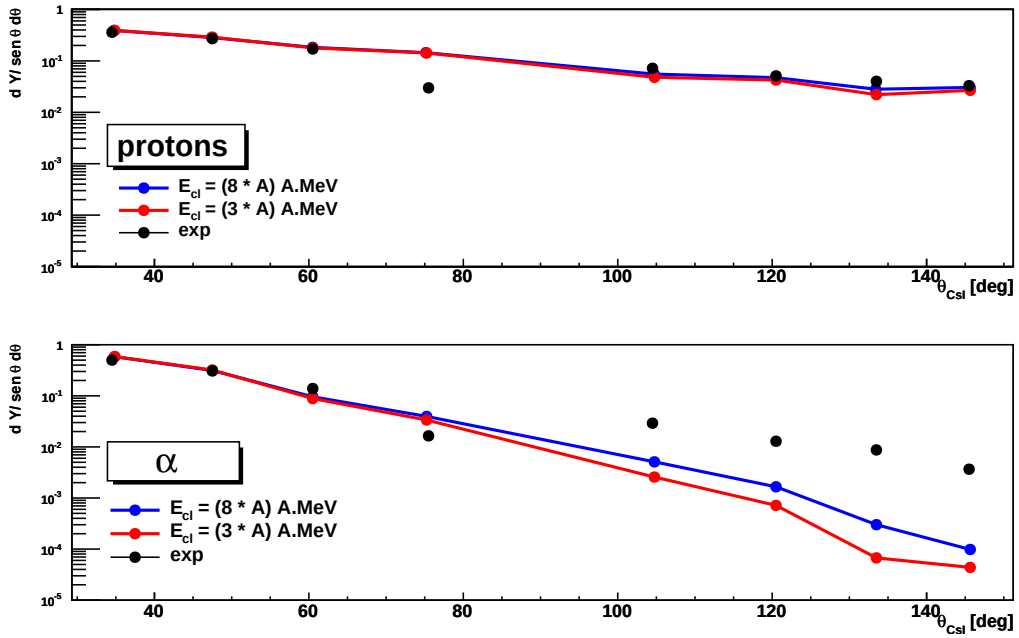

Figure 5.2: Angular distributions for protons (upper panel) and α particles (lower panel) detected in GARFIELD: in ordinate $dY/\sin\theta d\theta$, in abscissa the average θ angle of each of GARFIELD CsI detectors. Experimental data are given by black dots, model predictions are shown with dots connected by a line to guide the eye. The red line corresponds to $E_{cl} = (3 \cdot A)\ MeV$, the blue one to $E_{cl} = (8 \cdot A)\ MeV$. The reduced efficiency for $CsI5$ is evident in the figure.

est probability of having an event without any detected proton in GARFIELD.
As far as α particles are concerned, we can observe a slightly better reproduction of data for calculations with $E_{cl} = (3 \cdot A)\ MeV$ for lower n_α values, characterized by a larger statistical weight, while the choice $E_{cl} = (8 \cdot A)\ MeV$ goes in the direction of getting a better reproduction of lower statistics contributions, and the same effect is visible in the angular distribution, where code results for $E_{cl} = (8 \cdot A)\ MeV$ are closer to experimental data for backward GARFIELD detectors.

As a first summary of the presented comparisons, the proposed selection criterion given in (5.1) has allowed us to isolate from the total reaction cross section a contribution which can be identified with the formation and decay of a fused source: this makes possible the comparison between experimental data and our decay code predictions, in which the dynamics of the entrance channel is not taken into account. Global observables as multiplicity distributions for light charged particles can be in-

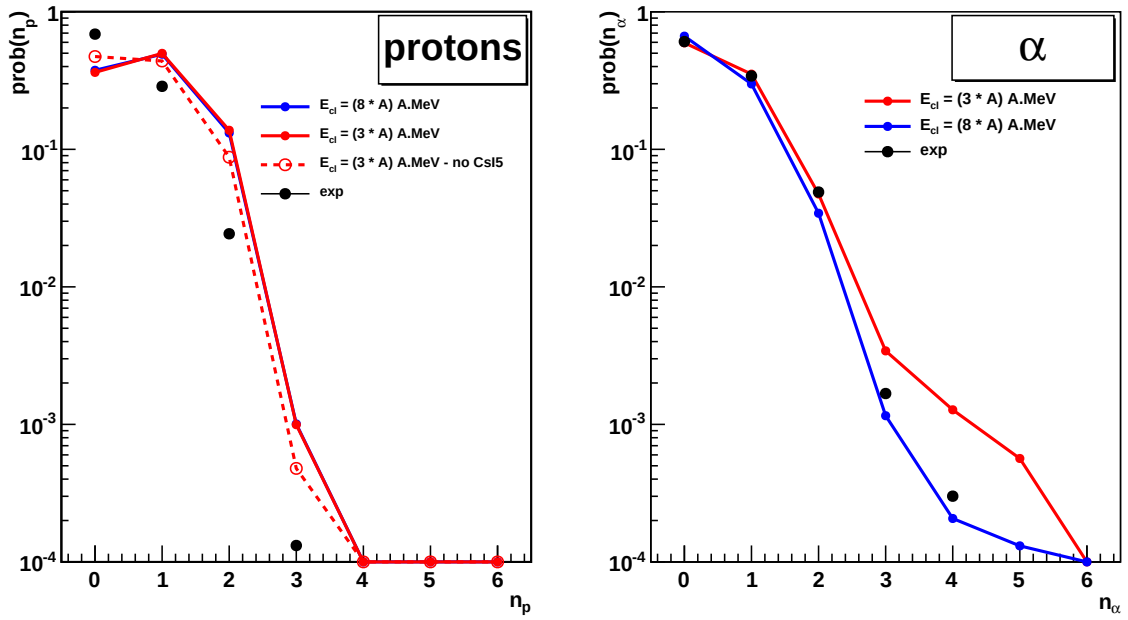

Figure 5.3: Multiplicity distribution of protons (left panel) and α particles (right panel) detected in GARFIELD. Experimental data are given by black dots, model predictions are shown with dots connected by a line to guide the eye. The red lines correspond to $E_{cl} = (3 \cdot A)\ MeV$, the blue one to $E_{cl} = (8 \cdot A)\ MeV$. In the left panel, the red dashed line is obtained by excluding the contribution of protons detected in $CsI5$. Always in the left panel, results for calculations with different E_{cl} values are almost indistinguishable.

deed well reproduced. However, from the results shown in fig.(5.1,5.2) for energy and angular distributions, we infer that no unique choice for the level density model implemented in the code allows for a good reproduction of observables concerning both protons and α particles emission from this source. The source does not show a fully equilibrated behavior, and this is particularly evident in the case of α particles emission. Given the $N = Z$ even-even nature of the ^{12}C projectile and target in the entrance channel of the reaction, we are then tempted to attribute any deviation from a statistical behavior in the decay of this source to α-clustering effects, and therefore to constrain the level density model in order to have a good reproduction of proton observables, with the purpose of investigating more in details α particle emission. This brings us to the choice of $E_{cl} = (3 \cdot A)\ MeV$, and calculations shown in the rest of this chapter are always performed under the assumption of this value for the E_{cl} parameter in our level density model.

5.2 Out-of-Equilibrium Effects

We can have a closer insight in the kinematics of the decay of the fused source by combining the information from angular and energy distributions: in fig.(5.4) and (5.5) we show respectively the energy spectra for protons and α particles detected in the different GARFIELD CsI. As it is evident from fig.(5.4), code calculations for the chosen level density model globally reproduce proton energy spectra, for all GARFIELD CsI, and only a slight increased experimental production at backward angles can be observed. On the contrary, as expected, no reproduction is achieved for α particles energy distributions at any CsI angle. Moreover, for more forward detectors, a bump in the α energy spectrum can be observed, which is less evident in the inclusive spectrum of fig.(5.1). Such a structure suggests the presence of a non-equilibrium component in α-emission.

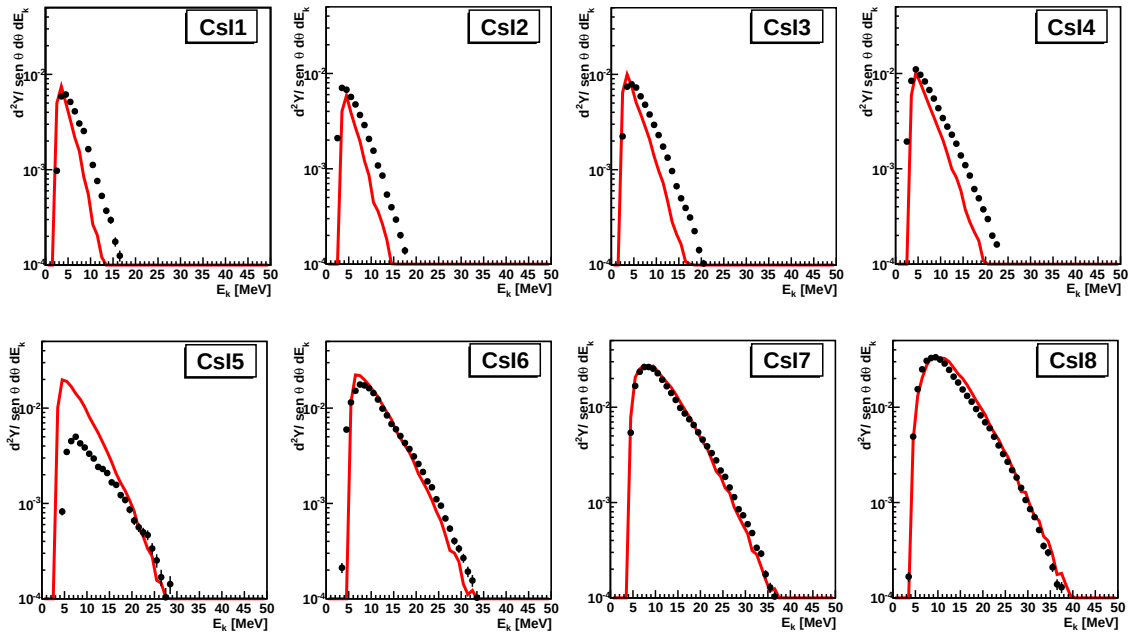

Figure 5.4: Energy spectra for protons detected in the different GARFIELD CsI: in ordinate $d^2Y/\sin\theta d\theta dE_k$, in abscissa the kinetic energy in MeV in the laboratory frame. Experimental data are given by dots, statistical errors are calculated and shown with bars. Model predictions are shown with red lines, corresponding to the $E_{cl} = (3 \cdot A)\ MeV$ choice. Going from the uppermost left plot to the lowermost right the average θ angle of the detector is decreasing. The name of the considered CsI is reported in each figure. The reduced efficiency for the $CsI5$ is evident in the figure.

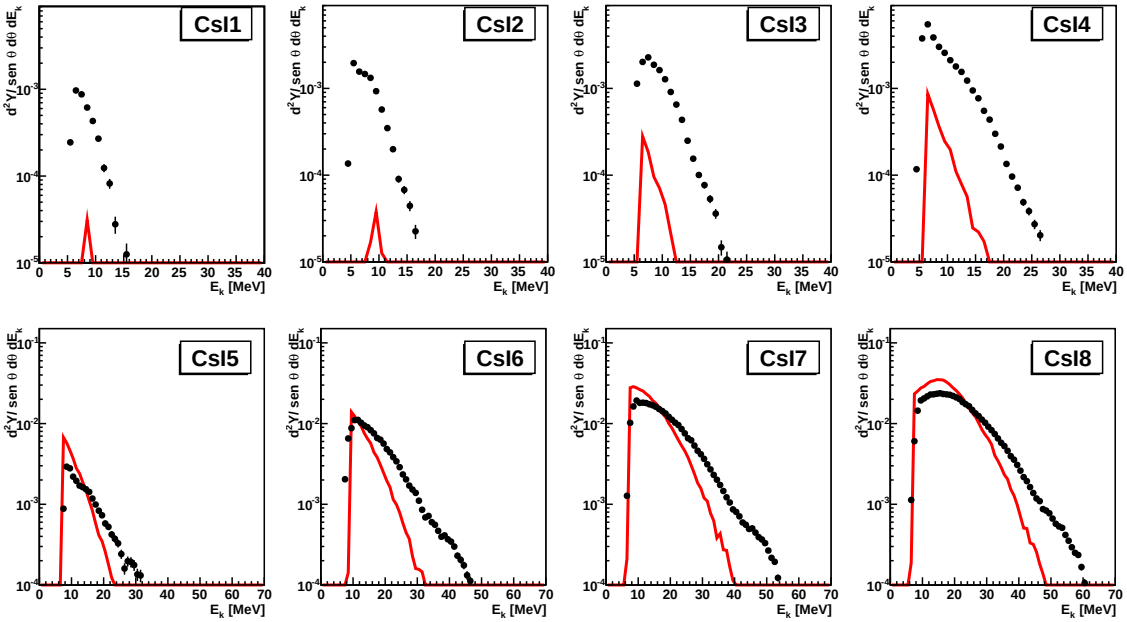

Figure 5.5: The same as in fig.(5.4), for detected α particles.

In order to investigate if a particular decay channel is associated to this component, we plot in fig.(5.6) the energy spectra for α particles detected in all GARFIELD CsI, in coincidence with a residue of chosen charge detected at forward angles (in the RCo), always for the subset of events fulfilling the selection criterion given in (5.1). In the left panel of the figure, the usual global normalization factor is employed for each distribution, *i.e.* all spectra are divided by the total yield of detected α particles, such that the sum of the contributions corresponding to all detected residues gives back the inclusive α energy spectrum shown in fig.(5.1). By looking at the left panel we can identify three lower statistics contributions, corresponding to a detected residue with charge $Z_{res} = 4$ (purple dots), 5 (red) and 10 (green). Higher statistics contributions come from $Z_{res} = 6, 7, 9$ (respectively, blue, yellow and light blue dots) and the dominant contribution is the one from α detected in coincidence with $Z_{res} = 8$, in which a bump in the energy spectrum is appearing. Two different autocorrelations have to be considered to compare the energy spectra shown in the left panel with each other: one is the relative probability for the production of residues with different charges, and the other one is a trivial effect of charge conservation. The maximum number of α particles which may be emitted in the decay of the fused source is given by $n_\alpha^{max} = (Z_{CN} - Z_{res})/2$. To get rid of these

effects, in the right panel of the figure we show the same energy spectra, multiplied by a normalization factor given for each residue as $c(Z_{res}) = [Y(Z_{res})/N_{ev} \cdot n_{\alpha}^{max}]^{-1}$. With this normalization, all spectra are found to be grouped together, with the exception of the one for α particles detected in coincidence with $Z_{res} = 10$. This may be attributed to our selection of the reaction channel, and in particular to the requirement $Z_{det} \geq 10$, which is fullfilled by the detection of a $Z_{res} = 10$ fragment even if detected alone.

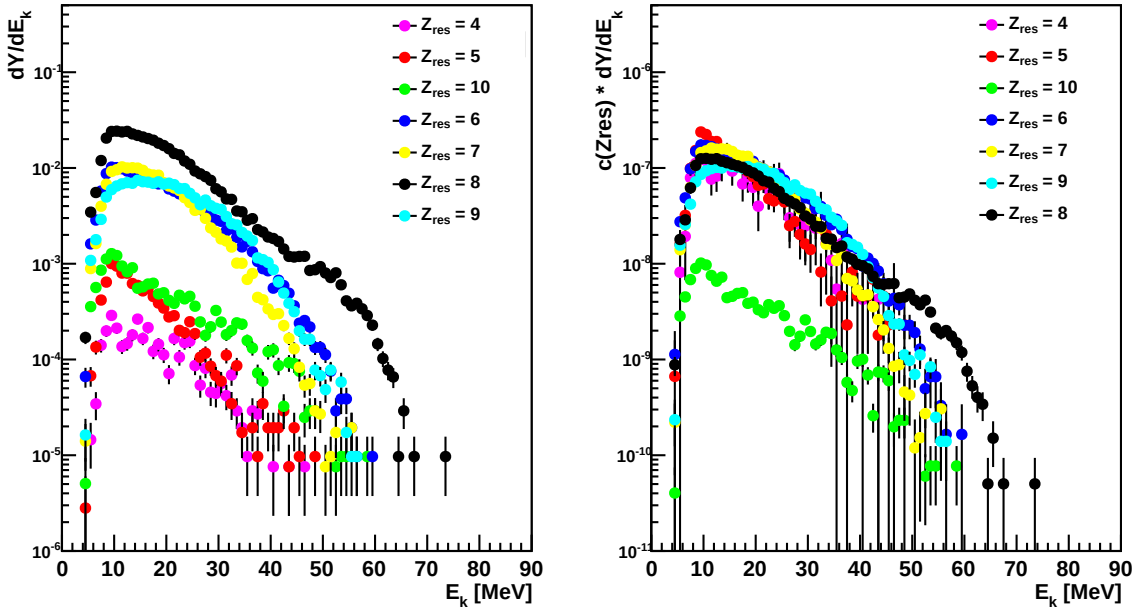

Figure 5.6: Experimental energy spectra for α particles detected in all GARFIELD CsI, in coincidence with a residue of given charge detected at forward angles (in the RCo). In ordinate dY/dE_k, in abscissa the kinetic energy in MeV in the laboratory frame. The adopted colore scheme is given in the legend of the figure. Left panel: normalization to the total number of detected α, independently on the charge of the residue. Right panel: the same energy spectra, multiplied by a normalization factor given for each residue as $c(Z_{res}) = [Y(Z_{res})/N_{ev} \cdot n_{\alpha}^{max}]^{-1}$, in order to get rid of autocorrelations (probability of a given Z_{res} residue, maximum number n_{α}^{max} of α particles allowed by mass and charge conservation) and to be able to compare the spectra in coincidence with different residues with each other. More details are given in the text.

As a result of this analysis, we can confirm that the energy bump in the α energy spectrum is mainly associated to decay channels in which an oxygen residue is measured at forward angles. We may think at this point that artificially removing these

channels from the data-set (and coherently removing them from the output of the calculations) could provide a better reproduction of α particles observables. This is only partially true, as we show in in fig.(5.7), where α particles observables are obtained under the request that no residue with charge $Z_{res} = 8$ is detected/produced at RCo angles. As expected, no bump appears in the energy spectrum on the left panel of fig.(5.7), but the experimental slope can not still be reproduced by a calculation with the same input level density necessary to reproduce proton observables. Moreover, as far as the angular distribution is concerned, we still observe an extra experimental yield of backward emitted particles with respect to the code predictions, which suggests that these two deviations from a statistical behavior may have different physical origins.

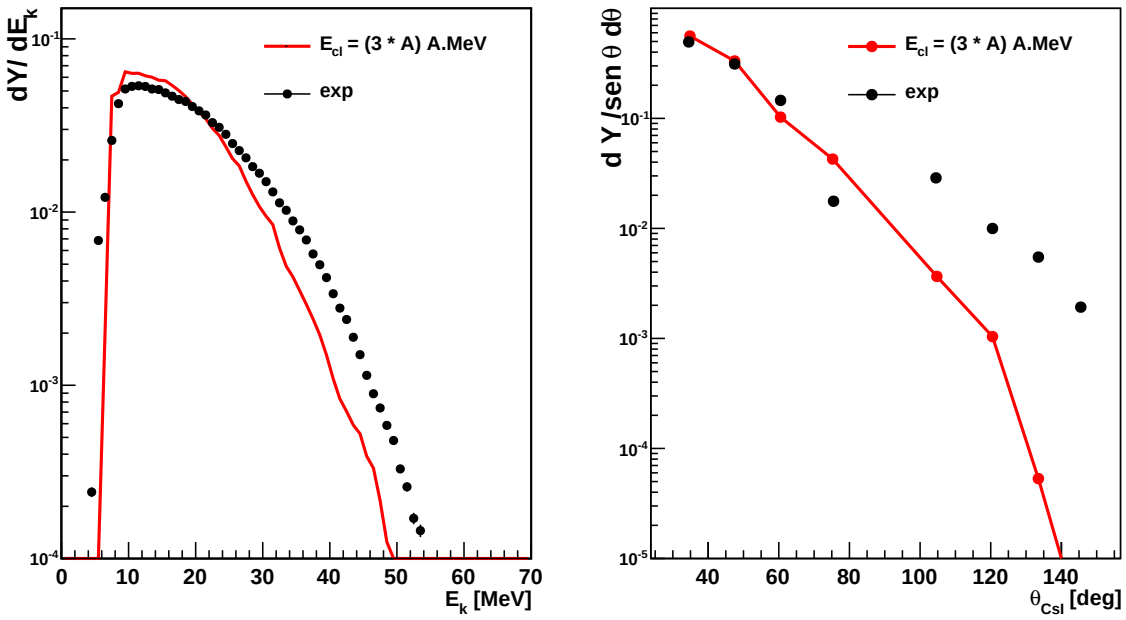

Figure 5.7: Energy (left panel) and angular distribution (right) for α particles detected in GARFIELD CsI which are not in coincidence with a $Z_{res} = 8$ residue. Experimental data are given by dots, statistical errors are given with bars. Model predictions are shown with a red line, corresponding to a chosen value of $E_{cl} = (3 \cdot A)\ MeV$.

In order to isolate kinematically these two different contributions to the out-of-equilibrium behavior, namely, the bump in the energy spectrum of α particles detected in GARFIELD at more forward angles and the extra-yield of backward

emitted α, we can exploit the symmetry of the entrance channel of the reaction in the center-of-mass reference frame. In fig.(5.8) we plot the correlations between the energy per nucleon E_{CM}/A and the emission angles θ_{CM} in the **CM** reference-frame for reaction products in ^{12}C(@7.9 $A.MeV$)+^{12}C collisions: dashed lines represent the loci for constant kinetic energy per nucleon E_k/A in the laboratory RF, increasing of one $A.MeV$ units starting from the first curve in the lowermost left corner of the $E_{CM}/A-\theta_{CM}$ plane; red lines give the portion of the plane covered by the detection of reaction products in the RCo, while each of the regions delimited by two black lines is associated to the detection in one of GARFIELD CsI, starting from $CsI8$ up to $CsI1$, going from left to right.

The green square in the right part of the plane identifies the energy-angular region in which an extra yield of α particles is observed, corresponding to α particles detected in GARFIELD backward CsI and with average kinetic energies of $E_k/A \sim$ 2. $A.MeV$ in the laboratory RF. Due to the symmetry of the entrance channel, we expect therefore that α particles falling in this region have a counterpart contribution, which is identified by the green square in the left part of the plane, centered at $180^\circ - \theta_{CM}$ with respect to the right one. As we understand from the figure, this contribution corresponds to forward emitted α particles, which are detected in the RCo, flying at energies very close to the energy of the beam. Because of the current status of the energy calibration for the RCo detector, we are not able at the moment to compare the energy spectra of α particles detected in the RCo to the statistical decay code predictions, but, from the kinematics considerations on fig.(5.8), we expect to find a significative deviation from an equilibrium behavior at very forward angles. This deviation may be connected to the contribution of pre-equilibrium emission followed by incomplete fusion, linked to the α cluster nature of the ^{12}C projectile. Therefore, what we observe as an extra-yield of α particles emitted at backward angles, may be originated from the same pre-equilibrium emission, but linked to the target, which is also a ^{12}C nucleus.
The small blue square on the left of the $E_{CM}/A - \theta_{CM}$ plane identify α particles which are detected in GARFIELD $CsI8$, in the energy region where a bump in the spectrum is evident ($E_k/A \sim 14 \div 15$ $A.MeV$). With the same $180^\circ - \theta_{CM}$ reflection, the counterpart of this contribution can be identified by the blue square on the right, which corresponds to α particles mainly detected in $CsI5$, with average energies of $E_k/A \sim$ 4 $A.MeV$ in the laboratory frame. Indeed, a small bump around $E_k \sim 16$ MeV can be observed in the energy spectrum for this detector, previously shown in fig.(5.5), in spite of its globally reduced efficiency. The two regions identified by blue squares correspond to central emission angles in the **CM**

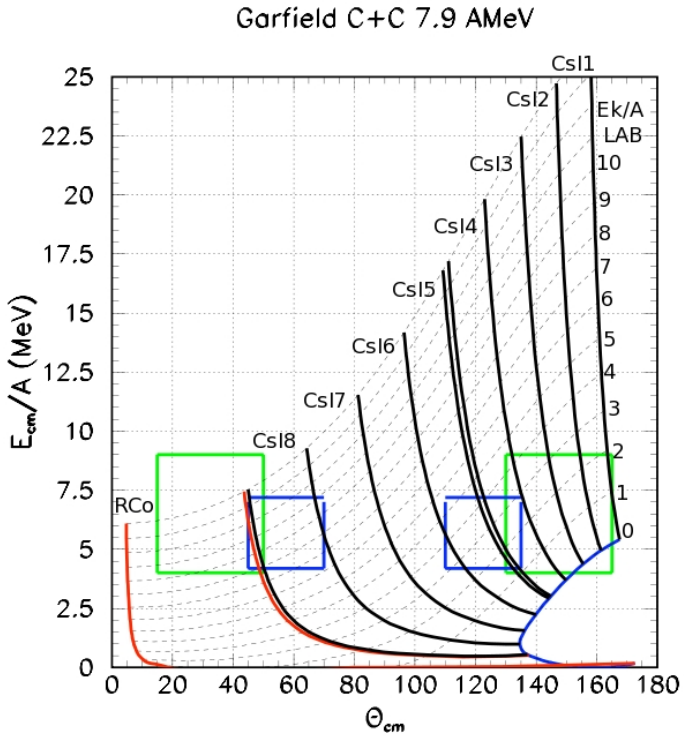

Figure 5.8: Energy per nucleon E_{CM}/A vs. emission angle θ_{CM} plane in the **CM** reference-frame for reaction products in $^{12}C(@7.9\ A.MeV) +^{12} C$ collisions: loci for constant E_{kin}/A in $A.MeV$ in the laboratory RF are given by dashed lines; red lines give the portion of the plane covered by the detection in the RCo; black lines represent the coverage of GARFIELD CsI, as indicated in the figure. Couples of green and blue squares identify symmetric contributions in the **CM** RF obtained by a $180° - \theta_{CM}$ reflection. Green squares identify the contribution of α pre-equilibrium emission in the entrance channel, from the projectile (left) and from the target (right); blue squares identify the contribution of α emission giving rise to bumps in the energy spectra of GARFIELD $CsI8$ and $CsI5$, linked to cluster emission from the fused source.

RF, and can therefore be associated to more dissipative collisions. Moreover, we have shown in fig.(5.6) that the bump in the α energy spectrum mainly corresponds to decay channels in which an oxygen is detected as an evaporation residue: we are then led to associate the presence of this bump to α cluster emission on the path towards thermalisation of the hot source formed in the collision, which in turn can be related to the possible preformation of α particles.
Concluding, we have kinematically isolated two different contributions to the out-of-equilibrium behavior in α particle emission: one seems to suggest the presence

of pre-equilibrium emission due to the α cluster nature of the reaction partners, and the other may stem from the possible preformation of α particles in the fused source. Once the energy calibration of reaction products detected in the RCo will be completed, we expect to be able to have a further confirmation of the presence of pre-equilibrium emission in the entrance channel. Comparison to code predictions for the emission at very forward angles could also allow an estimation of the decrease in the size of the fused source, because of pre-equilibrium emission. The decay of the average source in case of incomplete fusion can be simulated with the code, and this contribution can be added to the calculations for the decay of ^{24}Mg.
Finally, both these effects are taken into account in existing decay codes as MCFx [99], and comparison of our data to the predictions of such codes, or the direct implementation of pre-equilibrium emission in our Hauser-Feshbach code, represent interesting perspectives for this data-analysis, as discussed in more details at the end of this thesis.

5.3 Charge Distribution and Staggering

In fig.(5.9) we show the total experimental charge distribution of reaction products and the multiplicity distribution of charged particles and fragments, detected both in GARFIELD and in the RCo. Both observables are obtained under the usual selection condition (5.1), and are normalized to the number of events fulfilling this condition. Model calculations for the same distributions are shown together with data, both for our Monte Carlo Hauser-Feshbach code and for the GEMINI model, including the emission of IMF following the transition state formalism. Hauser-Feshbach calculations globally reproduce the charge distribution, in particular the observed trend of the odd-even staggering, with the exception of the yield of $Z = 4$ fragments, which are completely missing in the code predictions. This can be attributed to a different isotopic population of $Z = 4$ fragments, which are mostly produced as unstable ^{8}Be residues in the calculation, which further decay in two α particles. On the contrary, in the experimental data-set, ^{7}Be and ^{9}Be isotopes are produced, as it is visible from the pulse shape correlations shown in chapter **4** for fragments stopped in the RCo silicon detectors. This suggests the interest of a detailed comparison of calculated and experimental isotopic distributions, when the information on the mass can be extracted from data, *i.e.* for $Z < 6$ products in the case of this experiment. This comparison has not been included in this work, because of the current incomplete status of the charge and mass identification of reaction products from the Si energy vs. risetime correlations.

One of the decay mechanisms which may populate the intermediate region between the evaporated light charged particles and the residues, including the $Z = 4$ isotopes, could be the emission of intermediate mass fragments. As mentioned, this decay channel is implemented in GEMINI following the transition state formalism. From the comparison of the experimental charge distribution with the GEMINI code prediction, we see that the inclusion of this decay channel indeed populates the intermediate charges region. A general overestimate of the yield of $Z = 3, 4, 5$ fragments can be observed, together with a better reproduction of the yield of $Z = 6$, and finally with the inversion of the relative yield of $Z = 7$ and 8, which, on the contrary, is correctly reproduced by Hauser-Feshbach calculations. As far as the total multiplicity of charged particles and fragments is concerned, the mean multiplicity and the trend of the multiplicity distribution as a function of n_C are well reproduced both by our calculations and by GEMINI. The inclusion of IMF emission causes a general overestimate of higher multiplicity events, maybe because of secondary emission from fragments produced above the threshold for particle decay.

The comparison to GEMINI finally suggests that the inclusion of a decay channel other than light charged particles evaporation following the Hauser-Feshbach formalism could in principle improve the description of the charge and mass regions intermediate between the light evaporated particles and the residues. For instance, the inclusion of a simultaneous decay channel, which could be described in terms of the Fermi break-up formalism, would also go in this direction. This is discussed in more details in the conclusions of this thesis. Nevertheless, the slight better agreement we find in the residue region between experimental data and the Hauser-Feshbach predictions with respect to the GEMINI ones, suggests the reliability of our description of the sequential evaporation channel, and its dominant contribution. Moreover, as we have shown in chapter **3**, the slope of energy spectra of emitted particles, which have been used to constrain the level density model, is not strongly affected by the inclusion of other decay channel, and therefore the obtained constraints on the functional form of $a(E^*)$ can be considered reliable.
Finally, in fig.(5.10), we show the ratio of the experimental charge distribution $Y(Z)$ to a smoothed $Y_s(Z)$, which is obtained by means of a parabolic smoothing over 5 successive points, as it is done in [31], in order to put in evidence odd-even effects. The same ratio is evaluated for the Hauser-Feshbach and GEMINI code predictions. As it is evident from the figure, the result for $Y(Z)/Y_s(Z)$ for our decay code correctly reproduces the trend of the observed staggering for $Z \geq 7$, as far as the statistics allows for a safe computation of the smoothed yield. In particular, the

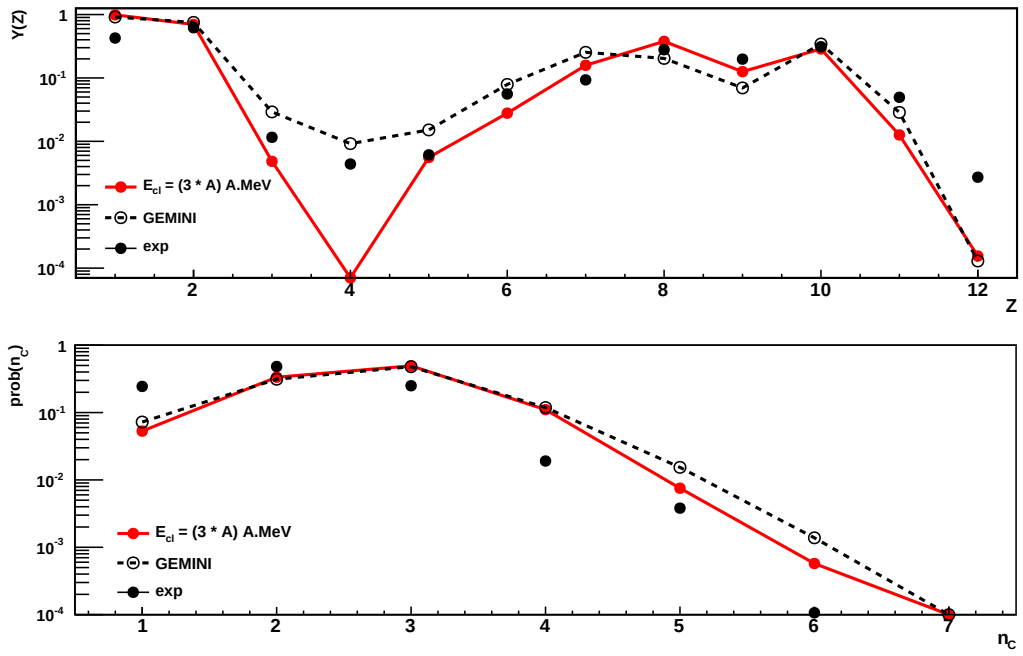

Figure 5.9: Upper panel: charge distribution of reaction products; lower panel: total multiplicity distribution of detected particles. Normalization is to the total number of considered events. Experimental data are given by dots, Hauser-Feshbach model predictions for the case $E_{cl} = (3 \cdot A)\ MeV$ are shown with red dots connected by a line. GEMINI calculations (including the emission of IMF following the transition state formalism) are also shown by empty dots connected by a dashed line.

peak at $Z = 6$ cannot be reproduced by the calculations, which may also suggest that the production of $Z = 6$ fragments can be partially related to the entrance channel of the reaction. In GEMINI calculations, the relative probability associated to $Z = 7$ and 8 is inverted with respect to the experimental case, and the oscillating trend is not correctly reproduced for $Z \leq 7$. For both Hauser-Feshbach and GEMINI predictions, the amplitude of the oscillations, when the relative yield for two neighbouring charges is correct, is slightly overestimated.

As mentioned, a better reproduction of the charge (and mass) distribution for reaction products could be in principle achieved, by implementing in the code competitive decay channels as IMF emission or Fermi break-up, coupled to our description of the sequential evaporation channel. Also the inclusion of pre-equilibrium emission in the entrance channel could improve the reproduction of the experimental yield of $Z = 6$, provided that this yield reflects some memory of the entrance channel of the

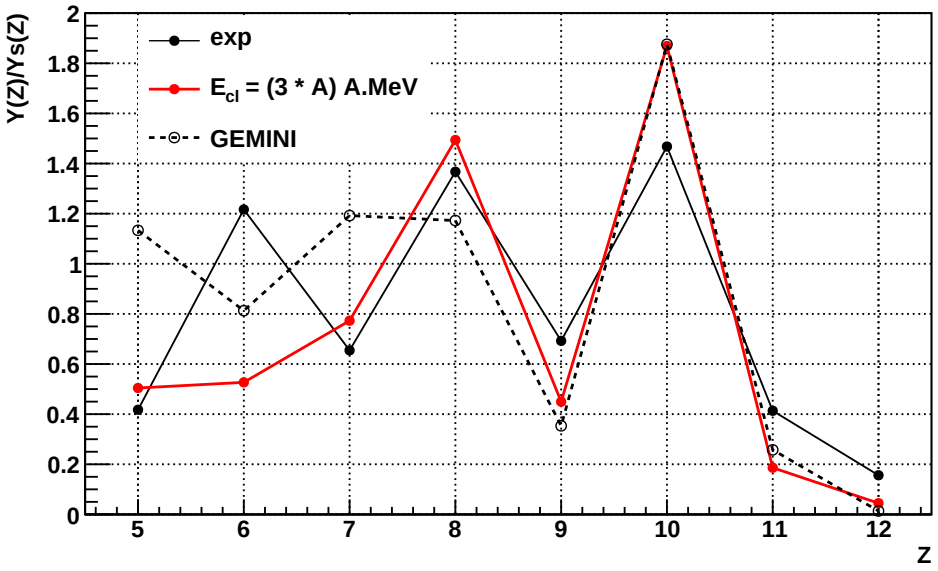

Figure 5.10: Staggering in the charge distribution of reaction products: in ordinate, ratio of the charge distributions $Y(Z)$ of fig.(5.9) to their smoothed $Y_s(Z)$, obtained by means of a parabolic smoothing over 5 successive points, as it is done in [31]. Experimental data are given by black dots, connected by a thin black line to guide the eye; Hauser-Feshbach model predictions for the case $E_{cl} = (3 \cdot A)\ MeV$ are shown with red dots connected by a red line. GEMINI calculations are shown by empty dots connected by a dashed line.

reaction. A different sorting of the events included in the analysis will be finally possible, according to dynamic rather than static conditions as the one given in (5.1), once the energy calibration for particles and fragments detected in the RCo will be completed. This will allow to recover some charge partitions which are excluded by the present selection criterion.

The mentioned possible improvements in the decay code, together with the new sorting of the events, could help us in achieving a better reproduction of the charge distribution, thus quantitatively reproducing the observed staggering. A reconstruction of the population of discrete states at the last but one step of the decay chain by means of the correlation function technique, as it is done in [35], will allow us to put constraints on odd-even effects also at finite temperature, thus extracting information on the temperature dependence of the pairing interaction. In particular we will be able to check if the pairing dependence of the level density as extracted from the fit of low-lying resonances in [67] is compatible with independent information on charged particle evaporation, proceeding from high-energy levels lying in the

continuum through discrete states.

Conclusions and Perspectives

Summary of contents

The aim of this thesis has been an attempt to progress towards the reconstruction of nuclear thermal properties by means of fusion-evaporation reactions. In particular, thermal properties of light nuclei have been addressed, for which a strong influence of nuclear structure is expected even at high excitation energy. Properties as the excitation energy dependence of the nucleon effective mass, symmetry energy, pairing correlations and the specificity of the chosen mass and excitation energy region ($A \sim 20$, $e^* \sim 3$ $A.MeV$) are discussed in chapter **1** of this work. The compound nucleus theory, through which thermal properties can be experimentally accessed, is detailed in chapter **2**.
To pursue the proposed investigation, two main efforts were undertaken in this thesis. On the theory side, a dedicated Monte Carlo Hauser-Feshbach code has been developed, which is at most constrained to existing data on ground state properties and low excitation energy spectra. Indeed, the code explicitly includes all the experimentally measured particle unstable levels, available from the online archive NUDAT2, and the implemented level density model ensures a good reproduction of this information. The reliability of the code has been tested, and the predictions for global observables linked to the decay of a compound nucleus source were found to be in good agreement with the results obtained with other existing statistical codes (GEMINI++, PACE4), which are commonly in use in the nuclear physics community. On the other hand, the inclusion of the information on discrete levels allows the calculation of more exclusive observables to be compared to data, as correlation functions in relative momentum, which cannot be done with existing codes. A detailed description of the statistical decay code, together with the code predictions for different observables of interest, is reported in chapter **3**.
Simulations performed with the newly developed code have been used to submit an experimental proposal to the PAC - Physical Advisory Committee - of *Laboratori Nazionali di Legnaro* - LNL - INFN, and the reaction $^{12}C +^{12} C$ at 95 MeV beam

energy, provided by the LNL Tandem XTU accelerator, has been measured, using the GARFIELD+Ring Counter(RCo) apparatuses. The measurement, the experimental apparatuses, the adopted procedures for data reduction, detector calibration and for the selection of the reaction channel are discussed in chapter **4** of this thesis. Finally, in chapter **5**, different results of the data analysis and of the comparison to the code predictions are reported.

Conclusions

In this work the selection of the fusion-evaporation channel out of the entire data set is only preliminary. At the moment, it is based on criteria on the completeness of the detected events and on the need to eliminate the direct channels contribution without having at disposal the energy calibration of the forward detector, in which evaporation residues are measured together with the scattered projectile (or its remnant) in less dissipative collisions. Starting from this preliminary selection, we were able to isolate from the total reaction cross section a contribution which can be identified with the formation and decay of a fused source. We estimate that the chosen selection criterion selects a subset of fusion events, though this subset is expected to be statistically representative. Global observables linked to the decay of this source, as the charge distribution of reaction products, as well as the multiplicity of light charged particles, are well reproduced by the calculations performed with the Hauser-Feshbach code, thus suggesting the formation and decay of an equilibrated source. In particular, a very good agreement with the code predictions is found for the energy and angular distributions of emitted protons detected in GARFIELD ($\theta_{lab} \geq 30°$). This allows to constrain the level density model implemented in the code, by fixing its only free parameter E_{cl} at the value $E_{cl} \approx (3 \cdot A)MeV$. The parameter E_{cl} determines the rapidity with which the energy dependent level density parameter $a(E^*)$ goes from the value necessary to reproduce the information on discrete levels, which represents a constraint in the energy region $e^* \leq 1\ A.MeV$ for $A \sim 20$, up to the value coming from studies on evaporation after fragmentation ($e^* > 2\ A.MeV$), covering a transition region of $\sim 20\ MeV$ for nuclei in this mass region. We want to underline the importance of our result on the excitation energy dependence of $a(E^*)$, which is obtained in this work making use of a level density model strongly constrained by spectroscopic information at low excitation energy. This makes the obtained constraint on the level density parameter more significant, since it removes the general concern of making use of a somewhat arbitrary functional form for the level density, which is usually approximated as the one of a

system of non-interacting nucleons.
Besides the good reproduction of these equilibrium features, strong deviations from the predicted behavior are put in evidence for α particles, which we tentatively attribute to α-clustering effects. We have shown in the analysis that two different contributions to this out-of-equilibrium behavior can be isolated kinematically: one is the extra yield of backward emitted α particles, which corresponds, because of the symmetry of the target-projectile system in the entrance channel, to forward emitted α particles, detectable in the RCo ($5^\circ \leq \theta_{lab} \leq 17^\circ$), with energy close to the beam energy. This seems to suggest the contribution of pre-equilibrium emission followed by incomplete fusion, linked to the α cluster nature of the reaction partners. Because of the current status of the energy calibrations for the RCo detector, we are not able at the moment to compare the energy spectra of α particles emitted at very forward angles to the code predictions, in order to verify our kinematic considerations.
A different mechanism seems to be at the origin of an energy bump, which is observed in the spectrum of α particles detected in the forward GARFIELD CsI: we have shown in the analysis that these particles are typically detected in coincidence with a $Z_{res} = 8$ fragment, and, taking into account the symmetry of the system, we have shown that they are emitted at central θ angles in the center-of-mass reference frame, and at reduced energies with respect to the beam energy. These α particles can be associated therefore to more dissipative events, corresponding to the decay of a fused source, preferentially leaving an oxygen residue. We may therefore attribute the presence of this energy bump to cluster emission on the path towards thermalisation of the hot source formed in the collision, due to the possible preformation of α particles.

Perspectives

In the near future, we plan to complete the energy calibration of the RCo detector. This will allow us to make use of kinematic rather than static conditions to select the reaction channel, thus enlarging the set of events which can be used for the analysis, relaxing the strict conditions which we have made use of in this work. Having at disposal a set of completely calibrated events, we will be able to further verify the adequacy of the model, and, in particular, to reveal the presence of the expected deviations in the spectrum of forward emitted α particles, connected to pre-equilibrium emission followed by incomplete fusion. Finally, we will also be able to calculate more exclusive observables as relative momentum distributions for

couples of coincident particles. From the experimental correlation functions, we will be able to recover the information on the population of discrete states at the last but one step of the decay chain. Also this information can be compared to the code predictions, and the comparison will allow us to put stringent constraints on finite temperature properties. In particular, we plan to perform the same analysis as in ref.[35], in order to confirm/infirm the results on the presence of staggering in finite temperature distributions, and to get information on the temperature dependence of the pairing interaction.

We also plan to compare our experimental data to the predictions of existing codes as MCFx [99], which makes use of the exciton model formalism and includes pre-equilibrium emission, both in the entrance channel of the reaction and as a possible consequence of cluster preformation in the fused source. This can be done through direct collaboration with the code owners.

Even more interesting would be in the future to directly implement in our decay code the exciton model formalism, which is based on assumptions completely compatible with the Hauser-Feshbach formalism. The advantage with respect to the comparison or coupling to existing codes would be the use of the same physical ingredients (in particular, level density and transmission coefficients) in a unified description of both equilibrium and out-of-equilibrium properties. This would allow to put even more stringent constraints on the physical quantities of interest.

An interesting perspective is also the implementation in our code of a simultaneous break-up channel, which could be described for instance in terms of the Fermi break-up formalism, taking into account densities of excited states [100]. As it is shown in this work, this would in principle improve the description of the charge and mass regions intermediate between the light evaporated particles and the residues. In particular, this inclusion will be necessary if we plan to investigate the properties of light systems at even higher excitation energy, where channels other than sequential decay are opening.

We have briefly discussed in this work the connection between the disappearance of compound nucleus states and the opening of multifragmentation: this translates in a high energy constraint on the level density parameter $a(E^*)$, which has to go to zero at a limiting excitation energy. This constraint could be deduced from the comparison of the predictions of a statistical code, in which both the evaporative and the fragmentation regimes can be attained, with experimental data for reactions at the threshold of multifragmentation. The feasibility of this project is demonstrated in Appendix **B** of this thesis, where we show some preliminary results on the coupling between the Microcanonical Multifragmentation Model - MMM [69] and our

Hauser-Feshbach code, which can be implemented in MMM as a secondary decay code, making use of the same level density model described in this work, with the addition of the decreasing part in the functional form $a(E^*)$, to mimic the existence of the nuclear limiting energy. The addition of the high energy constraints on $a(E^*)$ going to zero would mean to have at disposal a series of constraints, coming from independent measurements, covering the whole excitation energy range for the level density parameter. This is a promising long range perspective, which we plan to follow through direct collaboration with the MMM code owners.
On the experimental side, the results presented in this work will be at the basis of the submission of new proposals, concerning the study of different reactions involving light nuclei. In particular, it would be interesting for instance to populate the same ^{24}Mg compound nucleus with a different entrance channel, in order to disentangle the effects linked to the cluster structure of projectile and target in the reaction studied in this work. However, given the light nature of the system, it is easy to understand that very few projectile-target combinations can be proposed, without turning to unstable isotopes. Because of that, a letter of intents [101], based on calculations done with our newly developed code, has been submitted by the NUCL-EX collaboration on occasion of the last SPES International Workshop, held at LNL in November 2010. In this LoI, the reaction $^{17}F(@100\ MeV) +^{7} Li$, leading in case of complete fusion to a ^{24}Mg source at $e^* \sim 2.5\ A.MeV$ was explicitly listed among other possible ones to be studied. More generally, the future availability of light exotic beams, both at SPES (LNL, Italy) and SPIRAL2 (GANIL, France), will provide an inviting opportunity to investigate at the same time different physical issues: the open field of investigation goes from the competition of different reaction mechanisms, projectile break-up and fusion (given the weakly bound nature of the projectiles), to an extension to reactions with radioactive beams of the study on the statistical behavior of hot light nuclei presented in this work, including the isospin dependence of the nuclear level density [102].
Great efforts are currently undertaken in the nuclear physics community concerning the $R\&D$ of new performant detectors, which have also to be able to overcome the experimental difficulties related to measurements with low intensity and lower energy radioactive beams. In particular, as it is also discussed in our LoI, the coupling of new generation detectors for charged particles and γ (and neutrons) is highly desirable in our future studies on these topics, in order to have the maximum of information from the same experimental set-up, especially to ensure the selection of the reaction channel of interest.

Appendix A

Reference Frame Rotational Transformations

The angular momentum vector $\mathbf{J_0}$ of the decaying hot nucleus is given, and its space orientation in the **CM** RF (z-axis parallel to the beam velocity) is specified by the spherical coordinates angles $(\theta_{J_0}; \varphi_{J_0})$.
$\mathbf{J_d}$ is the angular momentum vector of the daughter nucleus, and its orientation is given by the angles $(\theta; \phi)$ in the RF whose z-axis is parallel to $\mathbf{J_0}$ (**J0** RF, fig.(A.1)).
We want to derive an expression for the angles $(\theta_{J_d}; \varphi_{J_d})$ as a function of $(\theta_{J_0}; \varphi_{J_0})$ and $(\theta; \varphi)$, which will give us the orientation of vector $\mathbf{J_d}$ in the **CM** RF.
This means writing the equations of the $\mathbf{J0} \xrightarrow{rot} \mathbf{CM}$ rotation of RF.

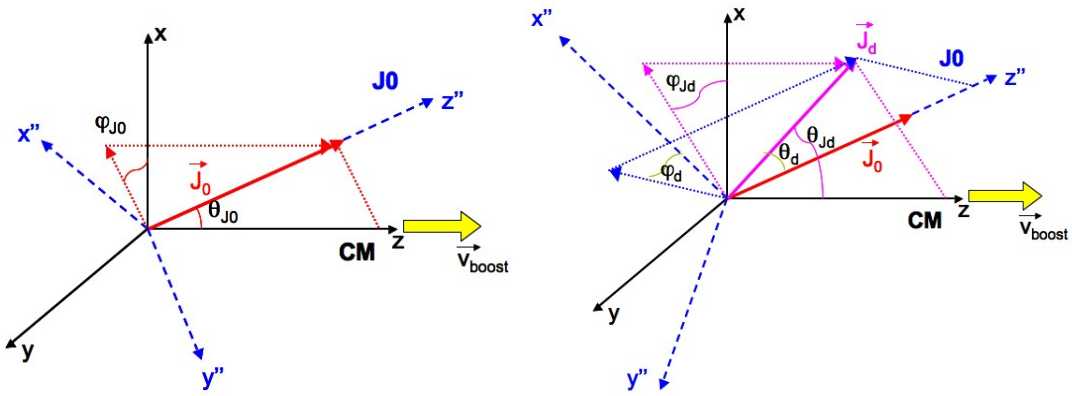

Figure A.1: Left side: **CM** e **J0** reference frames; right side: components of vector $\mathbf{J_d}$ in the two coordinate systems. The use of the notation (x'', y'', z'') for the axes of **J0** is made clear in the text.

In order to derive the equations for the rotational transformation we have to write the **J0** RF versors in terms of the initial **CM** RF ones. Let us decompose the transformation into two successive rotations, the first one by (φ_{J_0}) in the xy plane and the second one by (θ_{J_0}) in the zx plane. From now on we will write: $\varphi_{J_0} = \varphi_0$;

$\theta_{J_0} = \theta_0$.

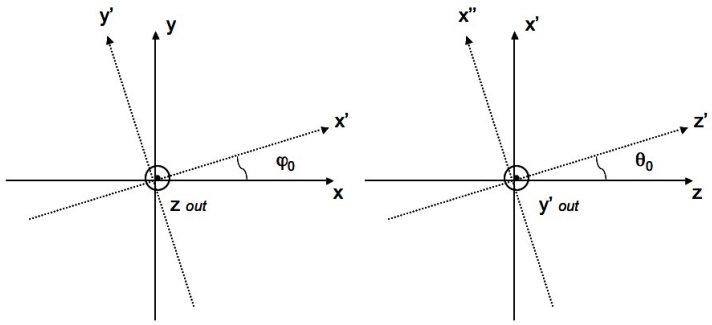

Figure A.2: On the left: rotation by φ_0 in the xy plane; on the right: rotation by θ_0 in the $zx^{'}$ plane.

For the first rotation in fig.(A.2) we have:

$$\begin{aligned} \hat{u}_x^{'} &= \cos\varphi_0\ \hat{u}_x + \sin\varphi_0\ \hat{u}_y \\ \hat{u}_y^{'} &= -\sin\varphi_0\ \hat{u}_x + \cos\varphi_0\ \hat{u}_y \end{aligned} \tag{2}$$

The z-axis is still perpendicular to the transformed $x^{'}$-axis.
For the following rotation (on the right side of fig.(A.2)) we find:

$$\begin{aligned} \hat{u}_x^{''} &= -\sin\theta_0\ \hat{u}_z + \cos\theta_0\ \hat{u}_x^{'} \\ \hat{u}_z^{'} &= \cos\theta_0\ \hat{u}_z + \sin\theta_0\ \hat{u}_x^{'} \end{aligned} \tag{3}$$

The $(\hat{u}_x^{''}, \hat{u}_y^{''}, \hat{u}_z^{''})$ versors of **J0** RF can be therefore written as:

$$\begin{aligned} \hat{u}_x^{''} &= \cos\theta_0\cos\varphi_0\ \hat{u}_x + \cos\theta_0\sin\varphi_0\ \hat{u}_y - \sin\theta_0\ \hat{u}_z \\ \hat{u}_y^{''} = \hat{u}_y^{'} &= -\sin\varphi_0\ \hat{u}_x + \cos\varphi_0\ \hat{u}_y \\ \hat{u}_z^{''} = \hat{u}_z^{'} &= \sin\theta_0\cos\varphi_0\ \hat{u}_x + \sin\theta_0\sin\varphi_0\ \hat{u}_y + \cos\theta_0\ \hat{u}_z \end{aligned} \tag{4}$$

A generic vector **v**, given in the **J0** RF, can be written in the **CM** RF thanks to

the transformations derived in (4):

$$\begin{aligned} \mathbf{v} &= v_1^{''}\ \hat{u}_x^{''} + v_2^{''}\ \hat{u}_y^{''} + v_3^{''}\ \hat{u}_z^{''} \\ &= (v_1^{''}\cos\theta_0\cos\varphi_0 - v_2^{''}\sin\varphi_0 + v_3^{''}\sin\theta_0\cos\varphi_0)\ \hat{u}_x \\ &\quad +(v_1^{''}\cos\theta_0\sin\varphi_0 + v_2^{''}\cos\varphi_0 + v_3^{''}\sin\theta_0\sin\varphi_0)\ \hat{u}_y \\ &\quad +(-v_1^{''}\sin\theta_0 + v_3^{''}\cos\theta_0)\ \hat{u}_z \end{aligned} \tag{5}$$

Vector **v** components in **J0** are:

$$\begin{aligned} v_1^{''} &= \sin\theta\cos\varphi \\ v_2^{''} &= \sin\theta\sin\varphi \\ v_3^{''} &= \cos\theta \end{aligned} \tag{6}$$

and for their expressions in **CM** we have:

$$\begin{aligned} \mathbf{v} &= v_1\ \hat{u}_x + v_2\ \hat{u}_y + v_3\ \hat{u}_z \\ &\textit{where} \\ v_1 &= \sin\theta\cos\varphi\cos\theta_0\cos\varphi_0 - \sin\theta\sin\varphi\sin\varphi_0 + \cos\theta\sin\theta_0\cos\varphi_0 \\ v_2 &= \sin\theta\cos\varphi\cos\theta_0\sin\varphi_0 + \sin\theta\sin\varphi\cos\varphi_0 + \cos\theta\sin\theta_0\sin\varphi_0 \\ v_3 &= -\sin\theta\cos\varphi\sin\theta_0 + cos\theta\cos\theta_0 \end{aligned} \tag{7}$$

Given the (v_1, v_2, v_3) components, the angles which give us the orientation of **v** in the **CM** RF can be therefore written as:

$$\begin{aligned} \theta_{v\ CM} &= \arccos(v_3) && \rightarrow \theta_{v\ CM} \in [0;\pi] \\ \varphi_{v\ CM} &= \arctan\left(\frac{v_2}{v_1}\right) && \rightarrow \varphi_{v\ CM} \in [-\pi/2;\pi/2] \end{aligned} \tag{8}$$

In our case, **CM** angles $(\theta_{J_d};\varphi_{J_d})$ of $\mathbf{J_d}$ can be obtained thanks to the equations derived in this Appendix.

Appendix B

Constraining the Level Density at High Excitation Energy

In this Appendix we present some preliminary results obtained by implementing the level density model discussed in chapter **3** of this work in the Microcanonical Multifragmentation Model [69], through direct collaboration with the code owners. In this thesis work, we have been able to give a constraint on the level density parameter dependence on excitation energy, for nuclei in the mass region $A \sim 20$, by comparing our Hauser-Feshbach calculations to exclusive fusion-evaporation data for the reaction ^{12}C (@95 $A.MeV$) $+^{12} C$.
In particular, we have constrained the increase of this parameter, starting from the low energy value determined in [67], necessary to fit the spectroscopic information on discrete levels, up to an asymptotic value, which is in turn constrained by fusion-evaporation or evaporation after fragmentation data [74]. At the energy of the reaction under study, the evaporative regime is by far the dominant, and no competitive break-up channels were implemented in our decay code: this obviously means that the code can be used to obtain predictions for the output of reactions at energies below the onset of multifragmentation (or break-up for lighter nuclei).
What we expect at higher energies, where the fragmentation regime can be attained, is that compound nucleus states start disappearing. This can be described in terms of the existence of a limiting nuclear temperature (or excitation energy per nucleon) [39]. A usual way to mimic the existence of a limiting temperature in multifragmentation applications is to add an exponential cut-off to the LD used in the calculations. This is also the case of MMM, where the following parameterization for $\rho(E^*)$ is adopted:

$$\rho(E^*) = \frac{\sqrt{\pi}}{12a^{1/4}E^{*\ 5/4}}\ \exp(2\sqrt{aE^*})\exp(-E^*/\tau), \tag{9}$$

with $a(A) = 0.114A + 0.098A^{2/3}\ MeV^{-1}$ and $\tau = 9\ MeV$.

It is clear that such a procedure is not satisfactory. Indeed the application of

an exponential cut-off affects in an uncontrolled way the level density for all excitation energies, even below the fragmentation threshold. In order to have a unique coherent description of compound nucleus decay, instead of applying a cut-off to the LD in the whole excitation energy range, it is necessary to coherently ascribe the disappearance of CN states to a decrease of $a(E^*)$ with increasing energy, when approaching the limiting excitation energy, while keeping an unmodified expression for $\rho(E^*)$. This means that, after a certain energy, the value for the LD parameter has to fall to zero, the more abruptly the more rapid is the threshold process of the onset of multifragmentation. The aim of this Appendix is to show that, if such a decreasing trend for the LD parameter is implemented in the level density model, in a decay code where both the evaporative and the fragmentation regime can be reproduced, then the comparison to data for reactions at the threshold of multifragmentation may provide an additional high energy constraint on $a(E^*)$ going to zero. The addition of this high energy constraint would mean to have at disposal a series of contraints, coming from independent measurements, covering the whole excitation energy range for the level density parameter.

We show in the following the results of MMM calculations for the decay of a $(A, Z) = (80, 40)$ source, by varying the input excitation energy per nucleon in the range $e^* = 1 \div 8\ A.MeV$, and by making use of the different input level densities shown in fig.(B.1), referred to as case **1**,**2** and **3**, and later detailed[1]. Also the standard $\rho(E^*)$ implemented in MMM is plotted as a reference in fig.(B.1).

In particular, we give the results for two different observables, linked to the onset of multifragmentation: the charge distribution at the break-up stage of the decay, and the average excitation energy of primary fragments as a function of their charge. Both these observables are therefore given before secondary decay of excited fragments take place. For each input level density, we also report in a table the average multiplicity of decay products per event NF (including nucleons), an asymmetry coefficient between the first and second biggest fragment, calculated as $asym = (Z_{1\ big} - Z_{2\ big})/(Z_{1\ big} + Z_{2\ big})$ and finally the percentages of evaporation, fission and multifragmentation - like decays, defined in an arbitrary way with respect to the number N_3 of $Z \geq 3$ fragments, being respectively N_3=1, 2, ≥ 3.

[1]All MMM calculations presented in this Appendix are performed with a fixed value of the freeze-out volume, which is an input parameter of the model, and is set in this case at the $V = 3V_0$ value. A free volume parameterization, taking into account intrinsic fragment volumes, is implemented in this version of MMM. This approximation is more realistic than the one used in the standard version, where fragments are assumed to have equal intrinsic volumes. The variation of the freeze-out volume with the initial excitation energy should also be taken into account.

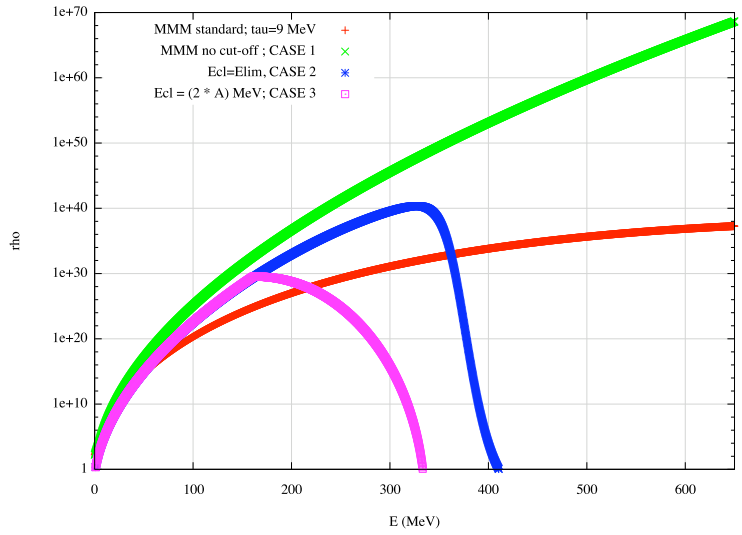

Figure B.1: For the $(A, Z) = (80, 40)$ nucleus, level density $\rho(E^*)$ functional forms used as an input for the MMM calculations presented in this Appendix: in red, the standard LD of eq.(9) implemented in MMM is given as a reference. In green: $\rho(E^*)$ resulting from the suppression of the exponential cut-off in the standard MMM expression of eq.(9), case **1**; in blue, $\rho(E^*)$ from eq.(10), with a decrease of the LD parameter obtained by a Fermi function factor acting at the limiting E_{lim} of ref.[39], case **2**; in pink, $\rho(E^*)$ from eq.(10), with a linear decreasing behavior of the LD parameter starting from $E_{cl} = (2 \cdot A)\ MeV$, case **3**. More details for each case are given in the text.

Case 1

Firstly, we have run MMM with its standard LD expression of eq.(9), by simply suppressing the exponential cut-off factor, *i.e.* taking $\tau = 10^{10}\ MeV$ as an input value, in order to verify the effect of an unlimited growth of the LD on primary partitions.
As anticipated, we can observe in fig.(B.1) that the use of a cut-off deforms the level density behavior even in the region where this latter is constrained by evaporation. What we observe from the observables reported in fig.(B.2) and from the values reported in table B.1 is that:

- the percentage of evaporation-like events decreases when the source excitation increases;
- coherently, by increasing e^*, the percentage of multifragmentation events increases as expected, even if the onset of multifragmentation occurs only at

e^* $A.MeV$	NF	asym	evap	fission	mult
1.	2.020256	0.961142	9.996537e-01	3.462604e-04	0.000000e+00
2.	2.158084	0.954625	9.830935e-01	1.690648e-02	0.000000e+00
3.	2.412448	0.931568	9.031242e-01	9.585344e-02	1.022328e-03
4.	2.768824	0.862999	7.161684e-01	2.709144e-01	1.291727e-02
5.	3.234441	0.732020	4.490304e-01	4.681276e-01	8.284198e-02
6.	3.809924	0.570686	2.186998e-01	5.270340e-01	2.542663e-01
7.	4.444491	0.439892	9.173253e-02	4.400822e-01	4.681853e-01
8.	5.040623	0.349554	3.911129e-02	3.078288e-01	6.530599e-01

TABLE B.1: Results for MMM calculation for the input level density of case **1**: NF is the average event multiplicity, including nucleons; $asym$ is an asymmetry coefficient between the first and second biggest fragment, defined as $asym = (Z_{1\ big} - Z_{2\ big})/(Z_{1\ big} + Z_{2\ big})$; the percentages of evaporation, fission, and multifragmentation - like events are defined with respect to the number of $Z \geq 3$ fragments, respectively as N_3=1, 2, $\geq$ 3, or 0 events.

$e^* = 5\ A.MeV$, which is higher than expected for a source of this size;

- break-up fragments internal excitation increases with the source excitation, but the value of this quantity is found to be much higher with respect to MMM predictions for an input LD with the exponential cut-off, and with respect to what is known from calorimetry on multifragmentation data [18, 19];

The following conclusion can be drawn from this illustrative example: if the growth of the LD is not moderated, when partitioning the system, even at high energy, it is more preferable to spend the available energy into internal excitation rather than spending it in producing fragments. The onset of multifragmentation is therefore delayed, and the excitation energy stored in primary fragments is high.

Case 2

As a second try, we have implemented in MMM our level density model, described in chapter **3**, and given by:

$$\rho(E^*) = \frac{\exp\left[2\sqrt{a\,(E^* - \Delta)}\right]}{12\sqrt{2}\sigma a^{1/4}\,(E^* - \Delta)^{5/4}} \tag{10}$$

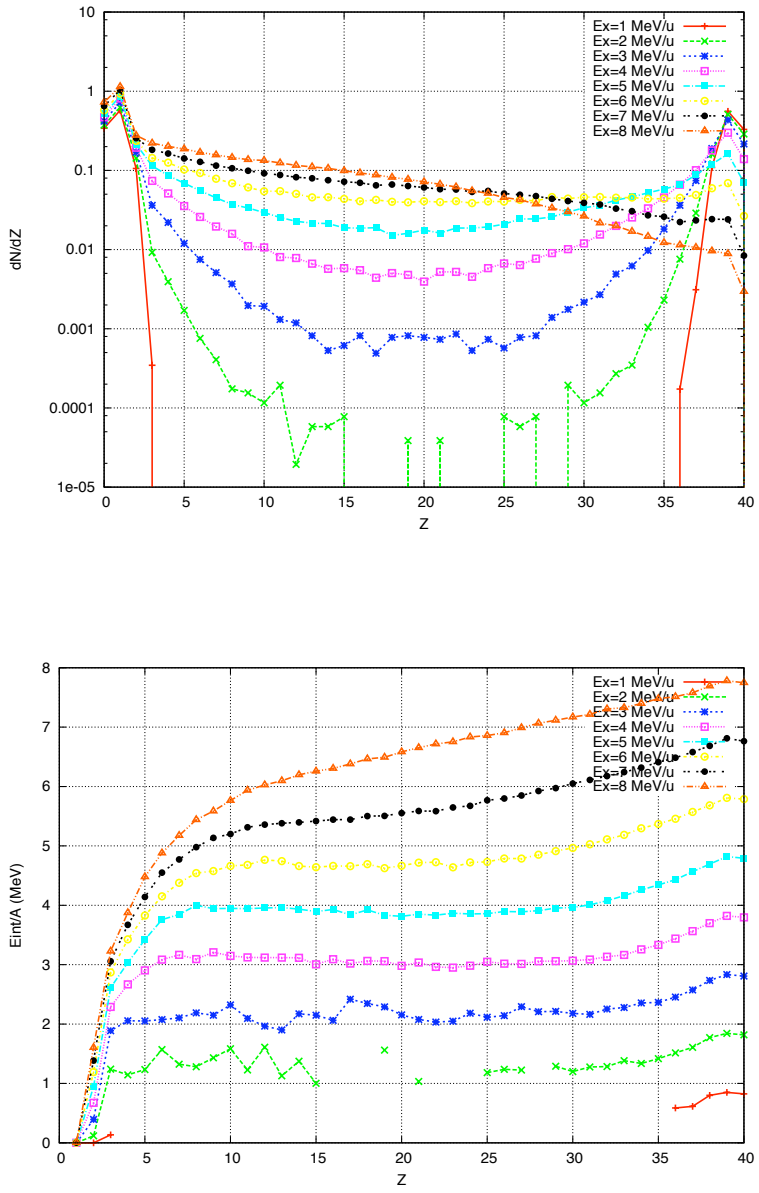

Figure B.2: MMM predictions for the decay of a $(A, Z) = (80, 40)$ source, with the LD model described in case **1**, and for different input source excitation energies ranging from $e^* = 1$ up to 8 $A.MeV$. In the top panel, charge distribution at the break-up stage of the decay; in the bottom, average excitation energy of primary fragments as a function of their charge. Normalization is to the number of simulated events.

e^* $A.MeV$	NF	asym	evap	fission	mult
1.	2.016237	0.477561	8.969124e-02	9.103088e-01	0.000000e+00
2.	2.662606	0.770432	5.303867e-01	4.273421e-01	4.227116e-02
3.	3.168366	0.706050	4.155123e-01	4.463352e-01	1.381525e-01
4.	3.696269	0.605499	2.707188e-01	4.616309e-01	2.676503e-01
5.	4.382287	0.48167	1.228095e-01	4.316833e-01	4.455072e-01
6.	5.104719	0.395731	6.147925e-02	3.235202e-01	6.150005e-01
7.	5.789191	0.34422	4.514071e-02	2.350612e-01	7.197981e-01
8.	6.405834	0.321400	4.476896e-02	1.843206e-01	7.709105e-01

TABLE B.2: As in Table B.1, results for MMM calculation for case **2**.

where $a(E^*)$ is such that $a(E_{cl}) \approx a_\infty$, with $a_\infty = A/14.61 \cdot (1 + 3.114 \cdot A^{-1/3} + 5.626 \cdot A^{-2/3})$. As discussed in chapter **3**, the E_{cl} parameter represents the energy limit at which the asymptotic value of the LD parameter is reached, and it has to be $E_{cl} \leq E_{lim}$, where E_{lim} is the limiting excitation energy. We are then interested in this case in exploring the behavior of $a(E^*)$ when E^* approaches E_{lim}. For the limiting excitation energy we adopt the following energy-dependent form, obtained from a fit on the results presented in [39]:

$$E_{lim}(A) = \begin{cases} (8 \cdot A)\ MeV & for \quad A \leq 40 \\ (4.99 - 61.68/\sqrt{A} + 487.3/A) \cdot A\ MeV & for \quad A > 40 \end{cases} \tag{11}$$

which yields $E_{lim}(80) \approx 4\ A.MeV$ for our source.

We have then assumed that $E_{cl} \approx E_{lim}$, *i.e.* that the asymptotic value of the LD parameter is reached at the limiting excitation energy, and the fall to zero of $a(E^*)$ has consequently to be abrupt at this limiting value. In order to mimic the rapid decrease of the LD parameter we have multiplied $a(E^*)$ by a Fermi function: $f(E^*, T, \mu) = 1/(1 + \exp(E^* - \mu)/T)$, where μ and T are two arbitrary parameters controlling the decreasing behavior. Values of the parameters in our calculations are: $T = 10\ MeV$, $\mu = 1.1\ E_{cl}$.

Results for this case, shown in fig.(B.3) and reported in table B.2, confirm that the addition of the cut-off in the LD parameter causes a shift towards lower energies of the onset of multifragmentation, which now represents the dominant contribution starting from $e^* = 5 \div 6\ A.MeV$. Primary fragments are still very excited at the break-up stage.

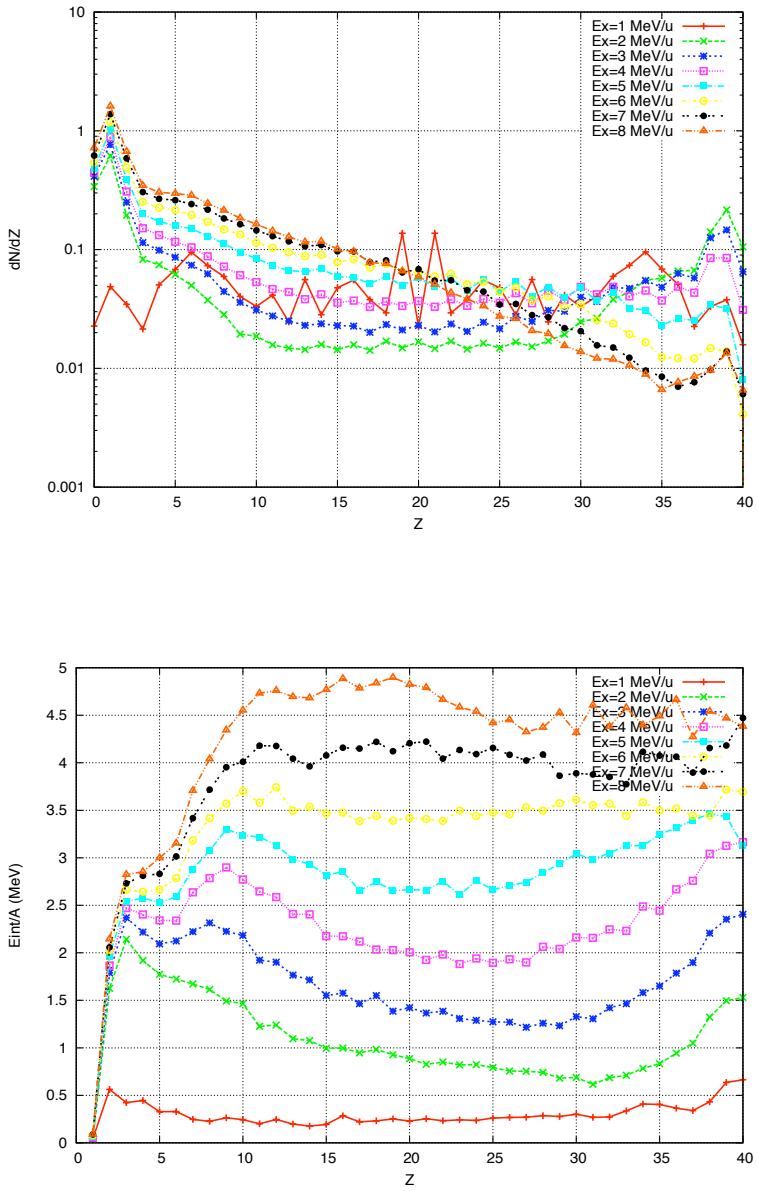

Figure B.3: The same as in fig.(B.2), with the LD model of case **2**.

Case 3

Starting from the same LD model of eq.(10), with the same parameterizations for $a_\infty(A)$ and $E_{lim}(A)$, we have assumed in this last case that the asymptotic value

e^* $A.MeV$	NF	asym	evap	fission	mult
1.	2.02534	0.630422	4.660628e-01	5.339372e-01	0.000000e+00
2.	2.190603	0.892525	8.390649e-01	1.594730e-01	1.462077e-03
3.	3.036082	0.563509	1.324091e-01	7.686728e-01	9.891818e-02
4.	4.308974	0.378543	1.311145e-02	2.631145e-01	7.237741e-01
5.	5.619426	0.291714	1.517168e-03	5.053639e-02	9.479464e-01
6.	6.953861	0.247165	3.285614e-04	1.023234e-02	9.894391e-01
7.	8.304090	0.219006	8.280077e-05	2.860390e-03	9.970568e-01
8.	9.641605	0.187680	4.780964e-05	1.024492e-03	9.989277e-01

TABLE B.3: As in Table B.1, results for MMM calculation for case **3**.

of $a(E^*)$ is reached at an excitation energy value E_{cl} lower than E_{lim}. The decrease of $a(E^*)$ then starts beyond E_{cl}, and is such that $a(E_{lim})$ is equal to zero. As a first guess, we have adopted the value $E_{cl} = (2 \cdot A)\ MeV$, and implemented a simple linear decrease of $a(E^*)$ from $a(E_{cl}) = a_\infty(A)$ to zero. Results for this case shown in fig.(B.4) and reported in table B.3 show that the onset of multifragmentation correponds to $e^* = 4\ A.MeV$, which is in agreement with what expected for a source of this size, and break-up fragments are generally less excited than in case **2**, because of the limited growth of $\rho(E^*)$.

Final remarks

The preliminary results reported in this Appendix show that the decrease of the LD parameter strongly affects the onset of multifragmentation. The interesting perspective of this work is to be able to experimentally constrain this decrease, by comparing data for reactions at the threshold of fragmentation to the predictions of multifragmentation codes, in which a level density model of the type described in this work is implemented. Finally, the Hauser-Feshbach code presented in this thesis can be used as a secondary evaporation code for excited fragments produced at the break-up stage. Such an approach allows us to obtain a unified description of evaporation and multifragmentation, coherently ascribing the transition between these two regimes to the behavior of the LD parameter $a(E^*)$.

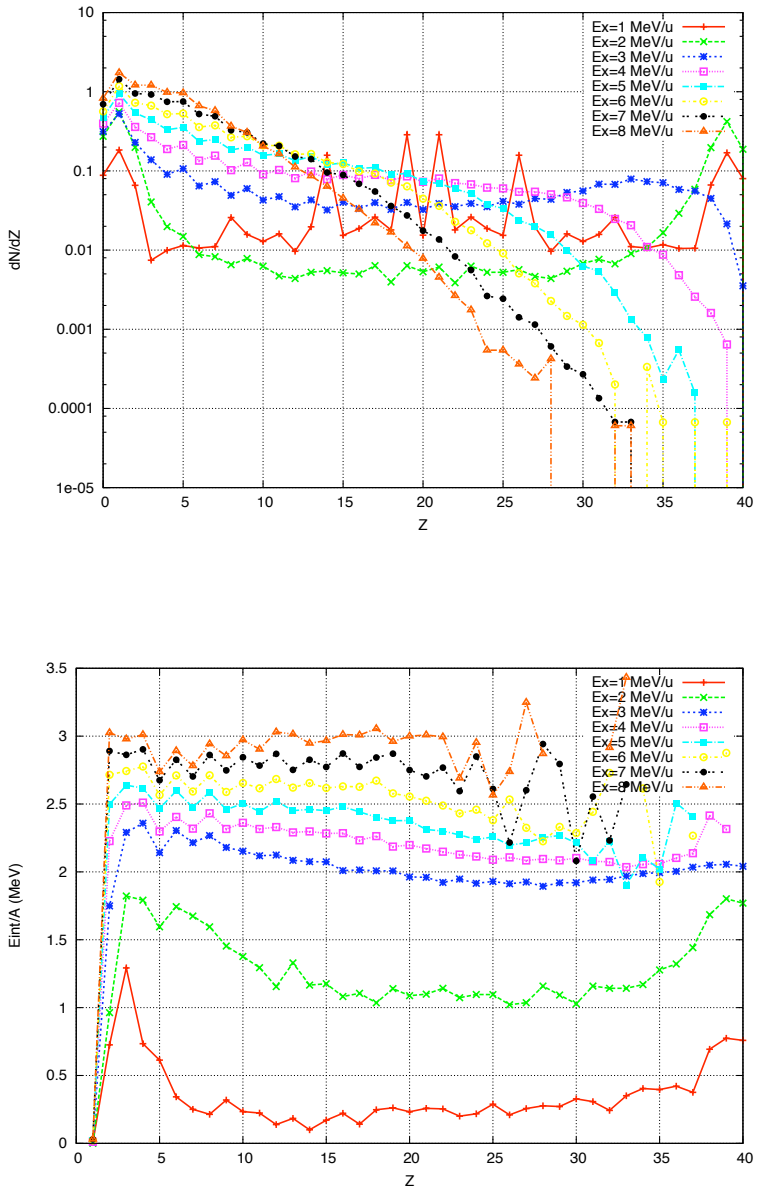

Figure B.4: The same as in fig.(B.2), with the LD model of case **3**.

Bibliography

[1] A. Bohr, B. R. Mottelson, Nuclear Structure Vols. I and II, Benjamin, New York, USA (1964).

[2] H. A. Bethe, Phys. Rev. 50 (1936).

[3] W. Dilg, W. Schantl, H. Vonach and M. Uhl, Nucl. Phys. A 217, 2, 269 (1973).

[4] A. V. Ignatyuk *et al.*, Sov. J. Nucl. Phys. 21 255 (1975).

[5] A. F. Fantina, *Supernovae Theory: Study of Electro-Weak Processes during Gravitational Collapse of Massive Stars*, PhD Thesis, Université Paris Sud - IPN Orsay, Universitá di Milano (2010)

[6] P. Donati *et al.*, Phys. Rev. Lett. 72, 2835 (1994).

[7] S. Shlomo, J. B. Natowitz, Phys. Lett. B 252, 187 (1990).

[8] S. Shlomo, J. B. Natowitz, Phys. Rev. C 44, 2878 (1991).

[9] G. Nebbia *et al.*, Phys. Lett. B 176, 1-2, 20 (1986).

[10] A. Chbihi *et al.*, Phys. Rev. C 43, 666 (1991).

[11] B. Fornal *et al.*, Phys. Rev. C44, 2588 (1991).

[12] G. Baym *et al.*, Nucl.Phys. A 175 225 (1971).

[13] P. Danielewicz, Nucl. Phys. A 727 233 (2003).

[14] D. V. Shetty *et al.*, J. Phys. G 36 075103 (2009).

[15] S. K. Samaddar, J. N. De, X. Viñas, M. Centelles, Phys. Rev. C 76, 041602(R) (2007).

[16] S. K. Samaddar, J. N.De, X.Viñas, M. Centelles, Phys. Rev. C 78, 034607 (2008).

[17] Ad. R. Raduta and F. Gulminelli, Phys. Rev. C 75, 044605 (2007).

[18] N. Marie *et al.*, Phys. Rev. C 58, 256 (1998).

[19] S. Hudan *et al.*, Phys. Rev. C 67, 064613 (2003).

[20] D. J. Rowe, *Nuclear Collective Motion, Models and Theory*, Methuen and co. LTD.

[21] K. L. G.Heyde, *The Nuclear Shell Model*, Springer Verlag (1990).

[22] J. M. Eisenberg, W. Greiner, *Microscopic Theory of the Nucleus*, North-Holland (1972).

[23] A. Schiller *et al.*, Phys. Rev. C 66, 024322 (2002).

[24] J. Su *et al.*, Phys. Rev. C 83 014608 (2011).

[25] A. Ono, AIP Conf. Proc. 884 292 (2007).

[26] I. Lombardo *et al.*, Phys. Rev. C 84, 024613 (2011).

[27] M. V. Ricciardi *et al.*, Nucl.Phys. A 733 (2004).

[28] M. V. Ricciardi *et al.*, arXiv-1007.0386v1.

[29] G. Ademard *et al.*, Phys. Rev. C 83, 054619 (2011).

[30] R. J. Charity *et al.*, Phys. Rev. C 63, 024611 (2001).

[31] M. D'Agostino *et al.*, Nucl. Phys. A 861 47 (2011).

[32] J. Pochodzalla *et al.*, Phys. Rev.C 35 1695 (1987).

[33] T. K. Nayak *et al.*, Phys. Rev. C 45 132 (1992).

[34] W. P. Tan *et al.*, Phys. Rev. C 69 061304(R) (2004).

[35] M. D'Agostino *et al.*, Nucl. Phys. A (2010) *in press*, doi:10.1016/j.nuclphysa.2011.11.011

[36] L. F. Canto *et al.*, Phys. Rep. 424 1 (2006) and references therein.

[37] S. Adhikari *et al.*, Phys. Rev. C 74 024602 (2006).

[38] C. Basu *et al.*, Phys. Rev. C 76 034609 (2007).

[39] J. B. Natowitz *et al.*, Phys. Rev. Lett. 89 212701 (2002).

[40] A. Gökmen *et al.*, Phys. Rev. C 29 1606-161 (1984).

[41] T. Neff, H. Feldmeier, Nucl. Phys. A 738 357 (2004).

[42] M. Freer, Rep. on Prog. in Phys. 70 2149 (2007).

[43] Ad. R. Raduta *et al.*, Phys. Lett., B, 705 65 (2011).

[44] H. Matsumura and Y. Suzuki, Nucl. Phys. A 739 238 (2004).

[45] G. Baiocco *et al.*, *Statistical (?) Decay of Hot Light Nuclei*, Experimental Proposal to the PAC Committe of LNL-INFN, July 2010.

[46] R. J. Charity, Phys. Rev. C 82 014610 (2010).

[47] R. G. Stokstad, *Treatise on Heavy-Ion Science*, ed. D.A. Bromley, Vol. 3 (1985).

[48] P. Fröbrich and L. Lipperheide, *Theory of Nuclear Reactions*, ed. Oxford Science Publications (1996).

[49] D. L. Hill, J. A. Wheeler, Phys. Rev. 89, 1102 (1953).

[50] J. M. Blatt and V. F. Weisskopf, *Theoretical Nuclear Physics*, ed. Dover Publications (1979).

[51] W. Hauser and H. Feshbach, Phys. Rev. 87 2 (1952).

[52] V. Weisskopf, Phys. Rev. 52 (1937).

[53] A. V. Voinov *et al.*, Phys. Rev. C76 044602 (2007).

[54] D. Vautherin, Adv. Nucl. Phys. 22 123 (1996).

[55] W. Nörenberg and H. A. Weidenmüller, *Introduction to the Theory of Heavy-Ion Collisions*, ed. Springer-Verlag (1980).

[56] S. Hilaire, Lecture given at the *Workshop on Nuclear Data and Nuclear Reactors: Physics, Design and Safety*, Trieste (2000).

[57] G. H. Lang *et al.*, Phys. Rev. C 48, 4, (1993).

[58] Y. Alhassid, *International Conference on Nuclear Data for Science and Technology*, 1283, Santa Fe, NM, USA (2004).

[59] Y. Alhassid, G. F. Bertsch and L. Fang, Phys. Rev. C 68 044322 (2003).

[60] H. Nakada and Y. Alhassid, Phys. Rev. C 78 051304(R) (2008).

[61] A. Gilbert and A. Cameron, Can. J. Phys. 43 1446 (1965).

[62] A. Kelić *et al.*, *ABLA07 - Towards a complete description of the decay channels of a nuclear system from fission to multifragmentation*, Proceedings of the Joint ICTP-IAEA Advanced Workshop on Model Codes for Spallation Reactions, ICTP Trieste, Italy, IAEA (Vienna,2008);

[63] S. Bjørnholm, A. Bohr and B. R. Mottelson, *Proc.Int.Conf. on the Physics and Chemistry of Fission*, Rochester 1973 Vol. 1, p. 367, (IAEA Vienna 1974).

[64] A. R. Junghans *et al.*, Nucl. Phys. A629 635 (1998).

[65] *http://www-nds.iaea.org/ripl2/*

[66] *http://www.talys.eu/*

[67] T. Von Egidy and D. Bucurescu, Phys. Rev. C72 044311 (2005); Phys. Rev. C 73 049901(E) (2006).

[68] M. G. Mustafa, M. Blann, A. V. Ignatyuk, Phys. Rev. C 48 2 (1993).

[69] Al. H. Raduta and Ad. R. Raduta, Phys. Rev. C 55 1344 (1997); 56 2059 (1997); 59 323 (1999).

[70] *http://www.nndc.bnl.gov/amdc/*

[71] *//www.nndc.bnl.gov/nudat2/*

[72] Z. Chen and C. K. Gelbke, Phys. Rev. C 38 6 2630 (1988).

[73] A. V. Ignatyuk *et al.*, Sov. J. Nucl. Phys. 21 255 (1975); A. S. Iljinov *et al.*, Nucl. Phys. A 543 450 (1979).

[74] J. Töke, W. J. Swiatecki, Nucl. Phys. A 372, 141 (1981).

[75] *http://www.chemistry.wustl.edu/˜rc/gemini++/*

[76] L. G. Moretto, Nucl. Phys. A 247 211 (1975).

[77] N. Bohr and J. A. Wheeler, Phys. Rev. 56 426 (1939).

[78] A. J. Sierk, Phys. Rev. C 33 2039 (1986).

[79] L. Bardelli *et al.*, Nucl. Instr. and Meth. A 491, 244 (2002);

[80] G. Pasquali *et al.* Nucl. Instr. ad Meth. A570 126 (2007).

[81] L. Bardelli *et al.* Nucl. Instr. ad Meth. A560 517 (2006).

[82] L. Bardelli *et al.* Nucl. Instr. ad Meth. A560 524 (2006).

[83] F. Gramegna *et al.*, Nucl. Instr. and Meth A389 474 (1997); F. Gramegna *et al.*, IEEE Nucl. Science Symposium, Rome (2004).

[84] M. Chiari *et al.* Nucl. Instr. and Meth. A484 111 (2002).

[85] R. Bassini *et al.* Nucl. Instr. ad Meth. A305 449 (1991).

[86] F. Tonetto *et al.* Nucl. Instr. and Meth. A420 181 (1999).

[87] A. Moroni *et al.* Nucl. Instr. and Meth. A556 516 (2006).

[88] *http://fazia2.in2p3.fr/spip/*

[89] L. Bardelli *A ROOT-based data-monitor software for the GARFIELD experiment* LNL Ann. Report. 2007.

[90] G. F. Knoll. *Radiation detection and measurement*, John Wiley & Sons, New York, (1989)

[91] Nucl. Instr. and Meth. B 194 503 (2002).

[92] N. Le Neindre, *et al.*, Nucl. Instr. and Meth. A 490 251 (2002).

[93] G.Marzocco, *Realizzazione di un sistema di trigger per esperimenti di fisica nucleare mediante dispositivi logici programmabili*, Bachelor's Thesis, University of Florence, (2010).

[94] L. Morelli *et al.* Nucl. Instr. and Meth. A 620 305 (2010).

[95] *http://root.cern.ch/drupal/*

[96] R. Mankel, Rep. Prog. Phys. 67 553 (2004).

[97] V. Avdeichikov *et al.*, Nucl. Instr. and Meth. A 501 505 (2003); Nucl. Instr. and Meth. A 466 427 (2001).

[98] J.Cugnon and D.L'Hote, Nucl. Phys. A397 (1983) 519.

[99] O.V.Fotina *et al.*, Int. Journ. of Mod. Phys. E 19 5, 6 1134 (2010); Phys. At. Nucl. 73 1 (2010).

[100] B. V. Carlson *et al.* J. Phys. Conf. Ser. 312 082017 (2011).

[101] G. Baiocco *et al.*, *Projectile Break-Up and Compound Nucleus Decay with light neutron-deficient beams provided by SPES*, SPES International Workshop, Legnaro LNL-INFN (2010).

[102] A. Brondi *et al.*, EPJ Web of Conferences 2, 04002 (2010).